Nanoengineering Si NPs and Er^{3+} distributions in co-doped a-Al_2O_3 thin films : Study of the energy transfer process towards the enhancement of the light emission at 1.5 μm

(Nano-estructuración de láminas delgadas de a-Al_2O_3 co-dopadas con iones de Er y nanopartículas de Si: optimización de la transferencia de energía nanopartícula-ion.)

Memoria presentada para optar al grado de Doctor en Física por:
Sara Núñez Sánchez

Tesis Dirigida por:
Profesora de investigación Rosalía Serna Galán

Tutor:
Catedrático José Manuel Calleja Pardo

Departamento de Física de Materiales
Facultad de Ciencias
Universidad Autónoma de Madrid

Instituto de Óptica "Daza de Valdés"
Consejo Superior de Investigaciones Científicas

Junio de 2010

Prefacio

Una pequeña historia científica...

Supongo que al lector le estará resultando extraño leer un prefacio en el comienzo de una tesis doctoral. Sin embargo me gustaría poder mostrarles las dificultades y satisfacciones que nos hemos encontrado en estos duros cinco años y medio de trabajo. Todo el proyecto de tesis comenzó desde un planteamiento y área de trabajo completamente distinto, que siendo ahora sinceros, no me satisfacía desde mi naturaleza óptica pero que mi naturaleza electrónica se consolaba ante la posibilidad de jugar con switching. Con la tozudez que aún no he conseguido aún dominar conseguimos ver conmutar luz pero no controlarla. Así que hubo que tornar el camino del trabajo y después de un año comenzamos de nuevo. Lo que en principio parece una desgracia fue una de las mayores fortunas que ha acompañado este trabajo, y así, comenzamos el camino de jugar con emisores de luz en la nano-escala y a descubrir las reglas del juego de la interacción de las nanopartículas de silicio y los iones de erbio. Volver a empezar fue duro, nueva literatura, nuevo sistema experimental pero... ¡Fantásticos experimentos!, ¡sencillos planteamientos!, los mejores de GPL aunque no te lo creas Rosalía. Pero pagamos los platos rotos de científicos expertos trabajando en un campo nuevo. ¡Cuántas veces debimos debatir Miguel la saturación de la emisión! ¡Qué obvio es ahora! Ese segundo año estuvo lleno de medidas atosigadoras buscando encontrar explicaciones a que ocurría en nuestras muestras, con una caracterización tediosa pero fundamental. Pero nadie dijo que fuese a ser fácil y entre el 2007 y 2008 las tornas volvieron a cambiar, artículos de Er^{3+} y nanopartículas de Si marcaban nuevas rutas de análisis espectroscópico y comenzaba el hundimiento de nuestra metodología de trabajo. Ya no llegaba con optimizar, había que entender el porqué. Así que 2008 y 2009 han sido años horribles, pasando de cortos APL a estar inmersa en largos PRB con ecuaciones y desarrollos que mezclaban cuántica con materiales y óptica. Así que tras este segundo varapalo a mi evolución científica, sola inmersa en algo que no controlaba y entendía, lo único que residía en mi corazón era abandonar y... surgió IOSA, con su fuerza y entusiasmo me mantuvieron a flote, mostrándome que las cosas pueden cambiar, trabajando se pueden hacer cambiar, ¡trabajando las hemos hecho cambiar chic@s!. Así que cuando estaba en el límite e IOSA ya no estaba resguardado bajo mis faldas, con 6 meses de financiación y sin apoyo institucional, apareció él, Pablo, un asturiano cabezota

y escéptico pero con unas ansias enormes de aprender. En el momento clave, encontré mi resonador científico, así que él sin ser consciente me devolvió la pasión, me incitó a una nueva evolución y este libro comenzó a crecer. 2009-2010 ha sido un año lectivo duro, unos luchando por sobrevivir mientras algunos, sin poder evitarlo, se han ido para siempre. Sin embargo no puedo dejar de tener ese sabor dulce de un año científicamente deslumbrador a pesar de haberlo pasado rodeada de cascotes cayendo, mudanzas de despacho múltiples o sin aire acondicionado.

No sé si sacaré rendimiento personal al gran esfuerzo realizado, la mayoría pensarán que ha sido una tontería, podía haber optado por un camino más sencillo. Pero yo y mi alma científica pueden sentirse satisfechas de lo que se refleja en cada una de las páginas de este libro. Senoras y señores que después de todo esto se atrevan a leer este manuscrito, espero que se diviertan lo mismo que lo he hecho yo jugando con Er^{3+}.

NUSA66
Sara Núñez-Sánchez,
Madrid, Junio 2010.

Resumen

Esta tesis es el resultado de cinco años y medio de trabajo de investigación en el diseño de nanoestructuras en lámina delgada de óxido de aluminio amorfo dopadas con iones de erbio y nanopartículas de silicio, con el fin de optimizar la distribución de dopantes en la nanoescala para conseguir mejorar las propiedades de emisión a 1.5 μm. Este trabajo se ha realizado en el *Instituto de Óptica Daza de Valdés-IO* bajo la supervisión de la *Profesora de investigación Rosalía Serna Galán.* Todas las estructuras estudiadas en esta tesis han sido producidas en el sistema de deposición por laser pulsado del *Grupo de Procesado por Láser* en el *Instituto de Óptica.* Así, el resto medidas de caracterización óptica como elipsometría o fotoluminescencia resuelta en tiemp, también han sido realizadas en las instalaciones del grupo *Grupo de Procesado por Láser* al cual pertenecen la tesinanda y su directora de tesis. La caracterización química y estructural mediante técnicas de microscopía electrónica de transmisión se realizaron durante una breve estancia en el departamento *Materials Science Division* del *Argonne National Laboratory* en Chicago-Illinois bajo la supervisión de la *Profesora Amanda Petford-Long.* El análisis composicional tuvo lugar gracias a la colaboración del *Doctor Javier García-López* del *Centro Nacional de Aceleradores-CNA*. Se llevaron a cabo medidas de catodoluminescencia en la *Universidad Complutense de Madrid* con la ayuda de la *Catedrática Bianchi Mendez* y el *Doctor Emilio Nogales.* El trabajo descrito en esta tesis ha sido publicado en revistas científicas y conferencias internacionales que se citan a continuación.

Revistas internacionales

1. R. Serna, S. Núñez-Sánchez, P.M. Roque, *Nanostructuring the Er^{3+} and Si nanoparticle distributions to enhance the 1.5 μm emission in codoped a-Al_2O_3 thin films*, ECS Transactions, 28 (3) 229-239 (2010)
2. S. Núñez-Sánchez, P.M. Roque, R. Serna and J. García-López, *Enhanced photoluminescence response of Er^{3+}-Si nanoparticle codoped a-Al_2O_3 films by controlled synthesis in the nanoscale and thermal processing*, Thin Solid Films, 518, (2009)
3. S. Núñez-Sánchez, R. Serna, J. García López, A. Petford-Long, M. Tanase, B. Kabius, *Tuning the Er^{3+} sensitization by Si nanoparticles in nanostructured as grown a-Al_2O_3 films*, Journal of Applied Physics 105 (2009)
4. J. Toudert, S. Núñez-Sánchez, M. Jiménez de Castro and R. Serna, *a-Si nanolayer-induced enhancement of the 1.54 μm photoluminescence in Er^{3+} doped a-Al_2O_3 thin films*, Applied

Physics Letters 92 (2008)

5. J.Toudert, S. Núñez-Sánchez, R. Serna, M. Jiménez de Castro, *Enhanced photoluminescence of nanostructured Er^{3+}-doped a-Si/a-Al_2O_3 thin films prepared by PLD*, Materials Science and Engineering B 146 (2008)

6. S. Núñez-Sánchez, et al., *The role of the laser fluence on the a-Al_2O_3 target in the nanostructure and morphology of VO_X :Al_2O_3 thin films prepared by PLD*, Applied Surface Science 254 (2007).

7. S. Núnez-Sánchez, et al., *Vanadium-Al_2O_3 nanostructured thin films prepared by pulsed laser deposition: Optical switching*, Applied Surface Science 253 (2007).

Comunicaciones en conferencias

Presentado por S. Núñez-Sánchez

1. *Jornadas de Jóvenes Investigadores en Óptica Visual 2010*, Madrid, Spain, 2010. *Abre las puertas de tu laboratorio: Óptica y divulgación científica.* S. Núñez-Sánchez. **Charla Invitada.**

2. *IBEDM 2009*, Tossa de Mar, Spain, 2009. *Nano-engineering of Er^{3+} and Si NP in a 2D distribution: Excited Er fraction higher than 50% in a-Al_2O_3 films*, , S. Núñez-Sánchez, P.M. Roque, R. Serna. **Oral.**

3. *IONS-5*, Barcelona, Spain, 2009. *Enhancement of 1.53 μm emission in Er^{3+}Si NPs codoped a-Al_2O_3 films: role of dopant distribution and size control in the nanoscale*, S. Núñez-Sánchez, R. Serna, M. Jiménez de Castro, J. García López, A. Petford-Long, M. Tanase, B. Kabius. Póster.

4. *Frontiers in Optics*, Rochester, NY, USA, 2008. *Performance of 1.53 μm emission in Er^{3+}Si NPs: nanostructured a-Al_2O_3 films for integrated amplifiers in silicon platforms*, S. Núñez-Sánchez, R. Serna. **Oral.**

5. *E-MRS 2008 Spring Meeting*, Strasbourg, France, 2008

   Implantation effects during PLD probed by Er luminescence in Er:Si:a-Al_2O_3 films, S. Núñez- Sánchez, M. Jiménez de Castro, R. Serna, J. García López. Póster.

   Enhancing the 1.53 μm emission in Er^{3+}:a-Al_2O_3 as grown films by nanoscale controlled codoping with Si nanoparticles, S. Núñez-Sánchez, R. Serna, M. Jiménez de Castro, J. García López, R. Serna, A. Petford-Long, M. Tanase, B. Kabius. **Oral.**

6. *CLEO/Europe-IQEC 2007*, Munchen, Germany, 2007. *Er^{3+} luminescence sensitization by Si-nanoparticles in a-Al_2O_3 thin films with a controlled nanoscale dopant distribution*, S. Núñez-Sánchez, M. Jiménez de Castro, J. Toudert, R. Serna, A. Petford-Long, M. Tanase, B. Kabius. **Oral.**

7. *E-MRS 2007 Spring Meeting*, Strasbourg, France, 2007.

   Influence of the laser fluence on the a-Al_2O_3 target in the structure and morphology of VO_X:a-Al_2O_3 thin films prepared by PLD, S. Núñez-Sánchez, R. Serna, M. Tanase, A. K. Petford-Long. Póster.

   Role of the Si nanoparticle size in the excitation of Er:Si codoped a-Al_2O_3 films prepared by PLD, S. Núñez-Sánchez, M. Jiménez de Castro, J. Toudert, R. Serna, J. García López. Póster.

8. *E-MRS 2006 Spring Meeting*, Nice, France, 2006.

   Photoluminescence enhancement in nanostructured a-Al_2O_3 films functionalized with Si nanoparticles and Er^{3+} S. Núñez-Sánchez, M. Jiménez de Castro, R. Serna. Póster.

   Vanadium-a-Al_2O_3 nanostructured thin films by pulsed laser deposition: optical switching, S. Núñez-Sánchez, R. Serna, M. Jiménez de Castro, J. García López, AK. Petford-Long, J.F. Morhanghe. Póster.

9. *3rd Nanospain Workshop*, Pamplona, Spain, 2006 *Switchable optical properties on VO_X:a-Al_2O_3 nanocomposite thin films prepared by PLD*, S. Núñez-Sánchez, R. Serna, M. Jiménez de Castro, AK. Petford-Long, J.F. Morhanghe. **Oral y Póster**

Presentado por co-autores

1. *E-MRS 2010 Spring Meeting*, Strasbourg, France, June 2010.

   Energy transfer process from Si Nanoparticles to Er^{3+}: critical dependence below the nanoscale, S. Núñez-Sánchez, P.M. Roque, R. Serna. **Oral**

   Amorphous silicon nanoparticle 2D-distributions with high density for enhanced multi-exciton generation harvesting, S. Núñez-Sánchez, R. Serna, A.K. Petford-Long, M. Tanase and B. Kabius. **Oral**

   Understanding the increase of optically excited Er ions through Si NPs by low thermal processing in optimized nanostructured systems, P.M. Roque, S. Núñez-Sánchez, R. Serna. **Oral**

   Enhanced photoluminescence performance of a-Al_2O_3:Er films due to off-axis pulsed laser deposition, R. Serna, S. Núñez-Sánchez, C. N. Afonso, F. Xu. **Oral**

2. *217th ECS Meeting*, Vancouver, Canadá, 25-30 Abril, 2010 *Tuning the RE sensitization by Si NPs in nanostructured a-Al_2O_3 film*, R. Serna, S. Núñez-Sánchez, P.M. Roque. **Charla Invitada.**

3. *E-MRS 2009 Spring Meeting*, Strasbourg, France, 2009. *Enhanced photoluminescence response of Er^{3+}-Si Nanoparticle codoped a-Al_2O_3 films by controlled synthesis in the nanoscale and low temperature processing*, S. Núñez-Sánchez, P.M. Roque, R. Serna. **Oral**

4. *IONS-5*, Barcelona, Spain, 2009. *Si NPs doped a-a-Al_2O_3 optical properties determination by spectroscopic Ellipsometry*, P.M. Roque, S. Núñez-Sánchez, R. Serna. Póster

5. *MRS Fall Meeting 2008*, Boston, MA, U.S.A., 2008. *Optimization of Si nanoparticle size in nanostructured Er-Si:a-Al_2O_3 thin films to enhance the Er^{3+} luminescence by photon and electron excitation*, S. Núñez-Sánchez , R. Serna, E. Nogales, B. Mendez. **Oral.**

6. 3^{rd} *EPS-QEOD Europhoton 2008*, Paris, France, 2008. *Efficient 1.53 μm emission in Er^{3+}-Si NPs codoped and nanostructured a-Al_2O_3 films for waveguide amplifiers*, R. Serna, S. Núñez-Sánchez, M. Jiménez de Castro, A. Petford-Long, M. Tanase, B. Kabius. **Oral.**

7. *15th International Conference on Luminescence and Optical Spectroscopy of Condensed Matter (ICL'08)*, Lyon, France, 2008. *Energy transfer processes in nanoscale controlled Er-Yb doped a-Al_2O_3 waveguides*, J. Cortes, R. Serna, S. Núñez-Sánchez, C. N. Afonso. **Charla Invitada.**

8. *9th International Conference on Laser Ablation 2007 (COLA07)*, Tenerife, Spain, 2007. *Enhancement of 1.53 μm emission in $Er^{3+}Si$ NPs codoped a-Al_2O_3 films: role of dopant distribution and size control in the nanoscale*, S. Núñez-Sánchez, R. Serna, M. Jiménez de Castro, J. García López, A. Petford-Long, M. Tanase, B. Kabius. Póster

9. *16th International Conference on Dynamical Processes in Excited States of Solids - DPC07*, Segovia, Spain, 2007. *Efficient luminescence response for nanoscale controlled Er-Yb distribution in a-Al_2O_3 waveguides*, J. Toudert, S. Núñez-Sánchez, M. Jiménez de Castro, R. Serna, J. Cortes, CN. Afonso, Y.Luo, P. Hoffmann. **Oral.**

10. *CLEO/Europe-IQEC 2007*, Munchen, Germany, 2007. *Efficient luminescence response for nanoscale controlled Er-Yb distribution in a-Al_2O_3 waveguides*, J. Toudert, S. Núñez- Sánchez, M. Jiménez de Castro, R. Serna, J. Cortes, CN. Afonso, Y. Luo, P. Hoffmann. **Oral.**

11. *E-MRS 2007 Spring Meeting, Strasbourg*, France, 2007. *Enhanced photoluminescence of nanostructured multilayer a-Si/Er^{3+}:a-a-Al_2O_3 films prepared by Pulsed Laser Deposition*, J. Toudert, S. Núñez-Sánchez, M. Jiménez de Castro, R. Serna. **Oral.**

12. *E-MRS 2006 Spring Meeting*, Nice, France, 2006. *The importance of controlling the Si nanoparticle-Er^{3+} separation for efficient Er^{3+} luminescence sensitization in codoped nanostructured a-Al_2O_3 thin films*, S. Núñez-Sánchez, M. Jiménez de Castro, R. Serna. **Oral.**

13. *E-MRS 2005 Spring Meeting, Strasbourg*, France, 2005. *Pulsed Laser Deposition and optical response of VO_X:a-Al_2O_3 nanocomposite thin films*, S. Núñez-Sánchez, R. Serna, M. Jiménez de Castro, J. García López. Póster.

14. *2nd Nanospain Workshop, Barcelona*, Spain, 2005. *Controlling the structure at the nanoscale to improve the response of Optical systems*, R. Serna, J. Gonzalo, J. Solís, J. Siegel, J. Margueritat, H. Fernández, V. Díez-Blanco, V. Resta, S. Núñez-Sánchez, M. Jiménez de Castro, C. N. Afonso. Póster.

Contents

Chapter 1

Introduction

Since 1936 Allan Turing and colleagues established the fundament of the modern computing, the humans have been looking for the control and processing of the information in order to create complex systems that could help us in our daily life and improve our social welfare state.[1, 2] The basic design unit is the switch that allows us to define binary states with which it is possible to compute and generate complex functions using algebraic functions. The contributions of John Von Neumman defined the new computer architectures, and the first general-purpose electronic computer ENIAC (Electronic Numerical Integrator And Computer) was created at the 1946, occupying whole rooms and using thousands of vacuum valves, crystal diodes, relays, resistors and capacitors and weighing 30 short tons. [3, 4] From the discovery of the bipolar transistor in the 1947 by John Bardeen and Walter Houser Brattain [5] and William Bradford Shockley [6] at the Bell Telephone Laboratories and the development of the first monolithic integrated electronic circuit by Jack Kilby [7] at Texas Instrument in the 1958 (with a size of 12mm x 1.5 mm^2 approximately) the number of integrated electronic components and the complexity of the circuits have grown exponentially allowing to create the most advanced robots and reduced computers from a miniaturized design unit, the semiconductor transistor.

A major challenge in the microelectronics industry is the reduction of the size of the components, specially the transistor, in order to integrate more complex circuits in the same area reducing the production cost per unit. However the reduction on size of the individual components causes the appearance of new fundamental physical effects and new physical properties that can not always be completely controlled. Although, there has been an impressive advance at the device and technology level during the last decade, the progress in the development of new system architectures dealing with billions of transistors is scarce. In this sense, new architectures for parallel data processing are under still current development.[8] In this context the development of integrated optical processing devices is presented as a promising alternative due the specially properties of photons as coherence, that allows to multiplex the optical signal at different wavelengths without interference

between them. Moreover the new properties of reduced semiconductors at the nanoscale such as quantum wells and quantum dots can be used to prepare active materials to develop optical sources, detectors or to obtain complex functionalities. The work reported in this thesis is a thoroughly study of the optical properties of an special nanoengineered material in order to obtain an efficient optical gain medium that can be used to efficiently process the light in a device of reduced size, produced by a fabrication technique compatible with the microelectronic industry and that can be integrated with other optoelectronics components.

1.1 Integrated Optics and the evolution of the microelectronics technologies

The revolution in the modern optics was the invention of the laser by T.H. Maiman in the 1960 at Hughes Research Laboratories in Malibu, which allowed fabrication of coherent light sources with exceptional properties. The research on Integrated Optics started when S.E Miller proposed the concept of integrated optics in the 1969 and he emphasized the similarity between the planar optical technology and the microelectronic circuits. [9] In the early of $70's$, various materials and processing techniques for optical waveguide fabrication were developed. However at the end of the seventy decade the research on integrated optical circuits decreased due to the difficulties on the design commercial structures in a short term and the expensive prize and difficulty of integration of lasers and Light Emitting Diodes (LEDs). Moreover the materials required to the optical devices are different from those used in microelectronics adding new difficulties. Therefore the researchers and developers efforts were focused on the preparation of glass optical-fibers and the enhancement of the performance of the electronic circuits, due their short-term profits. [10] Actually the advances on the microelectronic techniques in order to produced materials controlled at the nanoscale has driven the optoelectronics to the nanophotonics and towards a plausible integration of photonic circuits.

It is outmost importance to realize that the background or the origin of the integrated optics is different than the integrated electronics. While the integrated electronic started with the obtention of the first integrated transistor to use it as design units, the optoelectronics started when a broad branch of functionalities had been defined previously in the electronic and are used in complex circuits. Thus, until now, despite the large number of optical structures designed as power splitters, waveguide reflectors, directional couplers, polarizers, phase modulators, etc; [11], a device including optical photon storage and photon amplification has not been developed in a switch device in order to obtain similar control on the photon flux than the transistor acts on the electron flux in an electronic transistor.

Therefore in the Integrated Optics there are two design alternatives:

1. Find structures and materials that show similar behavior than the electronic transistor in order to profit of the previous development in high-level electronic design automation tools.

2. Find structures and materials that reproduce the behavior of functions of complex devices as amplification, rectification, etc. Thus, the complete circuit is considered a black box, with inputs and outputs.

The development of the integrated optics technology requires new materials that can be used as active medium to obtain complex functionalities, but these materials have be able to compatible with the C-MOS technology and actual microelectronic industry. Thus the processes involved in the material processing and in the structure fabrication have to be easily incorporated in a microelectronic foundry and with reduced fabrication steps. The evolution of the nanotechnology production techniques offers new alternatives in the production of active structures applicable in integrated optics circuits. The nanomaterials give new possibilities of photon flux control by defined refractive index periodic structures or materials as nanocomposites and open the opportunity of obtain customized functionalities in waveguide configurations. The aim of this thesis is to study the performance of a new nanostructured material based on Er^{3+} and Si NP— doped a-Al_2O_3 with control of dopants separation in the nanoscale and varying their content and distributions to enhance the emission at 1.53 μm for potential amplification.

1.2 Amplification and Er^{3+} and Si NP doped systems. Control in the nanoscale

The more basic functionality in analogical electronics is the amplification. The MOS-FET and bipolar transistor plays the role of limited amplifiers, therefore the tuned electronic amplifiers make use of resonant circuits with resistances, inductors and capacitors to limit the gain of the amplifier to the band of frequencies of interest. The Figure 1.1a shows the circuit corresponding to the most popular operational amplifier μ741 composed by 22 bipolar transistors, 1 capacitor and 11 resistances.[12] The electrons injected to the input signal comes from the continuous source connected between $+V_S$ and $-V_S$.

In contrast, in optics, the underlying principle for achieving coherent amplification of light is stimulated emission of radiation. Therefore the frequencies, work region and gain values are established by the atomic levels of the atomic entities or bands of absorbers and emitters used to dope the active medium.[13] The Figure 1.1b shows a scheme of an Er^{3+} ion that acts as emitter tuned with the pump energy and the signal to amplify,

thus when an electron is excited to the high atomic levels the photons from the incident signal incite the des-excitation route that provoke the stimulated emission increasing the coherence emission tuned the signal and proportional to the signal power.

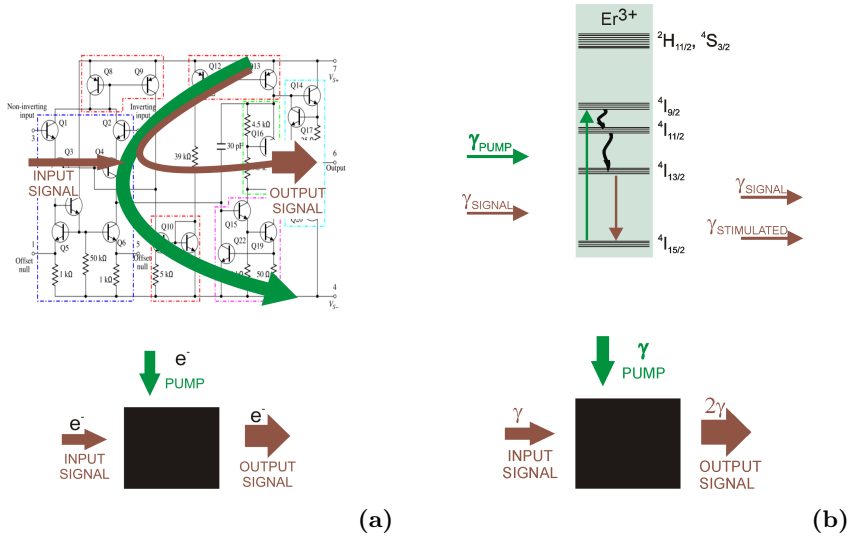

Figure 1.1: Comparison of fundamentals of the electronic and optical amplification. Figure 1.1a shows the circuit of the most used operational amplifier in analogical electronics, the μ741. The green arrows represent the flux of electrons that is injected to the input signal. The input and output is represented by the dark red arrows. Figure 1.1b shows a scheme of the stimulated emission produced in an Er^{3+} ion when it is pumped by two resonant wavelengths at different energies. The green arrows represent the pump flux and the dark red arrows represent the amplified signal.

In an electronic amplifier the flux of electrons is increased for a band of frequencies of interest, however in an optical amplifier we have to establish the working wavelength range to amplify. During the information age a large industrial development and institutional investment have been focused on bands of frequencies of interest for the telecommunications technologies based on silica fibers that have allowed the optical transmission over long distances with low attenuation, a high-bandwidth and a low manufacturing cost. But the wavelength bands were limited by the high transparency range of the silica established in the telecommunication windows. In this technological revolution the fiber optical amplifiers based on silica doped with Er^{3+} (EFDA) have been essential due to the overlap of the Er^{3+} emission band at 1.54 μm with the third window of optical communications. Therefore Er^{3+} doped integrated waveguide in a reduced size is essential for the a complete integration of optical circuits.

However, the development of integrated optical amplifiers waveguide is not trivial. While in the Erbium doped fiber amplifiers (EDFA) high gain values are reached due the possibility of large-doped optical fiber length, the integrated amplifiers require to obtain a high gain in a few centimeters. In addition the absorption cross section of Er^{3+} is low

(10^{-21} cm^2) and high concentrations ($10^{19}-10^{20}$ Er/cm) of dopants are required in a small device.[14, 15] One of the key points in design and production of materials for integrated amplifiers is how to incorporate high concentrations of dopant without erbium aggregation or Er^{3+} photoluminescence quenching (as coperative up-conversion, migration, etc) due to the interaction between adjacent Er^{3+} ions. Therefore optimize the spatial distribution of ions at the nanoscale is essential in order to obtain efficient amplifiers with a reduced size.[16, 17]

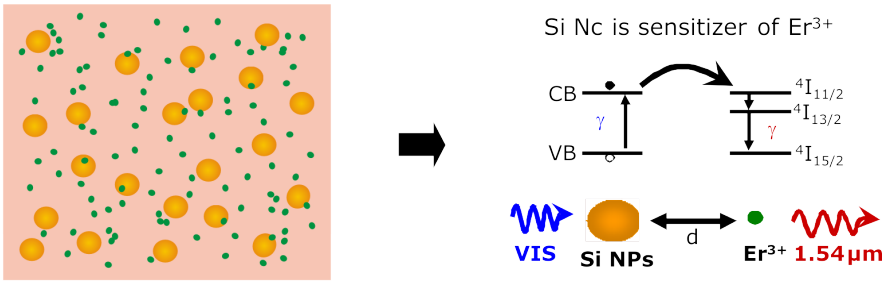

(a)

Figure 1.2: Scheme of an Er^{3+} and Si NP randomly doped material and the interaction of Si NPs and Er^{3+} ions.

Besides improving the distribution of Er^{3+} ions is necessary to optimize the pump bandwidth of Er^{3+} that can be excited only in the range of very narrow wavelengths, pumping wavelengths of 980nm and 1430nm in the most commonly traded devices. However the absorption of the Er^{3+} ions is poor with low absorption cross sections of 10^{-21} cm^{-2} orders of magnitude. In the last decade numerous studies about the possibility of used silicon nanocrystals as sensitizers of Er^{3+} in based silica (SiO_2) materials have been made (see Figure 1.2).[18] The silicon nanocrystals absorb very efficiently photons in continuous bands in the ultraviolet-visible with absorption cross sections from 10^{-19} cm^{-2} to 10^{-16} cm^{-2} that can be tuned by controlling the size of the nanocrystals and transfer energy to closer Er^{3+} ions. [19, 20] Moreover it has been proved that it is possible to obtain energy transfer from amorphous nanoparticles (NPs) to Er^{3+} ions and it is not necessary to obtain crystalline nanostructures.[21] Therefore, the most recent works are focused on the optimization of the fractions of Er^{3+} that could be excited through Si NPs and the study of the physical properties of the Er^{3+}-Si NP interaction in order to estimate the fundamentals parameters to obtain an accuracy control on the energy transfer process.

Actually low fractions of excited Er^{3+} has been reported and only recently percentages close to the 23% has been obtained while fractions of excited Er^{3+} higher than the 50% are necessary to achieve gain. [22, 23] Therefore, in order to optimize the number of Er^{3+} ions is essential to develop techniques to control the spatial distribution of the two dopants on the nanometer scale, whatever the composition of the host to control the

region of contact of the Er^{3+} ions and the Si NPs.[24, 25] Moreover the control on the nanoscale allow us to increase the concentration of ions without quenching phenomena and improving the relationship of Si NP-ion coupling and controlling the pump band with the size of the Si NPs.[17, 26]

The thin films in this work have been produced by alternate pulsed laser deposition (a-PLD) that it is a well now deposition technique in the microelectronic industry. This method of preparation allow us to control of the composition of the host independently of the dopants, therefore all the results can be extrapolated to other host of different compositions. Moreover the dopants are deposited in situ independently of the host and thus their position in the depth profile can be fine controlled. Also, by a-PLD is possible to obtain high density of Si NPs distributed in two dimensional plane (2D dopant distributions) allowing a high percentage of contact between dopants when they are deposited sequentially.

1.3 This thesis

The objective of this thesis is the design and preparation of nanostructured Si NPs sensitized Er^{3+} films to enhance their emission at 1.53 μm. This objective involves two main aspects. The first one from the materials point of view to determine the deposition conditions, dopant concentration and specially their spatial distributions by controlling their separation in the nanoscale. The second one is the thorough study of the energy exchange between Si NPs and Er^{3+} through the analysis of the photoluminescence response from the nanostructured films.

The method used to prepare the nanostructured films has been pulsed laser deposition from separate targets. This is a technique that allows to deposit dense films with good optical properties. The sequential deposition of the different components of the film from separate targets allows to deposit in a single step process two dimensional distributions of the dopants whose separation in the growth direction can be controlled accurately. This has allowed in this work to focus the study of the Si NPs-Er^{3+} energy exchange on the influence of the spatial distribution of dopants at the nanoscale. The independent deposition from the Si target to deposit the Si NPs has enabled the formation of Si NPs with different average sizes thus making possible the tuning of the Si NPs energy band-gap. In this study the use of a-Al_2O_3 instead of the conventional SiO_2 used in most works has shown the additional advantage of allowing to differentiate the local environment of the emitting Er^{3+} ions due to the different spectral characteristic of Er^{3+} light emission embedded in a-Al_2O_3 or in Si/SiO_2 hosts. This permits to obtain accurate information on the Er^{3+} location below the nanoscale. Finally a special characteristic of this study is that most of the photoluminescence characterization of the films performance in as

grown conditions thus unwanted diffusion processes that can induce the modification of the nanoscale engineered structures. This is very particular to this work since in most of previous works annealing of the Si NPs-codoped systems as part of their synthesis process. Only some annealing results will be discussed in order to add light to specific aspects of the material properties or to show how indeed annealing can alter the Si NPs to Er^{3+} energy transfer in optimized structures up to the point to inhibit it.

The thesis manuscript has been divided in four parts and two special chapters, the general introduction and the general conclusions. Every Chapter has a short preface and introduction.

The beginning is Chapter 1 that corresponds to the global introduction. Part I describes our experimental approach. The Chapter 2 describes the first steps in the design process of the Er^{3+} and Si NP doped a-Al_2O_3 host, the properties of the individual components, the growth process and how it is possible to obtain a high accuracy in the nanoscale by controlling in situ the the host, Si NPs and Er^{3+} deposition. In Chapter 3 the final designs of the Er^{3+} and Si NP doped a-Al_2O_3 nanostructures are described. It includes a first approximation to the Er^{3+} and Si NPs interaction system. It includes controlling the local position of Er^{3+} and Si NPs dopants below the nanoscale, controlling the Er^{3+} and Si NP 2D-distributions and their correlation, and finally, optimizing the Si NP sizes and the post-deposition treatments.

Previously to analyze the best parameters to optimize and tune the transfer process from the Si NPs and Er^{3+} ions a thoroughly study about the 2D Si NP distributions were done. Therefore Part II is focused on the properties of the amorphous Si NPs. Their structural, chemical local properties are analyzed in Chapter 4. Due to the difficulties to determinate a Si NP size through the electron microscopy images, we turned to the study of their optical absorbtion in order to establish a Si NP size in Chapter 5. The direct or indirect character and amorphous quality of the Si NPs are analyzed in order to obtain a reliable relation between the absorption band-gap and size. Once the Si NP size was established the parameters of the 2D distributions of Si NPs were determined in Chapter 6. Finally, in Chapter 7, the a-Al_2O_3-Si NP interface is analyzed in order to establish the role of the surface defects on the Si NP photoluminescence and in the Er^{3+}-Si NP interaction mechanisms.

The Part IV reports the first attempt to optimize the energy transfer from Si NPs to Er^{3+} ions maximizing the Er^{3+}-Si NP contact. Thin films formed by Si NPs of the same size but however with different separation distance between dopants are studied. Therefore, in Chapter 8 we are able to conclude that the most efficient thin film dopant configuration is when the Er^{3+} ions are in contact with the Si NPs. In Chapter 9 we study

how to maximized the contact between dopants and how distances below the nanoscale affects to the temporal response of the emission of Er^{3+}. A thoroughly study about how the physical processes inherent to the pulsed laser deposition affects the accuracy of the control on the distance between dopants, and thus the interaction mechanism including the back-transfer phenomena are shown in Chapter 10.

The extreme sensitivity of the Er^{3+}-Si NP interaction to the Er^{3+}-Si NP distances below the nanoscale has been demonstrated in the Part IV. Therefore amorphous aluminium oxide (a-Al_2O_3) nanostructured thin films doped by erbium ions (Er^{3+}) and amorphous silicon nanoparticles (Si NPs) of different Si NP sizes were produced in a maximized Er^{3+}-Si NP contact configuration in order to analyze the optimization of the Er^{3+} ions response nano-engineering the 2D-distributions of the two dopants and analyzed in Part V. The Chapter 11 shows that the amount of Er^{3+} excited dependent mainly on the fraction of achievable Er^{3+} that can be controlled tuning the Si NP and Er^{3+} 2D-distributions that define the percentage of Er^{3+} in contact with the Si NPs. A deep study on the mechanisms involved in the Er^{3+} and Si NP extreme coupling regime is in Chapter 12. Moreover the special features observed in the films doped with the smallest Si NPs are studied in Chapter 13, we related it to the number of defects as a function of the Si NP size and the deposition conditions that can be affected the priority of every interaction mechanisms. In Chapter 14 the Er^{3+} excitation and des-excitation dynamics are modeled by kinetic de-excitation equations obtaining fractions of excited Er^{3+} higher than 50% and closer to geometric parameters of the 2D Si NP distributions.

Finally, thermal processing effects on the Er^{3+} emission and to the spatial configuration of dopants is analyzed in Chapter 15 of the Part V.

At the end of the manuscript the Chapter 16 contains the global conclusions.

Part I

Experimental approach. Designing the Er, Si: a-Al_2O_3 nanostructures

Chapter 2

Designing nanostructured doped films

In this Chapter we discuss the fundamentals of nanoestructuring Si NPs-Er^{3+} doped thin films. The experimental approach in this work has been as follows: first the distance between Er^{3+} and Si NPs was optimized, second the Si NP average size and distribution was studied. These studies have been performed embedding the dopants in an amorphous aluminium oxide host (a-Al_2O_3)

2.1 Nanostructuring the dopant distribution

Control the distance between the Si NPs and Er^{3+} ions requires synthesis methods that allow an independent control of the Si NPs, Er^{3+} ions and host deposition conditions. An accurate control of the Er^{3+} ion and Si NP distribution is very difficult to achieve with most of the synthesis techniques.

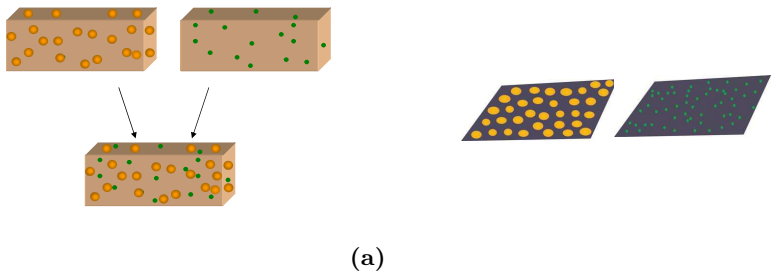

(a) (b)

Figure 2.1: Figure 2.1a. Schematic of 3D dopants distributions. Figure 2.1b. Schematic of 2D dopants distribution. The orange drops correspond to the Si NPs and the green points to the Er^{3+} ions.

Previous studies have shown that Si NP size and Er^{3+}-Si NPs separation are critical parameters that control the Er^{3+} sensitization by Si NPs, and therefore the luminescence response of the system. Some dopant distribution as multilayered structures restrict the dopants position in the plane so, their location is controlled in a random two dimensional distribution (2D-distribution).[27, 28] However, even in this case, the control of the Er^{3+} location is limited because the Er^{3+} ions are deposited embedded in the host even in this configuration. These layers are controlled in thickness and separation to the Si NP layers, but the Er^{3+} are distributed randomly within a host layer therefore limiting the control of the ions location respect to the Si NPs.[29] In addiction, in all these works, thermal process was necessary for the silicon aggregation in order to induce the Si NPs formation. The final Si NP size and the activation of the Er^{3+} ions are simultaneous controlled by the temperature reached in the thermal process. Nevertheless these two processes might not need the same conditions for optimization. Moreover the diffusion processes necessary to form Si NPs cause a non controlled dopant distribution and the change of the degree of relaxation-crystallization of the Si NPs is different as a function of the Si NP size [30]. For these two reasons, techniques that imply annealing procedures are not suitable to obtain thin films with a controlled location of dopants, and at the same time to form Si NPs with quality independently of the Si NP size. [20]

The questions are: 1.- *how to obtain a control on the Er^{3+}-Si NPs separation?* and 2.- *how to obtain a Si NP size controlled independently of the dopants location?*. As it usually

in physics, one way to solve a problem is reduce the number of degrees of freedom of our system **from 3D-distributions to 2D-distributions**. Our experimental approach is to eliminate the annealing process and restrict the dopant position in the plane, depositing them independently and independently of the host and using the special features of the PLD to control the distance between dopants below the nanoscale. The independent deposition will also allow to select the Si NPs size without affecting the separation of the Er^{3+} ions. Nevertheless Er^{3+} and Si NP random distributions in the plane are obtained.

Alternate pulsed laser deposition (PLD) offers the possibility of obtaining engineered structured thin films in which the ion-ion and ion-NP separation can be controlled in the nanometer range. The alternated Pulsed Laser Deposition (PLD) allows the **in situ formation of Si NPs** and **in situ deposition of optically active** Er^{3+} [16] obtaining a deposition of dopants initially *not necessarily embedded in the host.* The Si NPs **are formed** during the deposition process over the a-Al_2O_3 layer surface follows a Volmer-Weber growth process (see Figures 2.2a and 2.2b), as has been reported for metal NPs such as Cu and Ag.[31, 32] . The instantaneously independent ablation of Er target allows to deposit an in plane random distribution of Er^{3+} ions independently of host (see Figure 2.2c).[16] These especial features and the alternately instantaneous ablation of independent targets allows us to control:

1. The composition of the host independently of the composition and content of dopants.
2. The deposition in situ and independently of Er^{3+} and Si NPs.
3. The dopants distribution in the depth profile.

And everything in situ in a **one step** process at **room temperature** and without uncontrolled diffusion due to annealing process, allowing to obtain well defined structures for the study. This procedure opens a route to the development of one step low-temperature processing for co-doped nanostructured integrated devices.

2.2 Properties of the thin film components

Prior to the preparation of the nanostructured films we have studied the optical properties of Si and a-Al_2O_3 produced by PLD. So a thin layer of silicon has been deposited on a glass substrate and a thin layer of a-Al_2O_3 on a silicon ones. Subsequently the optical properties have been measured by spectroscopic ellipsometry. After that, the conditions to produce Si NPs and the parameters to control the Si NP size are studied.

2.2.1 a-Al_2O_3 host

Although most studies on Si NPs-Er^{3+} co-doping have been performed for silica, further understanding of the energy transfer from the Si NPs to the Er^{3+} ions may be achieved by

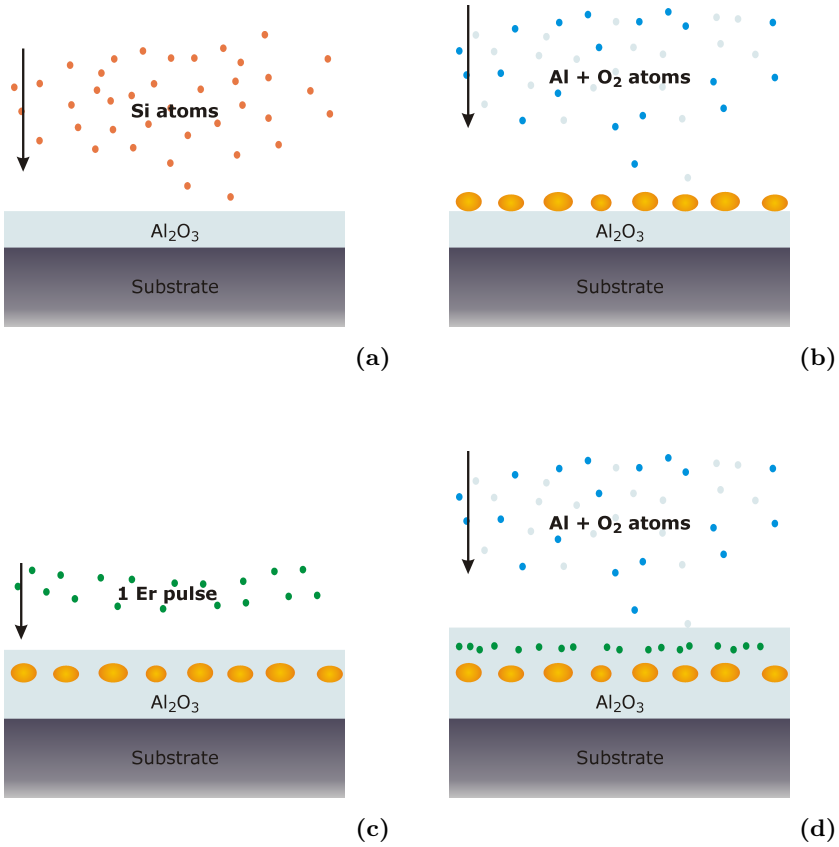

Figure 2.2: X-section schemes of sequences of the single step deposition method. 2.2a The Si NPs grew over the a-Al_2O_3 layer. 2.2b The Si NPs are cover by a thin a-Al_2O_3 layer. 2.2c Only one pulse was used to doped the nanostructure. 2.2d the Er^{3+} ions are separated form the Si NPs by a thin a-Al_2O_3 layer.

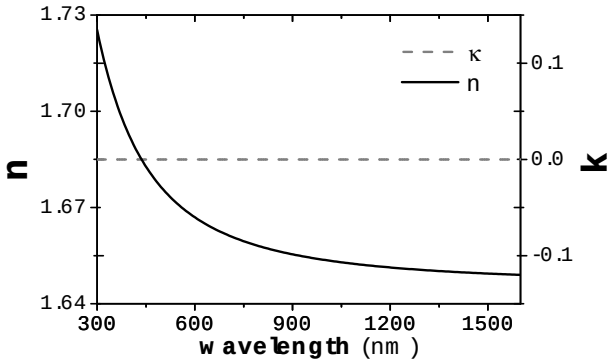

Figure 2.3: Real part of the refraction index and absorption of the a-Al_2O_3 produced by PLD

studying the efficiency of such energy transfer in non silica-based materials. Of these, we have selected the amorphous aluminum oxide (a-Al_2O_3) because it has been demonstrated to be an excellent host for Er^{3+} ions due to the high Er solubility and lower phonon energy compared to silica. In addition, the a-Al_2O_3 is a material with a wide transparency range (0.15-5.0μm).[33, 34] This allows us to have flexibility in the range of pumping the amplifier will only bounded by the characteristics of our Si NPs and ions doping. Indeed a net optical gain and losses have been reported for an Er^{3+}implanted Al_2O_3 waveguide prepared by sputter deposition[35] and more recent results have also demonstrated the fabrication of integrated ring lasers. On the other hand it has a high refractive index with respect to silica ($\Delta n > 0.20$), which allows the realization of planar guides on SiO_2 with high confinement and compatible with current silicon technology.

The Figure 2.3 shows the real and imaginary parts of the refraction index ($n = n + i\kappa$) fitted from the experimental ellipsometry raw data using a Cauchy model for the dispersion equation. The **absorption is negligible in all the optical range** while the real part of the refraction index decreases as a function of the wavelength. The low Er^{3+} content of the thin films does not change the optical properties of the a-Al_2O_3, and it has not been detected by ellipsometry or transmission measurements.

2.2.2 Silicon- Silicon NPs

a-Al_2O_3 thin films with Si NPs within were prepared by ablation from a pure polycrystalline Si target at room temperature. Therefore a first analysis of the optical properties of the silicon thin films produced by PLD will help us to establish an approximation to the structure of the Si NPs. The Figure 2.4 shows the optical constants of silicon produced by PLD (Si-PLD) and two reference materials, amorphous silicon (a-Si) and crystalline silicon (c-Si).[34] The optical constants of the silicon produced by PLD have been obtained by fitting spectroscopic ellipsometry data to a Tauc-Lorentz model. In the Figure 2.4 it is clear that the optical properties of Si-PLD are similar to those of the a-Si,

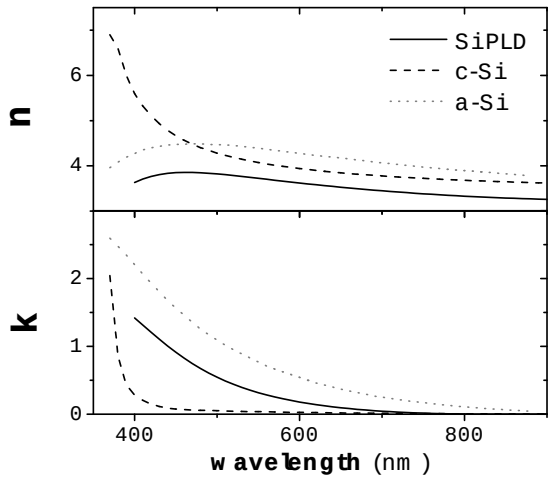

Figure 2.4: Real part of the refraction index and absorption for the crystalline silicon (c-Si, black dashed line), an amorphous silicon (a-Si, dark grey dot line)[34] and the silicon deposited by PLD (Si-PLD, black continuous line).

revealing the amorphous nature of the silicon deposited by PLD. The differences in the optical properties between the two a-Si thin films as related to differences in the amorphous quality (Figure 2.4). Thus, the **Si nanostructures produced by PLD are going to consist of amorphous silicon entities**. This will be confirmed by transmission electron microscopy in the Chapter 4.

2.2.3 Er^{3+} doped a-Al_2O_3 layers

Only one Er^{3+} pulse per layer is deposited to avoid clustering and prevent the formation of very high in-plane Er density areas and therefore reduce the energy migration, co-operative up-conversion and cross relaxation phenomena probabilities. The in-plane concentrations are changed by the laser energy density used to ablate the Er target. The Er^{3+} absorption is not detectable by optical measurements and therefore Er^{3+} content are obtained by RBS data.

2.2.4 Growth process. Control of host and Si deposition

a-Al_2O_3 thin films doped with Si NPs and Er^{3+} have been produced by alternated-PLD. The thin films have been grown in **vacuum atmosphere** (P$\sim 10^{-6}$ Torr) and **room temperature** on silicon and fused silica substrates. An ArF excimer laser was focused alternately on the independent silicon, metallic erbium and ceramic Al_2O_3 targets. The size of the Si NPs is controlled with the number of laser pulses used to ablate the Si target in each Si NPs layer deposition (see Figures 2.2a and 2.2b). One pulse per layer is used. The separation between the Si NP layer and Er^{3+} layer is controlled depositing an thin

intermediate layer of a-Al_2O_3 (see Figures 2.2b and 2.2d).

The deposition process was controlled by *in situ* reflectivity measurements during the thin films growth process. A diode laser at 670 nm was used to obtain the variations of the light reflected by the (*substrate + thin film*)-set at this wavelength. The variation of the intensity of the reflected beam was recorded in a computer using a silicon detector and standard lock-in techniques. From these data it is possible to simulate the reflectivity of the thin film as a function of the deposition time and then it is possible to determine the deposition rate of every material (detailed elsewhere). PONER TESIS AMELIA, poner algo del cambio de índice.

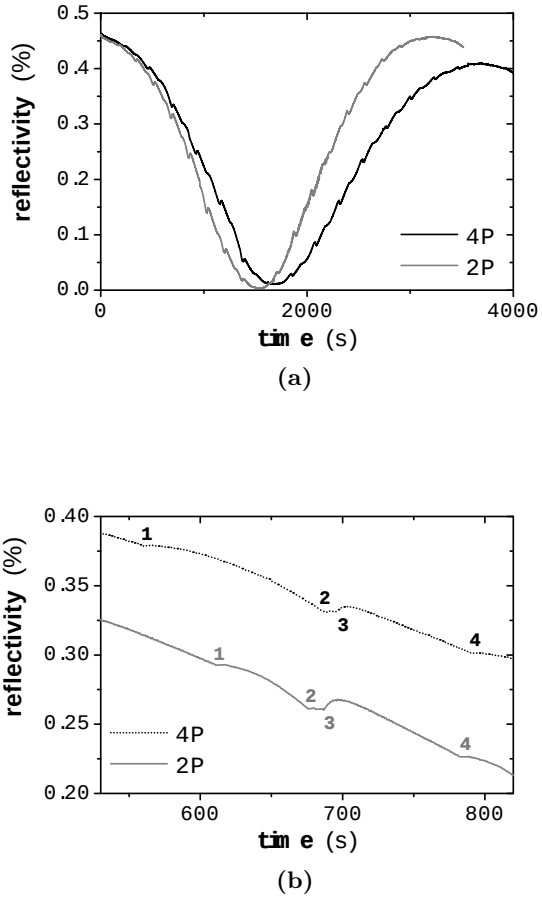

Figure 2.5: Evolution of the reflectivity of Si NP doped a-Al_2O_3 thin films during the growth process for two thin films containing Si NPs of different sizes. The parameter P is the number of pulses selected to form the smaller Si NPs in this thin film series. The Figure 2.5b shows a detail of the reflectivity evolution where the changes in the target are labeling with numbers.

In order to determine the initial amount of silicon to deposit and form Si NPs the variation of the reflected beam intensity as a function of time during the silicon deposition process was analyzed. The silicon calibration samples were grown on glass substrates. At the early growth stages the reflected beam should not change and must remain constant

due the diode emission wavelength at 670 nm. From the literature the band gap of amorphous Si NPs is from 1.5 eV to 4 eV (820nm-300nm),[36] then for the smaller Si NPs the absorption band will be located bellow the diode wavelength emission (670 nm) and only when a continuous silicon film is produced the reflectivity must show an increase. Therefore this allows to define the limit to deposit Si NP in defined conditions.

The Figure 2.5a shows the temporal evolution of the reflectivity during the growth for two a-Al_2O_3 thin films containing Si NPs of different sizes and therefore the time to deposit the silicon was different. The value P represents the initial value of pulses used to form the smaller Si NPs and selected in this thin film series. The reflectivity of the $4P$ thin film reach the minima and maxima later than the $2P$ due to the differences in the silicon deposition time. In addition the difference in the position of the Si NP band gap affects the evolution of the reflectivity as a function of the deposition time. Therefore the $4P$ curve is attenuated as a function on time because the $4P$ thin film is formed by Si NPs with a size that absorb in the laser diode emission wavelength while the Si NPs within in $2P$ are complectly transparent at 670 nm as it is observed by optical transmission measurements (see Figure 2.6).

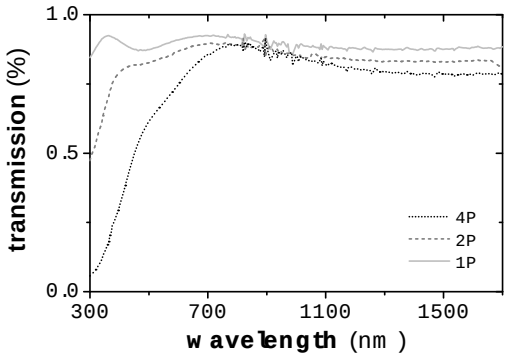

Figure 2.6: Transmission measurements of Si NP doped a-Al_2O_3 thin films with Si NPs of different sizes. The parameter P is the value of pulses selected to form the smaller Si NPs in this thin film series.

The in situ reflectivity measurements also allows to determine the moment when the Si NPs are covered by an a-Al_2O_3 layer. A zoom of a part of the Figure 2.5a is represented in the Figure 2.5b. The curves have been displaced in vertical for a better observation. From the time labeled 1 to the time labeled 2 the silicon is deposited. During this time (1 to 2) the reflectivity increases slightly due to the higher refractive index of Si, however during the a-Al_2O_3 deposition (from 3 to 4) the values of the reflectivity are recovered and then it can be considered that the Si NPs are complectly covered by the a-Al_2O_3. The flat from 2 to 3 points is just the time to change the targets pass through the Er^{3+} target.

The Si NP size can be tuned selecting the number of pulses to use to ablate the silicon

target. The variation of the absorption of the Si NPs as a function of the Si NP average size allows us to determine the average diameter of our Si NPs through transmission measurements (Figure 2.6, the analysis method is detailed in the Chapter 5).

2.3 Summary

In this approach a route to obtain doped a-Al_2O_3 films with nanostructured Er^{3+} and Si NP distributions has been defined. This is done by distributing each type of dopant in 2D-distributions, in which the Si NP size and host composition is controlled independently. Finally the Er^{3+} ions are deposited initially not embedded in the host and the distance between dopants is controlled by depositing intermediate a-Al_2O_3 layers with controlled thickness.

The silicon deposited by PLD is amorphous and thin films doped by Si NPs with different average sizes can be obtained by changing the number of the pulses used to ablate the silicon target.

Chapter 3

Er^{3+}, Si NPs: a-Al_2O_3 nanostructures and post-processing treatments

In this chapter the nanostructures that will be studied are defined. The thin films are optically active in as grown conditions, therefore our as grown thin films produced by alternated-PLD are specially designed and useful to study the Si NP size dependence on the Er^{3+} photoluminescence in Er^{3+}-Si NP doped systems with no Si NP quality dependence and changing the dopants distributions in the nanoscale. The nanostructured a-Al_2O_3 thin films were designed changing parameters such as the number of pulses used to ablate the silicon or the order of the dopants deposition in the deposition sequence.

Due to the fact that the Er^{3+} ions available to excited through the Si NPs can be affected by the presence of defects in the as grown thin films, two post-processing annealing procedures are suggested to improve the PL performance but trying to maintain the initial dopant distributions.

3.1 Controlling the Er^{3+} and Si NPs interaction distance

The films have been structured in the growth direction in order to maintain the Er^{3+} ions and the Si NPs in well-defined 2D-distribution layers with a controlled separation at the nanoscale, and thus to potentially tune the energy transfer from the Si NPs to the Er^{3+}. The Si NPs are formed in situ during deposition, and the films **have not been annealed after deposition**. As a result the Si NPs remain amorphous and the film is not modified by diffusion processes that might modify the original structure, as in most previous reports.[37, 38, 39, 40]

3.1.1 Test Er^{3+} and Si NPs doped a-Al_2O_3 system

The schematic structure of the films designed and prepared is shown in the Figure 3.1. Each film consists of nine Si NP single layers, each of which is sandwiched between five Er^{3+} layers on each side. The Er^{3+} layers are separated between them by 7 nm thick a-Al_2O_3 layers in order to minimize quenching of the luminescence due to Er^{3+}- Er^{3+} interaction.[17] Films with **different nominal separations s=0, 4, 7, 11 nm** between the Si NP layer and the first Er^{3+} layer on either side have been prepared by depositing a controlled amount of a-Al_2O_3. Note that the Er^{3+} ions are contained in the same layer as the Si NPs for the s=0 nm film. A single pulse on the Er target has been used to deposit the Er^{3+} ions.[26, 17] For the Si deposition 500 pulses on the Si target have been used in order to induce the formation of Si NPs. Finally, in order to obtain films with the same total thickness, and thus to compensate for the different values of s in each film, two a-Al_2O_3 buffer layers of thickness t have been deposited, one next to the substrate and another capping the film. The schematic structure of the film starting from the substrate can be described as *substrate / t-a-Al_2O_3 / 9×{5×a-Al_2O_3:Er / s-a-Al_2O_3 / Si NPs / s-a-Al_2O_3} / 5×a-Al_2O_3:Er / t-a-Al_2O_3*. For comparison purposes two reference films have been prepared: a film doped only with Er (Er only) and a film doped only with Si NPs (Si only), both with the same spatial distribution as the film with s=11 nm. The Table 3.1 shows a list of the produced thin films with the characteristic design parameters.

The selection of the Si NP size was decided in order to obtain a broad absorption band in the visible in the range of the available pump sources in the GPL laboratory. The value obtained for E_G is 1.7 eV associated to Si NPs with an average diameter in the range of 4-5 nm.[41, 42, 43, 44, 45]

3.1.2 Si NP - Er^{3+} interaction below the nanoscale

The PL analysis of the test system shows that only the Er^{3+} located at a distance below the 1 nm is sensitized through the Si NPs (see Chapter 8). Therefore the next step in our research was to study the interaction phenomena below the nanoscale. Our first

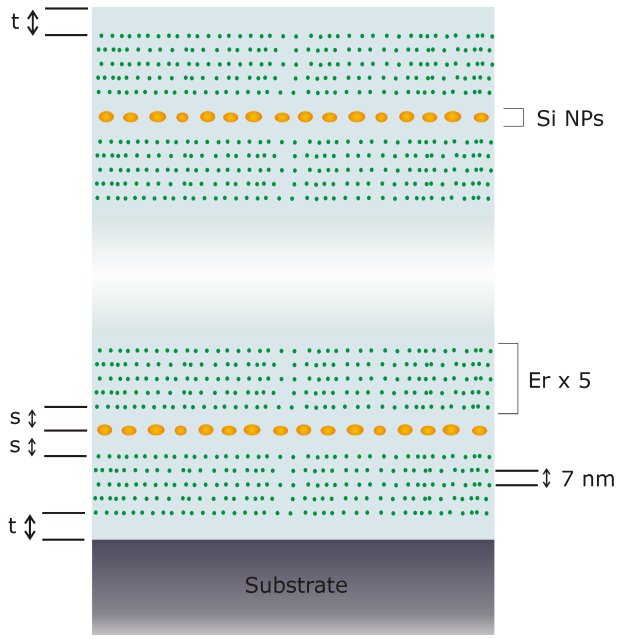

Figure 3.1: X-section scheme of the film distribution of Er^{3+} ions and Si NPs in the growth direction.

Label	Substrate	Er	Si	Design parameters	
		P/layer	P/layer	s (nm)	t (nm)
$S0$	Si/Fused SiO_2	1	500	0	103
$S4$	Si/Fused SiO_2	1	500	4	68
$S7$	Si/Fused SiO_2	1	500	7	37
$S11$	Si/Fused SiO_2	1	500	11	4
$Only - Si - S$	Si/Fused SiO_2	1	0	11	4
$Only - Er - S$	Si/Fused SiO_2	0	500	11	4

Table 3.1: Table of thin films produced to study the dependence of interaction on dopants distance. The thin film design parameters are listed.

approximation was to analyze how the order of the deposition of the dopants (Si NPs and Er^{3+}) affects the Er^{3+} emission.

Dopants deposition order

The thin film nanostructures are formed by 20 Er^{3+} doped Si NP layers separated by a 10 nm thick of a-Al_2O_3. The Si NP average diameter, amount of Er^{3+} thickness and number of doped layers is maintained and only the order in which the Er^{3+} and Si NPs are deposited has been changed. The deposition of dopants of the thin films is as follows:

1. $SE\phi$2.6: Er^{3+} deposited before the Si NPs formation (see Figures 3.2c and 3.2d)

2. $ES\phi$2.6: Er^{3+} deposited after the Si NPs formation. (see Figures 3.2a and 3.2b)

3. $SES\phi$2.6: Er^{3+} deposited in the middle of the Si NPs formation (see Figure 3.2e). In this case half of the number of the pulses on Si target for the Si NPs formation are deposited, then 1 pulse on the Er target is deposited and, finally, the rest of the pulses on the Si target to complete the Si NPs formation are deposited (see Figure 3.2f).

The Table 3.2 shows a list of the produced thin films with the characteristic design parameters. The Figure 3.2 shows schematically the deposition sequences and the final configuration of the films. Comparing the three different dopant configuration obtained after the deposition of the a-Al_2O_3 capping layer (Figures 3.2d, 3.2f and 3.2b), the differences in the distances between Er^{3+} and Si NPs dopants are below the nanoscale in the plane were the Si NPs rest. This special configurations obtained by the alternated deposition of dopants and the special features of PLD as the Si NPs formed in situ and Er^{3+} deposited in situ will help us to determine the extreme sensitivity below the nanoscale of the Si NPs to Er^{3+} transfer process and determine the fundamental mechanism involved in the transfer process.

Label	Substrate	Er P/layer	Si P/layer	Design parameters deposition order
$SE\phi$2.6	Si/Fused SiO_2	1	185	Si NPs - Er^{3+}
$ES\phi$2.6	Si/Fused SiO_2	1	185	Er^{3+} - Si NPs
$SES\phi$2.6	Si/Fused SiO_2	1	185	Si NPs - Er^{3+} - Si NPs
$Only - Er - 4$	Si/Fused SiO_2	1	0	Er^{3+}

Table 3.2: Table of thin films produced to study the dependence of interaction on order of the dopant depositions. The thin film design parameters are listed.

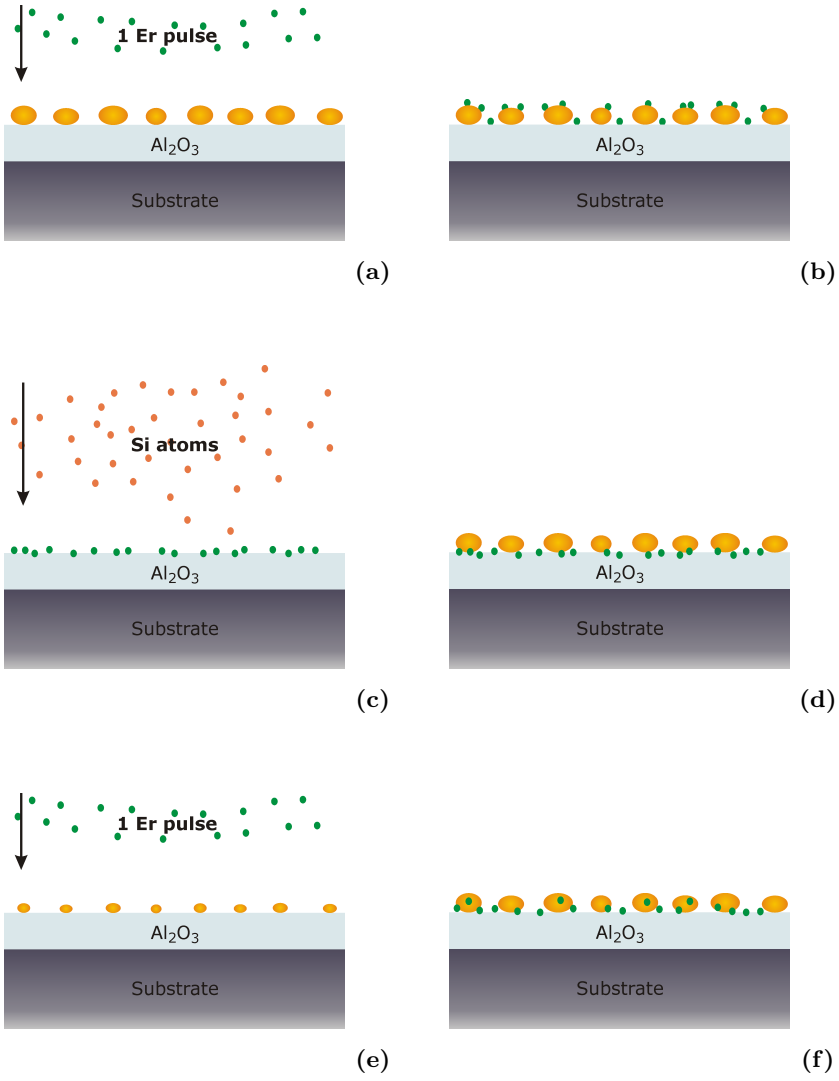

Figure 3.2: X-section schemes of sequences of the single step deposition method changing the Er^{3+} ions location bellow the nanoscale. 3.2a.- The Si NPs grew over the a-Al_2O_3 layer and only one pulse was used to doped the Si NPs. 3.2b.- A high percent of Er ions are located closer to the Si NPs or can be on them. 3.2c.- The Er ions were deposited in the previous step deposition to the Si NPs formation. 3.2d.- The Si NPs are formed on the Er^{3+} doped a-Al_2O_3 layer after the Er^{3+} deposition. 3.2e.- The Er ions are deposited in middle of the Si NPs growth process. 3.2f.- When the Si NPs are formed there are Er^{3+} that can be inside the Si NPs.

Intermediate a-Al_2O_3 layer with thickness below 1nm

In order to determine a figure of merit of the PLD deposition in the control of the dopants separation and how the Er^{3+} implantation can affect in the control of the dopant location new thin films with intermediate a-Al_2O_3 layers between the dopants were grown. The sequence of dopants was defined in the Figure 2.2. The nanostructured thin film are formed by 20 Er^{3+} doped a-Al_2O_3 layers and 20 Si NPs doped layers. Two different sizes were selected and for every size three thin films were prepared tuning the thickness of the intermediate a-Al_2O_3 layer from 0 to 1nm. The Si NPs were always deposited in first place. The Figure 3.3 shows schematically description of these thin films. As in the design of the nanostructured of the Section 3.1.1 a top and bottom a-Al_2O_3 layer was grown to obtain the same total thickness between thin films. The responsiveness of the Er^{3+} ions to the local environment will allow us to understand the Si NP cover phenomena during the PLD deposition and the Er^{3+} implantation depth.

Label	Substrate	Er	Si	Design parameters	
		P/layer	P/layer	s (nm)	t (nm)
$S(A-0.0)E\phi 2.2$	Si/Fused SiO_2	1	125	0	?
$S(A-0.5)E\phi 2.2$	Si/Fused SiO_2	1	125	0.5	?
$S(A-1)E\phi 2.2$	Si/Fused SiO_2	1	125	1	?
$S(A-0.0)E\phi 2.8$	Si/Fused SiO_2	1	210	0	?
$S(A-0.5)E\phi 2.8$	Si/Fused SiO_2	210	0	0.5	?
$S(A-1)E\phi 2.8$	Si/Fused SiO_2	1	210	1	?
$Only-Er-4$	Si/Fused SiO_2	1	210	-	?

Table 3.3: Table of thin films produced to study the figure of merit of the PLD in the control of location of dopants. The thin film design parameters are listed.

The Table 3.3 shows a list of the produced thin films with the characteristic design parameters.

3.2 Controlling the Er^{3+} and Si NPs distributions

In the Chapter 8 will be observed that only the Er^{3+} that is closer to the Si NPs is sensitive to be excited through the Si NPs. Therefore in order to study the dependence of the Er^{3+} emission on the Si NP size properties independently of Si NP - Er^{3+} distances, the Er^{3+} ions are deposited in situ following the Si NP formation (Figure 3.2a). In this deposition sequence the Er^{3+} ions are deposited on top of the Si NPs or in the Si NP inter-space (Figure 3.2b).

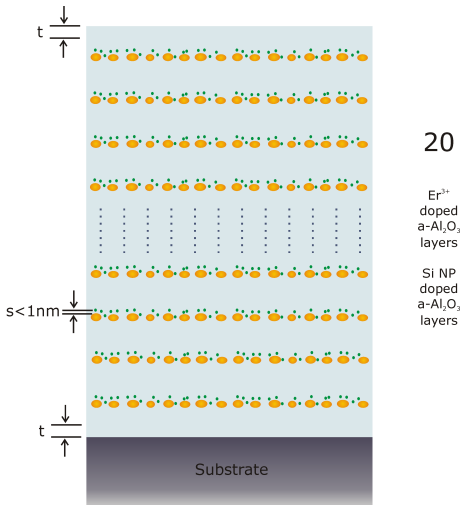

Figure 3.3: X-section scheme of one Er^{3+} and Si NP co-doped thin film with the Er^{3+} ions deposited at distances from the Si NPs below the nanoscale. The orange entities represent the Si NPs and the green points represent the Er^{3+} ions.

3.2.1 Optimizing the Si NP average size

The average diameter of the Si NPs was varied from 1.6 nm to 3.3 nm with the number of laser pulses used to ablate the Si target in each Si NPs layer deposition. The number of pulses on the Si target (P) has been varied from 300 to 1200 to produce three thin films with different Si NP sizes. Only one pulse per layer over the metallic erbium target is used to deposit the Er^{3+} ions, preserving the same Er content between thin films. A thick 10 nm layer of a-Al_2O_3 is deposited after the Er^{3+} doped Si NP layer to cover them and to embed them in the a-Al_2O_3 host. This sequence was repeated 20 times. Finally the nanostructured co-doped a-Al_2O_3 is formed by 20 layers of Er^{3+} doped Si NPs separated by 10 nm of a-Al_2O_3 (Figure 3.4). This thick a-Al_2O_3 layer is enough to avoid the particle-particle interaction [20] in the depth direction. For analysis purposes an Er-only doped reference film has been prepared preserving the Er^{3+} spatial dopant distribution.

In order to observe PL emission from the Er^{3+} ions in the co-doped films less than 20 Er^{3+} doped Si NPs layers are required, however to achieve enough PL signal from the only Er^{3+} doped reference film a minimum of 20 layers is mandatory.

3.2.2 Changing the Er^{3+} content

The typical $[Er^{3+}]$ areal density obtained depositing a single Er^{3+} pulse is around $\sim$ 5.0 10^{13} atm/cm^2. Quenching of the Er^{3+} photoluminescence due to Er^{3+} clustering has been demonstrated induced using more than one pulse per layer for Er^{3+} deposition. [26]

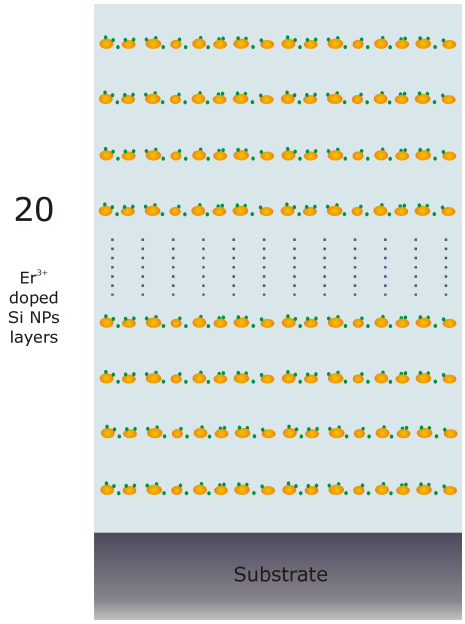

Figure 3.4: X-section scheme of one Er^{3+} and Si NP co-doped thin film with the Er^{3+} ions deposited following the Si NPs formation. The number of pulses on Si target has been varied between thin films from 75 to 250 to tune the size of Si NPs. The orange entities represent the Si NPs and the green points represent the Er^{3+} ions.

The unique effective method to change the $[Er^{3+}]$ density is to deposit only one pulse but using a higher laser energy density to ablate the Er target. Therefore, this has lead to produce thin films doped by two different Er^{3+} concentrations, $\sim$ 5.0 10^{13} atm/cm^2 and $\sim$ 8.0 10^{13} atm/cm^2, in thin films with the same 2D-distributions of Si NPs. In the new deposition conditions the number of pulses on the Si target (P) has been varied from 75 to 250. [1] The Table 3.4 shows a list of the produced thin films with the characteristic design parameters.

3.3 Thermal treatment at low temperatures

The test films (Section 3.1.1) were processed by a low temperature thermal treatment. This thermal treatment was used in order to optimize the PL emission is a conventional furnace in air annealing at different temperatures for 1 hour up to 700°C (starting at 400, 500, 600, 650 and finishing at 700°C). This treatment is similar to that performed in our previous works on Er doped a-Al_2O_3 films. All the thin films are characterized after every thermal step at the different temperatures.

[1] At a half of the PhD period the excimer laser was replaced (from a LP 200 to LPX-Pro coherent. The new laser beam size was different and then the density of energy reached at the a-Al_2O_3 target was different changing the deposition conditions. All the system was re-aligned and calibrated to obtain the same conditions however the deposition rates had changed.

Label	Substrate	Er (P/layer)	Energy (mJ/cm^2)	Design parameter Si (P/layer)
$SE\phi 1.0$	Si/Fused SiO_2	1	2.0	300
$SE\phi 2.2 - B$	Si/Fused SiO_2	1	2.0	600
$SE\phi 3.3 - B$	Si/Fused SiO_2	1	2.0	1200
$S\phi 1.0$	Si/Fused SiO_2	0	2.0	300
$ErRef2$	Si/Fused SiO_2	1	2.0	0
$SE\phi 1.6$	Si/Fused SiO_2	1	2.3	75
$SE\phi 2.2$	Si/Fused SiO_2	1	2.3	125
$SE\phi 2.6$	Si/Fused SiO_2	1	2.3	185
$SE\phi 2.8$	Si/Fused SiO_2	1	2.3	210
$SE\phi 3.3$	Si/Fused SiO_2	1	2.3	250
$Only - Er - 4$	Si/Fused SiO_2	0	2.3	0

Table 3.4: Table of thin films produced to study the dependence of interaction on Si NP sizes. The thin film design parameters are shown: number the Er^{3+} pulses per layer (Er-P/layer), energy density (Energy) and number of pulses on Si target per layer (Si-P/layer).

3.4 Summary

The alternate PLD is a flexible deposition technique that allows create multiple nanostructures to improve the emission of Er^{3+} ions using multi-dopants systems with control below the nanoscale. This novel nanostructures will show special properties and unique behavior that allow us to uncover new rewards and answers that will clarify some aspects on the interaction between Er^{3+} ions and Si NPs.

Part II

Properties of the 2D-distributions of amorphous Si NPs.

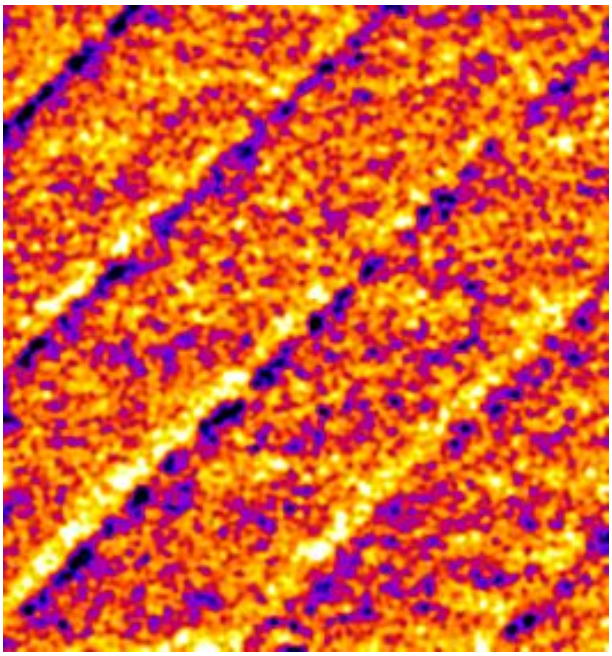

During the experimental evolution of the fluorescence measurements different experiments to characterized the physical properties of Si NPs was developed in parallel. However in the spectroscopic final analysis is fundamental to parameterize the distributions of Si NPs and to establish the physical properties of the Si NP distributions before the fluorescence analysis. For that reason, before the natural evolution of the experimental program a new thesis part is described where the different experimental measurements on the Si NPs properties have been described and analyzed.

The aim of this part is to characterize the physical properties of the amorphous silicon nanoparticles (Si NPs) produced by alternate pulsed laser deposition (PLD) using different experimental techniques: transmission electron microscopy and optical absorption. Once the fundamental properties of the Si NPs as energy band-gap or average size are established, the 2D-Si NP distribution parameters are determined using the RBS compositional analysis. Finally the a-Al_2O_3- Si NPs interface is studied by the fluorescence properties of the Si NP doped a-Al_2O_3 films. A relationship between the surface properties of the Si NPs and the parameters of the 2D-Si NP distributions is established.

The parameters of the 2D-Si NP distribution and the analysis of the a-Al_2O_3- Si NP interface will helps us to understand the Er^{3+} fluorescence behavior when it is localized close to the Si NPs.

[2]

[2]The EFTEM image is a thermal LUT representation of a small region of the Figure 4.7b post-processed by a background substraction and a band pass filter from 40 pixels to 2 pixels.

Chapter 4

Structural and chemical local properties

The structural and chemical properties of the Si NPs are analyzed by electron microscopy techniques. The transmission electron microscopy images reveals the amorphous nature of the Si NPs before and after a annealing process. In addition the electron energy loss spectroscopy gives us information about the chemical composition of the thin films components and their evolution with the thermal process. The electron microscopy in addition with the electron energy loss spectra allow us to determine the local chemical properties of the Si NPs and obtain a first approximation about the average diameter of the 2D Si NPs distributions.

4.1 Thin films for electron microscopy

Transmission electron microscopy (TEM) images are a photo of our thin films in the nanometer scale, where the information recorded is related to the electrons transmitted through the specimens after interaction with the atoms that form the sample. Therefore the structural properties of the Si NPs were determined by high resolution TEM (HRTEM) that allow us determine the crystallinity quality of the Si NPs within amorphous a-Al_2O_3. This work has been developed in collaboration with Amanda K. Pertford Long, Kabius and M. Tanase from the Argonne National Laboratory at IL-USA during a two months short stay. The electron microscope (Tecnai F20ST TEM operated at 200 kV with a point-to-point resolution of 0.24 nm) included an energy loss spectroscopy (EELS) stage. In the EELS measurements the electron beam emerging from the sample is passed through a magnetic prism and the flight path of the electrons varies depending on their energy. Recording these electrons at different positions with an electron spectrometer, it is possible to obtain a intensity spectrum containing chemical information (as the atoms bonds) from the thin films and Si NPs. TEM images formed only by electrons of particular kinetic energies has been done to analyze the local chemical properties of the Si NPs using an energy-filtered transmission electron microscopy (EFTEM) stage.

TEM microscopy requires special specimens, thin enough to allow the transmission of electrons. Therefore two kinds of thin film structures have been prepared for specific microscopy analysis, X-sections of the multilayer structures prepared by *lift-out* focus ion beam (FIB) and monolayers of Si NPs (embedded and not embedded in a-Al_2O_3) deposited on C-Mica substrates. The samples prepared on C-Mica substrates were separated from the substrate by immersion in de-ionized water and were picked up with copper TEM grids for observation. The multilayer structures were analyzed in the X-sections specimens but the overlapping of Si NPs at different depths makes difficult the determination of Si NP sizes.

4.2 Amorphous Si NPs embedded in amorphous Al_2O_3

The first specimen analyzed was an as deposited X-section of the test series ($S7$). The Figure 4.1a shows a TEM image of the as grown thin film doped with Si NPs and Er^{3+} ions with s=7 nm, whose Er^{3+} PL properties are analyzed in the Chapter 8. The image shows a very low contrast between the Si NP layers and the Er^{3+} doped a-Al_2O_3 deposited between them. The proximity in the atomic number between the silicon ($Z = 14$), aluminium ($Z = 13$) and oxygen ($Z = 8$) atoms gives low mass contrast in the TEM microcopy images. The image shows light ad dark layers. The lighter regions correspond to the contribution of the Si NP layers plus the a-Al_2O_3 where the Si NPs are embedded. The darker regions between them are associated to the presence of embedded Er^{3+} ions in the a-Al_2O_3 which are quite heavy ($Z = 68$).

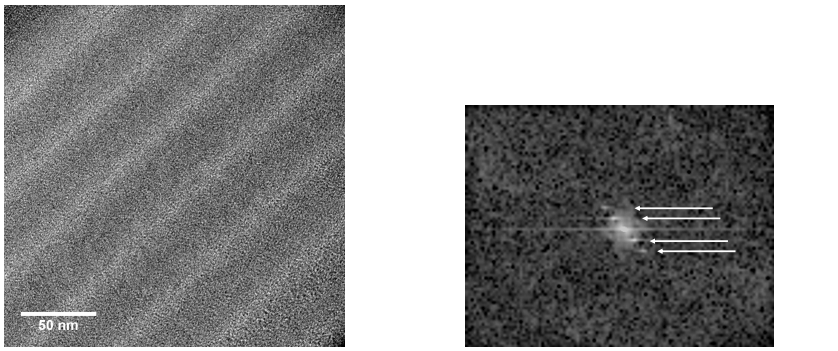

(a) (b)

Figure 4.1: Figure 4.1a is a TEM image of a cross section of the $S7$ thin film. The Figure 4.1b shows the Fast Fourier transform of the image of Figure 4.1a

Using a large objective aperture to visualize the atomic-scale structure of the Si NPs, **no crystalline structure has been observed**. The Figure 4.1b shows the fast Fourier transform (FFT) of the TEM image of the Figure 4.1a showing the well defined multi-layer structure. The light points indicated by arrows corresponds to the periodicity of the nanocomposite layers, but there are not small rings that can be associated to any crystalline structure.

The X-section specimens are very difficult to prepare and the superposition of Si NPs at different depths difficults the Si NP identification and definition of Si NP edges. In order to determine Si NP distribution parameters as Si NP size of Si NP density, a priori, the most suitable method is to analyze the TEM plan view images. Therefore single layer of Si NPs sandwiched between two a-Al_2O_3 layers has been deposited on C-Mica substrate for different Si NP sizes. The Figure 4.2 shows a plan view HRTEM image of a Si NP distribution similar to $SE\phi 3.3 - B$ thin film. Nevertheless, the weak darker drops are associated to the presence of Si NPs but the identification and measurement of size is not possible due to the poor Si NP edges definition and moreover because only the bigger Si NPs are detected. The Figure **??** shows a plan view from Si NP deposited on C-Mica without a-Al_2O_3 with a Si NP average size equivalent to $S\phi 1.0$. Dark small and spherical Si NPs can be difficulty identified with sizes below the nanometer scale.

The TEM and HRTEM images show that there is no crystalline structure in either the a-Al_2O_3 layers or the Si-rich areas, indicating the amorphous nature of both the a-Al_2O_3 and the Si NPs for all the thin films. Determination of an average Si NP size and morphology was not possible due to the low mass contrast between Al atoms and Si atoms. The X-section images reveal the well defined layered structure.

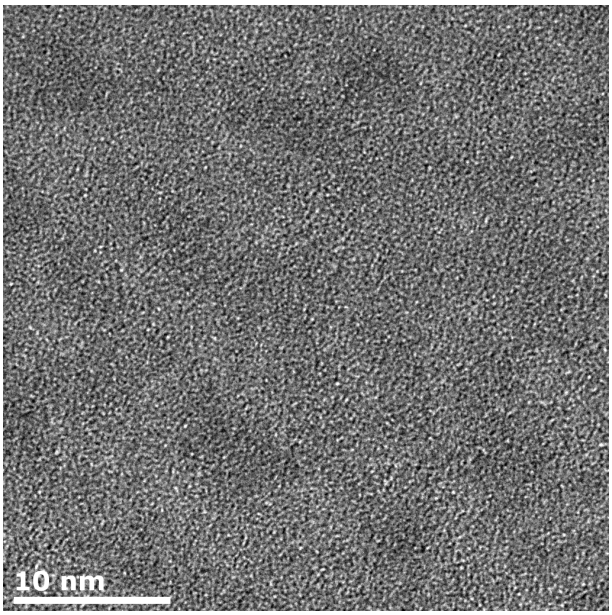

Figure 4.2: plan view image of one layer of Si NPs embedded in a-Al_2O_3 and deposited on C-Mica substrate. The Si NPs morphology corresponds with the $SE\phi 3.3 - B$ thin film.

4.3 Chemical environment. Si and Al components

Local chemical analysis is necessary to identify and understand the local Si NP properties of the 2D- Si NP distributions due to the difficulty of identifying sizes by TEM and HRTEM images. Therefore EELS analysis is required before the EFTEM images acquisition to determine the different element contribution for every specific specimen.

4.3.1 Chemical environment and EELS

The electron energy loss spectrum is composed by three main parts: the zero loss peak, the low loss region and the high loss region. Every part gives us different information about the chemical environment and the atoms bonding situation. [46]

1. The **zero-loss peak** is at 0 eV. It mainly contains electrons that still have the original beam energy, i.e., they have only interacted elastically or not at all with the specimen. The intensity of the zero-loss beam is high and only is useful to calibrate the energy axis.

2. The electrons that have induced plasmon oscillations contributing to the **low-loss region** ($E < 100$ eV). The plasmon generation is the most frequent inelastic interaction of electron with the sample and the intensity in this region increases with specimen thickness. Therefore the contribution of the constituent elements depends on their percentage in the structure.

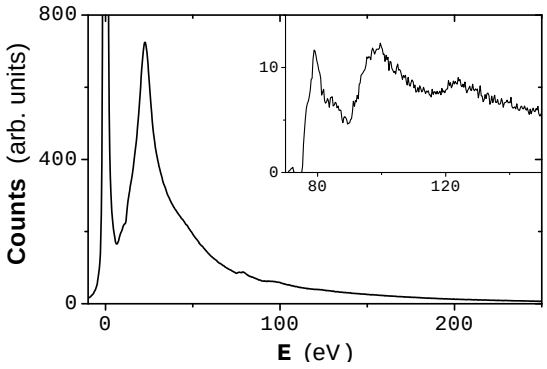

Figure 4.3: EELS spectrum of $S7$ in as grown conditions. The inset shows the atom core loss spectrum after subtract the pre-edge background

3. When an electron interacts with an atom a specific minimum energy must be transferred in order to expel an inner-shell electron and to ionize the atoms. This critical ionization energy is a energy threshold (E_C), which leads to ionization edges in the spectrum at energy losses that are characteristic for each element. Thus, EELS is complementary to X-ray spectroscopy, specially in the detection of light elements as in our case the silicon, aluminium and oxygen. Compared to the plasmon generation, the inner-shell ionization is a much less probable process, leading to a low intensity of the peaks. In this **high-loss region** ($E > 100\ eV$), the amount of inelastically scattered electrons drastically decreases with increasing energy loss, thus small peaks are superimposed on a strongly decreasing background. The critical ionization energy E_C is sensitive to the chemical situation of the element: e.g., the L edge of Cu metal and CuO are shifted in respect to each other (chemical shift). Thus this region, designated as **ELNES** (Energy-Loss Near-Edge Structure), mirrors the DOS and provides information about the atom bonding situation.

4.3.2 Si and Al components in as grown thin films

The X-section are the very attractive specimens to measure the EELS spectrum because it is possible to focus in a region of the sample without contribution from the substrate and analyze the chemical environment.

The Figure 4.3 shows the EELS spectrum of the cross section $S7$ thin film. At low energies the plasmon peak is observed at 22 eV while two smaller peaks are observed at energies higher than 60 eV over the background contribution from the higher peak at low energies. The Figure 4.4 shows the normalized low loss spectra of all the thin film reference element components [47] and the low energy spectrum of as grown cross section of $S7$ thin film. The maximum of the spectrum localized at energy of 22 eV is close to the position of the maximum of the low loss spectrums for the Si atoms forming SiO_2 or the Al atoms forming Al_2O_3. The inflection points observed at 6.5 eV and 11.5 eV are due to the

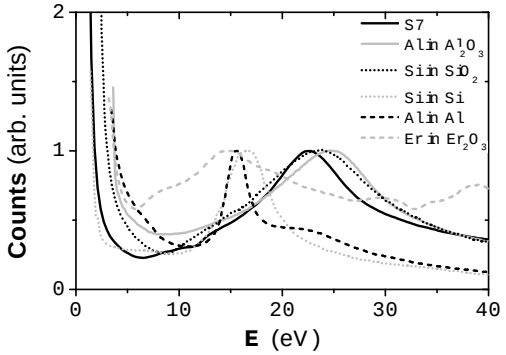

Figure 4.4: Normalized low loss spectra of GATAN references and *S*7 thin film.[47]

contribution of the Er^{3+} atoms bond to the oxygen atoms within the a-Al_2O_3 host. There are no detectable contributions from Al atoms bond to other Al atoms or Si in pure silicon.

In order to determine if the plasmon peak localized at 22 eV corresponds to silicon oxidized or a-Al_2O_3 we have analyzed the high energy loss spectrum and obtained the energy loss edge structures. The inset of the Figure 4.3 shows the ELNES spectrum obtained from the substraction of the background contribution to the spectrum at high energies. The background was estimated assuming a power dependence of the EELS intensity with the electron energy ($Counts = AE^{-\gamma}$) in the region between 60 eV and the edge. Three main peaks are observed at 79 eV, 99 eV and 123 eV and a hump at 85 eV. The energy peaks positions and the spectra shape is similar to the the energy loss near edge structure obtained for the a-Al_2O_3 in the references [48, 49]. Thus the EELS intensity comes mainly from the a-Al_2O_3 contribution because of the content of silicon is a low percentage of the total amount of atoms in the thin film being the silicon contribution shadowed/hidden by the EELS intensity that comes from the Al atoms. Thus, the plasmon peak observed at 22 eV corresponds to the Al in the a-Al_2O_3 and the shift towards lower energies compared to the reference spectrum (Figure 4.4)[47] is probably due to the amorphous nature of the a-Al_2O_3.

Because the intensity in the low energy region increases with specimen thickness, in order to distinguish contributions from chemical and atomic similar atoms as the aluminium and silicon is necessary to use samples where the content of the two elements are equitable. Consequently the EELS spectra has been analyzed for a single layer of Si NPs embedded on a-Al_2O_3 and deposited on C-Mica thin films and without Er^{3+} ions. The low-loss spectrum shows a plasmon peak localized at $25 - 26$ eV associated to the carbon remaining on the sample after pick up the sample with TEM grids. The ELNES peaks of carbon are localized for energies higher than 300 eV, thus the contribution of C s

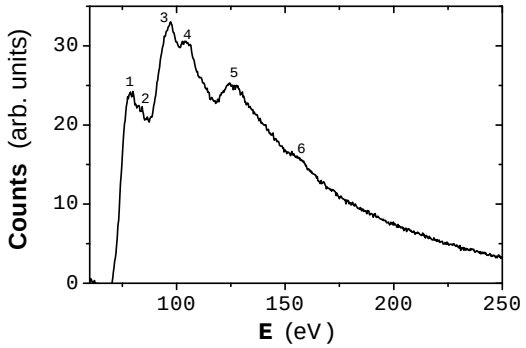

Figure 4.5: ELNES spectrum of a Si NP layer embedded in a-Al_2O_3 and deposited on C-Mica. The numbers indicate the maximums founded in the ELNES spectrum shape.

negligible in the spectrum region where the ELNES peaks of Al and Si atoms are localized (100 eV - 200 eV). The Figure 4.5 shows the ELNES spectrum of a Si NP monolayer thin film equivalent to the $SE\phi 3.3 - B$ multilayer film where 5 peaks can be identified (labeled 1, 3, 4, 5, 6) and a hump (labeled 2) associated to the energies (79, 97, 105, 127 and 83 eV) and 83 eV respectively. The peaks located at 79 (1), 97 (3) and 127 (5) eV and the hump at 83 eV are related to the contribution from a-Al_2O_3 host because the energy values are similar to the ELNES peaks obtained for the $S7$ film (see inset of Figure 4.3). However the peaks located at 105, 127 and 158 eV are due to the EELS high loss contribution from the silicon in the thin film in a oxidized state (SiO_2) or pure (a-Si). Therefore the presence of a-Al_2O_3 prevents us discerning the oxidation state of silicon.

In order to determine the ELNES spectrum of our silicon without the contribution of the Al in a-Al_2O_3 that hides the silicon oxidation state, Si NPs were deposited on C-Mica substrates without a-Al_2O_3 to analyze the EELS spectra of the silicon forming Si NPs. The spectra have been normalized to the unit to compare spectrum shapes and peak positions. Using the GATAN spectra as references [47], the thin film formed by smaller Si NPs (average size equivalent to $SE\phi 1.0$) shows silicon oxidized while the thin film formed with the bigger ones (average size equivalent to $SE\phi 3.3 - B$) shows mainly silicon in pure silicon (see Figure 4.6). Therefore the state of oxidation is Si NP size dependence and in the plan view with the bigger Si NPs the Si NPs are oxidized only at the surface while the core remains pure. We must emphasize that when the Si NPs are embedded in a-Al_2O_3 and then isolated from a reactive atmosphere, therefore less oxidation is expected. Thus the Si NPs can be oxidized at Si-a-Al_2O_3 interface but the Si NP core remains formed by pure a-Si. This has been shown for Cu nanoparticles of similar size. [31]

We have identified the oxidation state of the Si NPs reducing the a-Al_2O_3 contribution in the electron microscopy specimens. Plasmon peaks are observed in the low-loss region for all constituents of the thin films. They will be used to acquire EFTEM images from

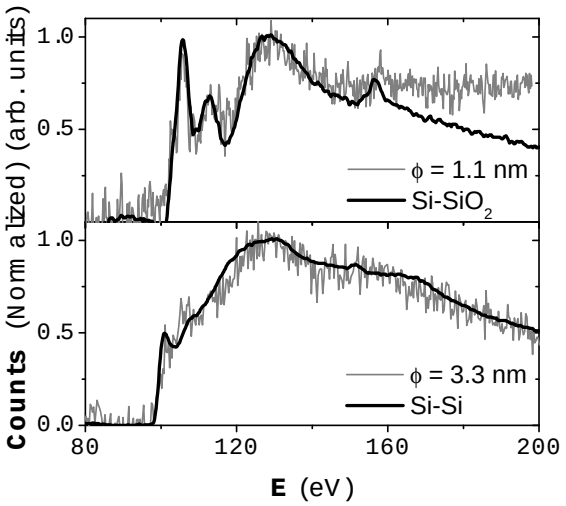

Figure 4.6: Normalized ELNES spectra of a Si NP layer deposited on C-Mica of two films with different Si NP average size distributions (1.1 nm and 3.3 nm average diameter, ϕ). The ELNES spectra are compared with the Si in Si and Si in SiO_2 references.[47] The grey lines represent the raw data and the black lines correspond to the GATAN references. The differences between the reference spectrum of Si atoms in SiO_2 host with the spectrum of the Si NP layer of small average size (1.1 nm) are related to the difficulty of estimation of the background contribution.

electrons of a particular energy.

4.4 Silicon forming agglomerates and distributed in layers

After analyzing the EELS spectra is possible to locate the different atoms in the sample and relate it to its oxidation state forming the image with only the electrons within a small range of energy. For that a slit is used to select the electrons diffracted for a specific energy range and the image is formed only with these electrons. The images formed filtering the energy of the electrons diffracted in the films are denominated EFTEM (Energy Filtered Transmission Electron Microscopy) images and compositional maps of the Si-rich areas was observed independently of their crystalline or amorphous structure.

The ELNES spectrum showed only contribution from the a-Al_2O_3 host and the obtained composition maps based on the pre-edge and post-edge images have had no enough definition. Furthermore, in the EELS spectrum obtained from the X-section of $S7$ thin film the contribution of Si in Si plasmon peak is hidden by the Al contribution. However, the EELS analysis of the plan view specimens shows that there is contribution from silicon in pure silicon in the high loss region. Consequently images filtering at the theoretical energies values where is localized the plasmon peak of the Si in Si were acquired.[50, 51] Therefore, EFTEM images filtering at 16 eV using a energy window width of 4 eV has been

acquired (see Figure 4.7a) obtaining bright regions distributed in layers that correspond to the presence of Si NP layers.

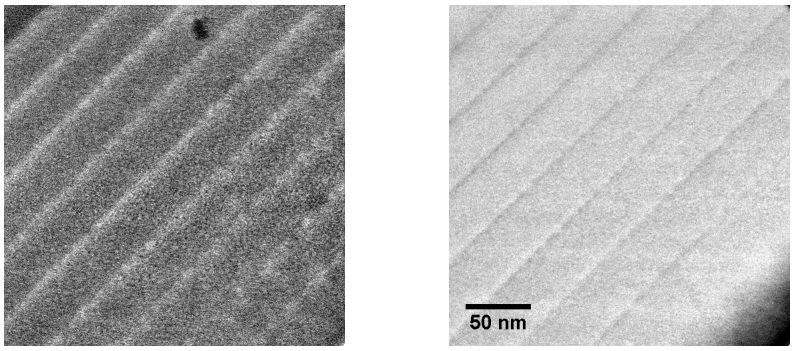

(a) (b)

Figure 4.7: The Figure 4.7a and the Figure 4.7b are two cross section EFTEM images of the as grown *S*7 thin film. The Figure 4.7a shows the cross section filtering at plasmon peak of silicon in pure silicon, the bright white regions are associated to the Si NPs contribution. The Figure 4.7b have been obtained filtering at 57 eV using a 5 eV window width localized at the aluminium in a-Al_2O_3 tail and outside of Si plasmon peak. Thus the black holes correspond to the presence of Si NPs.

In order to determine the presence of Si NPs and estimate a average size value, several intensity profiles in the Si NP layers have been obtained. However, due to the proximity of the pure Si plasmon peak to the Al plasmon peak in a-Al_2O_3, there is contribution from the a-Al_2O_3 deposited in the space between Si NPs and the determination of the Si NP average size from this EFTEM images is difficult with a poor Si NP edges definition.

Considering that the contribution to the EELS spectrum of pure Si is low in comparison with the contribution of the Al atoms, filtering at energy ranges where the contribution comes mainly from a-Al_2O_3 plasmon peak tail can be a route to obtain images where the dark regions are associated to the Si. Therefore EFTEM images were obtained by filtering in the energy range from 50 to 150 eV corresponding to the Al plasmon tail. The Figure 4.7b shows an image of the *S*7 X-section filtered at 60 eV and using an energy window of 5 eV. The Si NPs can be identified as dark holes. It is possible to enhance the image definition to localize the Si NPs using image filters in a post-acquisition process, but this post-process can deceive and lead us to mistake in the measurements. The EFTEM image shows in the abstract of this Part of the manuscript is a thermal LUT (color look up table) representation of a small region of the Figure 4.7b post-processed by a background substraction and a band pass filter from 40 pixels to 2 pixels.

Plotting intensity profiles in the images is possible to estimate the thickness of the nanocomposite and the in-plane dimensions of the Si NPs. The bottom graph of the Figure 4.8 shows a intensity profile in a line of 4 pixels width following the Si NP layers in the image of Figure 4.7b while the top graph of the Figure 4.8 shows a intensity profile in

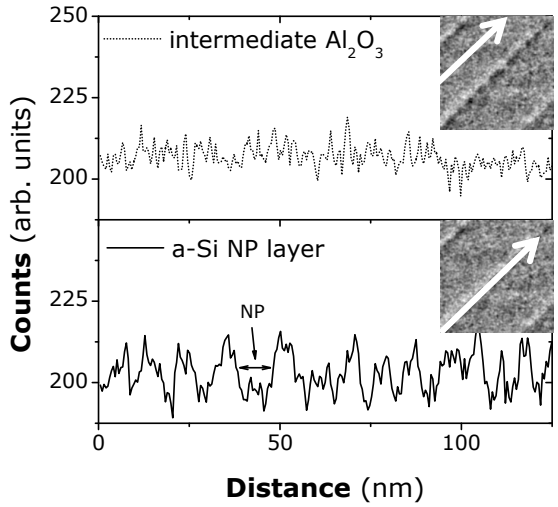

Figure 4.8: Intensity profiles of the as grown $S7$ thin film parallels to the nanocomposite layer (measured region indicated by an arrow line in the image insets). The top figure shows a intensity profile in at a-Al_2O_3 intermediate region of the image obtained filtering in the Al plasmon peak tail (Figure 4.7b). The bottom figure is the profile obtained in an Si NP layer using the same image, therefore the holes shows the presence of Si NPs.

the a-Al_2O_3 intermediate layer. The a-Al_2O_3 profile shows a random intensity response, however the region corresponding to the Si NPs shows holes with a significative absolute intensity variation and a width median value around 6 ± 2 nm. The average in-plane size has been determined assuming the width of the hole as the FHWM, note that the sample is a X-Section specimen and thus the size is probably overestimated due to the superposition of Si NPs in the same layer but at different depths.

The Figure 4.9 shows the in depth profiles of the $S7$ thin film obtained from images recorded at the Al plasmon peak tail and the Si plasmon peak. Measuring the width of the deeps of the intensity profile of the Al plasmon peak tail (top Figure of Figure 4.9) and the width of the intensity peaks (bottom Figure of Figure 4.9) of the Si plasmon peak it is possible to estimate the thickness of the Si NP layers. The median thickness obtained value for the two types of profiles is 4.6 ± 0.7 nm.

Therefore using the EFTEM images from the as grown X-section thin films it has been possible to estimate an average Si NP dimensions values.

4.5 Annealing. Amorphous Si NPs and a-Al_2O_3 stoichiometry.

As it has been described in the Chapter 3, the test films were processed by a low temperature thermal treatment in order to optimize the PL response of the co-doped thin films.

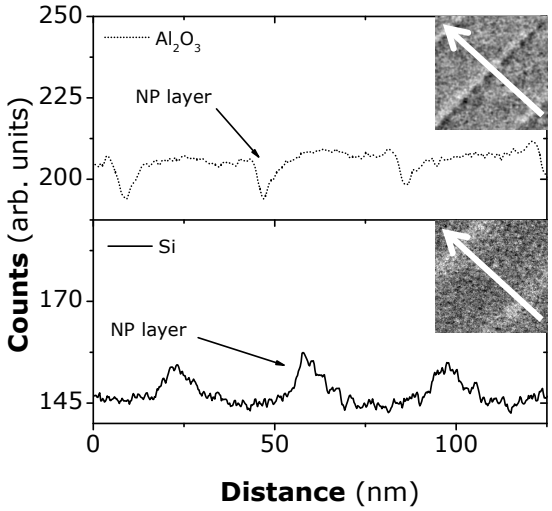

Figure 4.9: Intensity in depth profiles of the as grown *S*7 thin film (measured region indicated by an arrow line in the image insets). The top Figure correspond to the intensity profile obtained from the image of the Figure 4.7b filtered at the Al plasmon peak tail. The deeps correspond to the Si NP layer. The bottom Figure shows the in depth profile obtained from the image filtered at the Si plasmon peak.

The electron microcopy and the EELS spectroscopy gives us information about how the annealing process affects to the composition, crystallinity and structure of the multi-layer nanostructured thin films.

The Figure 4.10 shows two TEM images obtained from the annealed at 700 ï¿½C *S*7 film at different resolutions. The multi-layer structure is maintained after the slow thermal process (see Figure 4.10a). However, observing the thin film in more detail (Figure 4.10b), two linear regions with a higher density are observed and two brighter lines appear at both sides of the Si NPs layers.

HRTEM images have been recorded using small microscope apertures to enhance the spatial resolution although at the detriment of the mass contrast, in order to determine the crystallinity of the Si NPs. No crystalline structures have been detected in the Si NPs layers and the a-Al_2O_3 host (see Figure 4.11). Therefore the multilayered structure and the amorphous nature of the thin films is maintained after the thermal anneal process at 700 ï¿½C.

In order to determine the composition of the bright regions surrounding the Si NP layers (Figure 4.10b) the low-loss EELS spectrum corresponding to the *S*7 annealed thin film has been acquired and has been analyzed in conjunction with the ELNES spectrum. Significant changes have been observed in comparison with the EELS spectrum of the as

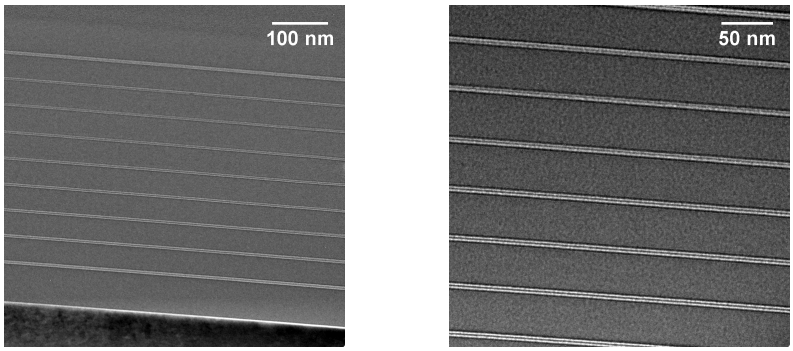

Figure 4.10: The Figure 4.10a shows a TEM image of a cross section of the $S7$ thin film annealed at 700 ï¿½C. The Figure 4.10b shows a TEM image of a smaller region of the Figure 4.10a where it is easily to observe two defined bright linear regions delimiting the Si NP layers.

grown thin film. In fact, the complete EELS spectrum shows a more defined shape and peaks than in the as grown thin film suggesting a better defined chemical environment (Figure 4.12). The mean peak at low energies is shifted to higher energies at 25 eV, a similar energy to the plasmon peak of the Al atoms in the $\alpha - Al_2O_3$. However the shape of the low energy loss is more similar to the Al atoms in poly-crystalline Al (with a hump at higher energies) than the Al in $\alpha - Al_2O_3$ and that can be related to a non stoichiometric a-Al_2O_3 with a slight excess of Al atoms. [52, 53] Furthermore, the contribution at lower energies appears more defined than in the as grown film $S7$. Fitting the spectrum at low energies (below 80 eV) to the sum of three main peaks one peak centered at 14 eV has been identified, close to the Si plasmon peak in pure silicon. The ELNES spectrum shows only information about the host properties, showing an ionization edge similar to the $\alpha - Al_2O_3$ (see inset of Figure 4.12) with isolated peaks at 79, 84, 99, 125 and 143 eV.

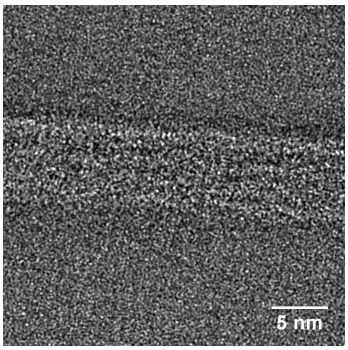

Figure 4.11: X-Section HRTEM image using a 5 nm scale from the $S7$ thin film annealed at 700 ï¿½C. Host and Si NP layers show amorphous structure.

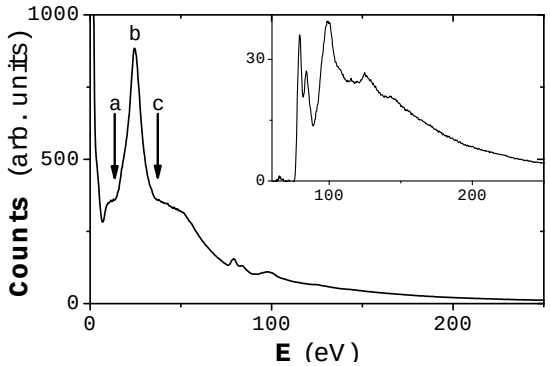

Figure 4.12: EELS spectrum of $S7$ after the slow anneal process. The inset shows ELNES spectrum. The letters correspond to the images in the Figure 4.13.

No other contributions have been observed due to the low percentage of Si or Er atoms in comparison with the Al that forms the host. But we would like to emphasize that the ELNES spectrum suggests a relocation of atoms that seem to link locally to form a more stable stable structure, these changes have to occur locally because the HRTEM images (Figures 4.11 and 4.10b) only show amorphous structures. The local transformation to crystalline Al_2O_3 has been observed previously in only Er^{3+} doped a-Al_2O_3 thin films only after anneal process at temperatures higher than 850 ï¿½C.[33, 54] Thus, under annealing at 700 ï¿½C, the host has not crystallized but the ionization edges reveals the reorientation of the Al atoms, suggesting a configuration more close to the $\alpha - Al_2O_3$ coordination.

According to the chemical information obtained from the EELS spectra stack EFTEM images have been measured from 12 eV to 150 eV with a minimum of the energy window width of 4 eV. Assuming that the peak observed below the 25 eV corresponds to the contribution of Si atoms in a Si environment, the image formed filtering the electrons at 16 eV (values for the Si in Si plasmon peak) will show the regions in the thin film formed by Si. The Figure 4.13a shows the EFTEM image filtering at 16 eV where the silicon nanocomposite layers are bright. The EFTEM image formed filtering center at the plasmon peak of Al in the a-Al_2O_3 at 24 eV shows surprisingly a higher concentration of Al atoms localized in the border of the Si-nanocomposite layer as is reflected in the Figure 4.13b by the two wavy bright lines close to the Si NPs. Taking into account that the new position of the a-Al_2O_3 plasmon peak suggests a relocation of atoms to a $\alpha - Al_2O_3$ configuration, it seems that the Al atoms close to the Si NPs are in a more stoichiometric a-Al_2O_3. In fact, the Si NP layers seem to act as a diffusion barriers to the oxygen atoms. However when the we filter at higher energies in the tail of the Al plasmon peak at the beginning of the plateau region of the hump at 28 eV, the image formed (see Figure 4.13c) shows a continuous contribution in all the a-Al_2O_3 intermediate layers between the Si nanocomposite layers. This hump could be related to the presence of Al-Al bonds that can be caused

by the decrease of oxygen atoms that have diffused towards the Si nanocomposite. The contribution of different elements can be merged in a unique image forming a composite map. The Figure 4.13d shows the RBG image composed by merging the previous images assigning the colors red to silicon, green to the Al plasmon peak and blue to the its tail, forming a composite map.

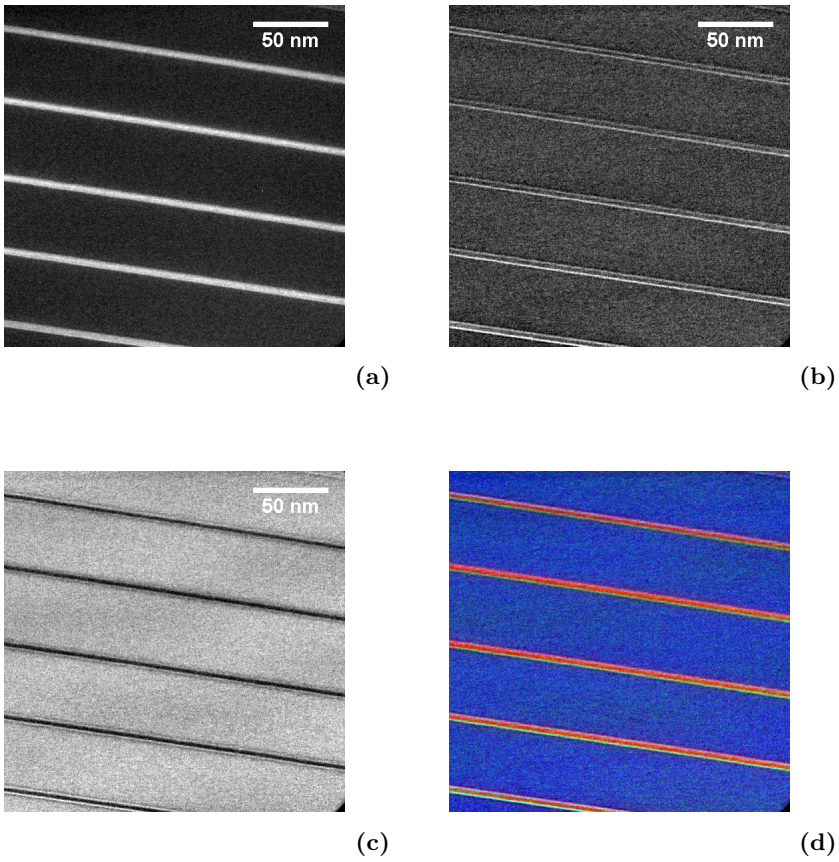

Figure 4.13: EFTEM images of the *S*7 thin film after the slow anneal process. The Figure 4.13a shows the contribution of pure silicon in the X-section, it was acquired filtering at 16 eV and using a window width of 4 eV. The Figure 4.13b was obtained filtering at the Al plasmon peak in a-Al_2O_3 (24 eV using a window width of 4 eV). The Figure 4.13c shows the image formed filtering in the tail of the Al plasmon peak in a-Al_2O_3 (28 eV- 4 eV width). The Figure 4.13d shows the RBG image composed by merging the previous images assigning the colors red to silicon, green to the Al plasmon peak and blue to the its tail, forming a composite map

In order to determine the presence of nanoparticles and estimate an average size value after the thermal process at 700 ï¿½C, several intensity profiles have been obtained. The Figure 4.14 shows the intensity profiles obtained parallel to the Si NP layers. The a-Al_2O_3 contribution is a plateau profile shown in the top Figure of Figure 4.14 and obtained from a a-Al_2O_3 inter-Si NP-layer region of the image recorded filtering at the tail of the plasmon

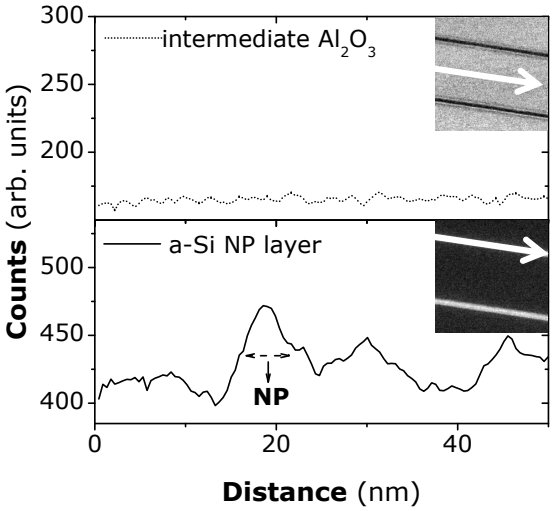

Figure 4.14: Intensity profiles obtained parallels to the Si NPs layer in the EFTEM images for the annealed $S7$ (direction of measurement indicated by a white arrow in the image insets). The top Figure reports the profile in the a-Al_2O_3 inter-Si NP-layer for the image recorded filtering at the tail of the plasmon peak (Figure 4.13c). The bottom Figure reports the profile in the Si NP layer for the image recorded filtering at the Si in Si plasmon peak (Figure 4.13a).

peak (Figure 4.13c). The presence of Si NPs is determined by the profiles drawn at the Si NP layer in the image obtained filtering at the Si in Si plasmon peak (Figure 4.13a). The average in-plane dimension of the Si NPs was estimated around 4 ± 1 nm measuring the average width of the peaks intensity profile (bottom figure of Figure 4.14).

In depth profiles have been traced in the EFTEM images of Figures 4.13a , 4.13b and 4.13c in order to determine the thickness of the Si nanocomposite layer. The intensity profile obtained from the image filtered at the Al plasmon peak in Al_2O_3 (Figure 4.15.a) shows two peaks that correspond to the presence of stoichiometric a-Al_2O_3 delimiting the Si NPs thus the Si nanocomposite layer thickness was estimated by the distance between these two peaks. The intensity profile (Figure 4.15.b) obtained from the image of the Figure 4.13c shows the stoichiometric a-Al_2O_3 as two small deeps closer to the large deep due to the presence of the nanocomposite layer, thus the distance between the secondary maxima defines the Si nanocomposite thickness. The in depth profile obtained from the image filtered at the Si plasmon peak (Figure 4.15.c) shows clearly the contribution only from the nanocomposite layer being the Si NP layer thickness measured by the FHWM of the peaks. With all these measurements the Si-nanocomposite layers thickness estimated is 3.8 ± 0.3 nm.

For the as grown thin films the Si NP in-plane average dimension is 6 ± 1 nm and the Si nanocomposite layer thickness around 4.6 ± 0.7 nm were obtained. However in the

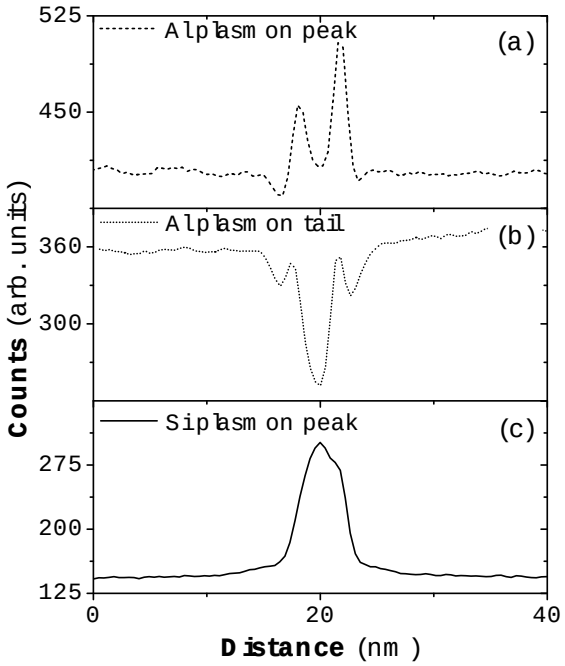

Figure 4.15: Intensity in depth profiles of the annealed $S7$ thin film (direction of measurement indicated by a white arrow in the image insets). The Figure 4.15.a corresponds to the intensity profile obtained from the image of the Figure 4.13b filtered at the Al plasmon peak tail. The Figure 4.15.b corresponds to the intensity profile obtained from the image of the Figure 4.13c filtered at the Al plasmon peak tail. The Figure 4.15.c corresponds the in depth profile obtained from the image filtered at the Si plasmon peak.

annealed thin film the in plane average dimension is $4 \pm 1\ nm$ and the Si nanocomposite layer thickness is $3.8 \pm 0.3\ nm$. If we also note that the EELS spectrum shows a more defined shape suggesting a repositioning of atoms we can conclude that after the anneal process the diffusion of oxygen and a relocation of atoms occurs and probably cause the oxidation of the regions close to the Si NP surface while the pure a-Si core of the Si NPs is reduced.

4.6 Conclusions

The electron microscopy analysis shows:

1. Well defined multilayer structures (FFT of multilayer is perfect)
2. Amorphous nature of all components before and after the annealing process
3. Presence of drops of silicon (formed Si NPs) in X-sections and plan views
4. Silicon oxidized in small Si NPs no embedded in a-Al_2O_3. Bigger Si NPs show no oxidation, therefore low probabilities of total oxidation in Si NPs embedded in a-Al_2O_3, only oxidation of the surface of Si NPs.
5. A first approximation of the Si NP size was obtained around nm for the $S7$ thin film.
6. Formation of Al densification or accumulation in the Si NP layers after the anneal process at 700ï¿½C. The Si NPs acts as a barrier to the Al diffusing thought the host due to the excess of Al in the no stoichiometric a-Al_2O_3 thin films.
7. The host has no crystallize but the ionization edges reveals the reorientation of the Al atoms to a configuration more close to the $\alpha - Al_2O_3$ coordination.
8. EFTEM images after the annealing process suggest a reduction of the Si NP average size after the annealing process.
9. No clear determination of size by microcopy due to the amorphous nature of host and Si NPs in the cases of smaller Si NPs. Other techniques are required to a in depth study.

Chapter 5

Morphological properties inferred from optical response

The presence of amorphous Si NPs embedded in amorphous aluminium oxide host has been observed by electron microscopy techniques. Therefore our Si NPs have 1 nm to 4 nm as average diameter showing quantum confinement. The analysis of the absorption of the Si NPs seems to be the unique route to estimate an average size and therefore the unique route to obtain the geometric parameters of the 2D-distributions at the nanoscale. In this Chapter the different methods to obtain the band gap energy of the amorphous Si NPs are discussed and a criteria to a average size estimation is established.

5.1 Size dependent optical response of semiconductor Si NPs

The HRTEM images has shown a weak presence of amorphous Si NPs embedded in a amorphous aluminium oxide matrix while the EFTEM images has shown clearly the Si NP formation during the growth process and their distribution in layers (Figure 4.2 and Figure 4.7a). But the amorphous nature of Si NPs and a-Al_2O_3 host and the proximity between the mass of silicon and aluminium makes difficult to identify the shape and size of the Si NPs by HRTEM or EFTEM. A usual approach to obtain information of the size of semiconductor Si NPs is based on the measurement on the PL response.[55] Nevertheless in the Si NP doped as grown thin films no PL has been observed. This is probably because of the high number of defects that act as non-radiative decay channels in the as deposited thin films (discussed in detail in the Chapter **??**). The absorption similarly to PL carries information on the electronic structure, but unlike PL the absorption is not sensitive to defects on Si NP surface or host. Therefore we have turned to the measurements of the absorption spectra in order to provide us information about the electronic structure and then about an average size of the Si NPs.

The thin films studied are a-Al_2O_3 thin films doped by Si NPs and Er^{3+} ions distributed in layers. The a-Al_2O_3 is transparent in all the UV-VIS range and the concentration of Er^{3+} is too low to be observed by optical absorption spectroscopy of the thin films. Therefore the absorption spectra is only related to the presence of the amorphous Si Si NPs. The Figure 2.6 shows the transmission of Si NP doped a-Al_2O_3 thin films obtained by selecting the number of pulses used to ablate the silicon target. The absorption edge shifts to longer wavelengths when the Si NP size is increased due to quantum confinement. Therefore our Si NPs are an special system as they show quantum confinement behavior being constituted by an amorphous indirect semiconductor. Before analyzing the relation between the optical properties and the average size of the 2D Si NP distributions we have to analyze the direct or indirect behavior of the amorphous Si NPs to understand the optical response and then inferred the Si NP band structure.

5.2 Absorption in semiconductors

The optical absorption spectra of semiconductors could provide a rich information about the semiconductor electronic properties such as band-gap, direct or indirect transitions, distribution of states or defects and impurity levels [56, 57, 58]. In semiconductors the photons can excite electrons from the valence band to the conduction band or/and interact with phonons or electrons in localized defects. Our main purpose is to obtain information about the band gap energy of the Si NPs, in fact only the region close to the fundamental absorption edge have been examined.

The first step is to analyze the direct or indirect behavior of our amorphous Si NPs is

to determine the mathematical approximation of the optical absorption edge that fits the absorption and subsequently to obtain the band-gap energy. The absorption edge is mainly related to the band to band transitions. These inter-band (band to band) transitions must preserve the k-selection rule imposed by the conservation of momentum that implies $\mathbf{k}_\gamma + \mathbf{k}_i = \mathbf{k}_f$ where $\mathbf{k}_i$ and $\mathbf{k}_f$ are the wave vectors to the initial and final electron states and $\mathbf{k}_\gamma$ corresponds to the incident photon. Due to the small momentum of the photons in the optical range ($p_\gamma = h/\lambda$, $k_\gamma = 2\pi/\lambda$), transitions involving only photons imply a very small momentum change. Then it is possible to make the approximation $\mathbf{k}_i \sim \mathbf{k}_f$, indicating that the inter-band transitions must preserve the wave vector.

This condition close to the band-gap involving only photons is possible when the semiconductor band diagram shows the minimum energy of the conduction band and the maximum energy of the valence band with the same wave vector as in the *direct semiconductors*. In *indirect semiconductors* as silicon, the participation of single or multiple phonons is necessary for the inter-band transition in the band-gap, thus the probability of transition is reduced and the momentum conservation rule can be written as $\mathbf{k}_i \pm \mathbf{k}_\Omega = \mathbf{k}_f$ where $\mathbf{k}_\Omega$ is the wave vector of the phonons involved. This difference is shown in the shape of absorption spectra and the probability of photon emission in indirect semiconductors is reduced.

5.2.1 Direct semiconductors

The absorption in the GAP is proportional to the probability of transitions and the joint density of states. Considering the simple general case of parabolic bands and in the case of allowed direct transition (direct semiconductors) in the region close to the band-gap,[58] the absorption is proportional to the root square of the energy as in the equation 5.1:

$$\begin{aligned} & \alpha = 0, \quad for \quad \omega < \omega_g \\ \alpha \propto (\omega - \omega_g)^{1/2} \quad & \Longrightarrow \quad \alpha \propto (E - E_g)^{1/2} \end{aligned} \tag{5.1}$$

where E_g is the energy of the band-gap.

The shape of the square of absorption for an example of direct semiconductor (PbS) is shown in Figure 5.1.[59] It is possible to obtain the value of the energy gap plotting the square of the absorption coefficient as a function of the photon energy. Then the curve shows a linear behavior and the intercept with the energy axis defines the direct energy gap value. Alternatively, the energy gap can be estimated as intercept with the energy axis in a semi-logarithmic plot of the multiplication of absorption coefficient for the energy.

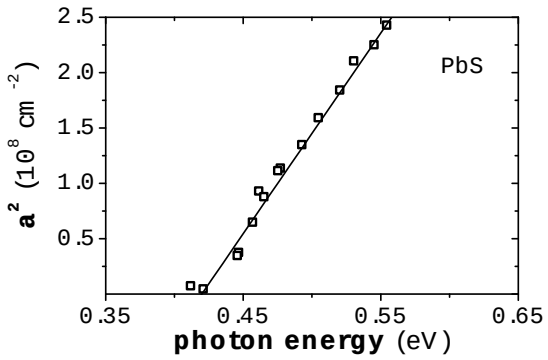

Figure 5.1: Plot of the square of the absorption coefficient of PbS as a function of the photon energy.[59]

5.2.2 Indirect semiconductors

In indirect semiconductors the minimum of the conduction band and the maximum of the valence band have associated different values of wave vector, then the presence of phonons are required to the inter-band transition. The conservation of momentum requires $\mathbf{k}_f + \mathbf{k}_\Omega = \mathbf{k}_i + \mathbf{k}_\gamma$. As momentum of the photon is negligible, then the conservation of momentum for an indirect transition can be expressed as $\mathbf{k}_f - \mathbf{k}_i = \pm\mathbf{k}_\Omega$.

Similarly, the conservation of the energy for the two cases of phonon emission and absorption can be expressed as:

$$\hbar\omega_{\gamma,e} = E_C - E_V + E_{\Omega,emitted} = E_{gap} + E_{\Omega,emitted} \tag{5.2}$$

$$\hbar\omega_{\gamma,a} = E_C - E_V - E_{\Omega,absorved} = E_{gap} - E_{\Omega,absorved} \tag{5.3}$$

where E_C and E_V are the energy level at conduction band and valence band respectively and the $E_{\gamma,e}$ is the energy of the photon in the case of a emission of a phonon and the $E_{\gamma,a}$ is the energy of a photon in the case of the absorption of a phonon.

From equations 5.2 and 5.3 it is evident that the initial and final states of the electron in the valence and conduction bands, can have an anergy range given by $\hbar(\omega_\gamma \pm \omega_\Omega)$, where ω_Ω and ω_γ correspond to the angular frequencies of the phonon and the photon respectively. It defines two energy regimes, where the particular transitions conserve the energy between the initial and the final states. The absorption is proportional to the probability of transitions and the joint density of states in each energy regime (it is possible to calculate by using the second order perturbation theory [57]). Then:

Transition with phonon absorption:

$$\alpha_a \propto (E - E_g + E_\Omega)^2 \quad for \quad E_\gamma > (E_g - E_\Omega) \tag{5.4}$$

Transition with phonon emission:

$$\alpha_e \propto (E - E_g - E_\Omega)^2 \quad for \quad E_\gamma > (E_g + E_\Omega) \tag{5.5}$$

An example of the general shape of the absorption edge for an indirect-gap semiconductor could be observed in the Figure 5.2 that shows the square root of the absorption coefficient of silicon as a function of the photon energy [60]. It is clear the presence of two linear regimes that can be analyzed independently. In fact, if the plots of $\sqrt{\alpha_e}$ and $\sqrt{\alpha_a}$ are extrapolated to the energy axis, the intersections associated gives as the values of $E_a = E_g - E_\Omega$ and $E_e = E_g + E_\Omega$. Then the band gap energy corresponds to the midpoint between the two energies $E_g = (E_a - E_e)/2$.

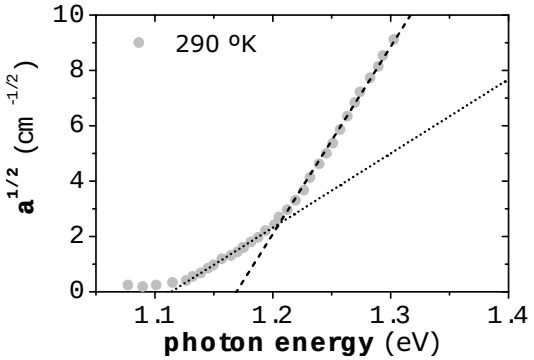

Figure 5.2: Dependence of the absorption constant on photon energy for bulk silicon (reference [60])

5.3 Direct or indirect Si NPs?

The silicon as a indirect semiconductor is a poor light emitting material. As was explained in the previous section 5.2 the indirect semiconductor needs the intervention of phonons to observe a radiactive photon emission, as a consequence, the probability for radiactive recombination is very low. The discussion about the use of silicon as an efficient emitter is still controversial [61]. But this is a different debate that not only concerns the direct or indirect character of silicon, and that involves other physical properties as defects, dangling bonds and nanocrystal surface passivation or oxidation.

In the nineties there was a great discussion about the indirect or direct nature of silicon nanoparticles (usually called quantum dots) to reduce the poor quality of silicon based emitters and to understand the possibility of improvement of the quantum efficiency of silicon in this systems. Theory works about how to turn the indirect character of the silicon to direct character through the reduction of the size of the Si NPs were developed, but still today no experimental evidence has been obtained of silicon direct character in small

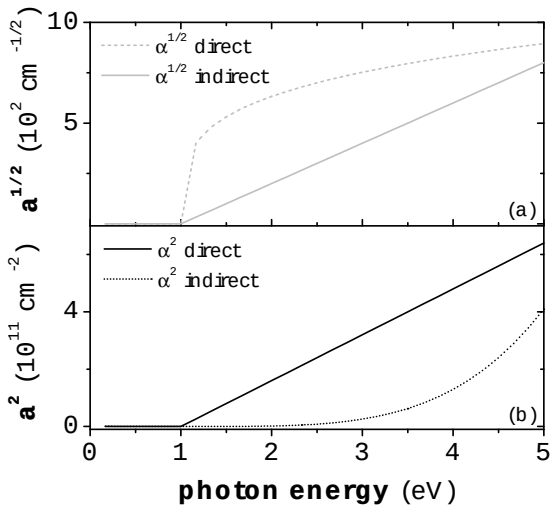

Figure 5.3: Behavior of the square and the root of the absorption a function of the photon energy for an indirect or a direct semiconductor for a simulation assuming the dependencies defined in the expressions 5.1 (Figure 5.3.a) and 5.5 (Figure 5.3.b).

nano-silicon.[41, 62, 63] Most standard quantum mechanics textbook explain the allowed states of the charges generated associated to a Si NP as the states of a single particle in a potential well but, however, in Si NPs the electrons and holes motion is governed by the silicon band structure and then to the silicon indirect character causing an interesting and complex physical problem to solve. In the most simple approximation of the electronic states of the nanocrystals as discrete levels as in the atoms, the optical matrix element that defines the allowed or nor allowed optical transitions must be evaluated. Therefore the wave functions of the confined carriers (electron and holes) are spread in the wave-vector space (k space) that breaks the usual k-selection rule (momentum conservation) for special Si NP sizes. [63, 41] It is possible to define the wave-functions of the electrons in the Si NP states as Fourier transform of the usual crystal basic function. These Fourier component plays the same role in the Si NPs as the phonons in the bulk material and then direct optical transitions become allowed (called zero-phonon transitions). In Si NPs this zero-phonon assisted transitions are possible for size scales smaller than 2.0nm [63] for crystalline Si NPs and 2.4 nm for amorphous Si NPs[64].

Our aim is to obtain the band-gap energy value to determine the Si NP average diameter of the 2D-Si NP distributions. Actually there is no reasonably evidence about the nanocrystal of silicon retain the indirect character [65, 66, 67] but, however, in other indirect semiconductor with similar properties, as Germanium [68, 69], direct character has been observed when the size is reduced enough. The electron microscopy analysis explained in the Chapter 4 shows the presence of very small Si NPs with sizes from 1 nm to

4 nm. Therefore in order to establish a estimation method it is is necessary to analyze the direct or indirect character of our the amorphous Si NPs from the absorption experimental data. The Figure 5.3 shows the square and the root of the absorption as a function of the photon energy for an indirect or a direct semiconductor, assuming the expressions 5.5 and 5.1. The linear behavior is only observed for the square of the absorption in a direct semiconductor and the root of the absorption for an indirect semiconductor. Therefore analyzing the linear tendency of the square or root of the absorption data it is possible to identify the direct or indirect character of the Si NPs.

5.3.1 Si NP absorption and determination of band-gap energy

In order to obtain the absorption of the Si NPs, transmission and ellipsometry measurements were performed in the thin films deposited on fused silica and silicon substrates, respectively. Thereby a preliminary ellipsometry was performed in the optical range from 300 to 1700 nm. A BEMA (Bruggeman Effective Medium Approximation) model was used to fit the optical constants of the nanocomposite layer including the absorption. The BEMA model does not account the band-gap variation with the Si NP size because the amorphous silicon used to fit the optical properties have the same optical properties between thin films. So the BEMA did not prove to be useful for obtaining the energy gap and other models must be used as Tauc-Lorentz oscillators.[1] However the optical constants obtained by fitting the spectroscopic ellipsometry data to a BEMA model are useful to estimate a range for the absolute value for the absorption and are helpful to corroborate the absorption calculated from the transmission measurements.

The transmission of the films is an indirect measurement of the absorption, but is clear, fast and non destructive method to characterize the optical properties. The Figure 2.6 of the Chapter 2 shows the transmittance from thin films embedding Si NPs of different sizes deposited on a fused silica substrate (transparent in all the measurement range). It is possible to observe how the absorption edge is shifted to lower energies when the number of pulses used to ablate the silicon increases indicating a increase of the size of the Si NPs.

The transmittance is the fraction of incident light at a specified wavelength that passes through a sample, $T = I/I_0$, where I_0 is the intensity of the incident light and I is the intensity of the light coming out of the sample. At normal incidence conditions we assume that the contribution of reflection is negligible, thus it is possible to use the *Beer-Lambert law* $T_{film} = Ie^{-\alpha z}$, where z is the thickness of the absorber. Consequently it is possible to obtain the absorption coefficient from transmission measurements using the expression 5.6.

[1] Actually this work is in progress by P.M. Roque at the IO-CSIC

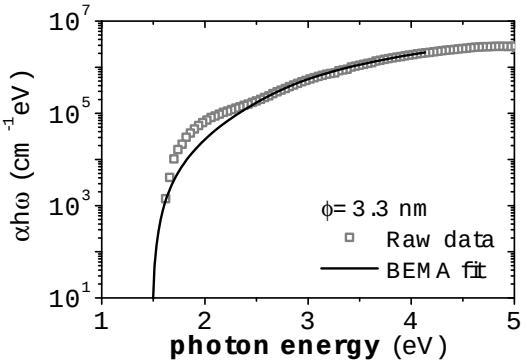

Figure 5.4: Logarithmic plot of the absorption coefficient as a function of the photon energy for a thin film doped by Si NP with an average diameter of 3.3 nm. The raw data correspond to the absorption obtained from the transmission measurements and the black line shows the BEMA fit model from the ellipsometry measurements.

$$\alpha = \frac{\ln(\frac{1}{T_{film}})}{z},\ where\ T_{film} = T/T_{substrate}. \tag{5.6}$$

The expression 5.6 have been obtained assuming that the reflected beam at normal incidence is zero. However the interference between the reflected beam and the transmitted beam in the interface substrate-thin film generates oscillations as a function of wavelength in the transmittance response that can make difficult identified the gap energy. Moreover the transmission measurements (Figure 2.6) shows a displacement in the IR region to lower values of transmission that affects more to the thin films with higher silicon content. The estimation of the absolute zero for the absorption of the nanocomposite is essential to obtain a correct band-gap energy value due that it is critical to determine the intercept with the Photon energy-axis that define the GAP. Therefore it is essential estimate the percentage of reflected beam at the air-thin film interface (R_{air-t}) and the thin film-substrate interface (R_{t-s}). Taking into account that the thin film and the substrate form a multilayer structure the absorption can be obtained by the expression 5.7:

$$\alpha = \frac{\ln(\frac{F_{real}}{T_{film}})}{z}. \tag{5.7}$$

where $F_{real} = (1 - R_{air-t})(1 - R_{t-s})$ and R_{1-2} is a function of the complex optical constant of the mediums ($\mathbf{n}_{medium}$) by the expression 5.8.

$$R_{1-2} = |\frac{\mathbf{n}_{medium-2} - \mathbf{n}_{medium-1}}{\mathbf{n}_{medium-2} + \mathbf{n}_{medium-1}}| \tag{5.8}$$

Label	Substrate	z (nm)	$n_{composite}$	Design parameter Si (P/layer)
$SE\phi 1.6$	Si/Fused SiO_2	15	1.97 + 0i	75
$SE\phi 2.2$	Si/Fused SiO_2	26	2.03 + 0i	125
$SE\phi 2.6$	Si/Fused SiO_2	44	2.05 + 0i	185
$SE\phi 2.8$	Si/Fused SiO_2	50	2.10 + 0i	210
$SE\phi 3.3$	Si/Fused SiO_2	70	2.40 + 0i	250

Table 5.1: Table of thin films produced to study the dependence of interaction on Si NP sizes. The total thickness of the sum of all the nanocomposite layers, the complex refractive index at 1.53 μm and the corresponding design parameter for each thin film are shown.

The $\mathbf{n}_{thinfilm}$ is valued as a weighted average of the a-Al_2O_3 and the nanocomposite optical constants. The nanocomposite optical constants were obtained by the ellipsometry analysis. The factor F_{real} varied form 0.92 to 0.95. The next issue is to identify the z value that corresponds to the sum of the thickness of all nanocomposite layers forming the nanostructured thin film because the a-Al_2O_3 and substrate are not absorbers in all the optical range. The simulations obtained from the ellipsometry fitting using a BEMA model gives us information about the thickness of each layer of Si NPs of the nanostructured thin films. As an example the Table 5.1 shows the z value and the optical constants for a series of films formed by Si NP with different average diameter.

The Figure 5.4 shows the agreement between the EMA model fitted simulation without interference oscillations and the absolute absorption obtained from transmission measurements for a thin film with Si NPs embedded with a average size around the 3.3 nm.

Direct character

Once the absorption absolute magnitude is obtained from the transmission measurements the shape and tendency of the curves are analyzed to determine the estimation of the band-gap as indirect or direct Si NPs.

The Figure 5.5 shows the square of the absorption coefficient for a-Al_2O_3 thin film doped with Si NPs with different average diameters. The curve of the absorption coefficient does not show a linear behavior as a function of the photon energy as in direct semiconductors. Note that almost all articles about direct semiconductor analyze the absorption only in the knee region close to the fundamental absorption edge [59]. The knee region closer to the absorption edge shows linear behavior at low absorption values. However the simulations of the square of absorption for an indirect semiconductor show closer to indirect than to direct semiconductor (see Figure 5.3), as a result the Si NPs in this work show indirect semiconductor character and only in the case of the smaller size

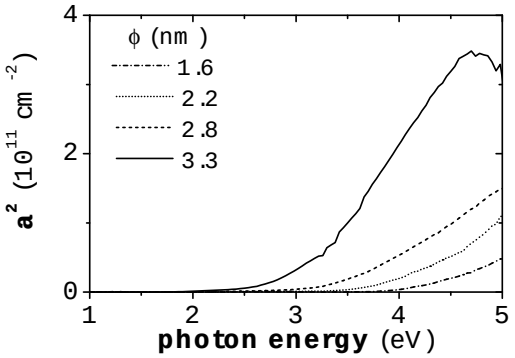

Figure 5.5: Square of the absorption coefficient for a-Al_2O_3 thin film doped by Si NPs with different average diameters obtained from transmission measurements.

the direct character is possible.

Indirect character

The root of the absorption of for a-Al_2O_3 thin film doped by Si NPs with different average diameters is shown in the Figure 5.6. A linear behavior is observed and only it is modulated due to the interference phenomena between the reflected and transmitted beam. The inset shows clearly the linear behavior in the absorption data obtained from the fit of the ellipsometry data using a BEMA model for the thin film with an average diameter of 3.3 nm superimposed to the experimental data from the transmissions. However in the description of the absorption of indirect semiconductor (Section5.2.2) two regimes were described one for the inter-band transitions that required the emission of phonons and another for the inter-band transitions that required the absorption of phonons. Therefore only one process of emission or absorption of phonons is observed. The Figures 5.2 and 5.6 suggest that the phonon absorption has been masked by the the free carrier absorption or can be replaced by the intra-band transitions. This phenomena has already been observed in previous works in bulk indirect semiconductors.[70] If we assume the lack of phonon absorption, our band-gap energy estimation will be slightly higher than the real band-gap energy.

Note that in the literature that refers to *zero phonon transitions* [63] or *conversion of an indirect optical transition into a direct one* [41] a critical nanoparticle size is defined as estimated below $2.0 - 1.5nm$. Indeed the inversion of the semiconductor character can be only observed in our films formed by the smallest Si NPs. The Figure 5.7 shows the square and the square root of the absorption coefficient as a function of the photon energy for the thin film formed by the smallest Si NPs. The shape of the curves suggests a direct character, however the definition of indirect or direct character of this Si NPs is not conclusive due to the spectral limitation of our measurement system and the oscillations

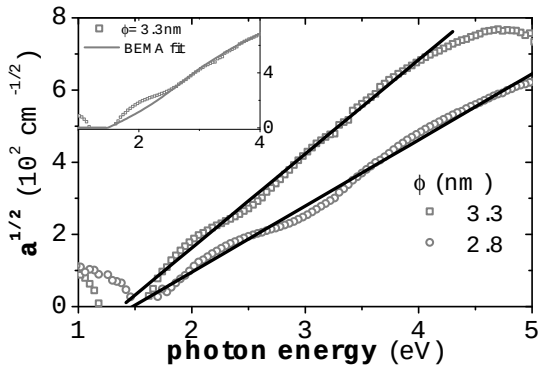

Figure 5.6: Root of the absorption for a-Al_2O_3 thin film doped by Si NPs with different average diameters. The grey empty square and circle points are the root of the absorption data obtained from the transmissions and the black lines the fitted linear behavior curves. The inset shows the root of absorption obtained from transmission measurements and the BEMA fit model obtained from the ellipsometry measurements.

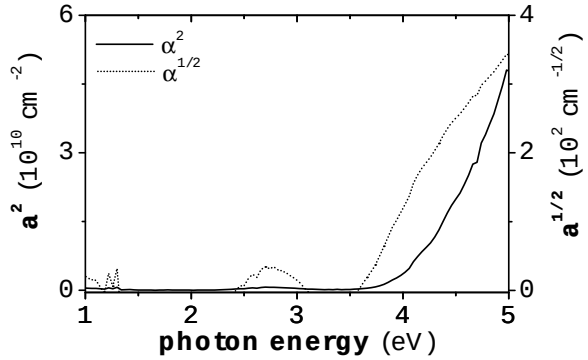

Figure 5.7: Square (black line) and the root (black dotted line) of the absorption a function of the photon energy for the a-Al_2O_3 thin film doped by the smallest Si NPs. The absorption was obtained from the transmission raw data.

in the optical response inherent to the transmission measurement that can hide the real absorption coefficient behavior.

In conclusion our Si NPs show a indirect semiconductor character for the thin films doped by the higher Si NP sizes, except for the thin film doped by the smaller ones for which it is not possible to obtain definitive conclusions. In order to be coherent in the methodology to estimate the band-gap thin films between samples, all the a-Al_2O_3 thin films doped by Si NPs were analyzed as indirect semiconductors. The band-gap values obtained for the thin films described the Chapter 3 are shown in the Table 5.2.

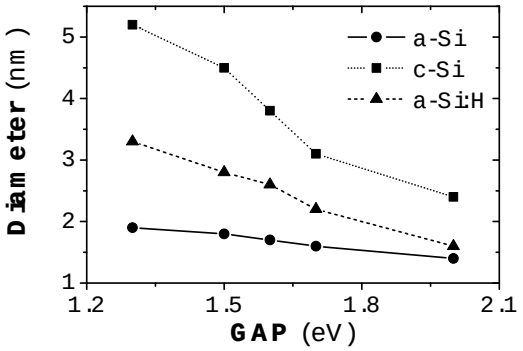

Figure 5.8: Average diameter of the Si NPs of the series to analyzed the size dependence as a function of the energy gap assuming either crystalline, amorphous or hydrogenated amorphous silicon qualities.

5.4 Energy band-gap and NPs average diameter

The energy gap gives us information about the electronic properties of our 2D-Si NP distributions, but a definition about an average size is useful to estimate the geometric properties at the nanoscale of the Si NP distributions.

In the tex-book the states for a semiconductor nanoparticle are defined as a number of discrete states as the states of a atomic particle, and then a Dirac delta is associated for every single state. Therefore the broad band observed for the absorption of our Si NPs embbeded in a-Al_2O_3 are related to the sum of all the dirac delta associated to the states of every Si NP size in a non monodisperse size distribution. The absorption of a quantum dot can be defined as:

$$\alpha(h\nu) \sim \frac{1}{h\nu} \sum | < n|p|n` > |^2 \delta(E_{n,n`} - h\nu)$$

where $| < n|$ is the state of the electron at the conduction band and the $|n` >$ is the final state of the electron at the valence band.[42] Obtaining a distribution of states with a maximum shifted of the band-gap energy, as we have observed in the a-Al_2O_3 thin film doped by the bigger Si NPs (see Figure 5.5). Our Si NPs distributions are not monodisperse and the absorption is the sum of the absorption of numerous Si NPs with various shapes and sizes. The main effect of this size dispersion is a broadening of the absorption spectrum of one Si NP. Therefore we define an average Si NP size or average Si NP diameter associated to the average band-gap energy. The shape of our absorption edge is similar to the theoretical as it can be observed in the reference [42] where for a Si NP with an energy gap of 1.67 eV obtained a maximum of the absorption around 4.75 eV, that it is a similar value of the absorption maximum obtained for the $SE\phi 3.3$ thin film with a Si NP size around 3.3 nm but with a band-gap energy of 1.3 eV.

Label	E_{GAP}	ϕ (nm)
$S0$, $S4$, $S7$, $S11$, $Only - Si - S$	1.2	4.4
$SE\phi 2.6$, $ES\phi 2.6$, $SES\phi 2.6$	1.6	2.6
$S(A-0.0)E\phi 2.2$, $S(A-0.5)E\phi 2.2$, $S(A-1)E\phi 2.2$	1.7	2.2
$S(A-0.0)E\phi 2.8$, $S(A-0.5)E\phi 2.8$, $S(A-1)E\phi 2.8$	1.5	2.8
$SE\phi 1.0$, $S\phi 1.0$	-	1.4
$SE\phi 2.2 - B$	1.7	2.2
$SE\phi 3.3 - B$	1.3	3.3
$SE\phi 1.6$	2.0	1.6
$SE\phi 2.2$	1.7	2.2
$SE\phi 2.6$	1.6	2.6
$SE\phi 2.8$	1.5	2.8
$SE\phi 3.3$	1.3	3.3

Table 5.2: Average diameters obtained form the absorption analysis for all the Er^{3+} and Si NP doped films

The relation between the Si NP diameter and the Si NP emission energy band-gap for crystalline, amorphous and amorphous hydrogenated nanoparticles have been theoretically estimated by Allan, Delerue and Lanoo in the 1997.[36] The Figure 5.8 shows the average diameter for the Si NPs obtained for the thin films produced to analyze the dependence of Er^{3+} PL on Si NP size as a function of the energy gap assuming either crystalline, amorphous or hydrogenated amorphous silicon qualities. As it can be seen the average size can change significantly depending on the nature of the silicon. For our case taking into account that the absorption is a priori less sensitive to surface properties than the photoluminescence, we have estimated our average Si NPs diameter as similar to the Si NPs formed by hydrogenated amorphous silicon because the dangling bons are in principle not going to contribute to the absorption edge. The average diameters obtained form the absorption analysis are listed in the Table 5.2.

The film with the smallest Si NPs $SE\phi 1.0$ does not show absorption band in the optical measurement range. In order to obtain a value of the Si NP average diameter, the band gap dependence on the silicon content has been analyzed for the thin films prepared specially to study the Er^{3+} PL dependence on the Si NP size. A linear behavior of the band-gap as a function of the silicon content per layer is observed. Thus assuming a linear dependence it is possible to estimate the average size for the $SE\phi 1.0$ thin film as 1.4 nm (Table 5.2) extrapolating the absorption.

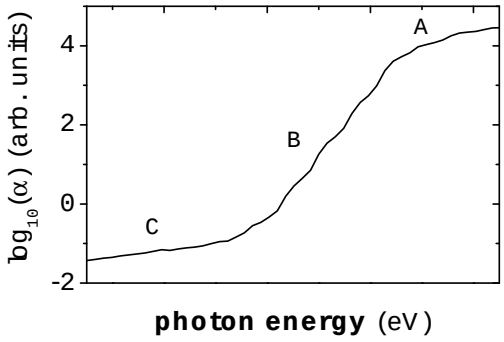

Figure 5.9: The three principal regions of optical absorption in an amorphous semiconductor. Dashed is a extrapolation of the region A. [71]

5.5 Amorphous and quality Si NPs

A work of Wood and Tauc [71] published at the seventies explain the absorption tails observed in the absorption edges of the amorphous semiconductors. They define three main regions in the absorption edge (see Figure 5.9). One defined as A correspond absorptions higher than $10^4\ cm^{-1}$ and where the absorption usually follows a quadratic dependence with the energy ($\hbar\omega\alpha \sim (\hbar\omega - E_g^{opt})^2$). It is associated to transitions between the band states.[72, 73] Two more regions are defined, one to the absorption from 1 to $10^4\ cm^{-1}$ (region B) and the other to the very low absorbtion edge with $\alpha < 1cm^{-1}$ (region C). These two regions are described with an exponential growth law ($\alpha \sim e^{\hbar\omega/E_t}$) and are associated to the tail states. The exponential edges observed in some crystals as Urbach tails are basically similar to the part B in the amorphous semiconductors. It seems therefore plausible to associated this exponential edges with similar physical mechanism. However the parte C are associated to deep potential fluctuations due to disorder, defects or impurities.

Observing the Figure 5.4 our Si NPs produced by PLD and embedded in a-Al_2O_3 does not shows the exponential tails and only the region A is obtained. This phenomenon has been reported previously, and sharp absorption edges have been obtained when the concentration of defects is small [74] and assuming that these tails states are associated to absorption induced by defects. Thus, taking into account these arguments our Si NPs shows an absorption edge that reveals a pure amorphous silicon with small number of defects. It will be discussed in the Chapter **??** by photoluminescence and cathodoluminescence measurements.

5.6 Conclusions

The absorption measurements show an indirect character for the amorphous Si NPs embedder in a-Al_2O_3 except the Si NPs with the smaller average diameter whose indirect or

direct character can be . The average diameters of all the designed 2D-Si NPs distribution have been estimated assuming a indirect character for all the Si NP sizes. The analysis of the absorption tails suggest the presence of pure amorphous Si NPswith reduced number of defects.

Chapter 6

Determining parameters of Si NP distributions

The Electron Microscopy has revealed the presence of Si NPs and their amorphous nature. Assuming the amorphous nature of the Si NPs and the optical band gap values obtained by the optical properties an average size of the Si NPs has been defined. Now, in this Chapter, it is described how the parameters of the two dimensional distributions of Si NPs have been determined from the Si content in the nanocomposite layer and the Si NP size. The Si content in the layers have been obtained from Rutherford backscattering spectroscopy (RBS) measurements and the values for the size of the Si NPs have been estimated from the optical measurements.

6.1 Compositional analysis by RBS

The Er- and Si-concentration depth profiles were determined by Rutherford backscattering spectrometry (RBS) using a 1.97 MeV $4He^+$ beam with the particle detector located at a scattering angle of 165 ï¿½. Simultaneously, in any special configuration we used a detector of Si(Li) placed at 135 ï¿½ for $PIXE$ measurements of the X-rays induced in the elements of the sample during ion bombardment. The beam size was set at 1 mm^2 to measure in a controlled point of the samples. The simulations of RBS spectra were performed using the program $SIMNRA$. [1]

The the low mass contrast between the two thin film components, silicon and aluminium, and the presence of silicon substrates or substrates based on silicon as fused silica or silica glass, make complicated to determine the amount of deposited silicon content. In order to eliminate the presence of silicon atoms beyond the silicon forming the Si NPs, our first experimental approach was to use special substrates for preparation of calibration thin films[2]. Therefore two amorphous silicon thin films were grown on LiF substrates, one at the begging of the production of the series and the other when the fabrication procedure had finished. The amount of silicon deposited per pulse will be determined by the mean of the silicon content per pulse between the two thin films in order to rule out the effects of target rail wear.

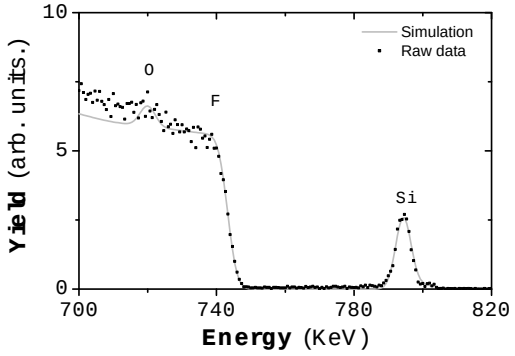

Figure 6.1: RBS spectrum of Si deposited on LiF substrate (black squared points). The grey line correspond to the simulation generated by the $SIMNRA$ program.[3]

The Figure 6.1 shows the RBS spectrum of the thin film of 7500 pulses on Si deposited on a LiF substrate. The silicon signal of the RBS spectrum is completely separate from the signal of LiF substrate as it was predicted. The signal from fluor and silicon atoms are observed besides a slightly signal associated to oxygen. This O_2 peak can be related to the presence of silicon native oxide formed at the surface of the thin film in contact

[1] The RBS analysis and measurements were performed at the CNA-CSIC at Sevilla by Javier Garcï¿½a Lï¿½pez y Yolanda Morilla Garcï¿½a

[2] In collaboration with M. Jimï¿½nez de Castro

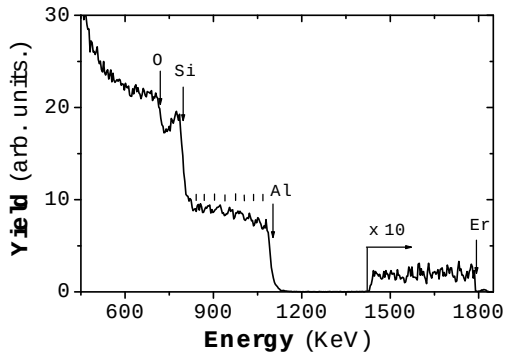

Figure 6.2: RBS spectrum corresponding to $S11$ film with s=11 nm. The surface channels of the different elements in the film are indicated.

with the air. For example the mean value of the Si deposition rate is 8.26 10^{12} cm^{-2} for the thin films produced to optimize the Si NP average size. Taking into account the Si deposition rate is possible to estimate the Si content deposited in each Si NP layer of the thin films (see Table 6.1).

Despite the compositional and atomic structure similarities of the components of the thin films, surprisingly, the RBS measurements performed for the multilayer nanostructures of the test thin films show clearly the presence of the Si NP layers. The RBS spectrum from the film with s=11 nm ($S11$) is shown in the Figure 6.2. Pay attention in the oscillations observed in the signals of Er which can be interpreted as a nonuniform in depth distribution of dopants. In the low energy region of the spectrum, the Al+Si signal contribution shows oscillations that are associated with the layered structure of the film. In the Al signal region of the spectrum, nine minima are observed, which correspond to the presence of the Si NP layers. Detailed quantitative interpretation of the RBS spectra was undertaken with assistance of the SIMRA code. The analysis shows that the Er areal density per layer is 3.4 10^{13} cm^{-2}, which is similar to that reported in our previous work on a-Al_2O_3:Er films.[26, 17] The Si areal density per layer is 7.0 10^{15} cm^{-2}, which is equivalent to an effective thickness of 1.4 nm, taking into account the density of the a-Si.[75] The total film thickness is 510 $\pm$ 10 nm and the s values determined for the films are 0, 4.0, 7.0, and 11.0 $\pm$ 0.5 nm, showing that a fine control of the deposited a-Al_2O_3 has been achieved.

The content of Si for the rest of Er^{3+} and Si NP co-doped thin films have been determined by RBS measurements of the multilayer structures. The Er deposited per pulse has been corroborated by PIXE analysis. The compositional content of the Si nanocomposite layers is reflected in the Table 6.1. Due to an updating of the excimer laser used in the ablation chamber that changes the spot size and energy density, the material deposited by pulse is different between series under similar deposition conditions. Nevertheless we would like to emphasize the reproducibility of the Si NP distributions.

When the content of silicon in a nanocomposite layer is the same for different thin films, independently of the deposition rate, the energy band-gap is located at the same photon energy. Thus it is assumed that the Si NP distribution (Si NP size, Si NP density, etc) is maintained and the determination of the absorption edge will be used to estimated the average size of the Si NPs.

Label	Pulses per layer	$[Si]_{layer}$ 10^{15} cm^{-2}
$S0$, $S4$, $S7$, $S11$, $Only-Si-S$	500	7.0
$SE\phi 2.6$, $ES\phi 2.6$, $SES\phi 2.6$	185	7.7
$SE\phi 1.0$	300	2.4
$SE\phi 2.2-B$	600	4.9
$SE\phi 3.3-B$	1200	9.8
$SE\phi 1.6$	75	3.1
$SE\phi 2.2$	125	5.2
$SE\phi 2.6$	185	7.7
$SE\phi 2.8$	210	8.8
$SE\phi 3.3$	250	10.4

Table 6.1: Table of RBS data of silicon content for all the thin films.

6.2 Densities, coverage and volume fractions of Si NP distributions

During the PLD process, the material is only deposited during a short time (a few microseconds) after the laser pulse, this special growth conditions lead to a higher density of nuclei than for a traditional vapor deposition techniques. Early works of the Laser Processing Group (LPG) about deposition of metal nanoparticles show how the diameter of the nanoparticles is increased and the number of nanoparticles is reduced when the number of pulses used to ablated the metal target is increased due to the coarsening and coalescence phenomena [32, 76]. Independently of the material from which the nanoparticles are formed an higher areal density of small nanoparticles has been obtained for nanocomposite thin films produced by alternated PLD that in other deposition techniques. In this section we are going to define the parameters of these high density Si NP 2D-distributions.

The **areal density of Si NPs** per layer can be estimated as in the expression 6.1

$$[SiNPs]_{2D} = \frac{[Si]}{\rho_{a-Si} V_{1NP}}, \tag{6.1}$$

where $[Si]$ is the areal density of Si, V_{1NP} is the volume of an average NP and ρ_{a-Si} is the density of amorphous Si [75]. The Si-concentration depth profiles were determined

by Rutherford backscattering spectrometry (RBS) and the volume of an average NP has been calculated assuming spherical Si NPs and using the value of the average diameter (d_{NP}) obtained from the Si NP band gap ($V_{1NP} = \frac{\pi}{6} d_{NP}^3$).

Once the density of Si NPs and the average diameter is established it is possible to determine the covered area (coverage), the volume fraction of silicon in the nanocomposite layers and the distance between centers of Si NPs.

The **covered area** (**coverage**) represents the maximum area occupied by the nanoparticles in a section of the film in the growth direction. It is the areal projection of the nanoparticles over a in-plane section. If we considerer that the Si NPs are spherical, the projection of the one Si NP in a plane parallel to the substrate is a circle with an area $A_{NP} = \pi r_{NP}^2$ where r_{NP} us the average radio of the Si NPs estimated by the optical absorption. Then, the percentage of coverage by the Si NPs in 1 cm^2 of sample is given by

$$f_{ac}[\%] = \frac{A_{Si}}{A_{TOTAL}} = [SiNPs]_{2D} * A_{NP}, \tag{6.2}$$

where A_{Si} is the area occupied for all the Si NPs and A_{TOTAL} is the total area considered.

Assuming spherical shape for the Si NPs is also possible to obtain the **volume fraction** that corresponds to the volume occupied by the nanoparticles in the total volume of the nanocomposite layer assuming that the thickness of the nanocomposite is the average diameter of the Si NPs. In this way the volume fraction of nanocomposite layer has been calculated by the expression 6.3.

$$f_v[\%] = \frac{V_{Si}}{V_{TOTAL}} = \frac{[SiNPs]_{2D} * V_{1NP}}{d_{NP}}. \tag{6.3}$$

As an example the thin films produced to study the optimum Si NP average size are analyzed in detail. The Si NP distribution parameters are listed in the table A.1. The coverage obtained is large with values close to 100% for the thin films in which the number of pulses on the Si target are larger an 185. Note that this has no physically meaning. This is inconsistency and these values can be justified if we analyze the experimental data that we are using to make the estimations. First, the density of our amorphous silicon has not been measured and the reference used is from amorphous silicon obtained by implantation.[75] Note that this choice was made because the PLD thin films are more dense that the thin films produced by other deposition techniques such as sputtering[77], therefore a value of amorphous silicon density more close to density of the amorphous silicon obtained by implantation than to density of the amorphous silicon obtained by sputtering is expected. In the case that a amorphous silicon density lower that the density for the implantation films is asssumed, the value of f_v and f_{ac} obtained by the expressions 6.1 and 6.2 will be higher

than the previously obtained and the new density of Si NPs implies a coverage higher that the 100% remaining a non physically possible value. Consequently, the Custer reference [75] seems a good approximation of the density of the amorphous silicon produced by PLD.

Label	ϕ (nm)	$[SiNPs]_{2D}$ ($10^{13}cm^{-2}$)	$f_{ac,raw}$ (%)	$f_{v,raw}$ (%)
$SE\phi 3.3$	3.3	1.2	**99**	67
$SE\phi 2.8$	2.8	1.6	**96**	64
$SE\phi 2.6$	2.6	1.7	**91**	61
$SE\phi 2.2$	2.2	1.9	73	48
$SE\phi 1.6$	1.6	3.0	60	40

Table 6.2: Areal density ($[SiNPs]_{2D}$), coverage (f_{ac}) and volume fraction (f_v) of Si NPs for the films prepared for the study of the Er^{3+} PL optimization as a function of Si NP diameter obtained from raw RBS data.

All the calculations have been done assuming that all the silicon is forming Si NPs. The RBS data gives us information about the content of every kind of atom in the thin film with atomic resolution independently of if these atoms are forming aggregates or are only distributed as individual atoms through the host. Previous LPG works [32] shown that part of the deposited atoms are dissolved in the thin films [76] and therefore do not form Si NPs. It has been shown that the content for other elements as Ag that are formed aggregates deposited by PLD calculated through RBS data is overestimated in comparison to the information obtained from Transmission Electron Microscopy (TEM) images or GISAXS data. Therefore the real content of Si that is formed nanoparticles is estimated assuming that only an average 60% (60% $\pm$ 20% depending on size) of the silicon is forming nanoparticles.[32] However note that the estimation of the average diameter from the absorption data is correct due to the fact that only the silicon forming Si NPs affects to the absorption of the nanocomposite layer and the silicon atoms distributed as individual atoms through the host can contribute to the increase of the real value of the refraction index but not to the absorption. Therefore, the new Si NP distributions parameters have been calculated assuming that only the 60% of the silicon contributes to the formation of the Si NPs and that the diameter is obtained from the absorption edge. The Figure 6.3 shows the real Si NP 2D-density and Si NP coverage percentage as a function of the Si NP diameter.

The distance between Si NPs has been calculated assuming that the Si NPs are homogenously distributed in the a-Al_2O_3 surface, that the Si NPs are spheres and that the partial area associated is a square centered at the Si NP. Then the distance between edges of adjacent Si NPs is given by $d_{edge-edge} = \sqrt{A_{NP}/d_{NP}}$, where d_{NP} is the average diameter of the Si NPs and A_{NP} is the partial area associated to the Si NP (in an area of 1 cm^2

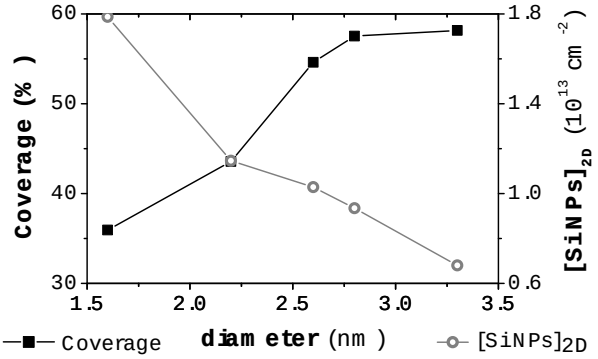

Figure 6.3: Si NP 2D-distribution parameters as a function of the Si NP diameter

is given by the expression $A_{NP} = 1/[SiNPs]_{2D}$). The dependence of distances between adjacent Si NPs on Si NP diameter is shown in the Table 6.3.

Label	ϕ nm	$[SiNPs]_{2D}$ $10^{13}cm^{-2}$	f_{ac} %	f_v %	$d_{edge-edge}$ nm
$SE\phi 3.3$	3.3	0.7	60	40	0.47
$SE\phi 2.8$	2.8	0.9	57	38	0.53
$SE\phi 2.6$	2.6	1.0	54	36	0.52
$SE\phi 2.2$	2.2	1.1	44	29	0.75
$SE\phi 1.6$	1.6	1.8	36	24	0.76

Table 6.3: Areal density of Si NPs ([Si NPs]), coverage (f_{ac}) and volume fraction (f_v) associated to the thin films with different Si NP diameter calculated from RBS corrected data.

6.3 Critical analysis of the parameters of the 2D-Si NP distributions

In order to determine the reliability of the approximations we have compared the Si:a-Al_2O_3 nanocomposite system with the Ag:a-Al_2O_3, Cu:a-Al_2O_3 and Fe:a-Al_2O_3 systems using the same deposition system and under similar deposition conditions [32, 33, 76]. In the metal:a-Al_2O_3 systems we have the advantage of the direct TEM images. When the Si NP coverage is is close to the 40% the number of the initial silicon nucleation sites is similar to the Cu. For example, when the silicon coverage is a 36% the density of Si NPs is 1.8 10^{-13} cm^{-2} and for the Cu at an coverage of 35% the density of nanoparticles is 1.0 10^{-13} cm^{-2} number, while for Ag at a coverage of 40% the density of Ag nanoparticles

is 0.2 10^{-13} cm^{-2}, and for the Fe nanoparticles the density is 7.8 10^{-13} cm^{-2} at an coverage of 39%. This is due to the fact the different atomic species have different mobility over the a-Al_2O_3 surface and is related to the affinity of the atoms that arrives over the substrate to bond to oxygen atoms.

$$dG = dF + d(PV) \tag{6.4}$$

Material	f_{ac} %	$[NPs]_{2D}$ $10^{-13}cm^{-2}$	-ΔH $10^{-6}J/Kgmol$	ΔF $10^{-6}J/Kgmol$
Ag	40	0.2	26-31	-11
Cu	35	1.0	155-167	-127 - -146
Si	36	1.8	438-911	-137 - -805
Fe	39	7.8	823-1122	-741 - -1015
Al	–	–	1675.56	-1577.61

Table 6.4: Heat and Free Energy of Formation of Oxides for different materials at 298K (room temperature).

The Gibs Free Energy (G) gives us information about the equilibrium and spontaneity condition for a chemical reaction at constant pressure and temperature. A reaction is spontaneously when (-ΔG) is negative. The Gibs Free Energy is related to the Free Energy of Formation of Oxides by the expression 6.4. In our deposition conditions we can considerer $d(PV) = 0$ and then $dG = dF$. Therefore the Free Energy of Formation of Oxides gives us information about the probability of a bond between an oxygen atom and the corresponding element (Si, Cu, Ag or Fe). The table 6.4 shows the the Standard Heat of Formation of Oxides (-ΔH) and the Free Energy of Formation of Oxides (ΔF) for the possible oxides constituent of the nanoparticles materials. A relation between the ΔF and the number of density of nanoparticles is observed. The ΔF is negative for all the oxides indicating spontaneity and when ΔF is decreased the density of nanoparticles is increased indicating a dependence of number of nuclei centers with the affinity of the atoms to the oxygen. The data obtained for the Si NP deposition is consistent with the rest of materials what further supports the results obtained.

The degree of oxidation of the Si NPs can now were considered. In this way we have to take into account the Standard Heat of Formation of the a-Al_2O_3. Our Si NPs are embedded in an oxide, the a-Al_2O_3 and the atoms constituent of the nanoparticles has to compete with the aluminium for the oxygen atoms. The Standard Heat of Formation gives us information about the energy necessary to induce the reaction at constant pressure and temperature. The -ΔH is positive for all the studied oxides but the value for the

Label	$[SiNPs]_{2D}$ 10^{13} cm^{-2}	f_{ac} %	f_v %	$d_{edge-edge}$ nm
$SE\phi 2.6$, $ES\phi 2.6$, $SES\phi 2.6$	1.0	55	36	0.52
$SE\phi 1.0$	2.1	33	22	0.77
$SE\phi 2.2 - B$	1.0	41	27	0.85
$SE\phi 3.3 - B$	0.6	54	36	0.67
$SE\phi 1.6$	1.8	36	24	0.76
$SE\phi 2.2$	1.1	44	29	0.75
$SE\phi 2.6$	1.0	54	36	0.52
$SE\phi 2.8$	0.9	57	38	0.53
$SE\phi 3.3$	0.7	60	40	0.47

Table 6.5: Si NP distribution parameters of all the thin films.

a-Al_2O_3 is higher than all of then, as a result, the probability of oxidation of nanoparticles embedded in a-Al_2O_3 is low. This has been demonstrated for the Fe and the Cu NPs deposited by PLD that show negligible oxidation.[76, 31] Therefore, when the atoms arrives to the substrate covered by the a-Al_2O_3 the number of nuclei is directly related to the affinity of the atoms to react with the oxygen of the a-Al_2O_3 surface. Nevertheless once the nanoparticles are formed further oxidation is not expected.

Applying the same analysis to the other series of samples, all the Si NP distribution of all thin films can be parameterized, see Table 6.5 for further details.

6.4 Conclusions

The atomic content of the different components of the nanostructures have been obtained by RBS. Combining the RBS data and the Si NP average diameter determined by optical absorption, the characteristic parameters of the Si NP distributions have been determined and corroborated by comparison with the distribution of metal nanoparticles.

Chapter 7

Defects in a-Al_2O_3 and surface of the Si NPs.

The aim of this Chapter is to analyze the relevant properties of the Si NP surface and its interaction with the a-Al_2O_3 embedding media (a-Al_2O_3-Si NP interface). These properties will be derived from cathodoluminescence (CL) and photoluminescence (PL) measurements. This analysis is a necessary step towards the interpretation of the Er^{3+} emission when it is located close to the Si NPs.

7.1 Introduction

Photoluminescence spectroscopy is a non-contact and non-destructive method of probing the electronic structure of materials. Controlled light is directed onto a sample, where it is absorbed in a process called photo-excitation. One way to dissipate this energy by the sample is through emission of light (luminescence). In the case of photo-excitation, this luminescence is called photoluminescence (PL). In our case, the PL spectrum provides the transition energies, which can be used to determine electronic energy levels and the band-gap of the Si NPs.

Thoroughly studies on the interface properties between bulk silicon and SiO_X and $Al_2O_3 - Si$ oxides have been carried out for microelectronic applications because phenomena at surfaces and interfaces tend to dominate the behavior of excitations and the performance of the microelectronic devices. These works indicate that the Si-Al_2O_3 interface are more robust than the Si-SiO_X interface, with lower number of defects (specially dangling bonds) and thinner layer of silicon oxidized at the interface, being the number of defects more limited volumetrically. [78, 79] There are studies about Si nanocrystals-SiO_2 interface defects but to our knowledge not for Si NPs embedded in a-Al_2O_3. [80]

Defects and impurities at interfaces provide new states for electrons and holes, altering their motion, lifetime, and transition energies. [81] Therefore, control the surface properties of the Si NPs could be a route to improve their emission efficiency or the interaction phenomena with the Er^{3+} ions. Consequently the study of the host and interface defects of Si NPs embedded in a-Al_2O_3 is one key to understand and complete the analysis of the energy exchange from Si NPs to Er^{3+} ions. Moreover a new host with different Si NP-host interface properties than the usual SiO_2 could provide a route to improve the Er^{3+} performance at 1.53 μm.

7.2 Are the amorphous Si NPs dark?

The advantages of PL analysis derive from the simplicity of optical measurements and the power to probe fundamental electronic properties. However the main drawback of PL analysis is that the sample under investigation must emit enough photons. For example, indirect-bandgap semiconductors as the silicon, have inherently low PL efficiency and non-radiative recombination processes tend to dominate the relaxation of excited populations. This problem can be increased by a poor interface quality, where discrete defect and impurity states abound causing rapid non-radiative events. Nevertheless, once a PL signal is detected, it can be used to characterize both radiative and non-radiative mechanisms due to the fact that it is a very sensitive and selective probe of such states. [81]

As it has been explained in the Section 5.3.1 the absorption is a good probe of the overall band structure of a semiconductor system. Therefore, the combination of the PL and the absorption measurements will give us information about the interface states of the Si

NPs to understand the Si NP - Er^{3+} energy exchange mechanisms and its phenomenology.

The usual emission range for emission of Si NPs is from 400 nm to 1000 nm [82, 83] and the peak emission band position and shape depend on the Si NP crystallinity degree, Si NP size and the host where the Si NP is embedded in. The shifted position of the PL spectra in relation with the absorption edge can be related to surface or interface defects [84] and Si NP interactions [85]. Several deposition methods have been use to produce Si nanoclusters embedded on oxide matrix (evaporation,[86] PECVD,[87, 88, 89, 90, 50, 82] implantation,[55, 91, 84, 92, 93, 94, 95] sputtering,[83, 96] electron beam evaporation,[85, 97] or PLD [98, 99]) leading the formation of crystalline[86, 55, 91, 84, 87, 83, 88, 85, 97, 92, 93, 96, 98, 94, 95, 99] or amorphous[89, 90, 50, 100, 82] Si nanoclusters embedded in SiO_2,[86, 55, 91, 84, 87, 83, 88, 85, 89, 90, 50] Al_2O_3 [97, 92, 93, 96, 98, 94, 95, 100] or other media as host[82, 99]. The PL peak position varied from 600 nm[55] to 1000 nm[83] for crystalline Si NPs embedded on SiO_2 from 450 nm [89] to 950 nm[50] for amorphous structures. Moreover the PL peak position and shape was very different for Si nanoclusters of similar sizes embedded in Al_2O_3 host with emission from 570 nm [93] to 750 [95] for the crystalline Si NPs and 500 nm for the amorphous [95]. The nature of the PL emission of Si nanoclusters in Al_2O_3 is still controversial due to a high contribution to the PL emission associated to host defects or impurities. [92, 93, 94, 95, 100]

The PL response has been obtained pumping with an Ar^+ ion laser tuned at 457.9 nm. The PL signal was detected at room temperature using an Acton 300i monochromator with grating for the VIS-NIR range, a Ge detector and standard lock-in techniques. The Figure 7.2 shows the PL spectra from 600 nm to 1400 nm from a Si NP doped only thin film ($Only - Si - S$ - reference of the thin films prepared to test the Er^{3+} and Si NPs doped a-Al_2O_3 system - Chapter 8) after different thermal treatments. These results will be discussed later in the Section 7.4. The spectra was corrected by the germanium detector curve response.

The black full line in Figure 7.2 shows the PL emission for the as grown $Only - Si - S$ thin film. No PL emission from Si NP has been detected in all the optical range. There is only a very weak background signal, that seems to increase for short wavelengths and can not be related to silicon emission. The same shape and intensity spectrum has been observed for all as-grown thin films (co-doped by Si NPs and Er^{3+} ions, only Er doped a-Al_2O_3 film and the a-Si nanolayer thin film). In fact, the same spectrum obtained despite they are completely different samples suggests the presence of no emitting Si NPs also called **dark amorphous Si NPs**. This definition was established by Kik et al. [101] to define the Si NPs that are not emitting due to the presence of Er^{3+} ions that can act as non radiative channels. In our case the emission is not observed in the usual region for the Si NPs indicating that a high number of non radiative channels for the Si NPs are present.

The production of the thin films at room temperature can justify the high number of Si dangling bonds, host defects and a poor Si NP surface pasivation, that can act as the non radiative channels. It has to be emphasized that no emission at 750 nm or 690 nm was detected, which is usual associated to Cr^{3+} and Ti^{3+} host impurities, respectively, pointing out the high purity of the a-Al_2O_3 produced by PLD. [93] In conclusion, a high number of host and Si NP surface defects, as for example Si dangling bonds, are present in the as grown thin films produced at room temperature. These defects are responsible of the lack of emission from the dark amorphous Si NPs, however our a-Al_2O_3 host is free of ions impurities that can give out any confusing PL signal.

7.3 Defects in the host

Photoluminescence occurs after excitation with light, but luminescence can be also observed under excitation with an electron beam, and in this case it is called cathodoluminescence (CL). This technique is usually used to investigate some characteristics of the specimens, such as trace impurities or lattice defects, as well as to investigate the crystal distortion. Also the CL allows to excite high energy states with the advantage that it is a technique not selective in energy. The PL spectra emission spectrum for the as grown thin films shows a background signal that suggest a possible emission at lower wavelengths. In order to corroborate the possible presence of a Si NP emission band below the 600 nm CL measurements were performed[1]. The samples were observed at 95 K, in a Hitachi S2500 SEM (Scanning Electron Microscope) in the CL mode of operation, at an accelerating voltage of 5-7 kV. The thickness of the thin films is 200 nm approximately, so the optimum acceleration voltage applied to the electron gun was varied from 5 kV to 7 kV to obtain a limited penetration of the electrons and to maximize the signal coming from the active medium. Visible light was detected using a Hamamatsu R-928 photomultiplier, and a cooled ADC germanium detector was used in the near infrared. More information about the measurement system is detailed elsewhere.[102]

As grown a-Al_2O_3 thin films co-doped by Er^{3+} ions and Si NPs of different sizes have been measured by CL ($SE\phi 1.0$, $SE\phi 2.2-B$, $SE\phi 3.3-B$) (not shown). The Figure 7.1 shows the typical emission spectrum for $SE\phi 1.0$. A peak emission in the green has obtained for all the co-doped thin films centered about 550 nm that it is related to the Er^{3+} $^4I_{15/2} -^2 H_{11/2}$ transition level. Also a broad UV-blue band extending from 300 to 500 nm was detected for all the films. Its emission band shape is independent of the Si NP size.

In order to determine the origin of this broad UV-blue emission band, a-Al_2O_3 samples

[1] External collaboration with Bianchi Mï¿½ndez and Emilio Nogales from the Group of *Micro- and Nanocharacterization of electronic materials* of the *Material Science* department of the *Universidad Complutense de Madrid*.

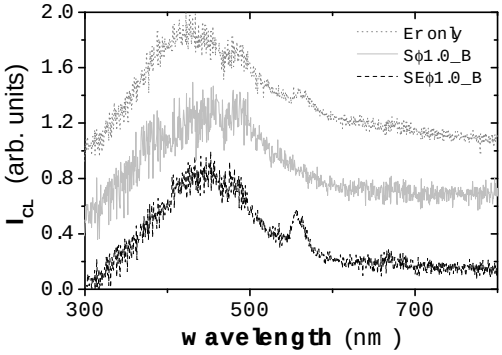

Figure 7.1: CL emission spectrum from as grown only Er doped film (dark grey dot line-$ErRef2$), only Si NP doped film (light grey line-$S\phi1.0$) and the corresponding Er and Si NP co-doped film (black dash line-$SE\phi1.0$). The spectrums have been displacement in the vertical direction to help the curves visualization

doped with only Er ($ErRef2$) and doped only with Si NPs ($S\phi1.0$) were also measured by CL. The Figure 7.1 shows the CL spectra for an only Er^{3+} doped film ($ErRef2$), the Si NP and Er^{3+} co-doped thin film ($SE\phi1.0$) and an only Si NP doped film ($S\phi1.0$) with the same Si NP diameter (1 nm). The UV-blue emission band is present in all the films independently of the Si NPs or Er^{3+} ions presence, therefore it has to be related to the a-Al_2O_3 host.

Different types of defects for sapphire had been reported and analyzed from their luminescence response. The same type of defects are expected in a-Al_2O_3. The oxygen vacancy defects are the most common and are divided in: *F centers* (oxygen vacancy with two electrons) that show an emission band centered at 413 nm, F^+ *centers* (oxygen vacancy with one electron) that show an emission band centered at 326 nm, F_2 *centers* (two oxygen vacancies with four trapped electrons) that show an emission band centered at 516 nm, F_2^+ *centers* (two oxygen vacancies with three electrons) that show and emission band centered at 380 nm and F_2^{2+} *centers* (two oxygen vacancies with two electrons) that show and emission band centered at 563nm.[103, 104] The CL spectrum of the $S\phi1.0$ without contribution from Er^{3+} ions was de-convolved by fitting three lorentzian-bands obtaining maximums at 380.5 ± 1.3 nm, 427.3 ± 2.1 nm and 484.6 ± 3.1 nm, that can be related to F_2^+ centers, F centers and F_2 centers, respectively.

In conclusion no emission related to the Si NPs has been detected in the visible and the infrared range. Also no emission from color centers or impurities as Cr^{3+} and Ti^{3+} has been observed. We have identified three main emission bands associated to F_2^+ centers, F centers and F_2. Previous works on emission of Si NPs embedded on sapphire reported a broad band centered at 570 nm associated to F_2 center defects. This difference could be related to the energy pump range that tunes the defects observed [105] and the amorphous host that generates a lower number of high ionization defects.

7.4 Annealing process and shinning amorphous Si NPs

The PL measurements along with the CL measurements give no clue of the presence of amorphous Si NPs in the as grown thin films, they seem to be dark. Most of the procedures to obtain efficient emission from Si NPs in crystalline or amorphous state require a post-deposited thermal anneal treatment.[87, 86, 82] Our Si NPs are formed in situ but it is expected that a low temperature anneal process could reduce the non radiative channels of the Si NPs embedded in an a-Al_2O_3 host produced at room temperature.

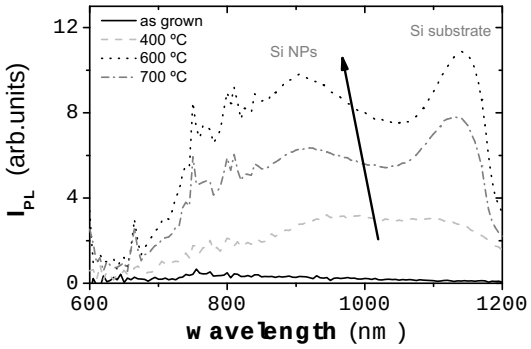

Figure 7.2: NIR emission spectra for a Si NP only doped thin film in as grown conditions (black line) and after slow thermal annealing treatments at 400 ï¿½C (light dash grey line), at 600 ï¿½C (black dotted line) and 700 ï¿½C (dark grey dash-dot line). The emission band center around 950 nm is related to the presence of the Si NPs and the emission band at 1131nm is from the silicon substrate.

A thin film only doped by Si NPs with an average Si NP diameter of 4.5 nm ($Only-Si-S$), has been annealed for 1 hour in 100 ï¿½C steps from 400 ï¿½C to 700 ï¿½C in an air conventional furnace. The Figure 7.2 shows the NIR emission spectra for the $Only-Si-S$ film after every annealing process. The as grown thin film showed no emission band in the range from 600-1200 nm (already discussed). After the first annealing at 400 ï¿½C, two strong broad emission bands are observed, one centered at 973 nm and the other at 1131 nm. The latter corresponds to the emission peak of silicon substrate from levels near the band-gap (1.12 eV, 1100 nm). The emission band centered at 973 nm is only observed from the thin films with Si NPs. Furthermore, as the temperature of the anneal process increases the emission band intensity increases. The peak position of the emission band associated with the silicon substrate remains constant while for the band associated to the Si NPs emission is shifted to shorter wavelengths from 970 nm to 910 nm at 600 ï¿½C. From the EFTEM and EELS measurements the Si NPs remain amorphous after the annealing process. Nevertheless a reduction in Si NP size was observed due to a surface oxidation of the NPs and a defect passivation. The reduction in size can lead to the observed shift to shorter wavelengths while the defect passivation can explain the increase in the PL

intensity.[95] After the 700 ï¿½C anneal process there is a decrease of the PL intensity while the peak position is shifted to longer wavelengths. This can be associated to a total oxidation of the smaller Si NPs and therefore only the larger ones with a larger Si core are able to emit light but their intensity is reduced. An Er only doped film has undergone in the same thermal treatment and does not show band emission in the wavelength range from 600 to 1000 nm, confirming the Si NPs related origin of this emission band.

Note that the emission band from the Si NPs is shifted more than usual to longer wavelengths in comparison with the absorption edge. This can be related to Si NP interaction phenomena between adjacent Si NPs [85] and it is consistent with the high Si NP density obtained in the Section **??**.

Emission from the Si NPs have been observed in the 910 nm to 970 nm range as in previous works about crystalline Si NPs embedded in SiO_2 host [83, 88, 85, 50], **but not yet reported from amorphous Si NPs embedded in a-Al_2O_3 thin films**.

In order to analyze the evolution of the oxygen vacancies defects of the a-Al_2O_3 after the thermal processes, one annealed thin film doped with Er^{3+} and Si NPs with a 4.5 nm average diameter has been measured by CL. The UV-Visible broad band observed for the as grown thin films in the Figure 7.1 remains the shape and peak positions post-annealed thin film, so the host F_2^{2+}, F_2^{+}, F_2, F^{+} defect centers are still present in the annealed films. This indicates that the oxygen vacancy defects are not the responsible for the dark state of the as grown amorphous Si NPs since the non radiative channels for the Si NPs have been eliminated by the anneal process leading to shiny Si NPs. These results suggest that the dark state of the as grown Si NPs is related to defects associated to the Si NPs as Si dangling bonds or Si NP surface defects. During the thermal anneal process a re-organization of the atoms on the Si NP surface occurs causing a reduction of the Si NP non-radiative channels. In addition, in this re-organization of surface states of the Si NPs a reduction of the Si NP size is suggested by the shift to shorter wavelengths (400 - 700 ï¿½C), however after the 700 ï¿½C anneal when the small Si NPs disappear in favor of the big ones a shift to to longer wavelengths is observed.

The number of surface defects and dangling bonds of the Si NPs are size dependent due to the fact that surface/volume ratio increases as the size of the Si NPs decreases. Thus the behavior in as grown thin films is expected to be different as a function of size. A special case of the smaller Si NPs is detailed in the Chapter 13.

We would like to emphasize that the defects on the Si NP surface embedded in a-Al_2O_3 are reduced by low temperature anneal process while high anneal temperature thermal process are usually necessary to reduce the surface defects of Si NPs embedded on SiO_2. It can be related to the interface a-Al_2O_3-Si NP where the defects are minimized in comparison with the SiO_2-Si NP interface.

7.5 Conclusions

A high number of host defects and Si NP surface defects are present in the Si NP doped as grown thin films. The host defects are related to oxygen vacancies and are still present in the thin films after the thermal processes. However, the Si NP surface defects are reduced from the 400 ï¿½C anneal to 600 ï¿½C and the emission from the Si NPs appears and increases. After the 700ï¿½C annealing process the emission band intensity decreases and is shifted to longer wavelengths probably due to the total oxidation of small Si NPs.

Note that although the as grown amorphous Si NPs do not show PL emission, however it will be shown in the next Chapters that they are exceptional sensitizers to the Er^{3+} ions and efficient absorbers to exchange energy with the close Er^{3+} ions.

Part III

Control of location of Er^{3+} and Si NPs below the nanoscale: maximizing Er^{3+}- Si NPs contact

Chapter 8

Establishing the game rules for the Si NPs - Er^{3+} interaction

Our first experimental approach was to check and determine how the separation between the Er^{3+} ions and the Si NPs in the nanoscale affects to the Er^{3+} PL emission in a not usual host, as the a-Al_2O_3. Films with 2D-distributions of Er^{3+} and Si NPs have been designed and prepared as it has been explained in the Chapter 3. The distance between the Er^{3+} and Si NPs has been varied from 0 to 11 nm by a a-Al_2O_3 intermediate layer. It is shown that only the Er^{3+} close to the Si NPs emits and therefore the PL emission is maximized when the Er^{3+} ions and the Si NPs are in the same layer.

8.1 Introduction

The interaction between the Si NPs and the Er^{3+} ions occurs on the nanometer scale and therefore is sensitive to the dopant distribution, [37, 38, 39, 106] and also can be affected by the presence of atomic defects.[40] Previous works on silica-based systems, Si has to diffuse upon thermal treatment in order that the Si NPs precipitate from the initial mixed amorphous Si-SiO_2 structure and thus there is little control over the Si NP distribution.[37, 38, 39, 40] It is therefore desirable to develop preparation techniques that allow the formation of the Si NPs in situ during film growth that reduce the number of defects [40] and maintain the crystalline or amorphous degree between thin films with Si NPs sizes within, as the alternated pulsed laser deposition.

The film structures have been defined in the Chapter 3 as the test films. They have been structured in the growth direction in order to maintain the Er^{3+} ions and the Si NPs in well-defined 2D-distribution layers with a controlled separation at the nanoscale by an intermediate a-Al_2O_3 layer.

8.2 Thin films absorption

The Figure 8.1 shows the absorption spectra measured for the reference films ($Only-Si-S$ and $Only-Er-S$) deposited on fused silica, and doped only with either Er or Si NPs. The oscillations are due to the light interference between the film surface and the film-substrate interface. The reference film doped only with Er shows a negligible absorption in the whole photon energy range. The spectrum for the reference film doped only with Si NPs shows also a negligible absorption in the infrared region and a clear absorption band in the visible region above 2 eV, due to the presence of Si NPs. The absorption spectra for all the films co-doped with Er and Si NPs are similar to that of the reference film doped only with Si NPs, further confirming that all films have the same Si content and linear optical properties.

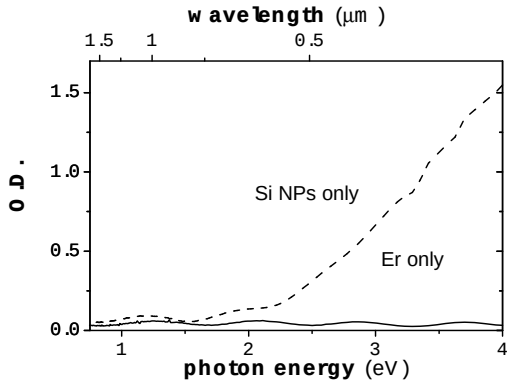

Figure 8.1: Absorption spectra of the a-Al_2O_3 film doped only with Er and the a-Al_2O_3 film doped only with Si NPs as a function of the photon energy (bottom) and wavelength (top)

The band-gap energy associated with the Si NPs has been estimated by assuming a dependence for an indirect band-gap semiconductor and fitting the absorption spectrum to the expression $(\alpha h\nu)^{1/2} - E_G$, where α, $h\nu$, and E_G are the absorption coefficient, the incident radiation energy, and the optical band-gap energy, respectively (detailed in the Chapter 5.3.1). The value obtained for E_G is 1.2 eV.[1] Reports on experimental measurements and calculations of E_G as a function of the size of Si NPs embedded in SiO_2 show that the value obtained corresponds to Si NPs with an average diameter in the range of 4-5 nm.[41, 42, 43, 44, 45] This result is in very good agreement with the results obtained from the EFTEM analysis (see Chapter 4), and therefore for analysis purposes from now on it will be considered that the average diameter of the Si NPs in the films is 4.5 ± 0.5 nm.

8.3 Er excitation and emission

The PL spectra excited at 476.5 nm are shown in Figure 8.2. The reference film doped only with Er shows no Er^{3+} related emission around 1540 nm, in agreement with the fact that at 476.5 nm there is no resonant Er^{3+} energy level for absorption. An Er^{3+}related signal is also not seen for the films co-doped with Si NPs and Er^{3+}, and with s=7 and 11 nm. In fact, the spectra for these two films are similar to those of the reference film doped only with Si NPs. The spectra show a flat weak band extending from 1400 to 1650 nm, which is related to the presence of Si NPs. The origin of light emission from a-Al_2O_3 containing Si NPs is very controversial,[96, 93, 107] and further analysis was detailed in the Chapter 7. In contrast, the film with s=0 nm shows a clear strong Er^{3+} emission with the maximum at 1540 nm. The film with s=4 nm also shows a small Er^{3+}related signal. This result is an evidence for energy transfer from the amorphous Si NPs to the Er ions for the films with s=0 and 4 nm. Under excitation at 514.5 nm and 488.0 nm, resonant excitation on the Er^{3+} ions, all the Er-doped films show the characteristic Er^{3+} emission.

The Figure 8.3 shows the emission at the 1.54 μm peak as a function of the pump wavelength at a fixed pump power (Photoluminescence excitation curves - PLE curves). The peak intensity has been measured as the difference between the emission intensity at 1.54 μm and the emission intensity at 1.40 μm to eliminate the contribution of the weak flat band that is related to the presence of Si NPs. The film where the Er^{3+} ions are in the same layer than the Si NPs (s=0 nm) shows a decreased linear tendency of the PL intensity at 1.54 μm independently of resonant and non resonant pump conditions for the Er^{3+} ions. Only at 488.0 nm the indirect excitation contribution is noticeable. As the thickness of the intermediate layer is increased (s= 4, 7, 11 nm) the emission intensity decreased up to one order of magnitude for the s= 4 nm thin film and and it is no observed no Er^{3+} resonant emission for s higher than 7 nm. The optical behavior is exactly the same for the s= 11 nm and s= 7 nm and similar to the Er only doped film showing the

[1] chequear valores

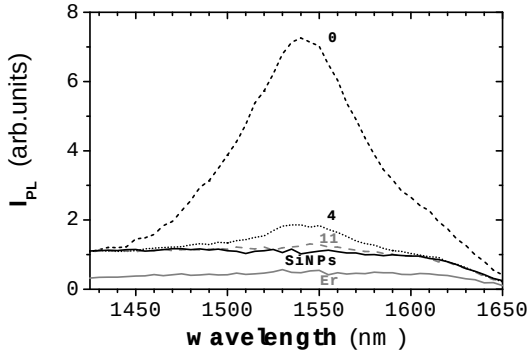

Figure 8.2: PL spectra for the Er^{3+} and Si NP co-doped a-Al_2O_3 films with different values of s, and for the the films doped only with Er^{3+} or with Si NPs. The value of s is indicated on the corresponding spectrum. The pump power used was 500 mW under non resonant excitation conditions

only resonant energy injection to Er^{3+} ions. The contribution of the indirect excitation film through Si NPs for the s=4 nm is only a 16 % while in the s=0 nm film the indirect contribution at 488.0 nm is a 92 % (the analysis of the PLE curves is detailed in the Appendix B). The higher indirect contribution in the s= 4nm film and the differences on the PL peak intensity values with the s=0 nm shows the extreme dependence of the Si NPs-Er^{3+} interaction on the dopant distances and then in the Er^{3+} excitation mechanism.

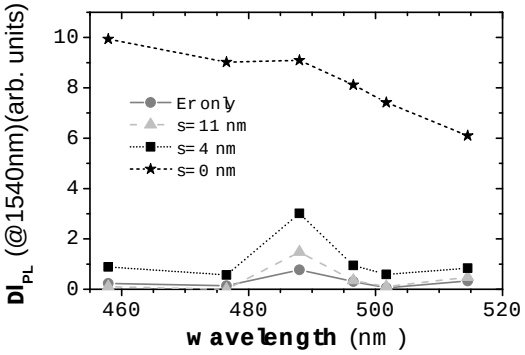

Figure 8.3: Photoluminescence excitation spectra at 1.54 μm for the thin films with differences thickness of the a-Al_2O_3 intermediate layers. A pump power of 200 mW has been used in all the wavelengths.

The differences between the thin films with different s values in the efficiency of the energy transfer process is maintained under different pump power regimes. The Figure 8.4 shows the intensity peak emission at 1.54 μm dependence on the pump power in non Er^{3+} resonant pump conditions (476.5 nm). The only Er^{3+} doped film shows a linear behavior with an increase with the pump power at resonant pump wavelengths (not shown). However the film with s= 0 nm shows a saturation behavior with the pump power at all the wavelengths due to the sensitization of Er^{3+} ions by the Si NPs that causes a excited

Er^{3+} fraction higher than in the Er^{3+} only film at lower pump powers. The saturation is due to the fact that the excited Er^{3+} ions reach maximum available through Si NPs. In this film the behavior is the same for all wavelengths. The s= 4 nm film shows a linear tendency where the PL peak intensity increases with the pump power, similar to the Er^{3+} only doped film. In this film the saturation behavior is not reached in this pump range due to the low percentage (16%) of the indirect contribution that is strong limited by the distance between dopants.

In order to analyze the results, Figure 8.5 shows the PL intensity of the films at 1.54 μm as a function of s, for excitation at 476.4 and 488.0 nm. It can be observed that for both excitation wavelengths the PL intensity decreases sharply as s increases. For reference, the PL intensity for the reference film doped only with Er at an excitation wavelength of 488.0 nm is also shown on the y-axis. The PL intensity value for the film doped only with Er is very weak, in agreement with our previous reports for Er:a-Al_2O_3 films which show that in the as-grown condition the films exhibit a negligible emission, and that it is necessary to anneal the films at temperatures higher than 750 °C for 1 h to achieve a significant signal.[26, 17] For excitation at 488.0 nm the film with s=0 shows an emission intensity that is one order of magnitude larger than that of the film doped only with Er. The emission under excitation at 488.0 nm is slightly higher than that under excitation at 476.5 nm. This can be due to the additional emission of directly pumped Er^{3+} ions, i.e., those that cannot be excited through Si NPs (around a 8%). Indeed, due to the controlled multilayer doping of the films it can be shown that not all Er^{3+} layers can be effectively excited by the Si NPs. For the film with s=7 nm no Er^{3+} PL-related emission is observed under pumping at 476.5 nm, which suggests that for the film with s=0 nm only the Er^{3+} layers in close contact contribute to the sensitized emission, since the next nearest Er^{3+} layers in the Er:a-Al_2O_3 doped region have been deposited at a distance of 7 nm from the Si NP layer due to the film design. This means that **only 18 layers out of the**

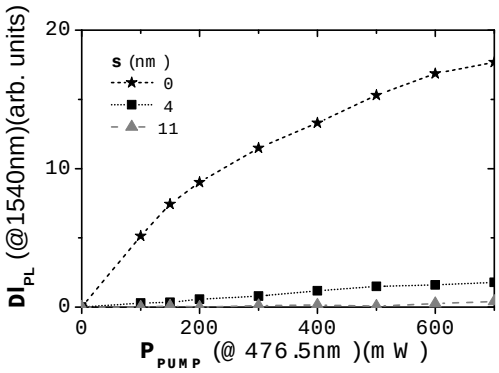

Figure 8.4: Intensity peak emission at 1.54 μm as a function of pump power at 476.5 nm (no resonant wit the Er^{3+} ions) for the thin films with s= 0, 4, 11 nm.

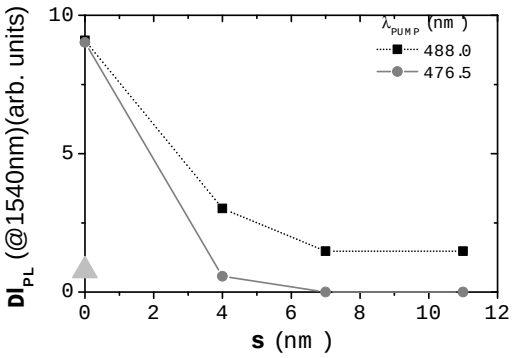

Figure 8.5: PL intensity as a function of s, excited at 476.5 nm (full grey circles) and 488.0 nm (full black squares). The PL intensity for the film doped only with Er excited at 488.0 nm is represented on the y-axis with a light grey full triangle.

total of 50 Er^{3+} have the potential to be sensitized, i.e., only 36% of the total Er in the film contributes to the sensitized signal. The results presented have interesting technological implications since they demonstrate that amorphous Si NPs formed in situ during the growth process are able to efficiently transfer energy to Er^{3+} ions. This shows that there is no need for thermal treatment to activate the energy transfer, and opens the possibility of fabricating devices co-doped with Er-Si NPs at low temperature. Note that although it has recently been confirmed that amorphous Si NPs can sensitize Er^{3+} ions to enhance both the Er^{3+} PL and electroluminescence,[43] annealing at temperatures in the range of 800-900 °C have been always required. Furthermore, in spite of the presence of defects in the as-grown a-Al_2O_3 films, there is evidence of significant energy transfer, indicating that although defects might modify the efficiency of the energy transfer process, as has been suggested in the case of Si-rich silica films,[40] they do not preclude it.

The results show that the controlled nanostructure of the films allows the energy transfer from the Si NPs to the Er^{3+} ions to be effectively tuned. It is also possible to estimate the critical distance for energy transfer from the surface of a Si NP to Er^{3+} in a-Al_2O_3. For this purpose it is important to analyze in detail the structure of the film with s=4 nm. In this film there is still clear evidence of excitation through the Si NPs. The two Er^{3+} layers nearest to each Si NP layer have to be considered separately because the effective Si NPEr^{3+} separation is different in each case. For the Er^{3+} layer deposited before the Si NPs it is a good approximation to assume that the Er^{3+}Si NP separation is the thickness of the deposited a-Al_2O_3 layer, i.e., 4 nm. This separation will be the minimum separation between an Er^{3+} ion and the lower surface of the subsequently deposited Si NP. In order to estimate the Si NP - Er^{3+} separation for the Er^{3+} layer deposited after the Si NPs, the thickness of the deposited a-Al_2O_3 layer must be considered, and also the volume of the Si NPs that is embedded within the a-Al_2O_3. It can be assumed that the total thickness of

the a-Al_2O_3 with embedded Si NPs is the sum of the effective thickness of the Si NPs 1.4 nm plus the effective deposited 4 nm thick a-Al_2O_3 layer, which yields a total thickness of 5.4 nm. Since the Si NPs have an average diameter of 4.5 ± 0.5 nm, then the Si NPs are totally covered before the next Er^{3+} layer is deposited. In this case the minimum separation of an Er^{3+} ion to the upper surface of a Si NP underneath will be of 1 nm. For Er^{3+} in silica-based systems characteristic energy transfer distances from 0.5 to 2-3 nm have been reported,[38, 37, 39] and therefore for the film with s =4 nm it is suggested that there is negligible energy transfer from the Si NPs to the Er^{3+} layers deposited before the Si NPs, which are at a separation of 4 nm, and that the effective energy transfer is mainly due to the Er^{3+} layer deposited after each Si NP layer. From these results it can thus be estimated that there is effective energy transfer from Si NPs to Er^{3+} ions in a-Al_2O_3 for a distance of 1 nm.

8.4 Conclusions

Efficient energy transfer from Si NPs to Er^{3+} ions in a non silica-based material a-Al_2O_3 has been demonstrated. The amorphous Si NPs are readily able to transfer energy efficiently to the Er^{3+} ions. Efficient energy transfer between Si NPs and Er^{3+} ions without the need for post-deposition annealing is demonstrated. The spatial distribution of the Er^{3+} and Si NPs has been controlled at the nanoscale, and it has been shown that the energy transfer depends critically on the Si NP - Er^{3+} separation and that it is optimized when the Er^{3+} ions and the Si NPs are in the same layer. The control of the spatial distribution of the Er^{3+} ions around the Si NPs at the nanoscale that has been achieved allows the amount of Er^{3+} sensitized by Si NPs to be effectively tuned. The present results suggest that a higher percentage of Er^{3+} ions can be sensitized by Si NPs if structures are prepared with one Er^{3+} layer per Si NPs layer.

Chapter 9

Maximizing Er^{3+}- Si NPs contact. Role of the Er^{3+} and Si NP location below the nanoscale on the Si NP-Er^{3+} interaction efficiency.

The previous Chapter **??** shows that only the Er^{3+} ions localized in the same layer than the Si NPs are efficiently excited through the Si NPs. Nevertheless for the optimized film structure (s=0 nm) two Er^{3+} ions doping layer were deposited close to the Si NPs: one deposited before the Si NPs formation and the other deposited after the Si NPs formation. In this Chapter new thin films have been designed depositing only one Er^{3+} ions doping layer per Si NP layer. In order to control the local position of the Er^{3+} ions respect to the Si NPs below the nanoscale the Er^{3+} ions were deposited following the next deposition sequences: one pulse of Er^{3+} deposited before Si NPs formation ($SE\phi 2.6$), one pulse of Er^{3+} deposited after Si NPs formation ($ES\phi 2.6$) and finally, one pulse of Er^{3+} deposited in the middle of Si NPs formation ($SES\phi 2.6$). The PL Er^{3+} emission properties are discussed as a function of the dopants location and related to the Er^{3+} and Si NPs interaction mechanism.

9.1 Introduction

Fifteen years ago, mixing Si NPs and Er^{3+} in oxide hosts was presented as an alternative to enhance the Er^{3+} emission at 1.53 μm towards the development of infrared integrated amplifiers pumped at low powers in the visible.[18] Works on complex deposition methods using different atmospheres, different host components, optimizing post-deposited annealing procedures to optimize Si NP sizes and the number of possible Er^{3+} non radiative channels have been performed. However, a few percent of Er^{3+} are achievable through Si NP excitation[22] due to the short range Si NP-Er^{3+} interaction. Therefore controlling both dopants concentration and their location in the nanoscale to place the Er^{3+} ions close to the NP surface seems to be the unique route to design and produce useful active structures.[25, 22]. Therefore we have performed a deposition procedure where the position of the dopants is restricted to a plane, working with localized 2D random dopant distributions instead 3D random dopant distributions and for which the maximization of the Er^{3+}Si NPs contact is obtained by the in situ deposition of dopants by alternated Pulsed Laser Deposition (PLD).

In the Chapter **??** efficient energy transfer from amorphous Si NPs to Er^{3+} ions has been observed in as deposited thin films. The energy transfer depends critically on the Si NP- Er^{3+} separation and it is optimized when the Er^{3+}ions are in the same layer than the Si NPs. Taking into account that in this test thin films only 18 Er^{3+} layer of a total of 50 are emitting, the contact between Er^{3+} ions and Si NPs has to be maximized in order to optimize the energy exchange from Si NPs to Er^{3+}. Moreover, the thin film $S4$ whose minimum effective Er^{3+}-Si NP separation was 1 nm shows a decrease up to one order of magnitude in comparison with the thin film where the Er^{3+} ions are in the same layer that the Si NPs. Therefore new thin films were been prepared depositing only one Er^{3+} pulse per Si NP layer locating both layers next to each other.

However, it is possible to analyze the highly sensitivity of the Si NP- Er^{3+} interaction phenomena below the nanoscale using the special features of the in situ independent deposition of dopants. Therefore, a single Si NP size was selected (ϕ=2.6 nm) and the order of deposition of dopants (Er^{3+}, Si NPs) was changed between thin films as it has been described in the Section 9 of the Chapter 3 following the deposition sequences:

1. $SE\phi$2.6: Er^{3+} deposited before the Si NPs formation. Er^{3+} under the Si NPs.
2. $ES\phi$2.6: Er^{3+} deposited after the Si NPs formation. Er^{3+} on top of the Si NPs.
3. $SES\phi$2.6: Er^{3+} deposited when the Si NPs are not completely formed in the middle of the Si NPs formation process. Er^{3+} partially under and on top of the Si NPs.

Comparing the schemes of the dopants in a single layer of Er^{3+} doped Si NPs between thin films for the different deposition configuration ($SE\phi$2.6, $SES\phi$2.6 and $ES\phi$2.6), and

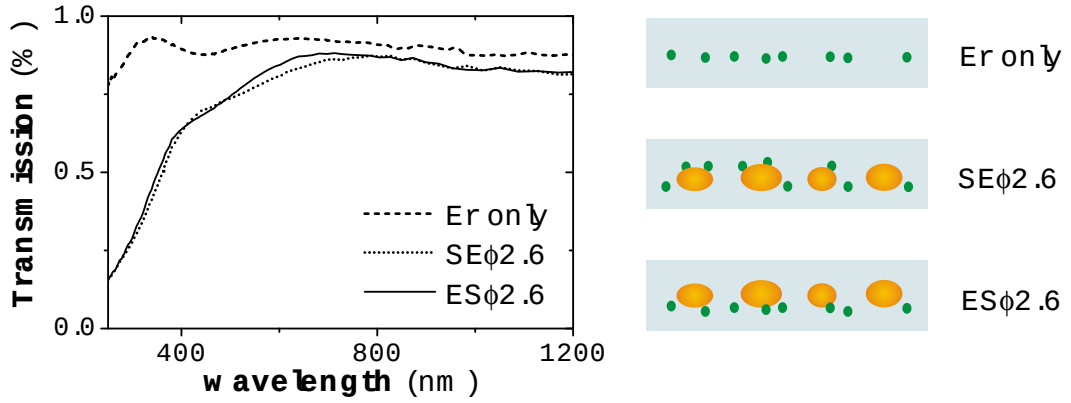

Figure 9.1: Transmission measurements for the a-Al_2O_3 doped by Er^{3+} and Si NPs films depositing the Er^{3+} before the Si NPs ($ES\phi$2.6, black solid line) and the Er^{3+} deposited after the Si NPs ($SE\phi$2.6, black dot line). The a-Al_2O_3 film doped only with Er^{3+} (black dash line) is shown as reference. The dopant spatial configurations are schematically detailed at the right diagrams.

taking into account that the average distance between edges of Si NPs in the plane has been established around 0.5 nm for a Si NP average size around 2.6 nm (Chapter 6), the differences on the Er^{3+} response are going to be only related to differences on the relative Er^{3+}-Si NP separation below the nanoscale. Moreover, this analysis allows us to show the accuracy of the PLD to control dopants location and increase the probabilities to achieve a higher amount of excited Er^{3+} than using other deposition techniques.

9.2 Maintaining 2D-dopant distributions

One pulse on Er^{3+} target was selected to obtain an areal density of 8.3 10^{13} atm/cm^2. In order to induce the Si NPs formation with a controlled average size, 185 pulses have been used to ablate the silicon target for every Si NP layer. The Er and silicon content per layer is maintained between thin films.

Figure 9.1 shows the absorption spectra measured for the two of the Er^{3+} and Si NP co-doped films ($SE\phi$2.6, $ES\phi$2.6) deposited on fused silica substrates and the only Er^{3+} doped a-Al_2O_3 film ($Only-Er-4$). The only Er^{3+} doped film shows the usual negligible absorption from the visible to the infrared in the measurement range. However, all the Er^{3+} and Si NP doped films show the same absorption band in the visible region due to the presence of the Si NPs of the same average size between thin films. It has been obtained a band gap energy of 1.6 eV which corresponds to an average size of 2.6 nm. We would like to emphasize the reproducibility of the 2D-Si NP distributions so the absorption edge obtained is the same for different thin films.

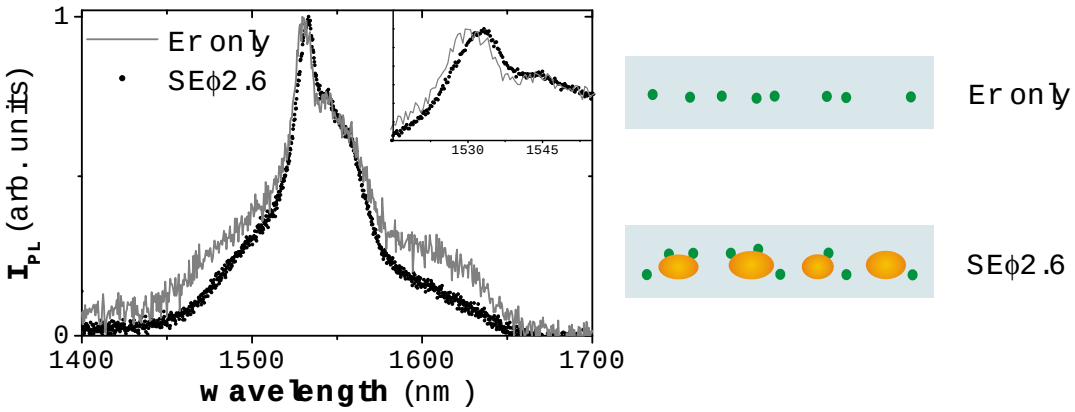

Figure 9.2: Normalized photoluminescence spectra to the maximum of intensity peak for only Er^{3+} doped film and the thin films where the Er^{3+} ions were deposited after the Si NPs formation. Inset: Zoom in to the emission peak region from 1515 nm to 1555 nm. The dopant spatial configurations are schematically detailed at the right diagrams.

9.3 PL and PLE

All the co-doped films show the typical Er^{3+} PL emission spectrum in the infrared centered at 1533 nm. The Figure 9.2 shows the normalized spectra to the maximum of intensity peak for the only Er^{3+} doped film an one of the Er^{3+} and Si NPs co-doped film ($SE\phi 2.6$) pumped at resonant wavelength. The emission spectrum for the only Er^{3+} doped a-Al_2O_3 film is centered at 1530 nm whereas the emission spectra for the co-doped films is narrower and shifted to longer wavelenghts. The Er^{3+} and Si NP doped films show enhancement of the absolute PL intensity from 16 to 36 in comparison with the only Er^{3+} a-Al_2O_3 doped film pumped at resonant wavelength. The photoluminescence excitation spectrum (PLE) was measured for all the thin films (see Figure 9.3). The only Er^{3+} doped a-Al_2O_3 thin film only shows significant emission at the resonant wavelengths with the Er^{3+} energy levels (488.0 and 514.5 nm). The excitation spectra for the Er^{3+} and Si NPs doped films show a decrease as a function of the pump wavelength. Therefore it is concluded that the Er^{3+} ions are mainly excited through the Si NPs. Indeed the slope of the excitation spectrum is similar for all co-doped thin films and only a intensity displacement is observed suggesting that the Si NP size determines the optical absorption and the dependence on the wavelength pump.

9.4 Fraction of excited Er^{3+}

The Figure 9.4 shows the evolution of the intensity peak at 1533 nm as a function of the pump power at resonant wavelength (488.0 nm). Similar curves are obtained at non

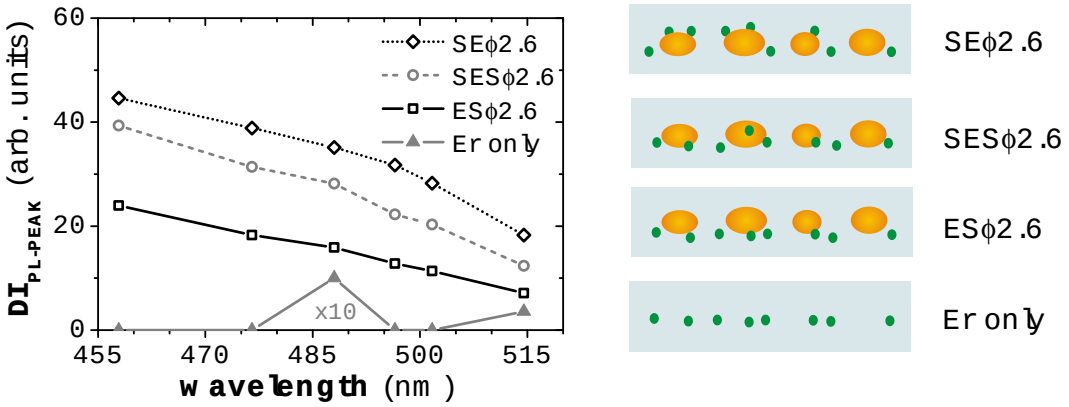

Figure 9.3: Photoluminescence excitation spectra for the a-Al_2O_3 film doped only with Er^{3+} (grey triangles-grey solid line) and the a-Al_2O_3 doped by Er^{3+} and Si NPs films depositing the Er^{3+} before the Si NPs ($ES\phi$2.6, empty black squares-black solid line), the Er^{3+} in the middle of the Si NPs formation ($SES\phi$2.6, empty grey circle-grey dash line) and the Er^{3+} deposited after the Si NPs ($SE\phi$2.6, empty black diamond-black dot line). A pump power of 200 mW has been used in all the wavelengths. The dopant spatial configurations are schematically detailed at the right diagrams.

resonant conditions. In the studied pump power range the PL intensity peak increases linearly with the pump power for the only Er^{3+} doped film. However the Er^{3+} and Si NP doped a-Al_2O_3 films seems to evolve towards a maximum intensity with different saturation values.

Assuming that for this 2D-Si NP distributions the in plane distance between Si NPs edges is 0.5 nm and taking into account that the interaction distance should be around 0.5-1nm for a resonance energy transfer (RET-Föster) interaction mechanism [37, 29] thus, the 100% of Er^{3+} ions can be excited through Si NPs. However the different saturation levels indicates a different maximum number or Er^{3+} ions that can be excited through the Si NPs for the Er^{3+} and Si NP doped a-Al_2O_3 films obtained with different dopant deposition sequences. Consequently, the number of excitable Er^{3+} ions through Si NPs is strongly limited by the dopants location below the nanoscale, showing an extreme sensitivity of the Si NP-Er^{3+} interaction to the spatial correlation between both dopants distributions.

When the system is in equilibrium the PL intensity (I_{PL}) that correspond to the transition from $^4I_{13/2}$ level to the fundamental state could be approximated by the expression B.1,

$$I_{PL} \sim f_{Exc-Er}\ N_{Er}\ \sigma_a\ \frac{\tau}{\tau_{rad}} \tag{9.1}$$

where N_{Er} is the total concentration of Er^{3+}, f_{Exc-Er} is the fraction of excited Er^{3+}, σ_a is the absorption cross section, τ is the measured lifetime and τ_{rad} is the lifetime in the absence of radiation less transitions. The areal concentration of Er^{3+} ions, the radiative

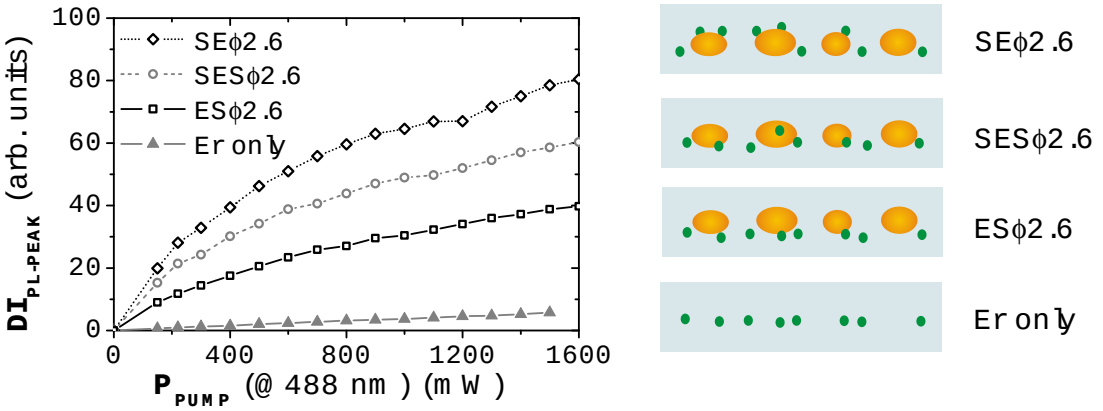

Figure 9.4: Intensity peak emission at 1.54 μm as a function of pump power at 488.0 nm the a-Al_2O_3 film doped only with Er^{3+} (grey triangles-grey solid line) and the a-Al_2O_3 doped by Er^{3+} and Si NPs films depositing the Er^{3+} before the Si NPs ($ES\phi$2.6), the Er^{3+} in the middle of the Si NPs formation ($SES\phi$2.6) and the Er^{3+} deposited after the Si NPs ($SE\phi$2.6). The dopant spatial configurations are schematically detailed at the right diagrams.

lifetime and the absorption cross section associated to the presence of Si NPs are the same for the co-doped thin films due to the same host, same Er^{3+} and Si content and the same absorption values between films. Therefore the decrease in the fraction of excited Er^{3+} respect to the film with the maximum emission can be estimated by the expression 9.2.

$$\Delta f = 1 - \frac{f_{Er-ES\phi 2.6}}{f_{Er-SE\phi 2.6}} = 1 - \frac{I_{PL-ES\phi 2.6}\ \tau_{SE\phi 2.6}}{I_{PL-SE\phi 2.6}\ \tau_{ES\phi 2.6}} = \{1 - \frac{I_{PL-ES\phi 2.6}}{I_{PL-SE\phi 2.6}}\}_{\tau_{SE\phi 2.6}=\tau_{ES\phi 2.6}} \quad (9.2)$$

The inset of the Figure 9.5 shows the decay curves of the three Er^{3+} and Si NP co-doped a-Al_2O_3 thin films obtained pumping at non resonant wavelength (476.5 nm). All the thin films shows the same response independently of the different dopants spatial configuration. Therefore the decrease in the fraction of excited Er^{3+} is only related with the ratio of the PL peak intensity. A 20% of the fraction of excited Er^{3+} is decreased from the $SE\phi$2.6 to $SES\phi$2.6. Up to a percentage of **53% of the fraction of excited Er^{3+} is decreased only by changing the deposition sequence of dopants** (from Er^{3+} deposited before Si NPs to Er^{3+} deposited after Si NPs, see Figure 9.5) proving the extreme sensitivity of the Si NP-Er^{3+} interaction to the spatial correlation between both dopant distribution and suggesting that the efficient interaction mechanism is more sensitive to the distance between dopants than the assumed Föster resonance energy transfer process.

9.5 Maximized Er^{3+} and Si NPs contact

We are going to analyze in detail the differences on the emission spectra shape in order to determine the relevance of the control of dopants location below the nanoscale and the significance of the accuracy in the Er^{3+} location to achieve a maximization of contact

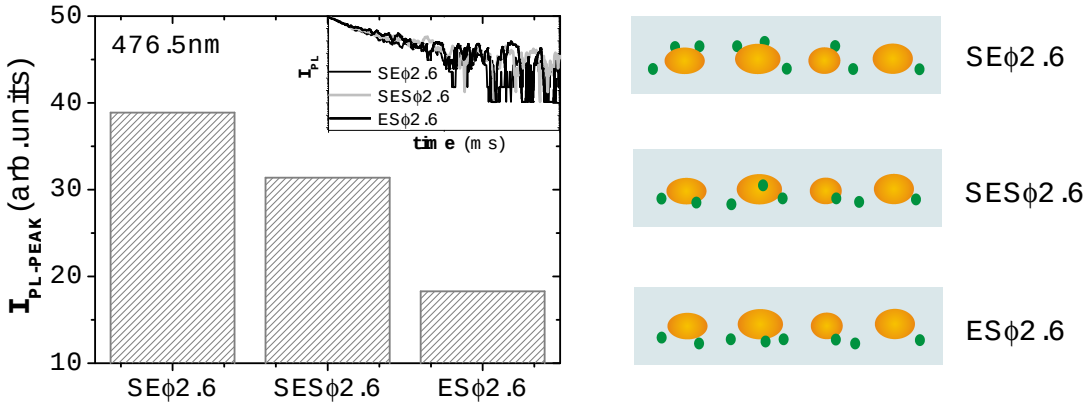

Figure 9.5: PL intensity peak at 1533nm for the three Er^{3+} and Si NP doped a-Al_2O_3 films obtained in non resonant pump condition ($\lambda_{PUMP} = 476.5nm$) at 200 mW. The inset shows the decay curves for the three Er^{3+} and Si NP doped a-Al_2O_3 films at the same pump conditions. The dopant spatial configurations are schematically detailed at the right diagrams.

between the Si NPs and Er^{3+} ions. The shape of the Er luminescence spectrum reflects the local environment around the ion[108], hence differences in the Er^{3+} emission shape could be related to different chemical composition associated to the host (a-Al_2O_3) or to the Si NPs (silicon). The Figure 9.2 shows the normalized spectra to the maximum of intensity peak for an Er^{3+} and Si NPs co-doped film ($SE\phi 2.6$) and the reference Er^{3+} only doped film. All the co-doped films show the same spectral behavior independently the dopants deposition sequence. Nevertheless the spectra for Er only doped film is broader than for the co-doped films ones, thus the Full With at Half Maximum (FWHM) is 50 nm for the Er^{3+} doped a-Al_2O_3 film in contrast with the 44 nm for the Si NP and Er^{3+} doped films. Moreover the peak intensity position in the co-doped films spectra is shifted a few nanometers to longer wavelength values than the peak position of the only Er doped film (from 1530 nm at Er^{3+} doped a-Al_2O_3 to 1533 nm in the Er^{3+} and Si NP doped a-Al_2O_3 films). The bandwidth reduction and the shift to longer wavelengths for all the co-doped films suggests that almost recollected emission comes from Er^{3+} localized in a $Si-O_2$ rich chemical environment rather than in an $Al-O_2$ environment,[14] which is consistent with the Er located at the surface of the Si NPs.

The maximized contact is confirmed by the PL temporal response. Prior works shows the lifetime dependence on the Er^{3+} and Si NP separation observing modification of the Er^{3+} radiative lifetime from the proximity to silicon nanoclusters by Purcell effect.[109] For Si nanoclusters with a diameter around 2.6 nm, variations higher than a 50% are estimated and observed for variations in the Er^{3+} and Si NPs separations below the nanoscale. However in our case all the Er^{3+} and Si NP doped a-Al_2O_3 films show the same temporal behavior (see inset Figure 9.5). Thus the Er^{3+} ions emit efficiently and seem to be located in the at the same distance of the Si NPs. Analyzing the differences in

the dopants distributions obtained by the changes in the order of the deposition of dopants imply that only the Er^{3+} in contact is efficiently excited, in agreement with the spectra shape behavior.

The a-Al_2O_3 host allow us to determine that only the Er^{3+} ions in contact with the Si NPs are emitting. Izeddin et al. [25] described the main three mechanisms of energy exchange between Si NPs and Er^{3+} ions (exciton interband recombination, relaxation of hot carriers through intraband transitions and dipole-dipole interaction) estimating their probability of excitation of Er^{3+}. The most efficient process is through recombination of confined electron and hole (interband transitions) but it is determined by the electron and hole wave-function at the position of the Er^{3+} ion, therefore this interaction has a contact character and only the Er^{3+} situated inside or at the surface of the Si NP have a relevant role. The observed PL response suggests a extreme coupling between the Er^{3+} and Si NPs due to the high accuracy in the nano-scale of the Er^{3+} location by alternated PLD deposition that allow us to locate the Er^{3+} on the surface of the Si NPs for the $SE\phi 2.6$ film and thus to maximize the contact between the two 2D-dopant distributions magnifying the transfer efficiency due through the maximization of the interband excitation mechanism.

On the other hand, we would like to emphasize that the fact that there are no differences in decay curves suggest that the PL temporal response is imposed by the quantum optical properties of the Si NPs that it is the same between thin films. Therefore, in our maximized-contact thin films, the main exchange mechanisms and main rules on the excitation and des-excitation of Er^{3+} ions are related to inter-band exciton recombination and intra-band electron relaxation and excitation, eliminating the complexity of the resonance energy transfer (RET) and the Föster interaction distances, and opening a new route to understand thoroughly the interaction mechanism between quantum dots and dipole emitters.

9.6 Conclusions

The alternated PLD allow us to control the Er^{3+} ions and Si NPs location below the nanoscale. Maximized contact is obtained in the thin films where the Er^{3+} ions are deposited following the Si NPs formation, therefore most of the Er^{3+} ions are on the Si NPs. The a-Al_2O_3 host reveals the $Si-O_2$ rich chemical environment of the Er^{3+}, thus the emitting Er^{3+} ions are located in the surface of the Si NPs. The amount of achievable excited Er^{3+} depends strongly of the dopants location below the nanoscale. However the PLE curves and the temporal response depends fundamentally on the quantum properties of the Si NPs and not on the separation between the two dopants. All the PL properties reveals that in thin films with maximized-contact (extreme-coupling) the main exchange

mechanism are related to inter-band and inter-band transitions and seems that the Föster interaction mechanism does not contribute significantly establishing a new extreme Er^{3+}-Si NPs coupling regime.

Chapter 10

Er^{3+} as a probe of the film growth mechanism involved in the Pulsed Laser Deposition. PLD accuracy

Thin films with maximized Er^{3+} and Si NPs contact have been obtained depositing in situ the Er^{3+} ions following the Si NPs formation as it has been described in the Chapter 9. However, a thoroughly study of the mechanism involved in the pulsed laser deposition (PLD) process is required due to the sensitivity of the Er^{3+} and Si NPs interaction mechanism below the nanoscale. In this Chapter we are going to analyze the accuracy of the PLD process to control Er^{3+} and Si NPs location and the mechanism involved in the Er^{3+} and Si NPs interaction processes.

10.1 Introduction

The deposition process to obtain a maximized contact thin films has been described in the Chapter 9 where the Er^{3+} ions are deposited following the Si NPs formation. Nevertheless for the thin film with the Er^{3+} deposited before the Si NPs the fraction of excited Er^{3+} decreased a 53% in comparison with the Er^{3+} deposited after the Si NPs formation. Thus, only changing the order of the Er^{3+} deposition after or before the Si NPs formation, a large decrease on the fraction of the excited Er^{3+} occurs. Consequently a discussion about what are the differences in the dopant location is still open. The Er^{3+} emission spectra for the Er^{3+} and Si NP doped films suggest that only the Er^{3+} in the a-Al_2O_3-Si NP interface is emitting. However, are really the Er^{3+} ions located on the Si NP surface or could they be inside of the Si NP?, Is the energy transfer process possible for Er^{3+} ions close the Si NPs but located in the a-Al_2O_3?

During the PLD process, a plasma plume is formed from the vaporized material generated by the ablation of the target. This plasma plume is constituted by a mixture of energetic species (atoms, electrons and ions). The thin film grows through the collection of a fraction of material by a substrate placed in the path of the expanding plasma. The plasma is characterized by the presence of species with a high kinetic energy species (10-200 eV) in comparison with other ion beam techniques as sputtering (5-10 eV) or thermal evaporation ($\sim$ 0.1 eV). [110, 111] These high energetic species can influence the growth process, in fact, their impact on the film surface can cause bond breaking, displacement or removal surface atoms. Phenomena as shallow implantation, interfacial mixing or re-sputtering have been reported:

- **Implantation** during the PLD depends directly on the mass of the atoms or ions involved, therefore it affects mainly the Er atoms. In our system for laser energy densities of a few $mJ\ cm^{-2}$ the velocities of the ablated species are typically around $1.4\ 10^4\ m\ s^{-1}$. [112] Taking into account the mass of Er the estimated kinetic energy of the species arriving at the substrate can be as large as 175 eV. An implantation depth of 1 nm have been obtained by TRIM simulations for laser densities around 3 $J\ cm^{-2}$ and below 0.5 nm for laser densities around 2 $J\ cm^{-2}$.[26]

- **Mixing** is a phenomenon that can occur when the mass of the previously deposited material is similar to the achieving species. Therefore it is expected to be relevant for the a-Al_2O_3-Si NPs interfaces.

- **Re-sputtering** affects to atoms with low adhesion energy to the substrate and it is significant to the material deposited before. In our case, the silicon atoms that arrive over the a-Al_2O_3 layer shows a hight affinity to bond to oxygen atoms, as shown by the high density of Si NPs obtained. Therefore, low re-sputtering is expected.

Our experimental approach is based on the study of the PL response of the thin films prepared changing the dopant deposition order described in the Chapter 3 and Chapter 9, and the comparison of these results with the properties of the new thin films produced with a thick intermediate a-Al_2O_3 layer between dopants with an associate thickness t of 0.5 and 1 nm and for two different Si NP sizes (see Chapter 3 Section). The two different average Si NP sizes studied are 2.2 nm and 2.8 nm and, they have been selected in order to study the a-Al_2O_3 Si NP coverage process and how the Si NP size can be affect to the Si NP and Er^{3+} transfer process at different Er^{3+} and Si NP separation. Also, an Er^{3+} only doped a-Al_2O_3 film was produced at the same deposition conditions and with the same Er^{3+} dopant content and distribution.

We are going to use the Er^{3+} as a probe to analyze how implantation and mixing phenomena fundamentally affects to the optimization of the Er^{3+} PL at 1.53 μm. Also the possibility of Er^{3+} excitation through Si NPs for Er^{3+} located at the a-Al_2O_3 will be shown and how it is possible to reduce the back-transfer phenomena from Er^{3+} to Si NPs but at expense of a reduction in the fraction of excited Er^{3+} ions.

10.2 Energy transfer without Er^{3+} and Si NP contact

The Figure 9.2 of the Chapter 9 shows the normalized emission spectra for the Er^{3+} only doped film and the thin film where the Er^{3+} ions were deposited after the Si NPs formation ($SE\phi 2.6$). As it has been explained previously all the Er^{3+} and Si NPs doped films ($SES\phi 2.6$, $ES\phi 2.6$) show the same emission spectrum shape than $SE\phi 2.6$ indicating a $Si-O_2$ rich chemical environment. Therefore, after analyzing the spectra shape in detail, we have concluded that only the Er^{3+} ions in contact with the Si NPs are emitting.

The Figure 10.1 shows the normalized spectra for the Er^{3+} and Si NP doped thin films where the separation between Er^{3+} ions and Si NPs was changed by depositing an intermediate a-Al_2O_3 of 0.5 nm and 1.0 nm thick layer. For instance, the Figure 10.1.a shows the normalized spectra for the Er^{3+} and Si NPs doped thin films within Si NP average size around 2.2 nm. The thin film where the Er^{3+} ions are deposited after the Si NPs formation ($S(A-0.0)E\phi 2.2$, t=0 nm) shows the same spectra shape than the $SE\phi 2.6$, centered at 1533 nm and with a FWHM of 44 nm indicating a SiO_2-rich chemical environment. However the thin films with an a-Al_2O_3 intermediate of 0.5 nm or 1.0 nm thick, $S(A-0.5)E\phi 2.2$ and $S(A-1)E\phi 2.2$ respectively, show an emission spectra peak centered at 1530 nm and with a FWHM of 50 nm as the Er^{3+} only doped a-Al_2O_3 film. Therefore the Er^{3+} ions are located in an a-Al_2O_3 chemical environment, and a layer of a-Al_2O_3 with a thickness value of 0.5 nm is enough to cover the Si NPs and separate the Er^{3+} ions from the Si NPs.

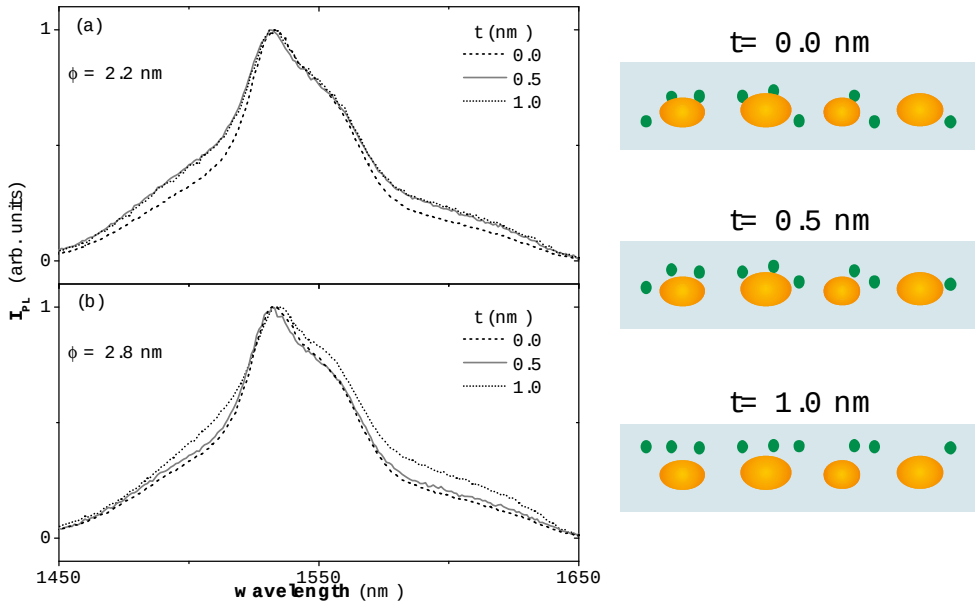

Figure 10.1: Normalized photoluminescence spectra to the maximum of intensity peak for the Er^{3+} and Si NP doped films with different t. The Figure 10.1.a corresponds to the thin films doped by 2D-Si NPs distribution with an average size of 2.2 nm. The Figure 10.1.b corresponds to the thin films doped by 2D-Si NPs distribution with an average size of 2.8 nm.

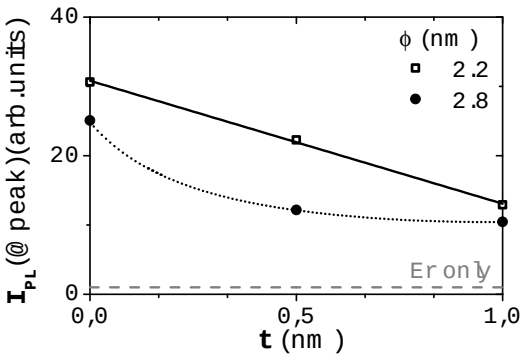

Figure 10.2: PL intensity as a function of t, excited at 488.0 nm at a 200 mW pump power. The average diameter estimated for the 2D-Si NP distribution are 2.2 nm and 2.8 nm. The PL intensity for the film doped only with Er is indicated at a dashed line.

The Figure 10.2 shows the PL intensity obtained at the emission peak at 1.5 μm for all the thin films including the Er^{3+} only doped a-Al_2O_3 film. All the Er^{3+} and Si NP co-doped films show PL enhancement in comparison with the Er^{3+} only doped film due to the presence of the Si NPs, whose PL intensity value decreases as a function of the thickness of the intermediate a-Al_2O_3 layer.

For the films with Si NPs embedded with an average size around 2.2 nm, the PLE curves show the same slope between thin films and only a displacement in the absolute value occurs (not shown - similar to Figure 9.3). Consequently the dependence of the Er^{3+} PL on the pump wavelength is mainly kept by the quantum properties of the amorphous Si NPs and is not influenced by the separation of the Er^{3+} and Si NP dopants. However the saturation curves (PL intensity as a function of the pump power at fix wavelength) indicates that the number of the achievable excited Er^{3+} through the Si NPs is lower for the films with an intermediate a-Al_2O_3 layer than the films with the Er^{3+} ions deposited following the Si NPs formation. Therefore it is possible to maintain the energy exchange between the Si NPs and Er^{3+} ions with PL enhancement factors higher than 10 by controlling the separation of the Er^{3+} ions from the Si NPs by an a-Al_2O_3 layer. The PLE curves are determined mainly by the Si NP size that determine their quantum properties while the number of excited Er^{3+} is ruled by the Er^{3+} and Si NP separation.

In contrast, for the co-doped thin films with Si NPs with an average size around 2.8 nm, the emission spectra shape is the same for the thin film whose Er^{3+} ions were deposited following the Si NPs formation ($S(A-0.0)E\phi 2.8$, t=0.0 nm) and the Er^{3+} and Si NPs doped a-Al_2O_3 film with an intermediate a-Al_2O_3 layer of 0.5 nm thick ($S(A-0.5)E\phi 2.8$, t=0.5 nm) (see Figure 10.1.b). Therefore it seems that the 0.5 nm of intermediate a-Al_2O_3 is not enough to cover the Si NPs and separate the Er^{3+} ions from the Si NPs. However the $S(A-1)E\phi 2.8$ with an intermediate layer of 1 nm (t=1 nm) shows a Er^{3+} emission spectrum shape associated to Er^{3+} ions located in a-Al_2O_3. In Figure 10.2 a strong decrease from t=0 nm to t=0.5 nm is observed and almost constant from t=0.5 nm to t=1.0 nm. The PLE curves show the same slope for all thin films and only a displacement in the absolute value occurs for t=0 and t=0.5 nm films while the t=0.5 and t=1.0 nm thin films shows the same tendency and PL values (not shown). In fact, the PL intensity saturation curves (not show) show differences between the thin films where the Er^{3+} ions are located at the same environment ($Si0_2$-rich) with a thickness t of 0.0 nm or 0.5 nm indicating a lower fraction of excited Er^{3+} ions for the t=0.5 nm. Surprisingly for t= 0.5 and t=1.0 nm the amount of achievable excited Er^{3+} through the Si NPs are the same. This result suggests that it is possible to obtain an efficient transfer process between Er^{3+} ions located in different environments but located close to the a-Al_2O_3-Si NP without significant reduction of the number of the excitable Er^{3+}.

10.3 Implantation depth and Si NPs covering process

In the Chapter 9 thin films with differences in the Er^{3+} and Si NP dopant configuration below the nanoscale were studied ($SE\phi 2.6$, $SES\phi 2.6$, $ES\phi 2.6$). The emission spectra shape reflect fundamentally a SiO_2-rich chemical environment for the emitting Er^{3+} ions . The small differences between the $SE\phi 2.6$ and $ES\phi 2.6$ suggests low percentage of interfacial mixing when the capping layer of a-Al_2O_3 is deposited. But the Er^{3+} ions can be implanted inside the Si NPs when they are deposited following the Si NPs formation. But other physical phenomena have to be taken into account as the self-purification mechanism in semiconductors nanoclusters that could explain the spiting out of the Er ions implanted in the Si NP core to the surface of the Si NP because this process is greater for smaller nanoparticles.[113, 114] In fact, it has been recently corroborated that impurities within a nanocluster can be energetically driven to the surface in Si nanocluster and Phosphor impurities with a critical size around 2 nm.[115] Therefore, the combination of the self-purification and the SiO_2-rich chemical environment observed suggests that all the Er^{3+} emitting is mainly located on the surface of the Si NPs and not inside them.

However, a 56 % higher fraction of the Er^{3+} is excited when the erbium ions are deposited following the Si NPs formation in comparison with the thin films where Er^{3+} ions are deposited before the Si NPs formation. This difference in the fraction of excited Er^{3+} can be only be related to Er^{3+} implantation into the a-Al_2O_3 when the Er^{3+} ions are deposited before the Si NPs formation. However the implantation phenomena inside the Si NPs when the Er^{3+} ions are deposited after the Si NPs formation can be masked by the self-purification or the possibility of no emitting Er^{3+} ions when they are in a Si-Si chemical environment. Thereby the Er^{3+} implantation in a-Al_2O_3 occurs and it is confirmed in the case of the $S(A-0.5)E\phi 2.8$ thin film. The intermediate a-Al_2O_3 layer thickness used is 0.5 nm and the Er^{3+} ions penetrate in the a-Al_2O_3 cover layer showing a SiO_2-rich chemical environment.

Moreover the Er^{3+} ions of the thin film $S(A-0.5)E\phi 2.2$ shows an a-Al_2O_3 chemical environment. Therefore the implantation depth of the Er^{3+} ions in the a-Al_2O_3 has to be lower than 0.5 nm. However in the case of the $S(A-0.5)E\phi 2.8$ thin film, the Er^{3+} ions deposited show a SiO_2-rich chemical environment. The differences between the two thin films with the same thickness of the capping layer are related to Si NP cover process during the deposition of the oxide layer. The intersticial spaces between Si NPs are preferentially filled while the Si NPs are cover by a thicker a-Al_2O_3 layer. As a result, in the case of the larger Si NPs, the amount of a-Al_2O_3 required to fill the space between the Si NPs is higher than for the smaller ones and, when the Er^{3+} ions are deposited, the capping layer is not complete and the cover layer over the Si NPs is much thinner than 0.5 nm. As a result the Er^{3+} ions penetrate the a-Al_2O_3 and contact with the Si NPs indicating

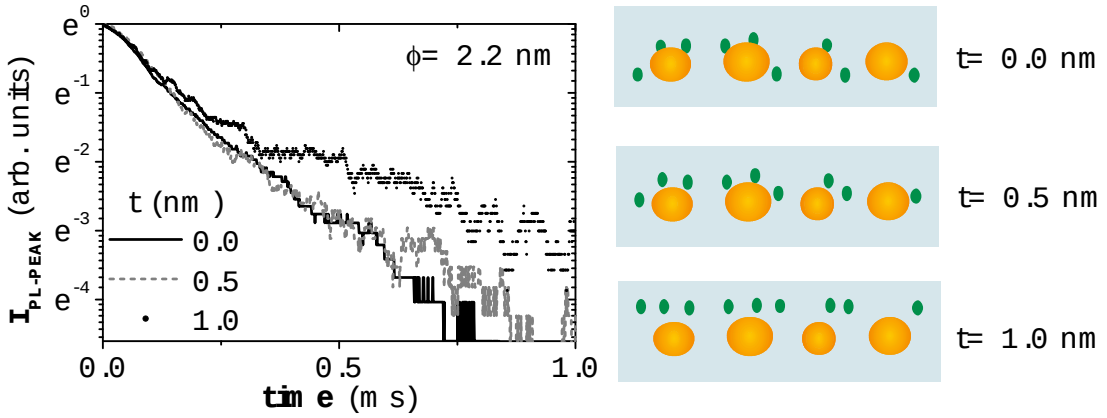

Figure 10.3: Decay curves for the Er^{3+} and Si NPs doped thin films with different thickness of the intermediate a-Al_2O_3 layer (t) and with a Si NP average size of 2.2 nm. The PL dynamic curves have been acquired pumping at 476.5 nm at a 200 mW pump power.

an implantation depth lower than 0.5 nm.

10.4 Er^{3+}-Si NP separation versus Er^{3+} to Si NP back-transfer efficiency

The Figure 10.3 shows the decay curves for the three Er^{3+} and Si NP doped a-Al_2O_3 films with Si NP average size of 2.2 nm and measured at non resonant wavelength pump conditions. The $S(A-0.0)E\phi 2.2$ and the $S(A-0.5)E\phi 2.2$ shows the same temporal behavior. However the $S(A-1)E\phi 2.2$ shows a lifetime enhancement in comparison with the other two Er^{3+} and Si NP co-doped films. The similarities between these co-doped films with t=0.0 and t=0.5 nm can be related to the small separation between dopants. Taking into account the expression 9.2, the amount of excited Er^{3+} is reduced in a 27% while, as it has been explained in the Chapter 9, the reduction in the Er^{3+} excited fraction between $SE\phi 2.6$ and $ES\phi 2.6$ is of a 56%. Consequently the amount of Er^{3+} that penetrate in the intermediate a-Al_2O_3 layer and it is located close to the Si NPs is higher than the amount of Er^{3+} that penetrates the a-Al_2O_3 before the Si NPs formation that causes a decrease of the 56% of the excited Er^{3+} between the $SE\phi 2.6$ and $ES\phi 2.6$ films. Furthermore the Er^{3+} excitation by Si NPs is efficiently controlled by Er^{3+}-Si NPs separation. Therefore the Er^{3+} and Si NPs interaction is extremely sensitive to the Er^{3+} separation below the nanoscale, showing that techniques with a high accuracy in the dopant location require a careful calibration below the nanoscale to obtain the maximum optimization of the Er^{3+} ions emission.

The lifetime values were obtained fitting a multi-exponential decay model with two

components, obtaining a 0.26 ms for the t=0 and t=0.5 nm and 0.39 ms for the t=1 nm (the analysis is detailed at Appendix C). The lifetime enhancement observed in the $S(A-1)E\phi 2.2$ can be interpreted in the frame of two phenomena: a reduction of the back-transfer phenomenon from the Er^{3+} to the Si NPs or to changes in the radiative probabilities by Purcell effects on the density of optical states.

Considering the Er^{3+} ions as donors and the Si NPs as acceptors and solving the rise times and decays as multi-exponential curves with n=2, the efficiency of the back-transfer process (E_{B-T}) can be estimated by the expression C.11:

$$E_{B-T} = 1 - \frac{(\alpha_1\tau_1 + \alpha_2\tau_2)_{DA}}{(\alpha_1\tau_1 + \alpha_2\tau_2)_D} \tag{10.1}$$

where the subscript DA corresponds to the Er^{3+} and Si NP doped film, the subscript D corresponds to the Er^{3+} only doped film and the subscripts 1 and 2 correspond to the two exponential components (see Appendix C). The percentage of back-transfer phenomena for $S(A-0.0)E\phi 2.2$ and $S(A-0.5)E\phi 2.2$ is 53% while the back-transfer for the $S(A-1)E\phi 2.2$ (t= 1 nm) is 33%. Thus, separating the Er^{3+} ions from the Si NPs reduces the back-transfer from the Er^{3+} ions to the Si NPs because the Si NPs can act as non-radiative centers for the Er^{3+} ions. However, not only the back-transfer phenomena is reduced and the efficiency of the energy exchange from the Si NPs to the Er^{3+} ions is also decreased.

Following an alternative approach to understand the Er^{3+} de-excitation it is possible to estimate the changes in the measured lifetime from changes in the probabilities of the non radiative channels. The measured lifetime ($\tau_{measured}$) is given by the expression 10.2 as a function of the Er^{3+} radiative lifetime (τ_{rad}) and the non-radiative lifetime (τ_{nr}).

$$\frac{1}{\tau_{measured}} = \frac{1}{\tau_{nr}} + \frac{1}{\tau_{rad}} \tag{10.2}$$

Taking into account that the $\tau_{rad} \gg \tau_{nr}$, the change ratio in the $\tau_{measured}$ is given by:

$$\frac{\tau_{measured-1}}{\tau_{measured-2}} = \frac{\tau_{nr-2}}{\tau_{nr-1}}. \tag{10.3}$$

The lifetime values for the $S(A-0.0)E\phi 2.2$ and the $S(A-0.5)E\phi 2.2$ are the same, therefore we can assume that when a Er^{3+} ion is close to a Si NP the preferential non radiative exchange channel is the Si NP and not the a-Al_2O_3 defects that are mask by the presence of the Si NPs. Thus the main non-radiative process is the back-transfer phenomena. Furthermore the probability of an event is proportional to the inverse of its lifetime and proportional to its efficiency therefore the non-radiative lifetime is going to be proportional to the inverse of the back-transfer efficiency. Consequently the ratio between

$\tau_{measured}$ between $S(A-0.0)E\phi 2.2$ (t=0 nm) and $S(A-1)E\phi 2.2$ (t= 1 nm) is given by

$$\frac{\tau_{measured-t=1}}{\tau_{measured-t=0}} = \frac{E_{B-T,t=0}}{E_{B-T,t=1}}, \tag{10.4}$$

where the relation of the lifetimes are the same that the relation of the back-transfer percentages. The relation between the measured lifetimes is 1.5 and the relation between the back-transfer percentages is 1.6. These similar values obtained are in agreement with our hypothesis that the main decay channels for the Er^{3+} ions are the Si NPs and not the a-Al_2O_3 defects.

The lifetime values between $S(A-0.0)E\phi 2.2$ (t=0 nm) and $S(A-0.5)E\phi 2.2$ (t= 0.5 nm) do not change and the same spectra shape for the two films (see Figure 10.1.a) indicates the same $Si-O_2$-rich environment. Therefore the emitting Er^{3+} ions are mainly located on the Si NPs surface and the back-transfer efficiency is the same independently of the excited Er^{3+} fraction. It is consistent with an Er^{3+}des-excitation mechanism through intra-band transitions that shows a dependence with the dopants separation proportional inverse to the four power. However the PL intensity decreased rapidly with the thickness of the a-Al_2O_3 spacer layer. Thus, taking into account the expression 9.2, the fraction of excited Er^{3+} decreases a 27 % between $S(A-0.0)E\phi 2.2$ and $S(A-0.5)E\phi 2.2$, indicating that the fraction of excited Er^{3+} depends strongly on the separation between Er^{3+} ions and Si NPs below the nanoscale. It is consistent with an efficient Er^{3+} excitation process that requires physical contact as Er^{3+} excitation through direct exciton inter-band recombination. Therefore the main mechanisms that rule the interaction between Er^{3+} ions and Si NPs are different for the excitation process and the de-excitation but not independents (it will be discussed more in detail in the Chapter 12).

On the other hand the Purcell effect can affect to the radiative lifetime which is decreased when a dipole emitter (as Er^{3+}) is close to an interface of materials with different optical properties. However the small size of the Si NPs and the results based on the back-transfer efficiency suggest that the lifetime behavior is mainly due only to a reduction of the back-transfer mechanism.

10.5 Conclusions

Low percentage of interfacial mixing. Implantation depth lower than 0.5 nm that affects strongly to the amount of excited Er^{3+} ions through Si NPs. The contact is not a taxative requirement and transfer energy from Si NPs to Er^{3+} ions is observed for Er^{3+} ions located in a-Al_2O_3 environment.

Changes on the temporal response are observed for small Si NP-Er^{3+} distances due to the reduction of back-transfer probability. All the results suggest that the most efficient Er^{3+} excitation process through Si NPs shows a contact character (inter-band

transitions) and a the back-transfer phenomena is less sensitive to the Er^{3+} and Si NPs distances (intra-band transitions).

Detailed knowledge of the processes involved during PLD deposition allows to implement the conditions for achieving a control of the dopants location below the nanoscale. Therefore the Er^{3+} and Si NP doped systems where the Er^{3+} ions and Si NPs relative separation can be customized, controlled and optimized are possible. It could be a promising route to achieve percentages of excitable Er^{3+} ions through Si NPs close to the 100% of the Er^{3+} population.

Part IV

Nano-engineering Er^{3+} and Si NP 2D-distributions towards a 100% of excited Er^{3+}: extreme Er^{3+} - Si NP coupling regime

Chapter 11

Extreme Er^{3+}-Si NP coupling regime

The extreme sensitivity of the Er^{3+}-Si NP interaction to the Er^{3+}-Si NP distances below the nanoscale has been demonstrated in the Chapters 9 and 10. In this Chapter amorphous aluminium oxide (a-Al_2O_3) nanostructured thin films doped by erbium ions (Er^{3+}) and amorphous silicon nanoparticles (Si NPs) of different Si NP sizes were produced using the maximized Er^{3+}-Si NP contact configuration. In the conditions of extreme coupling the Er^{3+}-Si NP separation can be considered well defined and unique, since only emission from Er^{3+} in contact is observed. This allows to observe new effects such as the Er^{3+} response as a function of the Si NP size. The diameter of the Si NPs was varied from 1.6 nm to 3.3 nm obtaining local densities of Si NPs one order of magnitude higher than the obtained by traditional techniques. Assuming a characteristic interaction length of 0.4 nm, it can be estimated by simple geometrical considerations that 100% of the Er^{3+} ions are potentially excitable in the films due to the Er^{3+} - Si NPs maximized contact. The spatial correlation between the two dopant distributions are estimated obtaining percentage of Er^{3+} ions in contact with the Si NPs from 40% to a 60%. The spectral and temporal analysis of the photoluminescence properties shows a extreme Er^{3+}-Si NP coupling where the average lifetime dependence on Si NP diameter is only related to the quantum properties of the Si NPs, since in these conditions there is not a distribution of Er^{3+}-Si NP separations. showing that not only the distance between Er^{3+} and Si NP affects to the transfer process efficiency and the relevance of maximized contact and nano-engineer the Er^{3+} and Si NP 2D-distributions.

11.1 Introduction

Towards a complete optimization of the Er^{3+} photoluminescence properties by Si NPs excitation it is necessary to engineer at the nanoscale the 2D-distribution properties such as areal densities, the Si NP average size and the relative position between Er^{3+} and Si NPs. The published research reports focused on the maximization of the Er^{3+} - Si NPs coupling have shown that the main limitation of the Er^{3+} - Si NP doped systems is to optimize the interaction distance between Er^{3+} ions and Si NPs to achieve a maximized number of excited Er^{3+} ions.[37] In addition, Si NP densities higher than 10^{19} cm^{-3} close to the optimized Er^{3+} ion concentrations are required in the volume where the Er^{3+} ions are to obtain a high percentage of sensitized Er^{3+} and good $[Er^{3+}]$/[Si NP] ratio.[22]. As it has been demonstrated in the Chapters 9 and 10 it is possible to maximize the contact between Er^{3+} ions and Si NPs depositing the Er^{3+} ions following the Si NPs formation showing the Er^{3+} an Si NP energy transfer a strong sensibility below the nanocale. The aim in this Chapter is to show how is possible to further nano-engineer the doped material optimizing simultaneously the Er^{3+} and Si NP concentrations, Si NP diameters and positioning the Er^{3+} and Si NPs very closely below the nanometer scale in high density two dimensional (2D) distributions of sensitizers.

Our single step deposition method has been developed to produce extreme coupling thin films in a vacuum atmosphere and at room temperature (RT). Moreover, anneal procedures are not necessary to active the Er^{3+} ions and as a result, problems as Si NP crystallization dependence on Si NP size, and the diffusion of Er^{3+} that are inherent to high temperature annealing to produce the formation of Si agglomerates or activate the Er^{3+} ions, are not present in our RT single step deposition method. Thus, the in situ formation of amorphous Si NPs and the deposition of active Er^{3+} features of RT alternated PLD will allow us to study the Er^{3+} photoluminescence (PL) properties of as grown Er^{3+}-Si NP extreme coupling a-Al_2O_3 thin films as a function of the Si NPs size in equivalent chemical and structural environments for the Er^{3+} ions.

11.2 Er^{3+} and Si NP 2D-distributions deposited in a maximized contact configuration

As it has been explained in the Chapter 9 the coupling between dopants can be maximized in a first step by depositing the Er ions following the Si NPs formation. In this chapter the maximization of the coupling Er^{3+}Si NP changing the distributions of the Si NPs and tuning the sizes in distance optimizing a-Al_2O_3 thin films maintaining the nature of the Si NPs (amorphous) is studied.

In order to tune the Si NP average size between thin films and change the Si NP 2D-distributions. The size of the Si NPs is controlled with the number of laser pulses used to

ablate the Si target in each Si NPs layer deposition. The number of pulses on the Si target (P) has been varied from 75 to 250 to produce five thin films with different Si NP sizes. The Si NPs are formed in situ and not cover before the Er^{3+} deposition. Only one pulse per layer over the metallic erbium target is used to deposit the Er^{3+} ions, preserving the same Er content between thin films. To obtain a maximized contact between Er ions and Si NPs, the Er^{3+} are deposited following the Si NP deposition without an intermediate a-Al_2O_3 layer. All thin films are formed by 20 layers of Er^{3+} doped Si NPs separated by 10 nm of a-Al_2O_3 as it has been described in the Section 5.4 of the Chapter 3. For analysis purposes an Er-only doped reference film has been prepared preserving the Er^{3+} spatial dopant distribution.

All the thin films are optically active in as grown conditions [16] independently of the Si NP size thus the photoluminescence (PL) properties have been measured in the as deposited thin films. Note that other procedures where annealing is needed to induce the nanoparticle formation or Er^{3+} activation involve phenomena as diffusion or crystallization of Si NPsThe diffusion processes cause a not controlled dopants location and the change of the degree of relaxation-crystallization of the Si NPs is different as a function of the Si NP size [30]. For these two reasons, the techniques that implies annealing procedures are not suitable to obtain thin films with a controlled location of dopants and the same Si NP quality independently of the Si NP size. Due it, our as grown thin films produced by alternated-PLD are specially designed and useful to study the Si NP size dependence on the Er^{3+} photoluminescence in Er^{3+}-Si NP doped systems in no Si NP quality dependence.

11.2.1 Tuning Si NP 2D-distributions

The thin films deposited on a fused silica substrate have been used to obtain the absorbance of the thin films through transmission measurements. Transmission and ellipsometry measurements have been performed in the 240 nm to 1700 nm wavelength range using an WVASE J.A.Woollam ellipsometer equipped with a xenon lamp and an UV-visible fiber optic. The Figure 11.1 shows the absorption spectra obtained in optical density units ($O.D. = \log(\frac{1}{T})$). The Er^{3+} only doped film shows a negligible absorption in whole photon energy range and the oscillations observed in the spectra are only due to the finite thickness of the thin film and the reflections at air-thin film and at thin film-substrate interfaces. All the spectra for the Er^{3+} and Si NPs doped films show a negligible absorption in the infrared region, however there are clear absorption bands in the visible range that can only be explained by the presence Si NPs . The absorption border shifts to the blue when the number of pulses on the Si target is decreased indicating a reduction in the Si NP size. The average diameter (ϕ) of the Si NPs can be estimated through the value of the optical gap as has been explained in the Chapter5.The relation between the deposition

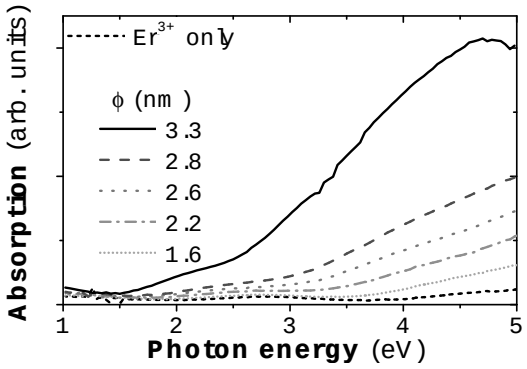

Figure 11.1: Absorption spectra of the nanostructured thin films. The Er^{3+} only doped a-Al_2O_3 film is represented by a short dash black curve. The average Si NP sizes of the Si NPs doped a-Al_2O_3 thin films are estimated as a-Si:H Si NPs with indirect character.

parameters and the average diameter of the Si NPs is shown in the Table **??**. Changing the number of pulses used to ablate the silicon target in every deposition of Si NP layer the average diameter of the Si NPs was tuned from 1.6 nm to 3.3 nm.

The Si NP coverage, the Si NP areal density, the Si NP volume fraction have been estimated using the protocol defined at the Chapter 6. The results are shown in the Table.

11.2.2 Correlation between Si NP and Er^{3+} 2D-distributions

During the PLD process, the material is only deposited in a short time (a few microseconds) after the laser pulse, this special growth conditions leads to a higher density of nuclei than for traditional vapor deposition techniques. Therefore by PLD is possible to obtain thin films with a higher density of Si NPs in comparison with other thin film deposition techniques. The density of Si NPs obtained was varied from 0.7 10^{13} cm^{-2} to 1.8 10^{13} cm^{-2}. These densities are areal densities nevertheless the majority of other groups' works report Si NP distributions in a volume with volume densities values around 10^{19} cm^{-3} by ion implantation technique [101], $5-7$ 10^{17} cm^{-3} by reactive magnetron sputtering [37] or 2 10^{19} cm^{-3} by optimized reactive magnetron sputtering [28]. In order to compare these values with the density of the PLD nanocomposite layer formed, the local volume density has been estimated in our samples. Therefore assuming that the height of the nanocomposite is equal to the average diameter of the Si NPs, the volume Si NP density vary from 2.1 10^{19} cm^{-3} to 1.1 10^{20} cm^{-3} (see table 11.1). The volume density for the $SE\phi 3.3$ is the lower for all the PLD thin films, but it is the equal to the maximum value obtained by the other deposition techniques (optimized reactive magnetron sputtering [28]). It is possible to reach values one order of magnitude higher in the case of the smallest Si NP size ($SE\phi 1.6$), obtaining a volume Si NP density of 11.2 10^{19} cm^{-3}. Then, it is possible

Label	ϕ nm	$[SiNPs]_{2D}$ 10^{13} cm^{-2}	$[SiNPs]_{3D}$ 10^{19} cm^{-3}	$d_{edge-edge}$ nm	$[Er]/[NP]$ no units	$[Er]/[NP]_{on}$ no units
$SE\phi 3.3$	3.3	0.7	2.1	0.47	11.1	6.7
$SE\phi 2.8$	2.8	0.9	3.3	0.53	8.9	5.1
$SE\phi 2.6$	2.6	1.0	4.0	0.52	8.1	4.4
$SE\phi 2.2$	2.2	1.1	5.2	0.75	7.2	3.1
$SE\phi 1.6$	1.6	1.8	11.2	0.76	4.6	1.7

Table 11.1: Areal density of Si NPs and volume density of Si NPs associated to the thin films with different Si NP diameter.

to obtain **one order of magnitude higher density of Si NPs** than using other techniques [101, 37, 28] in the volume where the Er^{3+} ions are randomly distributed in the nanocomposite volume. Then **the percentage of Er^{3+} ions that could be excited can be enhanced one order of magnitude**.

We have obtained a high density of Si NPs but we are interested in the correlation between the ions and the Si NPs. Furthermore we have considered: (1) the in situ deposition (2) the in plane random distributions. The Er^{3+} concentration is the same in all the films with a value of 8.3 10^{13} atm/cm^2 per layer and it is randomly distributed in the total area. When the Er^{3+} ions are in situ deposited following the Si NP deposition a percentage of ions is going to be deposited on the top of Si NPs, therefore the area of contact between the Si NPs and the Er^{3+} ions is the projection area of the NPs over the a-Al_2O_3 surface (Figure 11.2b). The Figures 11.2c and 11.2d show schematic diagrams of Er^{3+} ions and spherical Si NPs in plane distributions for two extreme average diameters (diameters of 3.3nm and 1.6 nm). A extreme coupling is expected due to the proximity of this two high local density. Assuming that the Er^{3+} ions are distributed randomly, **the percentage of Er^{3+} in contact with the Si NPs is equal to the percentage of Si NP coverage** and is from 60% to 40% of the total Er^{3+} for the $SE\phi 3.3$ and the $SE\phi 1.6$ thin films, respectively.

The number of Er^{3+} ions per Si NP ($[Er]/[NP]$) has been calculated assuming that the Er^{3+} ions and Si NPs are homogeneous randomly distributed. The number of Er^{3+} ions deposited on the Si NPs has been calculated using the percentage obtained for the Si NPs coverage in the Chapter 6. In order to determine if all the Er^{3+} ions present in the thin films are potentially sensitized by the Si NPs we have to take into account the between the edge of the Si NPs. The larger distance between Si NPs is 0.76 nm and correspond to the $SE\phi 1.6$ thin film, this distance decreases when the Si NP average diameter and the Si NP coverage increases. Note that all the models suggest a interaction distance below the 1nm or 0.5 nm (to amorphous Si NPs) [116, 37], therefore, in roughness aproximation **the 100% of the Er^{3+} ions are located at a distance below the interaction distance**

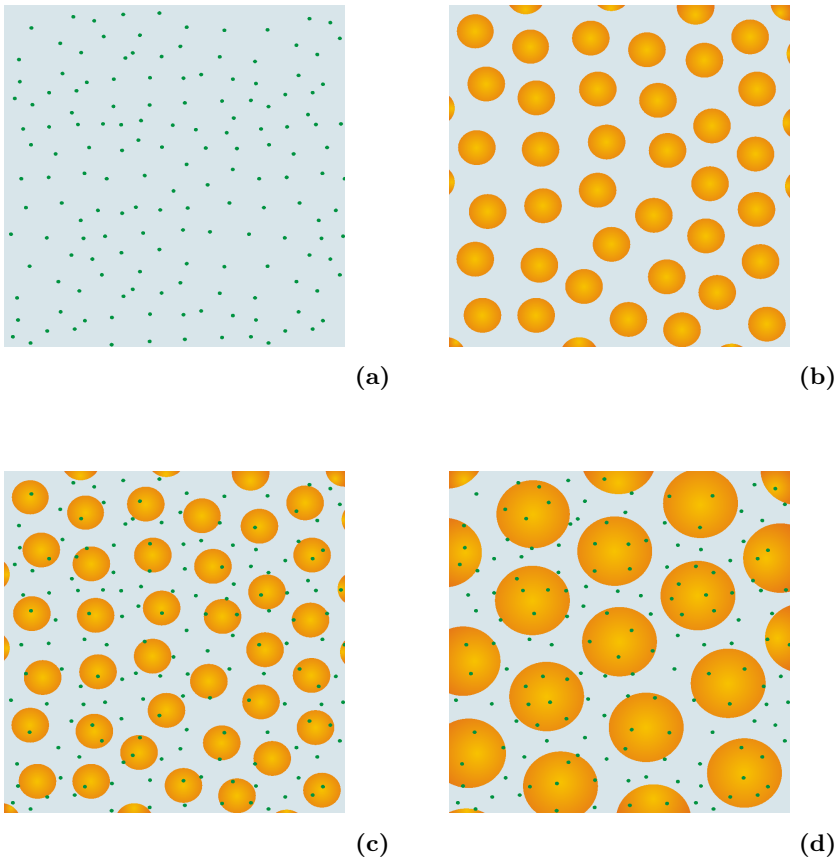

Figure 11.2: 11.2a) A example of a Er^{3+} ions in plane distribution. 11.2b) The projection of the Si NP in plane distribution for the film $SE\phi 1.6$. 11.2c The merger of the projection of the Si NP in-plane distribution for the film $SE\phi 1.6$ and the Er^{3+} ions in-plane distribution. 11.2d) The merger of the projection of the Si NP in-plane distribution for the film $SE\phi 3.3$ and the Er^{3+} ions in-plane distribution.

and they could be sensitized by the Si NPs.

However the Er^{3+} ions deposited in the interspace between Si NPs are located over the a-Al_2O_3 layer. If the Si NPs are spherical the distance from the Er^{3+} ion to the Si NP edge is higher than one half of the $d_{edge-edge}$ value. The worst Er^{3+} location is in the middle of two Si NPs. The maximum real distance between Er^{3+} ions and Si NPs ($d_{max,real}$)can be estimated using the pythagoras theorem by the expression 11.1 where ϕ_{NP} is the average diameter of the Si NP distribution and $d_{edge-edge}$ is the distance between edges of adjacent Si NPs. .

$$d_{max,real} = \frac{1}{2}(\sqrt{2\phi_{NP}{}^2 + d_{edge-edge}{}^2 + 2\phi_{NP}d_{edge-edge}} - \phi_{NP}) \tag{11.1}$$

The maximum distances obtained are from 0.88 nm to 0.63 nm, values lower than the maximum established for Foster energy transfer (around 1 nm). Therefore we reassert than **the 100% of the Er^{3+} ions are located at a distance below the interaction distance** and they could be sensitized by the Si NPs.

11.3 PL emission and the Er^{3+} chemical environment

Information about the location of the Er^{3+} ions must be the key to determine the real relevance of the correlation of the two dopant distributions and the accuracy in the Er^{3+} location and their relevance to obtain extreme coupling between the Si NPs and the Er^{3+} ions. Hence the shape of the Er luminescence spectrum reflects the local environment around the ion[108], differences in the Er^{3+} emission shape could be related to different chemical composition associated to the host (a-Al_2O_3) or to the Si NPs (silicon). The emission spectra are similar to the observed in the thin films analyzed in the Chapter 9. Therefore the spectra shape of Er only doped film is broader than the co-doped films ones thus, the Full With at Half Maximum (FWHM) is 50 nm for the Er^{3+} doped a-Al_2O_3 film and 44 nm for the Si NP and Er^{3+} doped film. Moreover the peak intensity position in the co-doped film spectra is shifted a few nanometers to higher wavelength values than the peak position of the only Er doped film (from 1530 nm for the only Er^{3+} doped a-Al_2O_3 to 1535 nm for the $SE\phi$3.3through 1533 for the $SE\phi$2.6). As it has been explained previously, the bandwidth reduction and the shift to longer wavelength in the co-doped film suggest that almost recollected emission comes from Er^{3+} localized at the surface of the Si NPs corroborating the maximized contact between Er^{3+} and Si NPs indecently of the dopants 2D-distributions. A detailed study of the spectra shape evolution is shown in the Appendix A.

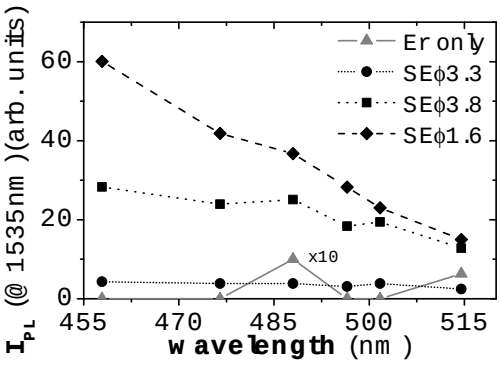

Figure 11.3: Photoluminescence excitation spectra at 1.53 μm for the 250, 210, 75 and Er-only thin films. A pump power of 200mW has been used in all the wavelengths. (Change to pump flux)

The most clear evidence of the phenomena of energy transfer from the Si NPs to the Er^{3+} ions is given by the excitation spectra of the co-doped thin films presented at the Figure 11.3. For comparison purposes, the excitation spectrum for the Er only doped film is also shown, where only PL peak intensity was detected at resonant pump wavelengths (488.0 and 514.5 nm, corresponding to the $^4I_{15/2} - ^4F_{7/2}$ and $^4I_{15/2} - ^2H_{11/2}$ transitions). All the co-doped films show a high Er^{3+} PL emission intensity at the non-resonant excitation wavelengths of 457.9, 476.5 or 501.7 nm. The excitation spectra shows a strong linear decreasing tendency due to the fact that the Si NP absorption decrease linearly as a function of the wavelength. Therefore all the Er^{3+} ions are mainly excited through the Si NPs in the Si NP and Er^{3+} doped films corroborating the strong coupling between the Er^{3+} ions and the Si NPs.

It is possible to estimate the percentage of Er^{3+} emission by indirect or direct pumped as it is explained in the Appendix B. The indirect excitation is the dominant process in all the pump wavelength range and it is responsible of the 88% to 95% (90% mean) of the total PL at 488.0 nm and only the the 13%-5% (10% mean) is due to the direct contribution. However the indirect excitation at 514.5 nm pump wavelength is negligible for all the co-doped thin films, except for the thin film doped with the smallest Si NP where a 35% of indirect contribution (0% mean) has been obtained.

Recent works suggest a main excitation through luminescent centers showing a linear tendency independently of the silicon content of the thin films.[117, 118] In order to compare the linear tendency between co-doped thin films the slope was calculated in the pump wavelength range. The slope of the excitation spectra increases as the average diameter of the Si NPs decreases revealing that the PL intensity dependence on the pump

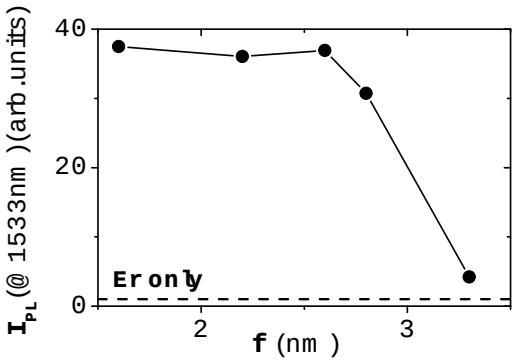

Figure 11.4: Photoluminescence peak intensity size at 1.53 μm as a function of the nanoparticle average diameter pumped at 488.0 nm wavelength at 150 mW power.

wavelength is more noticeable for the thin films with smaller Si NPs in the measurement range. In fact, it is remarkable that at this pump regime the PL enhancement factor changes from 20 to 60 for the $SE\phi 1.6$ film in a small wavelength range variation. Interestingly, all the co-doped a-Al_2O_3 thin films shows a linear slightly decreasing function as a function of the wavelength except the $SE\phi 3.3$ thin film. It shows a flat linear response in the studied wavelength range suggesting a saturation regime with the pump wavelength.

The Figure 11.4 shows the Er^{3+} 1.53 μm PL maximum intensity peak dependence on the average diameter of the Si NPs pumped at Er^{3+} resonant wavelength (488.0 nm). All the Er^{3+} and Si NPs co-doped thin films show improvement on the Er^{3+} emission intensity at 1.53 μm in comparison with the Er^{3+} only doped film, in fact a enhancement factor up to 40 has been reached for the film with the smaller Si NP embedded without anneal process required. The absolute PL intensity increases when the diameter of the Si NPs decreases, only PL peak shows a flat response for thin films with smaller NP average diameter (1.6, 2.2 and 2.6 nm) and it decreases gradually as the diameter increases from 2.6 to 3.3 nm. Similar behavior is observed at a non resonant wavelength (476.5 nm, data not shown).

Usually, the 1.53 μm PL peak intensity reported decreases as a function of the size [27, 19] and does not show a flat response, but there are several parameters different from the Si NP diameter that can affect the amount of Er^{3+} emission detected. When the system is in equilibrium the PL intensity (I_{PL}) that correspond to the transition from $^4I_{13/2}$ level to the fundamental state could be approximated by the expression B.1,

$$I_{PL} \sim f_{Exc-Er}\ N_{Er}\ \sigma_a\ \frac{\tau}{\tau_{rad}} \tag{11.2}$$

where N_{Er} is the total concentration of Er^{3+}, f_{Exc-Er} is the fraction of excited Er^{3+}, σ_a is the absorption cross section, τ is the measured lifetime and τ_{rad} is the lifetime in the absence of radiation less transitions. When the Si NP sizes were tuned from 1.6 to 3.3 nm, the σ_a and τ_{rad} change due to the optical properties dependence on the size (see Chapter5) but additionally the Er^{3+} ions locations are different regarding to the Si NP distributions are different between thin films. At section 11.2.2 we have concluded that the 100% of the Er^{3+} ions could be sensitized, however at a specific pump power their probability of sensitization is going to depend on the distance to the Si NP surface, and then the distribution between dopants are going to affect to the Er^{3+} peak intensity emission obtaining different f_{Exc-Er}. Taking into account that the absorption and the refractive index increase as a function the Si NP average diameter while the PL peak intensity value is maintained or decreases as a function the Si NP average diameter, then, the fraction of excited $Er^{3+}$and the lifetime values are the mainly dominant parameters in the PL intensity tendency.

The PL emission spectrum of all the co-doped films reveals that the Er^{3+} excited through the Si NPs is in a Si-O environment. Also the PL excitation curves shows a excitation mainly through the Si NPs and a clear dependence on the Si NP size. The PL intensity dependence on Si NP size reveals that the PL intensity emission depends mainly of the excited Er^{3+} fraction and the Er^{3+} lifetimes due to the extreme Er^{3+}-Si NP coupling that drops the importance of the absorption of the Si NPs.

11.4 PL decay curves and Er^{3+}-Si NP extreme coupling

The dynamics properties of excitation and des-excitation are perhaps one of the most important characteristics of an emitter. The lifetime decays and rise times of the Er^{3+} ions give us information about the how the Er ions interact with their environment, with other ions, with the host characteristics or the silicon sensitizers, independently of the number of ions emitting. Therefore the lifetimes and rise times will gives us a rich information about the coupling properties between Er^{3+} and Si NPs in our nanocomposite material.[119]

Conventional analysis of Er ions lifetimes resolve the decay profile as a single-exponential decay function as all the Er^{3+} are located in an optimized homogeneous environment. Heterogenous dopant distributions in an host with the non radiative channels minimized (by post-deposition treatments) and/or without sensitizers show single-exponential rise and decay times. However our extreme Er^{3+}Si NP coupling a-Al_2O_3 thin films has been analyzed in as grown conditions without post-anneal treatment and then a more complex decay and rise profiles are expected. The Figure 11.5 shows the PL normalized intensity decay curves for the Er^{3+} and Si NP co-doped a-Al_2O_3 films. The PL decay curves are not well described by a single-exponential decay and our first approach was to fit a stretched

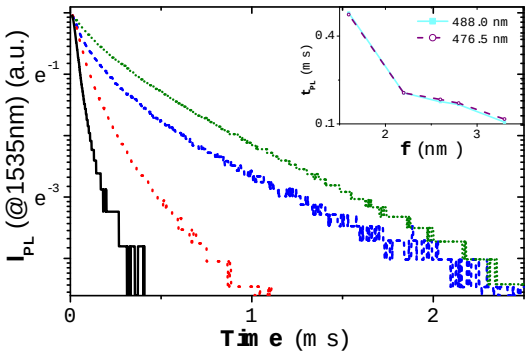

Figure 11.5: Normalized photoluminescence intensity at 1.53 μm decays pumping at resonant conditions at 488.0 nm and at 1.5W of power. The inset shows the lifetime values as a function of the Si NP diameter at resonant (488.0 nm) and non resonant (476.5 nm) pump conditions.

exponential function:

$$I(t) = I_0 e^{-(t/\tau_{KWW})^{\beta}}, \tag{11.3}$$

where I_0 is the fluorescence intensity at time t=0, τ_{KWW} is the decay constant and β is the inverse of the heterogeneity parameter ($h = 1/\beta$) with $0 < \beta \leq 1$ (more detailed in the Appendix C). [120] The stretched exponential behavior is present in a largely number of natural phenomena and their behavior have been associated to the stochastic geometry of systems. As as *Sturman* said the stretched exponential is *the quintessence of radomness* [121]. Our thin films contain 2D Er^{3+} and Si NP distributions randomly deposited over the substrate surface, then the number or multiple alternative des-excitation routes are randomly distributed and a stretched exponential tendency is expected. For a stretched exponential function the average lifetime is defined by $< \tau >= \frac{\tau_{KWW}}{\beta}\Gamma(\frac{1}{\beta})$.

No difference between the lifetime pumped at resonant or non resonant conditions (488.0 nm 476.5nm) has been observed (see inset Figure 11.5), therefore all the emission recollected comes from ions that are excited by energy transfer from Si NPs to Er^{3+} ions independently of the pump wavelength corroborating the Er^{3+} - Si NPs extreme coupling conditions. The average lifetime values vary from 0.048 ms for the thin film with the bigger Si NPs embedded ($SE\phi 3.3$) to 0.442 ms for the smaller ones ($SE\phi 1.6$).

11.4.1 Lifetimes distributions

As it is explained in the Appendix C from the parameters of the stretched exponential decay curves is possible to obtain information about the Er^{3+} lifetimes distribution $\rho(\tau)$

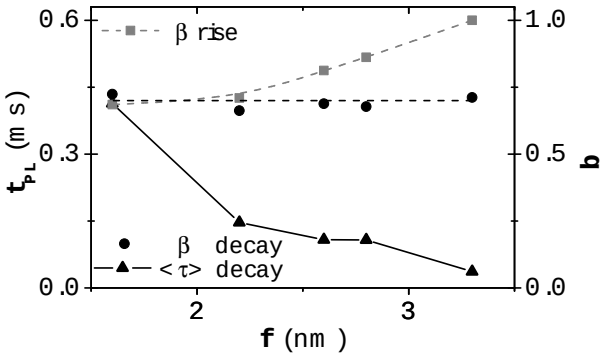

Figure 11.6: Variation of the β parameter from the stretched exponential fitting of the decay curves (Dark grey filled squares). Average time constants $< \tau >$ for the decay PL curves (light grey) and the associated τ_{KWW} as a function of the Si NP diameter (ϕ). The results correspond to the Er^{3+} and Si NP co-doped a-Al_2O_3 thin films.

from β and $< \tau >$ values. Moreover, recently the stretched exponential model was developed to analyze the Er^{3+} lifetime and rise-time distributions and determining their possible relation with β.[122] For every Er^{3+} ion it may reasonable to believe that the relaxation or excitation response is exponential, but in co-doped systems there are a large distributions of environments within the film, as Si NPs of different sizes, different relative Er^{3+} - Si NP locations and then Er^{3+} - Si NP separation distances, each with different characteristics.

The figure 11.6 shows that β_{decay} is constant and independent of the Si NP size while the $\tau_{KWW,decay}$ decreases as the diameter of the Si NPs increases for the co-doped thin films. Thus the lifetime distribution shape between co-doped thin films is similar (basically the same in a normalized lifetime representation) and only the curve is shifted to lower lifetimes as the size increases in a non-normalized representation. Indeed, this low variation in the β_{decay} parameter for all the co-doped film shows that the des-excitation distributions are the same for all the sizes and only the lifetime value changes as a function of the number of silicon dangling bonds or the back-transfer phenomena.

In addition, the β_{decay} value obtained for the Er only doped film is is lower with a value of 0.618 versus 0.789-0.750 for the co-doped films. Thus the lifetime distribution of the Er only doped film is broader than the lifetime distribution of the co-doped thin films. Consequently the heterogeneity of the Er only doped film is higher than the heterogeneity of the co-doped and therefore the Er^{3+} environment is more homogeneous in the extreme coupling Er^{3+}Si NPs thin films. The no differences observed in emission spectra shape for all the co-doped films in the Section 11.3 and the no differences on the shape of the lifetime distributions obtaining more homogeneous lifetimes distributions than the Er^{3+}

only doped film corroborated that the Er^{3+} ions emitting are localized in **the same environment** in the co-doped thin films independently of Si NP size, thus they are located on **the surface of the Si NPs** and the temporal response is only related to the Si NP properties and not to the a-Al_2O_3 host **demonstrating the extreme Er^{3+}Si NP coupling regime**. Thus the contribution of the Er^{3+} ions emitting in contact with the surface of the Si NPs is more homogenously that the Er only film where the presence of defects or other Er^{3+} ions can expand the temporal response distribution of Er^{3+} ions.

11.4.2 Rise-times distributions

On the other hand the β_{rise} is not constant and the values obtained from fitting the PL rise curves increases as a function of the Si NP size. As the diameter of the Si NP increases the β_{rise} is more closed to the 0.8 value (Gaussian distribution) and reach the unit value for the thin film with the larger Si NPs embedded, obtaining a mono-exponential PL rise curve related to one unique excitation mechanism. The rise PL dynamic curves are affected by the transfer process from the donors (Si NPs) to the acceptors (Er^{3+}) and then, by the Si NP excitation mechanism. In previous works the silicon nanoclusters show stretched exponential decays with β_{decay} values around 0.7-0.8 and lower β_{rise} values than the β_{decay}.[122]

The maximized contact in the extreme Er^{3+}-Si NP coupling thin films allow us to excited higher Er^{3+} fractions than in other dopant configurations and the Er^{3+} emission obtained comes from Er^{3+} ions located at the Si NPs surface. Thus, an especial β parameter behavior is expected in comparison with previous works. Kenyon et al. [122] did a exhaustive study about the values of β_{rise} and β_{decay} in a very Er^{3+} dissolved media where the separation between the nanoclusters and Er^{3+} ions are higher than 0.5 nm and only a 1%-4% can be excited through the Si NPs. In this work the values of β_{decay} are higher than the β_{rise}. This difference between the β_{rise} and β_{decay} values were associated that the rise curves values obtained are related to the excitation mechanism of the donors (Si NPs) and the decay curves are affected only by the acceptors and then, only by the radiative and non-radiative channels. In this thin film studied [122], the obtained rise-time rates are a contribution of both near and far Er^{3+} ions. In our thin films the Er^{3+} ions are located at the Si NP surface and then higher rise rates are expected and the rise time values are going to be more affected by the energy exchange mechanism. Consistently, **in the extreme coupling thin films** the β parameter tendency is completely different and **the β_{rise} are higher than the β_{decay}** and the rise rates correspond to an **Er^{3+}Si NPs near location**.

Note that the distribution shape associated to a higher β_{rise} than the β_{decay} parameter suggests a sharper rise-time distribution that defines a very well defined Er^{3+} excitation mechanism, however a lower β_{decay} than a β_{rise} parameter suggests a broader life-time

distribution that can be related to the interference of the host in the Er^{3+} des-excitation processes.

In summary the lifetime shape corroborate that the Er^{3+} ions emitting are located on the surface of the Si NPs. Furthermore the dependence of the Er^{3+} lifetime on the Si NP average diameter suggests a clear dependence of the transfer phenomena in the quantum properties of the amorphous Si NPs. Also the higher values for the β_{rise} than the β_{decay} indicates a new Er^{3+} PL dynamic behavior causes by the Er^{3+}-Si NP extreme coupling.

11.5 Conclusions

Extreme coupling thin films are possible nano-engineering Er^{3+} and Si NP 2D-distributions due to the Er^{3+}-Si NP maximized contact obtained by PLD. The excitation curves show clear dependence on Si NP size in 2D-distributions of amorphous Si NPs without differences in the crystallinity degree. The intensity of the emission obtained dependence mainly in the fraction of achievable Er^{3+} that can be controlled tuning the Si NP and Er^{3+} 2D-distributions that define the percentage of Er^{3+} in contact with the Si NPs. Extreme Er^{3+}-Si NP coupling thin films do not show lifetime distribution dependence on Er^{3+}-Si NP relative distances and new characteristic distribution parameters are obtained and related to the energy exchange mechanism. Under this dopants' spatial configuration Er^{3+} fractions higher than the usual are achievable and percentages close to the 100% of Er^{3+} in the samples can be able.

Chapter 12

Si NP-Er^{3+} interaction mechanisms

In the previous Chapter a new coupling regime named *extreme coupling* has been obtained through the maximized contact between the Si NPs and the Er^{3+} ions. In this new Chapter we discuss the processes of energy exchange between the Si NPs and the Er^{3+} ions and that are related with the maximized Er^{3+}-Si NP contact dopants configuration. The multi-exponential analysis of the temporal response reveals that main features of energy transfer process are related to the quantum properties of the Si NPs. The percentage of each interaction mechanism can be tuned with the Si NP size and the back-transfer phenomena can be reduced to zero in the case of the thin films within the smaller Si NPs.

12.1 Introduction

Applications of nanostructured silicon as absorbers for the incident photons are one of the key-points in the research in solar cells production due to the large number of micro-electronic process specializes in the production and manipulation os silicon. In comparison with the bulk silicon, the silicon quantum dots (Si NPs) show new features which gives new material properties increasing the emission efficiency and tuning the absorption properties.[61] Moreover thoroughly studies in amorphous nano-structures produced at room temperature and not annealed and their quantum properties are required due to the reduction of cost in the fabrication and the simplification of the deposition procedures of amorphous material. In order to increase the efficiency of the charge recollection in the nano-structure by multi-exciton generation (MEG) or space separated quantum cutting (SSQC), high density of Si NP distributions with separations between Si NPs below 1 nm and without contact between the Si NPs are mandatory to improve the charge exchange between adjacent Si NPs.[123, 124, 125]. Therefore our high density 2D-distribution of Si NPs can be an ideal nano-device to used as solar cell absorber. In this chapter we used the Er^{3+} ions as probe of the SSCQ phenomena in amorphous Si NPs and we analyze the possibility of tuning the efficiency of the phenomena at a pump fixed rage as a function of the diameter of the Si NPs.

Furthermore the maximized contact obtained between the Er^{3+} ions and the Si NPs and the new extreme coupling regime observed can give us more precise information on the internal exciton transitions between energy levels in the amorphous Si NPs, their dependence on size and their interaction with the Er^{3+} ions. The extreme sensitivity of the efficiency of the interaction with the Er^{3+} location studied in the Chapter 9 suggests that the main energy transfer mechanism involved is the inter-band exciton recombination ruled by the contact character. However in a Si NP-Er^{3+} contact configuration the intra-band exciton relaxation plays also a important role due to the SSQC phenomena.

In addition, since the nineties the discussion in Er^{3+} and Si NP doped materials about the Er^{3+} temporal response dependence on the Si NPs size is still open. The non controlled spatial dopant distribution and the thermal treatments needed to activate the Er^{3+} ions and/or to form the Si NPs have hindered the analysis of Er^{3+} lifetimes and rise-times as a function of the Si NP size in Si NPs with the same quality. [126, 20] Recently, models that related the differences on the parameters of the stretched exponential decay of the Er^{3+} ions to different location of the Er^{3+} ions respect to the Si NP has been developed. [122, 106] However the sum of Er^{3+} at different locations makes difficult to distinguish the different interaction mechanisms. In this work we present a simple method based on multi-exponential functions where two components are defined as a function of the interaction mechanisms in the extreme coupling regime where it is assumed that only the Er^{3+} in contact is emitting. This analysis method reveals us the percentage of excited

Er^{3+} population by intra-band exciton relaxation and inter-band exciton recombination as a function of the Si NP size depending strongly on the Si NP size. Therefore SSQC phenomena is observed for first time in high density amorphous Si NPs and it can be tuned with the relation between the band-gap of the Si NPs and the pump photon energy. The thin films are active in the as-deposited and non-annealed conditions thus the properties are only related to the quantum properties of the amorphous Si NP 2D-distributions with the same quality in all thin films.

Previously to show how the Er^{3+} temporal response reveals the interaction mechanisms in extreme coupling Si NP-Er^{3+} thin films, we explain the energy exchange processes between Si NPs and Er^{3+} ions and the Si NPs and Er^{3+} roles as donors and acceptors.

12.2 Processes of energy exchange of Si NPs and Er^{3+}

The Si NP mediated Er^{3+} excitation can proceed by a variety of physical processes as exciton transfer, resonance transfer, dipole-dipole transfer, etc. The energy exchange processes can be classified as a function of the distance between donor and acceptor and the transfer process efficiency. In our a-Al_2O_3 doped system the Si NPs act as donors and the Er^{3+} ions act as acceptors. The donors are the absorbers of the energy of incident photons and they become in a excited state. Finally this energy will be transfered from the donor to the acceptor by interactions ruled by the quantum electrodynamics. [127] Finally, in our Si NP-Er^{3+} doped system, the acceptors turn in light emitters.

In order to explain the different interaction mechanism it is necessary to understand the quantum properties individually of the Si NPs and Er^{3+} ions and their functions as donors or acceptors. In the following sections the absorption and energy transfer processes are described.

12.2.1 Si NPs as donors. Generation of excitons

The Si NPs are the absorbers of the incident photons. The photon absorption in a Si NP are caused by inter-band, intra-band or excited-state absorption processes. These processes are described schematically in the Figure 12.1. [128] The inter-band absorption process is the only optical absorption possibility for an intrinsic semiconductor quantum-dot under equilibrium. Our Si NPs are formed by an intrinsic semiconductor however, during the pumping time to reach a absorption saturation level, the Si NPs are not in equilibrium and the intra-band and excited-state absorption processes are posible. Even so, we discard the the intra-band absorption and excited-state absorption from direct photons because the photon energy range associated for these processes is mainly in the infrared rage while our pump photon energy is in the visible. Nevertheless these absorption processes are present

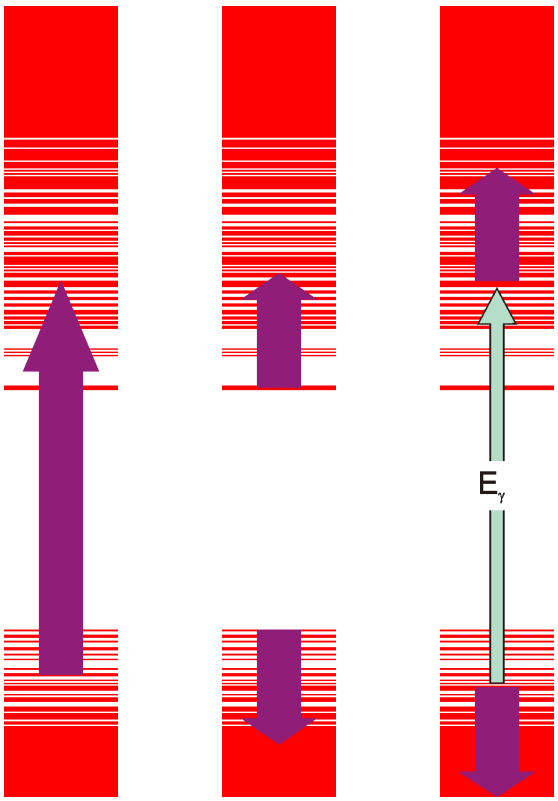

Figure 12.1: Schematic representation of the three different absorption processes in Si NPs: 12.1a inter-band, 12.1b intra-band and 12.1c excited-state absorption. The purple arrows indicate the direct photon absorption transitions and the blue arrow indicates the optical pumping.[128]

in the back-transfer phenomena when an excited Er^{3+} ion transfer its energy to a closer Si NP and in the space-separated quantum cutting (SSQC) phenomena between adjacent Si NPs when the exciton relaxes through intra-band transitions transferring its energy to the adjacent Si NP. [128, 25, 124]

Considerer that the Si NPs are the absorbers of the incident photons whose photon energy is larger than the band-gap of the Si NP by inter-band transitions, the exciton generation and its related relaxation processes can be classified in three situations as a function of the pump energy:

1. If the energy of the photon (E_γ) is large but similar to the Si NP band-gap (E_g), $E_\gamma \gtrsim E_g$, then an exciton (electron-hole coupling pair) is generated. See Figure 12.2a.

2. If the energy of the photon is larger than the Si NP band-gap but lower than two times the band gap, $2E_g > E_\gamma > E_g$, then an exciton in the high energy levels of the Si NP is generated. This "excited" exciton can relax to lower energy levels in the conduction band and to higher energy levels in the valence band through intra-band transitions. The intra-band transitions are allowed in the Si NPs due to the relaxation of the k-rule due to the quantum confinement. See Figure 12.2b.

3. If the energy of the photon is larger than several times the band-gap energy of the Si NPs, $E_\gamma > nE_g \; with \; n > 2$, more than one exciton can be formed for only one absorber photon by impact ionization and Auger recombination (Multi-exciton generation - MEG).[129, 130, 131] See Figure 12.2c.

In our case MEG cannot be observed since we are pumping energy in the visible, from 2.3 eV to 2.6 eV.

12.2.2 Er^{3+} as acceptor. Energy exchange from Si NPs to Er^{3+} ions.

Once the pump light is absorbed by the Si NPs its energy can be transferred to the Er^{3+} ions by Auger process or dipole-dipole interaction. The transfer mechanism depends on the distance between the Er^{3+} ion and the Si NP and in the excited state of the Si NPs. As a function of the pump energy the energy exchange processes can be classified as:

1. When $2E_g > E_\gamma > E_g$ the energy can be transferred by dipole-dipole or Auger process through exciton recombination.

2. When $2E_g > E_\gamma > E_g$ the exciton generated corresponds to an electron in a high conduction band energy level and a low valence band energy level. Thus the Er^{3+} ions can be excited through exciton intra-band relaxation transitions and exciton recombination. This process is named space-separated quantum cutting (SSQC)

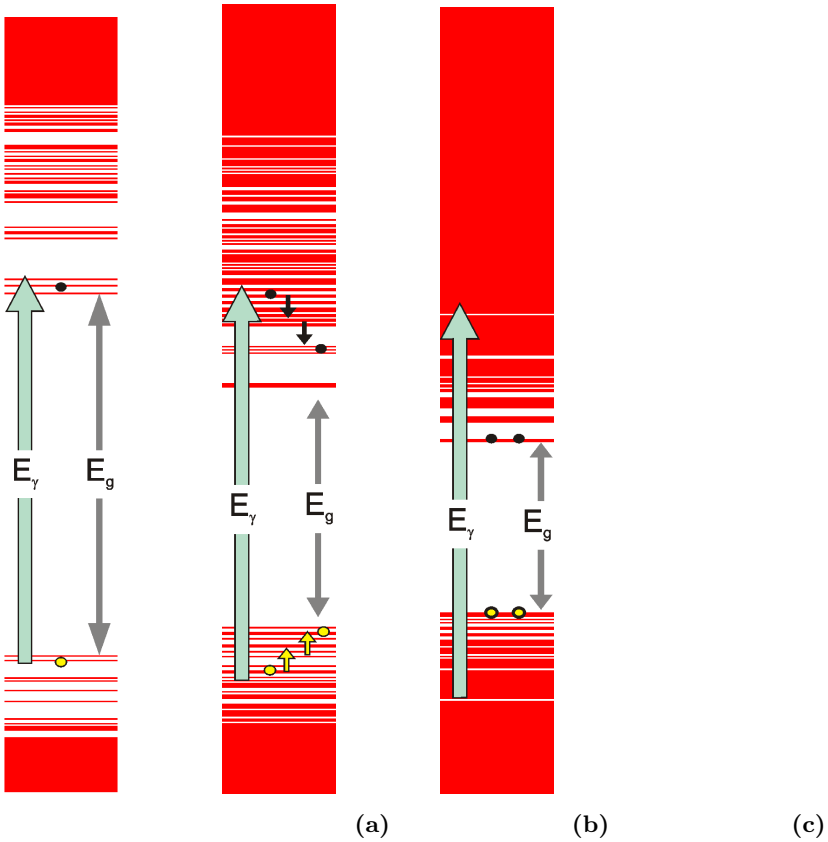

Figure 12.2: Schematic representation of the exciton generation and relaxation in Si NPs. 12.2a $E_\gamma \gtrsim E_g$. 12.2b $2E_g > E_\gamma > E_g$. 12.2c $E_\gamma > nE_g$ *with* $n > 2$. The blue arrows indicate the incident photon energy, the black arrows and yellow arrows indicate the intra-band transitions of electron and holes respectively. The black points are the electrons in the conduction band and the yellow points the holes in the valence bands. The Si NP energy levels correspond to the Si NP^o states obtained by Bulutay et al. for crystalline Si NPs of diameters of 1.36, 2.45 and 4 nm. [128]

and is the ultra-fast division of the energy from an absorbed photon into two or more spatially separated states through the intra-band transitions.[123] Therefore when the energy of the incident photon exceed the band gap plus the first excited Er^{3+} state energy, it is possible to excite more than one Er^{3+} ion per absorbed photon (see Figure 12.3).

3. when $E_\gamma > nE_g \; with \; n > 2$ several excitons are generated by MEG, and every exciton can transfer energy to several Er^{3+} ions through the two transfer process described above.

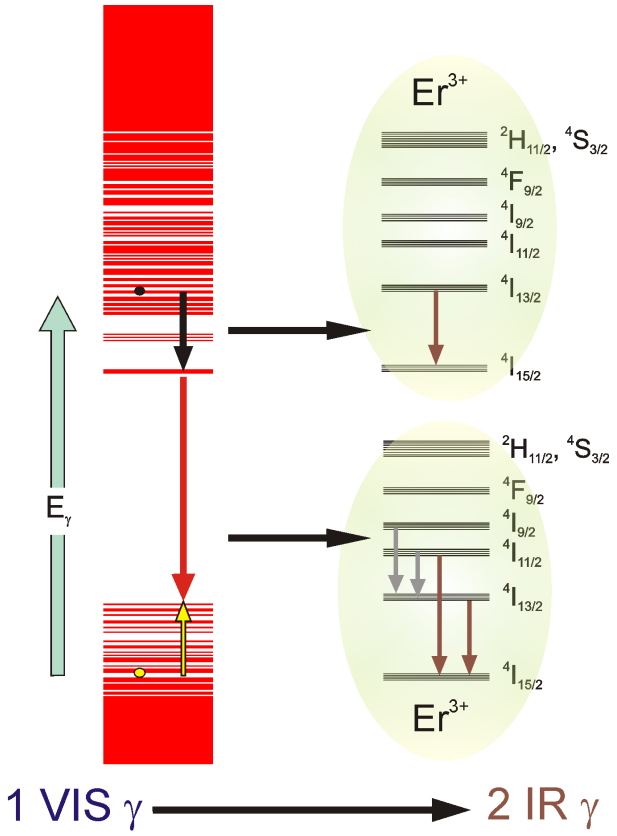

Figure 12.3: Schematic representation of the space separated quantum cutting. One incident photon at the visible produces two photons in the infrared range.

Summarizing, in order to determine the process involved in our Si NP-Er^{3+} extreme coupling thin films it is necessary to take into account our energy pump range and the ban-gap of the Si NPs. The band-gap of our Si NPs is from 1.3 to 2.0 eV and our pump energy range is from 2.3 to 2.6 eV. Therefore, in our pump energy regime, the Er^{3+} can be only exited through Si NPs excited by the excitons generated in the process 1 and 2, and the MEG process does not occur. Thus **the Er^{3+} ions can be excited by**

exciton relaxation through intra-band transitions and by recombination of exciton through inter-band transition by direct photon generation of one exciton.

12.2.3 Interaction mechanism as a function of the distance Er^{3+}-Si NP.

The interaction mechanism can be classified as a function of the range of the interaction distance that reveals the transfer mechanism. Moreover, the efficiency of the process is stronger limited by the distance between donors and acceptors. Now, we classify the interaction mechanisms in *long-range*, *short-range* and *contact character* and show their relation with the photon absorption process in the Si NPs and the exciton subsequent relaxation and recombination.

Long-range. *Dipole-dipole interaction: FRET.*

The Föster resonance energy transfer (FRET) is a spectroscopic process for which the energy passes radiatively or non-radiatively from dipole donors (Si NPs) to dipole acceptors (Er^{3+}) over long distances (1-10 nm) through dipole-dipole interaction. In Er^{3+} and Si NPs system, the FRET interaction process is due the dipole-dipole interaction of an exciton in the Si NP and an Er^{3+} ions located in the a-Al_2O_3. The donor must have a strong absorption as the Si NPs and the acceptor must be able to absorb at the donor emission wavelength. Föster show how to express this overlap in terms of oscillators strengths of quantum spectroscopic dipoles, for that, he emphasized the term resonance in his theory because the strong requirement is that the donors and acceptors be in resonance to bring about energy transfer. The efficiency of this process and the characteristic interaction distance (R_0) can be estimated as a function of the donors' photoluminescence properties in the absence and presence of acceptors. In the first studies of the Si NP-Er^{3+} interaction process, the long-range dipole-dipole interaction has been proposed assuming that the main contribution to the excitation of Er^{3+} through Si NPs comes from non-radiative recombination of carriers in Si NPs.[132, 133, 134] So the differences on the Er^{3+} PL enhancement and the PL temporal response were analyzed as a function of different location of the Er^{3+} ions to the Si NPs. The R_0 value was estimated of 0.4 nm for crystalline Si NPs and 1 nm for amorphous Si NPs. The complexity of the FRET and the differences on the Er^{3+} temporal response as a function of the Si NPs and Er^{3+} ions did not allow to study in detail others interaction mechanism independently. REF

Since the emission spectra shape and the lifetimes distributions discussed in the Chapters 11 and 9 shown that the Er^{3+} ions emitting are localized at the surface of the Si NPs, the Föster resonance energy transfer is discarded as one of the main mechanism in the excitation of the Er^{3+} ions through Si NP.

Short-range. *Er^{3+} excitation and de-excitation due to intra-band transitions.*

The Er^{3+} ions can be exited through intra-band relaxation of the excitons. This mechanism is ruled by the Auger excitation of an Er^{3+} ion as a result of the intra-band transitions of a hot carrier that has been generated from a photon absorbed with an energy higher than the Si NP band-gap. This process is **double sided** and the Er^{3+} ions can de-excite through intra-band absorption (see Figure 12.1b). Due to the degenerate states of the Si NPs, the probability of Er^{3+} de-excitation should be higher for the processes that does not require any phonons to be emitted or absorbed.

Er^{3+} excitation through relaxation of the excitons through intra-band transitions has been estimated in the sub-microsecond regime for crystalline Si NPs. However the exciton lifetime for amorphous Si NPs is two orders of magnitude higher than for the crystalline Si NPs, thus a slower temporal response than the sub-microsecond regime is expected for the Er^{3+} excitation trough amorphous Si NPs. The estimated distance range is from 0 to 1 nm.

Contact requirement. *Er^{3+} excitation by the recombination of excitons.*

Another way to transfer energy from a Si NP to an Er^{3+} ion is through the recombination of exciton by Auger recombination through inter-band transition. The band structure of the Si NPs shows indirect character for thin films with Si NPs within with sizes above the 1.5 nm. [41] In our a-Al_2O_3 thin films, only the $SE\phi1.6$ film could show a direct character, as a result, in most of the thin films the confined carriers recombination should be accompanied by multiphonon emission process due to the momentum conservation rule (k-rule). Therefore, in order to comply the momentum conservation rule, the Er^{3+} ions should be at a distance below the lattice constant of silicon and the efficiency of the interaction is determined by the electron and hole wave-functions in the position of the Er^{3+}. Therefore the interaction requires the physical contact between the Si NPs and the Er^{3+} ions.[25].

It has been measured that the Er^{3+} ions that are excited by energy transfer from inter-band recombination of the confined carriers at the microsecond regime for crystalline Si NPs shown the natural Er^{3+} de-excitation behavior.

The **efficiency** of the transfer process (probability of an event-W) has been estimated in two recent papers for a specific Si NP size.[135, 25] It can be varied up to five orders of magnitude between energy transfer processes. These great differences are illuminating and reveal the great differences in the efficiency of the process that justified the low excited Er^{3+} fraction in previous works [22, 23, 136, 137] and the large excited Er^{3+} fraction obtained in the extreme coupling thin films (see Chapter 14). Considerer than the maximum distance from the Er^{3+} ions to the Si NPs is half of the distance between Si NPs surfaces and the exciton rate in an amorphous Si NP is 10^3 s^{-1},[36] the relation of efficiencies can be estimated as the expression 12.1.

$$W_{interband-recombination} \approx 10^3\ W_{intraband-relaxation} \approx 10^5\ W_{dipole-dipole} \tag{12.1}$$

As a result the more efficient transfer process is the excitation of the Er^{3+} ions by inter-band exciton recombination, in fact this process is 5 orders of magnitude more efficient than the dipole-dipole interaction that it is the main transfer mechanism in the previous works. [122, 22]

Since our maximized Er^{3+} and Si NP contact configuration has been obtained showing a main emission from Er^{3+} ions in contact with the Si NPs and taking into account the transfer process probabilities, the main interaction mechanisms should be related to exciton Auger recombination (inter-band recombination) and Er^{3+} Auger excitation (intra-band relaxation). Consequently we study thoroughly the temporal photoluminescence response as a multi-exponential decay of two components that allow us to estimate the back-transfer through intra-band transitions and it is linked with the dependence of the excitation curves and the pump energy range used.

12.3 Er^{3+} temporal response and the multi-exponential decay $(n = 2)$

The analysis realized in the Chapter 11 of the stretch exponential decay has gave us information about the emitted Er^{3+} location at the surface of the Si NPs and now, the multi-exponential decay curves give us information about the interaction mechanism inherent to the energy transfer processes from Si NPs to Er^{3+} ions and from Er^{3+} ions to Si NPs. It is consistent with the discussion about the distribution of lifetimes defined by the stretched exponential, where there are contributions from **fast and slow dynamic components in a distribution with a mean lifetime**. The photoluminescence measurements have been performed pumping at 488.0 nm at 1.5 W. Therefore the experimental photoluminescence decay and rise curves at 1.53 μm were fitted a multi-exponential decay law with a discrete value n=2 (the analysis is detailed in the Appendix C). Each temporal component of the dynamic response is associated to two different Er^{3+} environments and then to two different excited Er^{3+} population. In addition, the multi-exponential decay allow us to calculate the fractional contribution of each Er^{3+} population by the expression 12.2 where α_i is the amplitude of each component at the initial time and τ_i the associated temporal value.

$$f_i = \frac{\alpha_i \tau_i}{\alpha_i \tau_i + \alpha_i \tau_i}, \ where \ i, j = fast, \ slow \tag{12.2}$$

The Table 12.1 shows the values of the two decays ($\tau_{fast,slow}$) and the average lifetime ($\bar{\tau}_{decay,rise}$) associated and calculated by the expression C.10. The analysis shows one fast

component from 0.48 to 0.168 ms for the decay lifetimes and from 0.044 to 0.140 ms for the rise times. Furthermore the slow decay component is very similar for $SE\phi 2.2$, $SE\phi 2.6$ and $SE\phi 2.8$, however the in the $SE\phi 1.6$ shows a extraordinary higher value and the $SE\phi 3.3$ shows a very short component specially in the rise curve. Since we have assumed that the Er^{3+} ions are going to be excited mainly by exciton relaxation through intra-band transitions or by recombination of excitons through inter-band transitions, we assume that this two temporal components are related to the inter-band and intra-band transitions of excitons. For crystalline Si NPs the temporal response associated to the Er^{3+} excitation by hot carriers intra-band transitions excitation is in the sub-microsecond regime while the temporal response associated to Er^{3+} excitation by recombination of exciton is in the micro-second regime.[25, 106] Therefore we assume that **the fast component corresponds to the Er^{3+} excitation through exciton intra-band relaxation and the slow component to the Er^{3+} de-excitation through exciton recombination**. However, we considerer that we can measure the two temporal components due that exciton recombination rate is two orders of magnitude lower for amorphous Si NPs than crystalline ones.

Label	$\tau_{fast-decay}$ ($\pm$0.010 ms)	$\tau_{slow-decay}$ ($\pm$0.010 ms)	$< \tau >_{decay}$ ($\pm$0.010 ms)	$\tau_{fast-rise}$ ($\pm$0.010 ms)	$\tau_{slow-rise}$ ($\pm$0.010 ms)	$< \tau >_{rise}$ ($\pm$0.010 ms)
$SE\phi 1.6$	0.168	0.699	0.605	0.140	0.596	0.502
$SE\phi 2.2$	0.084	0.346	0.260	0.075	0.281	0.165
$SE\phi 2.6$	0.081	0.338	0.202	0.069	0.263	0.134
$SE\phi 2.8$	0.074	0.334	0.209	0.063	0.279	0.128
$SE\phi 3.3$	0.048	0.304	0.098	0.044	0.044	0.044

Table 12.1: Lifetime and rise-time values from two components in a multi-exponential decay law. Pumping at 488.0 nm at 1.5 W.

Besides the measurement of the lifetime and rise-time values, it is interesting to analyze different Er^{3+} populations emitting and exciting in the co-doped thin films to study in depth the interaction mechanism between the Er^{3+} ions and the Si NPs in the extreme coupling conditions. The pre-exponential factors $\alpha_{fast,slow}$ (expression C.8) represent the contribution of each component at the initial time thus they represent the contribution of each Er^{3+} population to the ground-state in equilibrium. From the $\alpha_{fast,slow}$ values and the lifetime and rise times associated is possible to determine the fractional contribution for each Er^{3+} population by the expression 12.2. The Figure 12.4 shows the fractional contribution of the two Er^{3+} populations associated to the Er^{3+} and Si NP doped a-Al_2O_3 thin films as a function of the Si NP diameter (ϕ) for the excitation and des-excitation temporal response. Note that the rise-time shape of the $SE\phi 3.3$ shows a single-exponential trend thus obtaining the same rise-time value for the fast and slow

components and obtaining a 100% of excitation of the Er^{3+} ions by the fast process as it has been observed in in the Chapter 11. In order to identify the two temporal components with the two main energy exchange mechanism the excitation and des-excitation are analyzed separately. Thus, we assume than the fast component corresponds to Er^{3+} excitation and des-excitation through intra-band transitions of the confined carriers and the slow components can be related to Er^{3+} direct excitation by exciton recombination through inter-band transitions and Er^{3+} natural des-excitation in the host media.

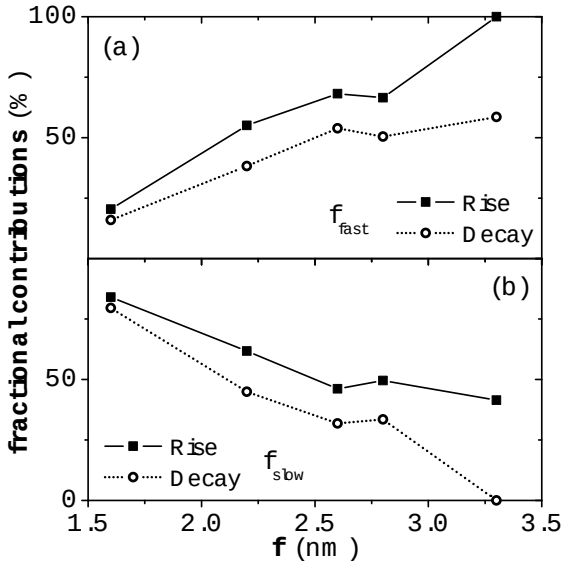

Figure 12.4: Fractional contributions for the two temporal components obtained the photoluminescence decay and rise curves. The f_{fast} corresponds to the fast component and the f_{slow} corresponds to the slow component.

Excitation

There are four Er^{3+} excitation mechanism that can be affect to the excitation dynamics pumping at 488.0 nm:[25]

1. By Er^{3+} direct absorption of a photon in a resonant energy with its atomic levels. It is unlikely because only Er^{3+} excitation through Si NPs has been proved in our extreme coupling thin films.

2. By energy transfer from inter-band exciton recombination in the Si NPs.

3. By intra-band transitions of carriers in the Si NPs with a a very strong non-radiactive quenching.

4. By dipole-dipole interaction. It has low probability as shown previously due to the maximized contact obtained in or extreme coupling thin films.

The percentage of population of Er^{3+} ions excited through the fast mechanism ($f_{fast,rise}$) increases from 20% to 100% as a function of the diameter of the Si NPs increases. On the other hand the percentage of population excited associated to the slow component ($f_{slow,rise}$) decreases as the diameter of the Si NPs decreases. Therefore there are two excitation mechanism that are related to the diameter of the Si NPs and then in turn to their quantum properties. The Figure 12.2 shows the energy levels for three Si NPs with different energy gap (studied detailed in the reference [128] for crystalline Si NPs, similar energy level structures have been obtained for amorphous Si NPs [138] where the amorphization reduces the fundamental gap increasing the absorption strength in the visible range). When the size of the Si NP increases the band-gap energy is reduced, therefore at a fixed pump photon energy for the largest Si NPs the exciton generated is located at higher energy values with respect to the band edges where the intraband levels are more closer and more numerous in comparison with the thin films with smallest Si NPs. Therefore there are more likely intra-band transitions and the probabilities of transfer energy to an Er^{3+} by relaxation of the excitons through intra-band transitions increases with the Si NP size. As a result the increment in the fractional contribution of the fast component to the excited Er^{3+} population as the Si NP size increases corroborates that the fast component corresponds to the Er^{3+} excitation through intra-band transitions as it was initially assumed.

Since we have assumed than due to the maximized contact between Er^{3+} and Si NPs in the extreme coupling thin films the two main excitation mechanism are related to inter-band transitions and inter-band exciton recombination, the slow component corresponds to the Er^{3+} population excited through inter-band recombination. In this case, when the pump energy is fixed and the size is reduced the exciton generated is energetically located closer to the band edge and the probability of inter-band relaxation channels are reduced, as it is observed with the reduction of the population of the slow component as a function of the Si NP diameter increases.

Des-excitation

Because the unique transfer mechanism that it is double-sided is the confined carriers relaxation or excitation through inter-band transitions, there are only two de-excitation paths for the excited Er^{3+} ions:

1. Natural des-excitation emitting a photon at 1.53 μm in the embedding host media.
2. Des-excitation by carriers confined in the Si NPs.

The number of rapidly des-excited Er^{3+} ions ($f_{fast,\ decay}$) increases from a 16% to a 51% as a function of Si NP diameter, thus the $f_{fast,\ decay}$ increases as the energy gap of the Si NPs decreases. The similar behavior of the fast component in the excitation and des-excitation suggests that the Er^{3+} population des-excited through the fast mechanism

are related to the back-transfer process by intra-band transitions from the Er^{3+} ions to the Si NPs. Consequently, the percentage of the Er^{3+} population excited by intra-band transitions ($f_{fast,\ rise}$) is higher than the percentage of the Er^{3+} population des-excited through intra-band transitions ($f_{fast,\ decay}$) (see Figure 12.4.a). In fact, the percentage of the Er^{3+} ions des-excited through intra-band transitions has to be lower than the percentage of the Er^{3+} excited through exciton intra-band relaxation. [25]

The slow component population ($f_{slow,\ decay}$) decreases from 84% to a 49% as the diameter increases. This des-excitation mechanism is related to the natural des-excitation of the Er^{3+} ions in the a-Al_2O_3-Si NP interface, therefore the lifetime associated to the slow decay is very similar between co-doped thin films and only a 12% (from 0.346 to 0.304 ms) is reduced when the Si NP size is increased from 2.2 to 3.3 nm. However the slow lifetime component obtained from the PL excitation time curves shows a decrease of a 73% from 3.3 to 2.2 due to the sensitivity of the inter-band excitation process to the Si NP band-gap, where the exciton recombination rate increases with the Si NP band-gap.[36] The decrease of the 12% observed in the temporal component of the natural des-excitation of the Er^{3+} as a function of the Si NP diameter is due to the presence of silicon dangling bonds at the surface of the Si NPs whose number increases as a function of the Si NP diameter. The $SE\phi 1.6$ is a special case and it will be explained in detail in the Chapter 13.

We have assumed that the fast component of the des-excitation temporal response is related to the Er^{3+} des-excitation through intra-band transitions, thus the percentage of population of this component has to be similar to the back-transfer efficiency (E_{B-T}) from the Er^{3+} ions to the Si NPs. The E_{B-T} can be estimated by the lifetime decay values and the amplitude components of the Er^{3+} only doped films and the Er^{3+} and Si NP co-doped thin films considering the Er^{3+} as the donor and the Si NPs as the acceptors (detailed in the Appendix C). The Figure 12.5 shows the similarity if the back-transfer efficiency mechanism and the percentage of fast component of the decay and the rise curves that it is in agreement with our initial hypothesis of the relation between the fast components of the decay and rise curves with the intra-band transitions.

Summarizing, the two temporal components have been obtained in the multi-exponential analysis that are related to the two main process of energy exchange between the Si NPs and Er^{3+} ions: the intra-band transitions and the inter-band exciton recombination and generation. The fast components have been associated to the intra-band transitions and corroborated by the back-transfer efficiency. The slow components are related to the inter-band Er^{3+} excitation and the Er^{3+} natural relaxation for the rise and decay curves, respectively.

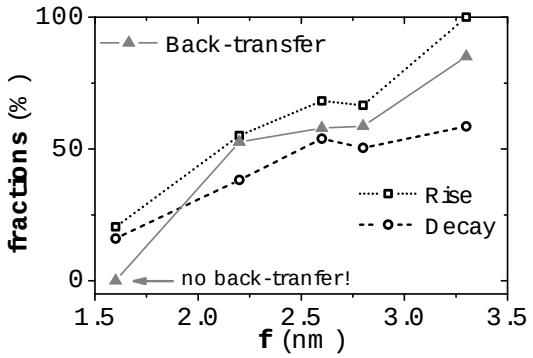

Figure 12.5: The fractional contribution of fast component in the Er^{3+} decay curves (f_{fast}) taken from Figure 12.4.a and the back-transfer efficiency. The $SE\phi 1.6$ does not show back-transfer phenomena due the tuning of the band gap and the Er^{3+} ions levels allowing only inter-band transitions. The percentage of the fractional contribution of the fast component for the $SE\phi 1.6$ is the same that the Er only f_{fast}

12.4 Tuning the Si NP-Er^{3+} interaction mechanism

We have observed a well fitted multi-exponential curve with $n = 2$ for the decay and rise curves of the temporal response of the Er^{3+} PL emission at 1.53 μm. We have associated this two temporal components with the main excitation and des-excitation mechanisms. The fractional contribution of each contribution of Er^{3+} population is varied as a function of the Si NP size and in turn as a function of the band-gap of the Si NPs. In order to study thoroughly the tuning of the interaction mechanism with the band-gap of the Si NPs, the photon energy pump must be taken into account as selector of mechanism. The excitation of the Er^{3+} ions by exciton relaxation through intra-band transitions is related to the SSQC phenomena. The condition to obtain Er^{3+} excitation through intra-band exciton relaxation is that the pump energy has to be higher than the sum of the energy of the first excited state of the Er^{3+} and the band gap of the Si NP (see expression 12.3 and Figure 12.3). Therefore the minimum pump energy to obtain Er^{3+} excitation through inter-band exciton relaxation is $E_{\gamma,minimum} = E_g + 0.8\ eV$.

$$E_\gamma > E_g + \Delta E,\ where\ \Delta E_{minimum} = 0.8\ eV \tag{12.3}$$

The Figure 12.6 shows the variation of the band-gap as a function of the Si NP diameter and the higher and lower pump photon energy levels obtained using as pump source an

Ar^{+} laser. At pump wavelength of 488.0 nm the Er^{3+} ions can be excited through inter and intra band transitions for all the co-doped films except for the $SE\phi 1.6$ that shown the lower fractional contribution of the fast component and that shows a special behavior with temporal components higher than the Er^{3+} only doped film, as it has been explained in the previous section. Taking into account the pump energy used and the Si NP band gap, in our pump range, only the $SE\phi 1.6$ could shows an excitation mostly by inter-band exciton recombination and the $SE\phi 2.2$, $SE\phi 2.2$, $SE\phi 2.8$, and $SE\phi 3.3$ show the two interaction mechanism, transfer energy from Si NP to Er^{3+} ions by inter-band exciton recombination and intra-band exciton relaxation transitions.

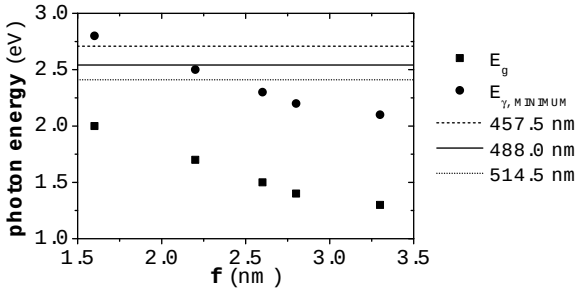

Figure 12.6: Band gap energy of the Si NPs (E_g) and the minimum pump energy to obtain Er^{3+} excitation through inter-band exciton relaxation ($E_{\gamma,minimum}$) as a function of the Si NP diameter. The photon energy associated to the pump wavelengths 457.5, 488.0 and 514.5 nm are represented as horizontal lines.

In order to corroborate this behavior we have compared the ratio of variation of the effective absorption cross section and the ratio of variation of absorption per Si NP in the pump range. The ratio of variation of the absorption cross section (σ_{ratio}) can be estimated by the slope relative of the PLE curves by the expression 12.4 (the estimation of the $Slope_{PLE}$ is detailed in the Appendix B). The ratio of variation of the absorption (α_{ratio}) is estimated from the absorption measurements and the density of Si NPs obtained in the Part 5 by the expression 12.5. The ratio of variation of absorption cross section is obtained by PLE measurements and therefore is related to the absorption cross section of the system Si NP-Er^{3+}, however the ratio in the absorption is only related to the presence of the Si NPs.

$$\sigma_{ratio} = \frac{\sigma_{514.5}}{\sigma_{457.5}} = (1 - Slope_{PLE})\frac{\varphi_{457.5}}{\varphi_{514.5}} \; where \; \varphi = pump \; flux \tag{12.4}$$

$$\alpha_{ratio} = \frac{\alpha_{514.5}}{\alpha_{457.5}[SiNPs]} \tag{12.5}$$

The Figure 12.7 shows the ratio of variation of the absorption cross section as a function of the ratio of variation in the optical absorption of the Si NPs. Two regimes can be defined below and above the thin film with Si NP diameter around 2.2 nm. When the slope of the curve changes it indicates that for the Si NPs of these sizes the increment of the absorption cross section is higher in comparison with the absorbtion and therefore it indicates that the number of photons generated at 1.53 μm is higher for the same number of incident photons. Therefore when the slope of the curve of the Figure 12.7 increases the excitation mechanism as exciton relaxation through intra-band transitions are playing a stronger role and more than one photon at 1.53 μm per incident photon in the visible can be generated increasing the ratio between absorption cross sections. In fact the thin films within Si NPs with diameters higher than 2.2 nm, the condition to observe Er^{3+} excitation through intra-band exciton relaxation (expression 12.3) is satisfied for all the pump wavelength range.

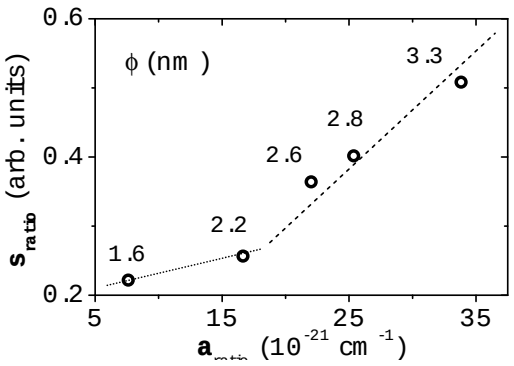

Figure 12.7: Ratio of variation of the absorption cross section as a function of the ratio of variation in the optical absorption of the Si NPs per Si NP. The diameter of the Si NPs is indicated with numbers.

In summary, when the pump photon energy range is fixed by the manufacturing requirements it is possible to establish an adequate Si NP size to obtain the more efficient transfer process, i.e. Er^{3+} excitation through inter-band exciton recombination, thanks to the contact and de-tuning the probability of back-transfer mechanism not allowing the exciton intra-band transitions.

12.5 Conclusions

Due to the maximized contact of the Er^{3+} ions and the Si NPs a modeling of the two interaction mechanism related to the Si NP quantum properties and internal transitions of the excitons in the energy levels of the Si NPs. The high PL emission efficiency observed for the Si NP-Er^{3+} extreme coupling thin films is related to maximized contact that

allows to select the most efficient transfer process by Auger recombination of the excitons in the Si NPs that are impossible to reach by 3D random dopant distributions. The Er^{3+} excitation through intra-band exciton relaxation increases as a function of the Si NP size being the unique excitation mechanism in the thin film within the larger Si NPs. However the intra-band des-excitation mechanism are also responsible for the back-transfer efficiency. As a consequence it can be reduced to zero when the Si NP ban-gap is close to the pump wavelength. The SSQC phenomena is observed for first time in amorphous silicon Si NPs and it can be tuned with the relation between the pump photon energy and the band-gap energy. The SSQC phenomena and the high density 2D Si NP distributions with separation between Si NPs below the 1 nm (detailed in the Chapter 6) shows that this amorphous nanostructures are specially useful to use as photon absorbers and carrier generators for application in solar cells.

Chapter 13

Small a-Si nanoparticles: special features

In the Chapter 12 the Er^{3+} and Si NP co-doped a-Al_2O_3 thin films within the smallest Si NPs shows null back-transfer processes. Controlling the back-transfer phenomenon is mandatory to obtain gain and improve the emission at 1.53 μm in the Er^{3+} and Si NP co-doped system. In this Chapter the PL temporal response of this thin film ($SE\phi$1.6) is thoroughly studied as a function of the defects in the interface a-Al_2O_3-Silicon, the Si NP size and the deposition conditions.

13.1 Introduction

Controlling the surface properties of the Si NPs could be a route to improve their emission efficiency and the transfer energy exchange from Si NPs to Er^{3+} ions. It has been shown how the defects generated by impact ionization reduced the number of Er^{3+} ions available for the Si NPs mediated luminescence. [40] This reduction on the Er^{3+} and Si NP pair coupling make impossible to achieve gain through Er^{3+} excitation by Si NPs. Therefore a high accuracy control on the Si NPs surface defects and interface Si NPs-host is a mandatory requirement to obtain large Er^{3+} excited fractions.

In order to reduce the number of defects and impurities on the Si NP surface, the in situ formation and deposition of dopants could be the key to optimize the number of Er^{3+} ions available. On the other hand use a host with better interfacial properties will reduce the Si NP surface defects inherent to as grown deposited Si NPs. The Si-Al_2O_3 interface has shown to be more robust and with lower number of defects than the Si-SiO_2 interfaces.[78, 79] Therefore the surface defects of Si NPs embedded on a-Al_2O_3 are expected to be reduced in comparison with a SiO_2 host and the efficiency of the energy transfer process improved.

In the Chapter 12 the back-transfer phenomenon of energy transfer from the Er^{3+} ions to the Si NPs has been analyzed observing a negligible back-transfer in the case of the $SE\phi 1.6$ thin film. Now in this Chapter we study the lifetime enhancement observed in this thin film and its dependence on the surface defects, Si NP size and deposition conditions.

13.2 Nanoparticle size: lifetime enhancement

In the Chapter 11 the Figure 11.4 shows the Er^{3+} 1.53 μm PL maximum intensity peak dependence on the average diameter of the Si NPs. All the co-doped films show PL intensity enhancement, and the PL peak intensity of the $SE\phi 1.6$ increases as much as factor 60 at the non resonant pump wavelength of 457.9 nm (see Figure 11.3). The $SE\phi 1.6$ thin film corresponds to the Er^{3+} and Si NP co-doped a-Al_2O_3 thin film with the smallest embedded Si NPs, thus the absolute absorption of the thin film at this wavelength is the lower of all the films. As a result the observed PL intensity enhancement has to be related to an improvement either in the lifetime or in the excited Er^{3+} fractions. In this case both occur.

The Figure 13.1 shows the PL normalized intensity decay curves for the Er only doped film and the co-doped films pumped at 488.0 nm. The lifetimes values obtained are very short, from 0.605 to 0.098 ms for the co-doped thin films and 0.489 ms for the Er^{3+} only doped film. The measured lifetimes depend on the non radiative channels by the

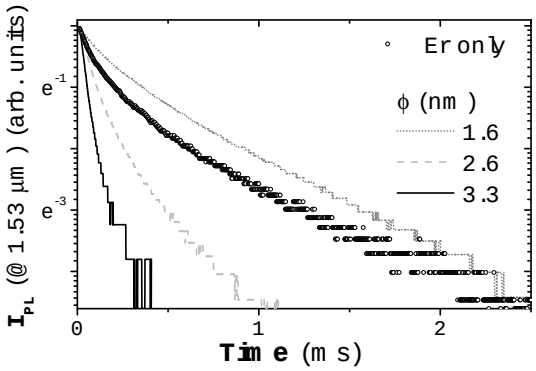

Figure 13.1: Normalized photoluminescence intensity at 1.53 μm decays pumping at resonant conditions at 488.0 nm and at 1.5W of power for the thin films with and Er areal content of 8.3 10^{13} atm/cm^2. Energy density .

expression:

$$\frac{1}{\tau_{measured}} = \frac{1}{\tau_{rad}} + \frac{1}{\tau_{non-rad}} \tag{13.1}$$

where $\tau_{measured}$ is the measured lifetime, τ_{rad} is the radiative lifetime and $\tau_{non-rad}$ is the non-radiative lifetime. Previous works on Er^{3+} doped a-Al_2O_3 show that all the Er^{3+} deposited by PLD in as grown thin films are optically active [16] however there are a high number of non-radiative channels in the as grown thin films that can be removed by post-deposited heat treatments. REF AmeliaYB Thus, the existence of these non-radiative decay channels justified the short $\tau_{measured}$ value obtained in the as grown thin films. However all the co-doped films show a reduction on the lifetime due to the interaction with the Si NPs except the $SE\phi 1.6$ whose **lifetime is surprisingly enhanced with respect the Er^{3+} only doped film lifetime**. The reduction of the lifetime is the usually observed phenomenon and it was justified by presence of the Si NPs that act as non-radiactive channels for the Er^{3+} ions or by the Purcell effect, where the Er^{3+} lifetime is reduced because is localized closer to an index contrast interface SiO_2-Si NPs. In our deposition configuration the Er^{3+} ions are located on the surface of the Si NPs thus the Purcell effect doesn't play any role. However, the function of Si NP as non-radiative channel in a Er^{3+}-Si NP contact configuration is strongly asserted and the transfer energy from Er^{3+} to Si NPs through intra-band transitions is highly efficient as shown in the previous Chapter 12. In fact, the back-transfer phenomena from Er^{3+} ions to Si NPs seems to be uncontrollable and unavoidable linked to the transfer energy from the Si NPs to the Er^{3+} ions. Consequently the $SE\phi 1.6$ lifetime enhancement suggests that the back-transfer phenomenon requires and intermediate entity.

Si NP pasivation studies in Si-rich oxide show that the Si NP presence influence the Er^{3+} properties acting a des-excitation non-radiative route through silicon dangling bonds.[118] Therefore the lifetime behavior could be explained by the variation of the number of the silicon dangling bonds in the surface of our amorphous Si NPs as function of the Si NP size. Larger Si NPs have a larger a-Si/a-Al_2O_3 surface and thus a larger number of dangling bonds that imply a larger number of Er^{3+} non-radiactive channels shortening the Er^{3+} decays. Assuming the role of dangling bonds as non-radiative channels we can considerer that for the in the case of the $SE\phi 1.6$ the dangling bonds are reduced due to the small size of the Si NPs.

Estimations about probabilities of defects interaction and recombination in crystalline Si NPs can give us an estimation of their properties and the relation with the dangling bonds. Let's suppose a Si NP with a dangling bond. When the Si NP absorbs a photon an electron and a hole are generated. Then there is a probability of interaction between the neutral dangling bond and the electron-hole pair generated. This probability is expressed as the the capture cross sections that have been calculated by Delerue et al.[42] and it depends strongly on the size. The capture cross section is comparable to the exciton radiative recombination in the Si NP. The non-radiative capture is higher than the radiative recombination and thus dangling bonds are likely to quench the photoluminescence. However only for small crystallites (GAP higher than 2.6 eV) the non-radiative capture on a silicon dangling bond becomes less efficient that the intrinsic radiative recombination. Therefore the presence of one dangling bond at the surface of a crystallite must destroy the radiative de-excitation properties for the larger Si NPs while for the smaller ones the electron-hole pair is not affected. If the interaction between the Si NPs radioactive states with silicon dangling bonds is reduced then the routes of interaction between Er^{3+} and dangling bonds are affected and then the lifetimes could show different dynamics. These arguments are corroborated by the model developed by Allan et al.[36] for amorphous Si NP, where he energy levels as a function of the Si NP size confinement energy diagram shows a intermediate defect level associated to the presence of dangling bonds (strongly localized states). This intermediate state disappears for Si NPs with sizes below 1.5 nm in not passivated thin films. That is a similar value of the Si NPs embedded in the $SE\phi 1.6$ thin film.

The discussion above explains why the films with the smaller Si NPs show longer lifetimes. But, why is the lifetime value for the $SE\phi 1.6$ film higher than the lifetime value for the Er only doped film? If the dangling bonds are reduced and this does not affect the energy exchange, why are not the Er^{3+} ions of the $SE\phi 1.6$ affected in the same way by the host defects?.

The superposition postulate [139] of the quantum mechanics, the states of a physical

system belong to a vector state and, consequently, can be linearly overlapped. Therefore the quantum probability of interaction between an electron in a Er^{3+} ion and the exciton resides in the Si NP, the Si NP surface dangling bonds or the host defects that can be defined as the integration in all the space of the superposition of the individual states. We can define the wave function for the electron at the first excited state of the Er^{3+} ion as $\mid \Psi_{Er} >$, the wave function for the exciton as $\mid \Psi_{NP} >$, the wave function for the silicon dangling bond as $\mid \Psi_{Dangling} >$ and the wave function of a host defect as $\mid \Psi_{Host-defect} >$. Also we can define the interaction operator as (Θ). The probabilities (P) of interaction are proportional to the application of the quantum operator of the interaction and the quantum states involved by:

$$\begin{aligned} P_{Dangling} &=<\mid \Psi_{Er} \mid \Theta \mid \Psi_{Dangling} > \\ P_{Host-defect} &=<\mid \Psi_{Er} \mid \Theta \mid \Psi_{Host-defect} > \\ P_{NP-exciton} &=<\mid \Psi_{Er} \mid \Theta \mid \Psi_{NP} > \end{aligned} \tag{13.2}$$

These probabilities (expressions 13.2) are defined as the integral in all the space of the states implied and the interaction operator $P = \int_V \Psi_{e^- - Er}(\Theta \Psi_{defect})\, dV$. They are strongly dependent on the spatial distribution of the states functions. The host defects and silicon dangling bonds are very localized states and then only are going to affect to the Er^{3+} ions localized closer them. In the Chapter 9 it has been demonstrated that only the Er^{3+} in contact with the Si NPs are contributing to the PL emission, then the Er ion is localized in the Si NP surface and then it interacts preferentially with the silicon dangling and the electrons in the Si NPs. In fact the Er ion is dissociate itself of the host defects, being affected only by the interaction with the Si NP states and the dangling bonds ($P_{Host-defect} << P_{Dangling},\ P_{NP-exciton}$). In the case of the thin films embedded large Si NPs, the dangling bonds are going to interact with the Er^{3+} as a non-radiative channel and then a reduction in the lifetime is observed. However in the co-doped thin films with the smaller Si NPs embedded the surface dangling bond states disappear [36] and then the only interaction route are the electrons in the Si NPs and controlled by the confinement states reducing the non-radiative des-excitation routes and the lifetime enhancement occurs.

In conclusion the extreme contact of the Er^{3+} in our thin films causes that the interaction with the Si NP is preferential and that the Er ion is dissociate of the host defects, being affected only by the interaction with the Si NP states and the dangling bonds. The presence of dangling bonds reduces the Er^{3+} decays in the thin films with large Si NPs within and plays the role of interaction entity in the back-transfer phenomenon. The strong reduction of the dangling bonds for small Si NPs and the strong location of their states can be used to decrease the radiative recombination rate of the Er^{3+} ions as it has been observed in the $SE\phi 1.6$ thin film.

13.3 Control of defects by deposition conditions: lifetime enhancement control

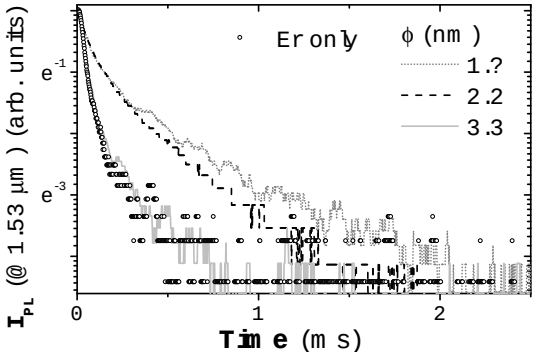

Figure 13.2: Normalized photoluminescence intensity at 1.53 μm decays pumping at resonant conditions at 488.0 nm and at 1.5W of power for the thin films with and Er areal content of 5.0 10^{13} atm/cm^2. Energy density .

In the previous section we have showed that the number of dangling bonds or Si NP surface defects are reduced for a specific Si NP size range. However in the optimization of Er^{3+} and Si NP co-doped system it is required a optimization of defects and improvement of lifetime for the largest possible number of Si NP sizes in order to allow larger degree of freedom in the nanostructures design specially in the selection of the absorption of the system. It has been demonstrated that the ion bombardment or ion irradiation can reduced the number of Er^{3+} ions available through indirect excitation by Si NPs.[40] The high kinetic species generated in the plasma plume during the PLD process can damaged the Si NPs surface in the Si NP covering process creating a large number of surface defects and dangling bonds. In order to determine the influence of the deposition energy on the Si NP surface defects we compare the lifetime behavior observed for the thin films produced at 2.0 mJ/cm^2 energy density and 2.3 mJ/cm^2 energy density. The Figure 13.2 shows the PL decay curves obtained at 1.53 μm and pumping at 488.0 nm for $SE\phi 1.0$, $SE\phi 2.2 - B$, and $SE\phi 3.3 - B$ co-doped thin films and their Er^{3+} only doped film reference $ErRef2$. The lifetime enhancement is not only observed for the thin film co-doped by the smallest Si NP size and the $SE\phi 2.2 - B$ within Si NP with 2.2 nm as average diameter shows a decay curve slower than the Er^{3+} only reference film. In fact the $SE\phi 3.3 - B$ embedded Si NPs with a average diameter of 3.3 nm shows a similar behavior than the Er^{3+} only doped film and the lifetime is not reduced in comparison with the Er^{3+} only doped film. Consequently the surface defects depend not only on Si NP size, but also on the deposition conditions that control the kinetic energy of the species with which the atoms and ions reach the substrate. Therefore selecting the correct deposition conditions is possible to

reduce the back-transfer phenomena and induce a enhancement of the lifetimes values for different sizes due to the strong localization on the Si NP surface of the function states of the excited Er^{3+} ions that interact preferentially with the surface states of the Si NPs. Similar effects are expected by pasivation of defects through annealing but this offers in situ control.

13.4 Conclusions

For first time, an enhancement on the Er^{3+} lifetime has been observed in Er^{3+} and Si NP co-doped system in comparison with the Er^{3+} only doped film. The Er^{3+}-Si NP extreme coupling regime allows to improve the Er^{3+} lifetime due to the localization of the excited Er^{3+} on the Si NP surface that preferentially interacts with the Si NP exciton or surface defects instead with the host defects. The surface defects and the back-transfer phenomenon responsible of the shortening the decay times can be controlled with the host composition, the Si NP size and the energy density used to ablated the targets. Maximizing the Er^{3+} and Si NP contact it is possible to select the chemical environment and the quantum environment controlling the Er^{3+} quantum radiative or non-radiative channels' probabilities. This procedure opens a high accuracy new route to improve and to maximize the emission at 1.53 μm of the Er^{3+} and Si NP co-doped systems.

Chapter 14

Fractions of excited Er^{3+} higher than 50%.

Prior Chapters as 11 and 12 show the extreme coupling regime properties and its relation with the Er^{3+}-Si NP interaction mechanisms. We have demonstrated that in thin films with maximized contact the complexity of the Föster resonance energy transfer (FRET) is eliminated and the temporal response depends only on the quantum properties of Si NPs. The challenge is obtain fractions of excited Er^{3+} higher than 50% in order to obtain population inversion and analyze the extreme coupling regime as the route to achieve gain through Er^{3+} indirect excitation. In this new Chapter the Er^{3+} excitation dynamics and the required properties to achieve gain using well know and reliable models are studied. It is shown that Er^{3+} excited fractions up to 55% can be reached at low pump powers in Er^{3+}-Si NP extreme thin films without cooperative up-conversion and excited-state absorption.

14.1 Introduction

The special properties of the Er^{3+}-Si NPs thin films in the extreme coupling regime suggest that it is the unique doping route towards a 100% of excited Er^{3+} fractions. Fractions of excitable Er^{3+} of few percents have been usually obtained [22, 140, 137] and only recently a 23% has been reported,[23, 136] whereas a minimum of 50% of Er^{3+} population inversion is required to achieve gain. The short range Si NP-Er^{3+} interaction was the main limiting factor that required thin films with a high density of Si NPs to increase the percentage of Er^{3+} in contact with the Si NPs. [37]. Also a fine nano-engineering of the dopants location is required in order to place the Er^{3+} ions close to the NP surface.[25] Our work shows how it is possible to nano-engine the doped material optimizing simultaneously the Er^{3+} and Si NP concentrations, Si NP sizes and positioning the Er^{3+} and Si NPs very closely on the nanometer scale. [24] Now we demonstrate that through Er^{3+}-Si NP extreme coupling we have solved the issue of low fraction of excited Er^{3+} and how we have obtained fractions of excited Er^{3+} higher than 50% at low pump powers. The maximum fraction of excited Er^{3+} will be also discussed.

A laser gain medium is a medium which can amplify the power of light, desirable properties include: a high transparency of the host medium in this wavelength region, a pump wavelength for which a good pump source is available with an efficient pump absorption and for high gain, low threshold pump power that implies a high product of emission cross section (σ) and upper-state lifetime (τ). The a-Al_2O_3 shows excellent properties as a broad and hight transparency in the infrared (explained in detail in Chapter 2). Furthermore the incorporation of Si NPs increased the total absorption of the thin films in the visible that it is a good wavelength range for integrated LED pump sources. Therefore, in order to evaluate the performance of our thin films as gain material we estimate the effective excitation cross section of the Er^{3+} and Si NPs and the pump energy required to achieve the inversion of population defined by the pump threshold beyond which the 50% fraction of excited Er^{3+} is obtained.

14.2 Er^{3+} excitation and des-excitation dynamics

In the Chapter 11 it has been shown that the temporal behavior and lifetimes are independently of resonant or non resonant pump conditions. In order to use a pump wavelength with a broad range of pump power, the PL measurements where performed at 488.0 nm pump wavelength using an Ar^+ ion laser at 300 mW and 1.5 W pump powers that correspond to pump fluxes of 1.2 10^{20} $s^{-1}cm^{-2}$ and 6.0 10^{20} $s^{-1}cm^{-2}$ (area of the spot beam $\sim$ 0.4 mm^2), respectively. Taking into account the relation between the interaction mechanisms and the temporal response modeled by a multi-exponential decay with $n = 2$ described in the Chapter 12, the analysis of decay times and rise times was realized assuming this multi-exponential temporal behavior.

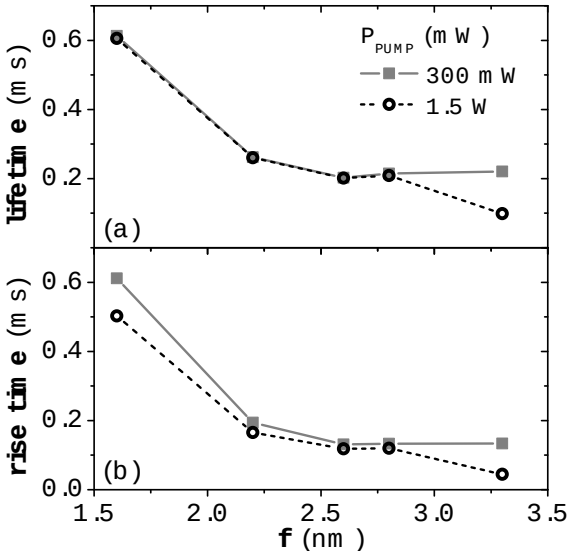

Figure 14.1: Figure 14.1.a.- Lifetimes values at 0.3 and 1.5 W pump powers for the co-doped a-Al_2O_3 films. Figure 14.1.b.- Rise times values at 0.3 and 1.5 W pump powers for the co-doped a-Al_2O_3 films.

Figure 14.1.a shows the Er^{3+} lifetimes values obtained for the Er^{3+} and Si NPs co-doped films as a function of the size of the Si NPs at the two different pump powers. The reduction of the lifetimes when the size of the Si NPs is increased was related with the increase of the number of the silicon dangling bonds that act as no-radiative channels and the back-transfer phenomenon that is increased when the energy band gap is reduced. Similar decay times are obtained for all the co-doped films independently of the pump power used except for the thin film with the larger Si NPs. As a result, no Er^{3+} quenching phenomena as cooperative up-conversion (CUP) phenomena or Er^{3+} excited state absorption (ESA) is observed except for the $SE\phi 3.3$ thin film. Taking into account that the Er^{3+} distribution in the plane is the same for all the thin films independently of the Si NP size, the differences on the Er^{3+} lifetime value with the pump power for the $SE\phi 3.3$ can be related to the Auger Er^{3+} des-excitation phenomenon or with an increase in the ESA due to a high ratio $[Er]/[Si\ NP]$.[141] However, the fact that the PL shows no saturation and the films with higher PL intensity at non resonant wavelength (476.5nm) than at the resonant wavelength (488.0 nm) suggest that ESA is not the main mechanism.

The rise time values decrease when the excitation pump power increases (Figure 14.1.b). A reduction of the rise time values while the des-excitation rates are maintained implies a higher excitation rates. Consequently an increase in the excited Er^{3+} fraction

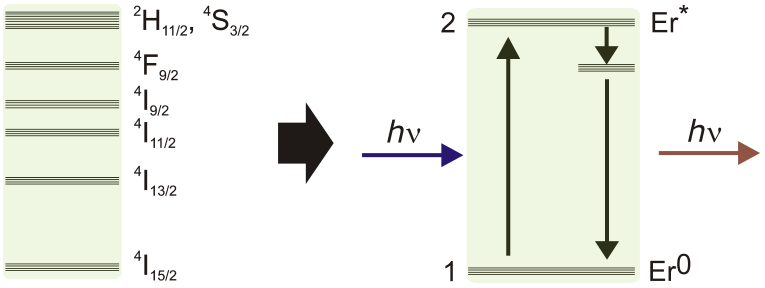

Figure 14.2: Schematic representation of Er^{3+} ions as two-level system.

with the pump power is expected and a larger value of effective absorption cross sections.

14.3 Er^{3+} effective excitation cross sections

In laser physics the transitions cross sections are used to quantify the likelihood of optically induced transition events, as for example the absorption or stimulated emission. For a laser ion in a certain electronic state, the transition rate (in events per second) is given as the corresponding cross section (σ) times the photon flux (φ) (see expression 14.1).

$$R = \frac{1}{\tau} = \sigma\varphi \tag{14.1}$$

Therefore it is possible to define an absorption cross section and an emission cross section. Since the natural emitters show fluctuations in the definition of the energy levels, as the Er^{3+} ions that show Stark splitting thus one electronic level involves several Stark manifolds, is convenient to use the effective cross sections which are the averages of the cross sections of different sub-levels. The concept of effective cross sections is very useful, particularly for media with strong spectral broadening as the Er^{3+} in our a-Al_2O_3. An optimized material for gain applications requires high absorption and emission effective cross sections in order to achieve a high ratio of absorption and emission events and because the gain is proportional to the effective excitation cross section.[142]

In the Er^{3+} and Si NP co-doped systems the Si NPs are the absorbers and the Er^{3+} ions are the emitters. We can only obtain information about the Er^{3+} photoluminescence dynamics because the amorphous Si NPs are dark. Considerer the Er^{3+} ions isolated and assuming their energy levels system as a two level system, discarding the presence of the Si NPs on the Er^{3+}-Si NPs doped system. The Figure 14.2 shows a schematic representation of the Er^{3+} ions levels as two level system where the state 2 corresponds to the excited Er^{3+} state (Er^*) and 1 to the Er^{3+} ground state (Er^0).[122, 133] We can write the rate

equation for the generation of an excited Er^{3+} as follows:

$$\frac{dN^*_{Er}}{dt} = \sigma_{eff}\varphi(N_{Er} - N^*_{Er}) - \frac{N^*_{Er}}{\tau_{PL}} \tag{14.2}$$

where N^*_{Er} is the number of Er^{3+} in the excited state, φ is the pump photon flux, N_{Er} is the total concentration of Er^{3+}, τ_{PL} is the lifetime of the Er^{3+} in the excited state (taking into account the radiative and non radiative channels) and σ_{eff} is the effective excitation cross section. This effective excitation cross section represents the cross section associated to indirect excitation process of the Er^{3+} through the Si NPs. Solving the equation 14.3 the temporal evolution of the number of excited Er^{3+} is:

$$N^*_{Er} = \frac{\sigma_{eff}\varphi\tau_{PL}N_{Er}}{\sigma_{eff}\varphi\tau_{PL}+1}\{1 - e^{-[(\sigma_{eff}\varphi+\frac{1}{\tau_{PL}})t]}\}. \tag{14.3}$$

Taking into account that the photoluminescence (PL) intensity has to be proportional to the number of excited Er^{3+}, the behavior of the PL dynamic response is parameterized as the increase of the excited Er^{3+} population. Thus the excitation rate is the exponent of the exponential decay, obtaining:

$$R_{rise} = \sigma_{eff}\varphi + \frac{1}{\tau_{PL}} \tag{14.4}$$

Since the excitation rate is the inverse of the rise time (τ_{rise}), the effective excitation cross can be estimated by the expression 14.5.

$$\sigma_{eff} = \frac{1}{\varphi}(\frac{1}{\tau_{rise}} - \frac{1}{\tau_{PL}}) \tag{14.5}$$

Figure 14.3 shows the σ_{eff} as a function of the Si NP size at a fixed pump power of 1.5 W that corresponds to 6.0 10^{20} $s^{-1}cm^{-2}$. In addition, the optical absorption values at 488 nm obtained for the Er^{3+} and Si NPs co-doped films are represented in the right axis (values obtained in the analysis of the Chapter 5.3.1). At 1.5 W pump power (φ = 6 10^{20} $s^{-1}cm^{-2}$ $cm^{-2}s^{-1}$), the values obtained are close to the excitation cross sections for the Si NPs ($\sigma_{eff-NP} \sim 10^{-17}$ cm^2) for all Si NP sizes and four orders of magnitude higher that the emission cross section expected for Er^{3+} doped Al_2O_3 ($\sigma \sim 6$ 10^{-21} cm^{-2}).[143] The σ_{eff} is not the same for all the thin films and a clear increase with the Si NP size is observed. The behavior of the optical absorption and the σ_{eff} as a function of the Si NP size is the same indicating a direct relation between the absorption of the Si NPs at 488 nm and the observed σ_{eff} for the Er^{3+}. The absorption is only due to the presence of the amorphous Si NPs embedded on the a-Al_2O_3 host and the increase of its value as a function of the size is related to the shift to higher Si NP gap energies when the Si NPs

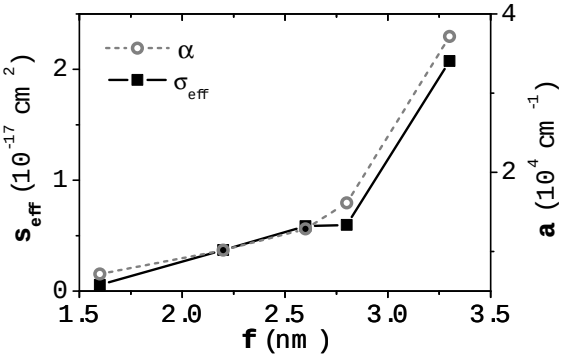

Figure 14.3: Left axis: Er^{3+} effective absorption cross sections for an excitation pump power of 1.5W. Right axis: optical absorption for the Er^{3+} and Si NP co-doped a-Al_2O_3 films caused by the presence of the Si NPs.

size is reduced. Thus, a physical property dependent in the quantum properties of the Si NPs at 488.0 nm is transferred to the Er^{3+} ions due to the extreme coupling and contact between Er^{3+} ions and Si NPs.

Einstein developed a quantum picture of the absorption and emission of radiation. His analysis introduces the Einstein A (A_E) and Einstein B (B_E) coefficients associated to the spontaneous and stimulated emission and absorption.[142, 144] It is found that the stimulated emission coefficient should be proportional to the coefficient of the absorption process for the same transition. That rule does not apply to effective cross sections, where it is necessary to apply the McCumber theory where there is a direct relation between the effective absorption cross section an the emission cross section ($\sigma_{emission}(w) \propto \sigma_{absorption}(w)e^{\hbar w/K_BT}$).[145] Therefore in a co-doped system where the Si NPs are the absorbers and the Er^{3+} ions the emitters a direct relation between the effective excitation cross section of the Er^{3+} ions and the effective absorption cross section of the Si NPs which is directly related to the Si NP optical absorption of the Si NPsis expected. However, to our knowledged, variation of the Er^{3+} effective excitation cross section as a function of Si NP size has not been reported yet in thin films with Si NPs of different sizes and with the same crystallinity quality and less related to the Si NP optical absorption. Furthermore, the direct relation of Er^{3+} effective excitation cross section at 1.53 nm and the Si NP absorption at 488.0 nm has never been proven experimentally.

14.4 Fractions of excited Er^{3+} higher than 50%.

In this section we discuss a model for the Er^{3+} and Si NP interaction based in well known previous works.[22, 134, 133] The interaction model reported by Pacifici et al. [134] applied the rate-equation analysis to the Si nanocrystal-Er^{3+} material system, fundamentally

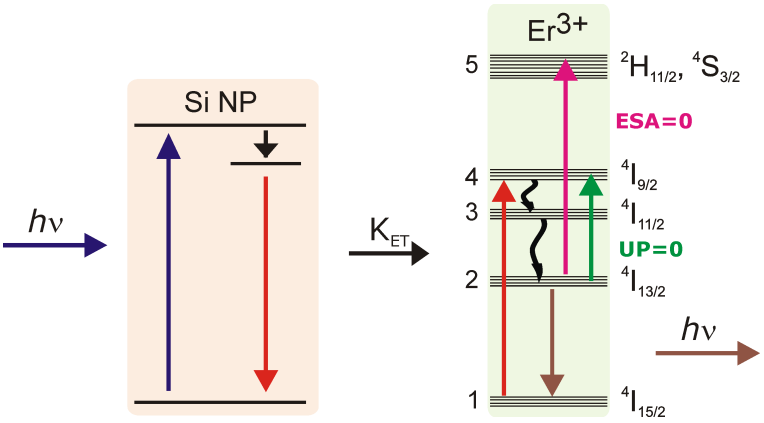

Figure 14.4: Schematic description for the interaction model between Si NPs and Er^{3+} ions.

based on the one of five levels of Er^{3+} ions interacting with a quasi-two-level scheme of Si NPs (see Figure 14.4). In this model the coupling constant is the same for all of the Si NPs interacting with Er^{3+}, thereby assuming that each Si NP is separated from Er^{3+} by the same distance. These conditions are perfect for our extreme Er^{3+}-Si NP coupling regime, indeed the Er^{3+} ions show the same environment and the Er^{3+} emitted are in contact with the Si NPs, therefore the same coupling constant is expected for all Er^{3+}-Si NP couples.

The Er^{3+} concentration values of the thin films analyzed in the model developed in the reference [134] are large and as a result the cooperative up-conversion is present and it is a energy loss path that tended to mask the underlying physics. Since the no existence of differences on the Er^{3+} lifetime with the pump flux prove the no contribution of phenomena as cooperative up conversion (shown in the Section 14.2). In our case, the cooperative up-conversion is not a complicating factor due to the nano-structuring in the depth profile of the Er^{3+} ions distributed in layers and only differences in the $SE\phi 3.3$ that have been related to hot carriers generation.[17] Therefore, at the pump energy range used the CUP or ESA can be neglected and we are going to considerer that their effects are taken into account with the experimental Er^{3+} lifetime instead of the intrinsic decay. As the non radiative transitions ($^4H_{11/2} \longrightarrow ^4 I_{9/2}$-5 to , $^4I_{9/2} \longrightarrow ^4 I_{11/2}$-4 to 3 and $^4I_{11/2} \longrightarrow ^4 I_{13/2}$-3 to 2) are fast in the nano-second range (10, 10 and 2.5 ns respectively)[22] the Er^{3+} ions excited in the higher energy excited states quickly relax and these relaxed ions contribute to increase the Er^{3+} population at the first excited state ($N_3, N_4, N_5 \longrightarrow N_2$). Therefore we can considerer the Er^{3+} as a quasi-two level system obtaining the Er^{3+} rate equation:

$$\frac{dN_2}{dt} = K_{ET} N^*_{NP} N_1 - \frac{N_2}{\tau_{PL}} \tag{14.6}$$

where the N_2 is the Er^{3+} population in the first excited state, the N_1 is the number of Er^{3+} ions in the ground state, K_{ET} is the energy transfer coefficient and the N^*_{NP} is the Si NPs population in the excited state.

Taking into account that $N_3, N_4, N_5 \longrightarrow N_2$ then $N_{Er} = N_2 + N_1$ and in the steady state conditions (dN_2/dt=0), it is possible to determine the excited Er^{3+} fraction solving the equation 14.6. The solution shows that the fraction of excited Er^{3+} is given by the expression 14.7.

$$f_{Exc-Er} = \frac{N_2}{N_{Er}} = \frac{1}{1 + \frac{1}{\tau_{PL} K_{ET} N^*_{NP}}} \tag{14.7}$$

Furthermore we can introduce the σ_{eff} of the Er^{3+} ions in the equation 14.7, obtaining the fraction of excited Er^{3+} as a function of the pump flux and the temporal response of the Er^{3+} ions (expression 14.8).

$$K_{ET} N^*_{NP} = \sigma_{eff} \varphi \implies f_{Exc-Er} = \frac{\varphi}{\varphi + \frac{1}{\sigma_{eff} \tau_{PL}}} = \frac{1}{1 + \frac{\tau_{rise}}{\tau_{PL} - \tau_{rise}}} \tag{14.8}$$

Figure 14.5 shows the fractions of excited Er^{3+} ions for the Er^{3+} and Si NP co-doped a-Al_2O_3 thin films pumping at 1.5 W as a function of the average diameter of the Si NPs. The excitable Er fractions are close to the Si NPs coverage, indicating that the Er^{3+} ions directly in contact with the Si NPs and localized at the surface are the preferentially excited and the main contributing to the PL emission. This is confirmed by the fact that for the co-doped films the maximum of the PL spectra is shifted to the IR and the bandwidth decreases when compared to the Er only doped film PL spectrum, pointing out that the PL emission in these films comes mainly from Er^{3+} localized in Si-O environment rather than in an Al-O environment, which is consistent with the Er located at the surface of the Si NPs. Therefore the excited Er^{3+} fractions seems to be controlled by the percentage of Er^{3+} ions in direct contact with the Si NPs and it can explain the low percentage of Er^{3+} ions observed in previous works.

The fractions of excited Er^{3+} ions vary from 17% to the 56% obtaining excited Er^{3+} fractions higher than the 50% in not PL saturable thin films. Since the more efficient excitation mechanism is the inter-band exciton recombination that requires physical contact between Er^{3+} and Si NPs, the coverage area should indicate the maximum value of fraction of excited Er^{3+} achievable by this mechanism. Therefore the maximum fractions of excited Er^{3+} achievable through inter-band exciton recombination ranges from 33% to 60%. However, other mechanism as excitation through exciton intra-band relaxation have been proved to excite also the Er^{3+} ions therefore the Föster RET transfer can play a role when the Er^{3+} in contact is saturated. In conclusion the coverage establishes the

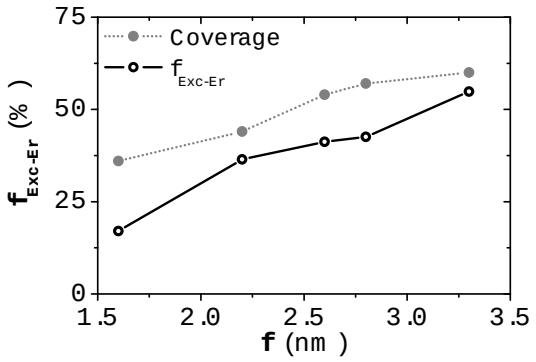

Figure 14.5: Fractions of excited Er^{3+} ions for the Er^{3+} and Si NP co-doped a-Al_2O_3thin films at pump power condition of 1.5 W as a function of the diameter of the Si NPs. The coverage area of the 2D-distributions of Si NPs corresponding to the different thin films is also shown.

minimum of fraction of excited Er^{3+} that can be achievable by the most efficient transfer process, through inter-band exciton recombination, and thus the fraction of Er^{3+} that can be excited at low pump powers. However to establish the maximum fraction of excited Er^{3+} achievable it is necessary to take into account the distance dependence of the other mechanisms.

14.5 Maximum excited fractions

Taking into account the expression 14.7 we can model the maximum fraction of excited Er^{3+} achievable by the Si NPs (f_{Max-Er}). The maximum fraction of excited Er^{3+} is defined as the fraction of excited Er^{3+} that we can obtain when the pump flux reachable is infinite:

$$f_{Max-Er} = \lim_{\varphi \to \infty} f_{Exc-Er}. \tag{14.9}$$

However we need to obtain the density of excited Si NPs and its dependence on the pump flux. The interaction model defined in the Section 14.4 the Si NPs act as donors and the Er^{3+} ions as acceptors. We defined the energy levels and parameters of the donors that are described as an quasi-two level system. A Si NP absorbs the incident pump photons with an efficiency that it is related with their absorption cross section (σ_{NP}) and the pump flux (φ). The exciton generated will recombine and transfer energy to a close Er^{3+} ion with an interaction efficiency defined by the energy transfer coefficient K_{ET}. The lifetime associated to the Si NPs is defined as τ_{NP}. Therefore the rate equation for the Si NPs is

defined as:

$$\frac{dN_{NP}^{*}}{dt} = \sigma_{NP}\varphi N_{NP}^{0} - \frac{N_{NP}^{*}}{\tau_{NP}} - K_{ET}N_1N_{NP}^{*} \tag{14.10}$$

where N_{NP}^{*} is the Si NPs population in the excited state, N_{NP}^{0} is the density of Si NPs in the ground state and N_1 is the number of Er^{3+} ions in the ground state and that can be excited through the Si NPs. The total density of Si NPs is related with these two parameters by $[SiNPs] = N_{NP} = N_{NP}^{*} + N_{NP}^{0}$.

In the steady state conditions ($\frac{dN_{NP}^{*}}{dt} = 0$) the density of excited Si NPs is

$$N_{NP}^{*} = \frac{N_{NP}\ \varphi}{\varphi + \frac{1}{\sigma_{NP}\tau_{NP}} + \frac{K_{ET}N_1}{\sigma_{NP}}}. \tag{14.11}$$

Taking into account the expression 14.9 and 14.8, we can establish the relation between f_{Max-Er} and f_{Exc-Er} as follows:

$$f_{Exc-Er} = \frac{\varphi}{\varphi + \frac{1}{\sigma_{eff}\tau_{PL}}} = f_{Max-Er}\frac{\varphi}{\varphi + \frac{1}{\sigma_{eff}^{*}\tau_{PL}}} \tag{14.12}$$

redefine the effective excitation cross section σ_{eff}^{*}. Now we can insert the excited population of Si NPs given by the expression 14.11 into the equation 14.7 and rearrange the terms to obtain an sigmoidal curve of a two level system ($\frac{1}{1+x}$) in order to obtain the values of the parameter σ_{eff}^{*} and f_{Max-Er}. As a result the f_{Max-Er} is defined as follows:

$$f_{Max-Er} = \frac{1}{1 + \frac{1}{K_{ET}N_{NP}\tau_{PL}}}. \tag{14.13}$$

The energy transfer coefficient K_{ET} depends on the interaction distance from the Si NP to the Er^{3+}. Regarding our dopants spatial configuration distributed in a plane and where the Er^{3+} ions are deposited following the Si NPs formation we can define the energy transfer coefficient for every Si NP using cylindrical coordinates, the Si NPs lie on the plane z=0 and establishing the origin of the coordinates in the core of the Si NP. Two regimes are defined one that correspond to the Er^{3+} ions deposited on top of the Si NPs (K_1) and other to the Er^{3+} ions located in the a-Al_2O_3 in the intersticial spaces between adjacent Si NPs (K_2):

$$K_{ET}(\rho) = K_1(\rho) = K_0 \ when\ \rho \leq r_{NP} \tag{14.14}$$

$$K_{ET}(\rho) = K_2(\rho) = K_0 e^{-(\rho - r_{NP}/r_0)}\ when\ \rho \geq r_{NP}[22] \tag{14.15}$$

where r_{NP} is the radius of the Si NP and r_0 is the interaction distance defined by a Föster Resonance Energy Transfer that is the long-range interaction mechanism. K_0 is

defined as the transfer coefficient when the Er^{3+} ions are closets to the Si NPs that has been estimated in the literature as $K_0 = 3\ 10^{-15}\ cm^3\ s^{-1}$ for 3D dopants distribution. In order to estimate this parameter for a 2D dopant distribution we use the relation between the volume of one Si NP and its surface area $K_{2D,0} = \frac{Surface_{NP}}{Volume_{NP}} K_{3D,0}$ obtaining $K_{2D,0} = \frac{3}{r_{NP}} K_0$.

In order to estimate the maximum excited Er^{3+} fraction we have to integrate the fraction of Er^{3+} ions excited per Si NP in all the interaction area that it is defined by the the distance r_0 from the surface of the Si NPs. Therefore the maximum of fraction of excited Er^{3+} achievable through Si NPs by high density 2D-distributions is given by:

$$f_{Max-Er} = N_{NP} \int_0^{r_{NP}+r_0} \int_0^{2\pi} \frac{\rho d\rho d\theta}{1 + \frac{1}{K_{ET} N_{NP} \tau_{PL}}}. \tag{14.16}$$

Replacing the energy transfer coefficient in the equation 14.16 there are two terms that define the maximum Er^{3+} than could be excited through the Si NPs. The first term is the maximum Er^{3+} that could be excited by exciton inter-band recombination and the second term corresponds to the Er^{3+} excited through exciton intra-band relaxation or Föster interaction.

$$f_{Max-Er} = \frac{\pi N_{NP} r_{NP}^2}{1 + \frac{1}{K_{2D,0} \tau_{PL} N_{NP}}} + 2\pi N_{NP} \int_{r_{NP}}^{r_{NP}+r_0} \frac{\rho d\rho}{1 + \frac{1}{K_{2D,0} N_{NP} \tau_{PL} e^{-(\rho - r_{NP}/r_0)}}}. \tag{14.17}$$

Figure 14.6 shows the coverage area of the Si NPs and the maximum fraction of excited Er^{3+} achievable in our dopant distributions i.e. first term. The first term of the expression 14.17 shows similar values than the coverage, however taking into account the Er^{3+} localized in the a-Al_2O_3 that separates the Si NPs represents by the second term, fractions close to the 100% could be achieved at high pump fluxes (see Figure 14.6).

14.6 Conclusions

For the first time a direct relation between the optical absorption of the Si NPs and the effective excitation cross section of the Er^{3+} ions coupled to Si NPs has been observed experimentally. It proves that the physical properties and emission efficiency of the Er^{3+} only doped systems are different that the Er^{3+} and Si NP doped systems. Furthermore the Er^{3+} effective excitation cross section increases with the Si NP size observing a clear relation between the Er^{3+} temporal response and the quantum properties of the amorphous Si NPs. Fractions of excited Er^{3+} higher than the 50% has been obtained due to the maximized Er^{3+}-Si NP contact for low pump flux proving the extreme coupling between the Er^{3+} ions and the Si NPs. Fractions closer to the 100% are achievable due to the geometrical properties and the high spatial correlation of the two dopant 2D-distributions. This new nano-structured material is a suitable candidate as gain media at 1.53 μm pumping

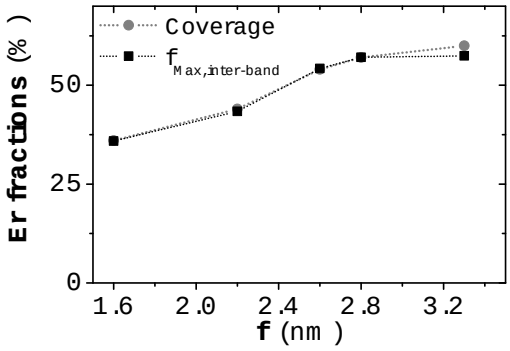

Figure 14.6: Maximum fractions of excited Er^{3+} ions for the Er^{3+} and Si NP co-doped a-Al_2O_3thin films at pump power condition of 1.5 W as a function of the diameter of the Si NPs. The coverage area of the 2D-distributions of Si NPs corresponding to the different thin films is also shown.

in a broad band in the visible using low pump fluxes in waveguide configurations.

Part V

Low temperature thermal post-processing

Chapter 15

Si NPs-Er^{3+} interaction upon low temperature thermal processing

The Er^{3+} ions are active after de deposition, but generally thermal treatments are applied to Er^{3+} doped a-Al_2O_3 thin films to reduce the host defects and improve the emission at 1.53 μm. In the previous Section 8.1 it has been shown that is possible to obtain efficient energy transfer between Si NPs and Er^{3+} ions in Er^{3+} - Si NPs co-doped a-Al_2O_3 films without the need for post-deposition annealing and this energy transfer process depends critically on the Si NPs - Er^{3+} separation and it is optimized for a characteristic interaction distance below 1 nm. [24] In this Chapter an annealing procedure to further enhance the photoluminescence (PL) performance (intensity and lifetime) of the Er ions in the films are investigated and discussed. Note that as a contrast to the synthesis methods in which annealing was required to form the Si NPs, in this work the Si NPs are already present in the films before annealing.

The thermal treatment studied in order to optimize the PL emission is a conventional furnace in air annealing at different temperatures for 1 hour up to 700°C (starting at 400, 500, 600, 650 and finishing at 700°C). This treatment is similar to that performed in our previous works on Er doped a-Al_2O_3 films. All the thin films are characterized after every thermal step at the different temperatures.

15.1 Evolution of photoluminescence intensity

At resonant Er^{3+} excitation condition the PL spectra shape for all the thin films is similar to the spectra measured at as grown film, only the contribution from the Si NPs by the flat band is increased. This emission band is further analyzed in the Chapter 7.

The non resonant Er^{3+} excitation through Si NPs is lost after the first anneal procedure at 400 °C except for the s=0 nm thin film (see Figure 15.2). Therefore the interaction between Er^{3+} ions and Si NPs is only maintaining in the dopants configuration where the Er^{3+} ions are closer to the Si NPs. From now, only the evolution of the PL emission of the Er^{3+} ions for the s=0 and the only Er doped film is mainly analyzed.

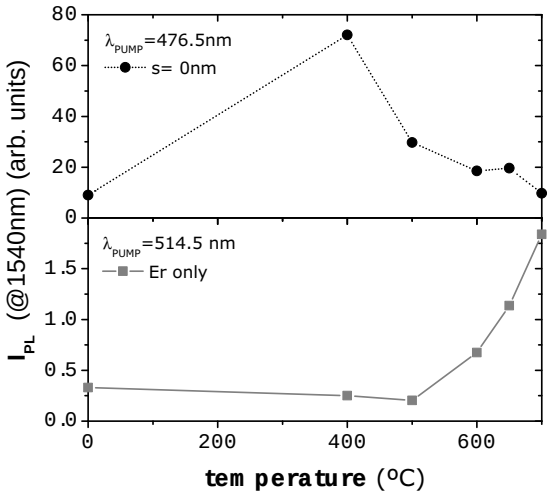

Figure 15.1: PL peak intensity as a function of the temperature of the different steps of the annealing procedure. Up graph - black full circles s=0 film. Bottom - gray full squares Er only film. Note the different scales.

The Figure 15.1 shows the PL peak intensity at 1.54 μm a function of the temperature achieved in the different steps of the annealing procedure for the s=0 film and the Er only doped a-Al_2O_3 film. The PL intensity of the s=0 film increases up to 400 °C a factor 8 but it is slightly decreased as the temperature of the thermal treatment increases until get at intensity values similar to the as grown thin film. This behavior is observed at resonant (not show) and non resonant pump conditions showing a Er^{3+} excitation mainly through Si NPs. In contrast the Er^{3+} only doped films shows no improvement of the PL intensity until 600 °C where the Er^{3+} emission increases gradually. [17, 26] Consequently the thermal annealing process improve the Er^{3+} ions environment but it affects to the Si NPs or to the region of interaction Si NPs - Er^{3+} whose result is the reduction of the energy exchange from the Si NPs to the closer Er^{3+} ions.

The energy transfer from Si NPs to Er^{3+} ions is reduced after the 400 °C annealing

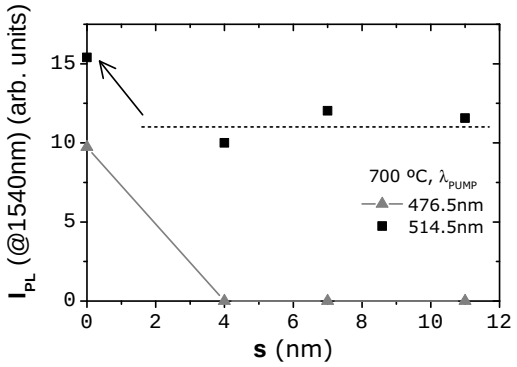

Figure 15.2: IPL peak intensity as a function of s parameter after 700°C thermal treatment

process for the s= 4. In addition, at resonant pump conditions (514.5 nm), the PL intensity achieved after the 700 °C is similar for all films between thin films except for the s=0 nm for which the PL intensity is higher due to the significant contribution of the Er^{3+} ions sensitized by Si NPs (see Figure 15.2).

15.2 Evolution of lifetime

The Figure 15.3 shows the intensity decays at 1.54 μm for four different thin films after the thermal annealing process at 700°C. Strong differences have been obtained between the the co-doped film with s=0 and the Er only doped film and the Si only doped film. The only Er doped film shows a stretched exponential curve behavior that deviates little from a single exponential behavior. In fact the 700 °C is not yet the optimum annealing temperature and the number of defects in the host are not completely eliminated (analysis detailed in Appendix C). The only Si doped film shows a fast decay associated to the emission flat band that can not be measured because it has associated a temporal value below the resolution of the system. The co-doped thin film with s=0 shows clearly two decay independent components. The fast component can be associated to the flat band emission related to the presence of Si NPs due to the similarity with the only Si doped film decay curve, while the slow component is associated to the Er^{3+} ions emission. Note that the decay curves obtained for the co-doped thin film are different for the pump wavelength in resonant or non resonant pump conditions, however these differences are related to the dependence of the intensity emission of the flat band on the pump wavelength and not in differences in the Er^{3+} excitation mechanism. In fact the temporal behavior of the slow and fast components are the same at different pump conditions.

The Figure 15.4 shows the lifetimes evolution as a function of the annealing temperature. The Er^{3+} lifetimes values increases as the temperature of the annealing process

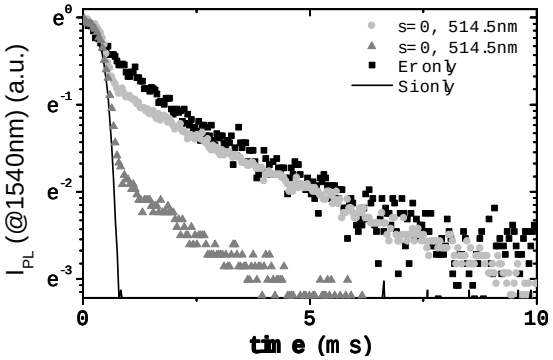

Figure 15.3: Decay curves for the s=0 film at resonant (514.5 nm) and non resonant (476.5 nm) pump conditions and for the Er only doped film and Si only doped film after the 700 °C annealing process.

is increased. The behavior is the same between the two films revealing that the Er^{3+} de-excitation mechanism are affected by the thermal treatment in the same way independently of the presence of Si NPs. Comparing the lifetime (Figure 15.4) with the PL intensity evolution for only Er doped film (Figure 15.1), annealing induces the reduction of the non-radiative channels and as a result both lifetime and intensity increase. In contrast, for the co-doped film at 400 °C the PL intensity decreases while the lifetime increases. This suggest there is a decrease of the non radiative channels too but also a reduction of the number of the excited Er^{3+} induced by the annealing procedure.

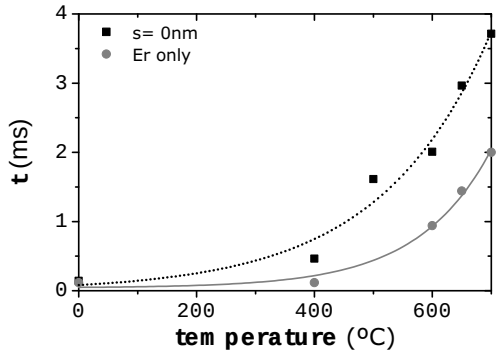

Figure 15.4: Lifetime values a function of the annealing temperature for the only Er doped film and the slow component of the s=0 film.

15.3 Conclusions

The optimum dopant distribution in as deposited thin films has been determined in the previous Section 8.1. The annealing process upon 400 °C is a successfully post-processing treatment and an improvement in the PL intensity Er^{3+} emission closer to one order of

magnitude is observed. After the annealing step at 400 °C the PL intensity decreases as the lifetime increases indicating a reduction in the number of the excited Er^{3+} through the Si NPs, so the Si NPs to Er^{3+} energy transfer is inhibited. Changes at the Si NP surface upon annealing are suggested as the main responsible for the observed behavior.

Chapter 16

Conclusiones Generales

En esta tesis se han establecido las condiciones de diseño y preparación de láminas nanoestructuradas de a-Al_2O_3 co-dopadas con nanopartículas (NPs) de silicio e iones de Er^{3+} mediante la técnica de depósito por láser pulsado. El depósito de los dopantes de forma independiente y la formación de las nanopartículas in situ durante el crecimiento ha permitido establecer las condiciones en las que se obtiene una emisión a 1.5 μm optimizada y las características particulares de los procesos de transferencia de energía de las NPs de Si a los iones de Er^{3+}. Esta transferencia de energía se ha estudiado por primera vez en NPs amorfas formadas sin necesidad de tratamiento térmico. Este avance, que hemos podido conseguir gracias a las características únicas de nuestros procedimientos, ha permitido variar el tamaño de las NPs sin modificar las propiedades de la matriz, determinando así sus propiedades electrónicas. Otra característica relevante y singular de las condiciones de crecimiento de las láminas ha sido la posibilidad de controlar la situación espacial de las NPs y los iones dopantes, que ha arrojado nueva luz sobre los procesos de transferencia en función de la distancia entre los dopantes, tanto en la nanoescala como por debajo de ella. Esto incluye, de forma particularmente destacable, el contacto (s=0), que no se había demostrado nunca anteriormente en ningún sistema codopado NPs-Er^{3+}.

Las conclusiones principales que se derivan de los estudios presentados en esta tesis son:

- Las nanopartículas de Si que se producen in situ durante el proceso de crecimiento son amorfas y se encuentran distribuidas en capas bien definidas. Su tamaño y el número de NPs por capa se controla variando el número de pulsos utilizados para ablacionar el blanco de silicio durante el proceso de depósito de láser pulsado obteniendo distribuciones de NPs muy densas (entre 11 10^{19} y 210^{19} $cm-3$) y de diámetros variables entre 1.6 nm y 4.5 nm, mostrando confinamiento cuántico y alta absorción en el visible.

- Se ha conseguido transferencia de energía eficiente de las NPS al Er^{3+} en láminas

basadas en alúmina en muestras recién depositadas a temperatura ambiente en vacío con factores de realce cercanos a dos órdenes de magnitud. La eficiencia de la transferencia de energía de las NPs a los iones de Er^{3+} depende críticamente de la separación entre dopantes. La transferencia de energía más eficiente se ha obtenido cuando existe contacto entre ambos, esto es, los iones de Er están situados en la superficie de las NPs de Si. Así se establece que la condición para obtener láminas optimizadas bajo depósito por láser pulsado secuencial es que los iones de Er^{3+} se depositen a continuación de la formación de las NPs de silicio en vacío y sin interponer ninguna capa de a-Al_2O_3.

- En muestras con contacto entre NPs de Si e iones de Er^{3+} se ha observado y caracterizado un nuevo régimen de acoplo entre NPs y Er^{3+}. En este régimen de acoplo extremo se han analizado en profundidad las propiedades temporales de la emisión a 1.53 μm. Éstas corroboran que los iones de Er^{3+} que emiten eficientemente están localizado preferencialmente en la superficie de las NPs y que su respuesta temporal depende fundamentalmente de las propiedades cuánticas de las NPs y no de la distancia del ión a la NP.

- Se han obtenido fracciones de iones de Er^{3+} excitado superiores al 50% siendo viable excitar el 100% del Er^{3+} activo en muestras con acoplo optimizado entre las NPs y los iones de Er^{3+}. Esto demuestra la viabilidad y las prometedoras propiedades de láminas de a-Al_2O_3 co-dopadas con Er^{3+} y NPs de Si en condiciones de acoplo extremo para el desarrollo de materiales de ganancia.

- Se han estudiado en profundidad los diferentes mecanismos de interacción entre NPs de Si e iones de Er^{3+} a partir de la respuesta temporal de fotoluminiscencia. Es posible estimar el porcentaje de iones de Er^{3+} excitado mediante recombinación directa excitónica inter-banda o por relajación excitónica por transiciones intra-banda. Debido al contacto establecido entre los iones de Er^{3+} y las NPs el procentaje de iones de Er^{3+} excitados mediante cada mecanismo se controla con las propiedades cuánticas de las NPs y la sintonización de sus niveles de energía con los niveles atómicos del Er^{3+}. Gracias a la presencia de esos dos mecanismos de excitación es posible optimizar la excitación de los iones de Er^{3+} mediante mecanismos de división de energía como el "Space separated quantum cutting" de forma que obtenemos emisión de dos fotones a 1.53 μm a partir de la excitacón con un único fotón en el visible optimizando la energía transferida al Er^{3+}.

- El papel de los distintos defectos en las láminas ha sido analizado. Muestras dopadas sólo con NPs de silicio recién preparadas y sin ser sometidas a tratamientos térmicos muestran por catodoluminiscencia una cantidad elevada de defectos en la matriz. Por otra parte los defectos en la superficie de las NPS que se generan durante el crecimiento de las láminas influyen en las propiedades fotoluminescentes de las láminas

dopadas con NPs de Si. Así, sólo se observa emisión de las NPs cuando las muestras son sometidas a procesos térmicos post-depósito.

- Los iones de Er^{3+} situados cerca de las NPs muestran una interaccion preferente con estas y no con los defectos de la matriz. Esto explica la emisión eficiente observada en muestras recién depositadas con una alta densidad de defectos en la matriz de a-Al_2O_3.Este resultado implica que es posible controlar las probabilidades de transición de los iones de Er^{3+} mediante la reducción de los defectos superficiales de las NPs. La reducción de defectos se consigue mediante la reducción de tamaño de las NPs y el control de la densidad de energía usada en el láser de ablación durante el depósito. Así en las muestras con NPs de menor diamétro medio se ha observado realce del tiempo de vida del Er^{3+} para la emisión a 1.53 μm respecto a las muestras sólo dopadas con Er^{3+}.

- Se ha conseguido obtener un aumento de la emisión a 1.53 μm del Er^{3+} de un orden de magnitud mediante procesos térmicos a baja temperatura (hasta 400 ^{o}C). Para temperaturas superiores se pierde la transferencia de energía de las NPs al Er^{3+} por posible pérdida de contacto que puede estar relacionada con el aumento del espesor de la capa de SiO_2 en la superficie de las NPs de Si. El trabajo futuro se orientará en el estudio de procesos térmicos a bajas temperaturas para poder obtener altas fracciones de Er^{3+} excitado sin pérdida de contacto y con menor energía de bombeo.

Appendix A

Analysis of the spectra shape. Er^{3+} chemical environment

The degenerate energy levels of the Er $4f$ states will split due to the Stark effect when Er is incorporated into a solid host. Hence the shape of the Er luminescence spectrum, which is due to optical transitions between the various Stark levels, reflects the local environment around the ion.[108]. We have used this feature to study the chemical environment of the Er^{3+} ions and to help us to understand better their spatial location. It is going to be shown how the use on a non Si-based host can be useful to provide information on the Er-NPs interaction.

For example, the Figure (citar) of the Chapter 9 shows the normalized spectra to the maximum of intensity peak for an Er^{3+} and Si NPs co-doped film (Si-185-Er) and the reference Er^{3+} doped film. All the co-doped films shows the same spectral response independently of the Si NP size, only the Er only doped film shows a different behavior. The spectra shape of Er only doped film is broader than the co-doped films ones thus, the Full With at Half Maximum (FWHM) is 50 nm for the Er^{3+} doped a-Al_2O_3 film and 44 nm for the Si NP and Er^{3+} doped film. Moreover the peak intensity position in the co-doped film spectra is shifted a few nanometers to higher wavelength values than the peak position of the only Er doped film (from 1530 nm at Er^{3+} doped a-Al_2O_3 to 1535 nm in the Er^{3+} and Si NP doped a-Al_2O_3 films). The bandwidth reduction and the shift to longer wavelength in the co-doped film suggest that almost recollected emission comes from Er^{3+} localized in Si-O chemical environment rather than in an Al-O environment,[14] which is consistent with the Er located at the surface of the Si NPs.

Evaluation of $^4I_{15/2}$ and $^4I_{13/2}$ Stark-level energies

A thorough study about the spectra shape and Er^{3+} the emission lineshapes in the S, C and L bands of the third telecommunication window was performed, specially in the C band (the *erbium window*).

The Figure A.1 shows the Stark components of the $^4I_{15/2}$ and $^4I_{13/2}$ levels that had

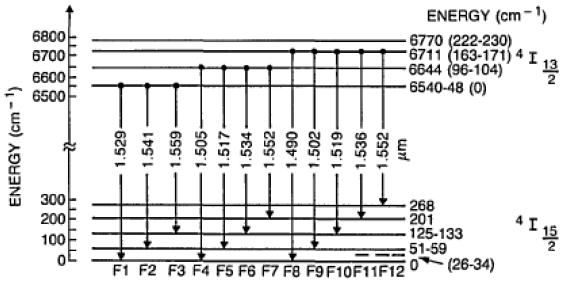

Figure A.1: Energy diagram showing the Stark components of the $^4I_{15/2}$ and $^4I_{13/2}$ manifolds and the assignment of observed fluorescence transitions.

been established in the reference [146] for an Er^{3+} doped aluminosilicate glass fiber. Playing with the temperatures is possible to tune the number of transitions observed but at room temperature all of them are going to be present, but the proximity between the fluorescence peaks (F4-F9, F5-F10, F6-F11, F7-F12) allow us only to discriminate 7 emission lines, as it is usually obtained for silica based fibers [145].

The shape of the emission lines is going to be determined by the homogeneous or inhomogeneous nature of the host. Homogeneous mechanism generally give rise to Lorentzian lineshapes, while inhomogeneous processes tend to produce Gaussian spectral lines [147]. Our host is an amorphous material then Lorentzian lineshapes are expected but considering that we are going to compare with a nanocomposite material formed by Si NPs and a-Al_2O_3 we are going to considerer inhomogeneous broadening. Also, our deposited a-Al_2O_3 in as grown conditions contain lot of defects and excess of aluminium ions and could be considerer and inhomogeneous media for the Er^{3+} ions.

Using loretzian lineshapes for the co-doped films the best fits have been obtained. The Figure A.2-b shows all the lineshapes and the complete fit for the Si-75-Er thin film and in the table appears the fitted peaks details. The loretzian adjustments suggest a homogeneous broadening and then the all the emission that is detected comes from Er^{3+} in similar sites. Thus, taking into account the position of the emission peaks similar to the silica fibers [145] we can conclude that almost the Er^{3+} emitting are sited in the Si NP surface.

In the other hand, the Figure A.2-a shows the spectra decomposition for the Er only doped film. Homogeneous broadening, but different positions for the peaks. The wavelength positions can be associated to an a-Al_2O_3 chemical environment (see Table A.1). [145]

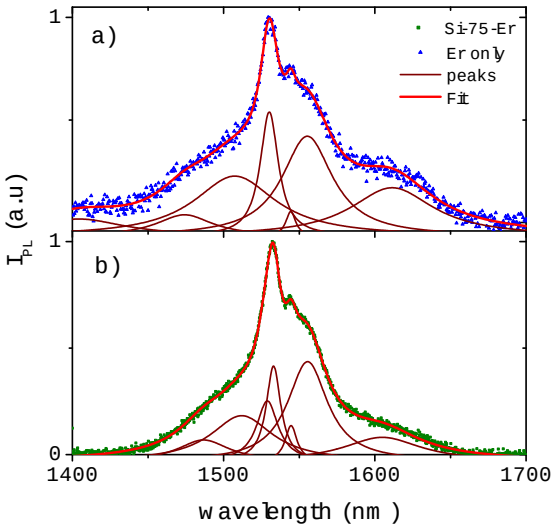

Figure A.2: Experimental emission cross section line shapes of ${}^4I_{15/2}$ to ${}^4I_{13/2}$ transition for an Er^{3+} only doped film A.2-a and for an Er^{3+} and Si NP doped film (Si-75-Er) A.2-b. The dots are the experimental data, the red lines the complete fit and the wine lines are the peaks that the fit is composed of.

Er^{3+} and Si NP doped film			
Peak position (nm)	Width (nm)	Height (a.u.)	Area (a.u.)
1487	42	0.13	6.6
1512	50	0.27	16.9
1529	17	0.36	7.7
1533	12	0.56	8.2
1545	10	0.21	2.5
1556	32	0.59	23.8
1605	63	0.14	11.2
Only Er^{3+} doped film			
1404	76	0.11	10.1
1474	45	0.13	7.5
1507	66	0.37	30.3
1530	15	0.76	13.9
1544	8	0.15	1.5
1555	41	0.61	31.2
1611	67	0.30	24.8

Table A.1: Peak positions and parameters of the descomposed components of the an Er^{3+} and Si NP doped film

Appendix B

Analysis of the excitation photoluminescence spectroscopy

One of the improvements of the Er^{3+} and Si NP co-doped systems is the widened pump bandwidth in the visible wavelength range, where a lot of low cost light emission devices are available (LED'S). While the co-doped systems can be pumped in all the visible range where the Si NPs are strong absorbers, the only Er^{3+} doped systems can only be pumped at the discrete wavelengths of the upper Er^{3+} ions energy levels (see Figure B.1) that have associated low absorption cross sections. The intensity emission at the maximum peak decreasing as a function of the pump wavelength is the most usual behavior in co-doped systems. It is related to Si NP absorption dependence on the wavelength pump range that it is passed on to the Er ions PL emission through the energy transfer phenomena. In that way, the dependence of the emission at 1.53 μm as a function of the excitation wavelength **gives us rich information about the transfer energy phenomena** and it was analyzed in all the series. Low pump powers (200mW) was selected to obtain enough energy at all available Ar^{+} visible emission lines to pump at the same photon flux independently of the pump wavelength.

The PLE curves observed are going to depend on the size of the Si NPs and the distribution of the two dopants. So decreasing linear PLE curves has been observed (Figure poner) showing a strong energy transfer process between Si NP and Er^{3+} and where the slope is dependent on the Si NP size. Also, PLE spectra showing the linear decreasing curve as a function os the wavelength but with singularities where a local higher emission intensity was detected at wavelengths resonant with the Er^{3+} energy levels has been observed, showing the contribution of the direct pumped Er ions and the indirect pumped Er ions at the same time (Figure poner). And, finally only Er^{3+} emission has been detected at resonant wavelengths in the films where the Si NP-Er^{3+} transfer phenomena is not succeed (Figure poner). This analysis have been done for every series of thin films and analyzed changing the parameters at the nanoscale (distance and size) and the post-deposition treatments.

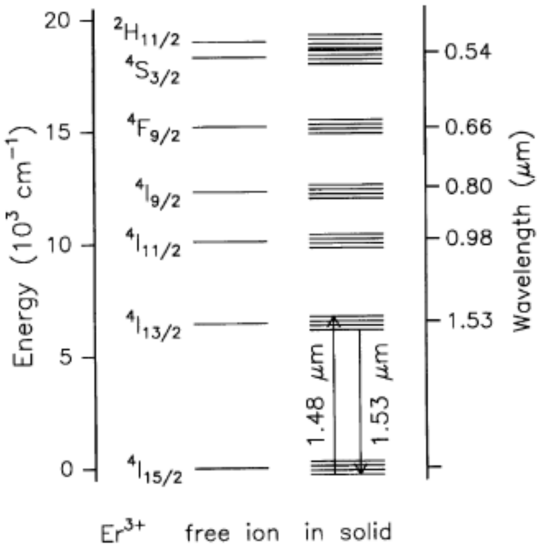

Figure B.1: Energy levels of Er^{3+}Data are shown both for the Er^{3+} free ion, and for Er in a solid host

We are going to defined **two different pump conditions** and we are going to name as *resonant* and *non-resonant* pump conditions. At non-resonant pump conditions the Er^{3+} ions emission can only be due to the sensitization of the ions by Si NPs and then it is going to be detected when the transfer process happen. At the resonant pump conditions the Er ions could be excited directly pumped at the resonant energies with the Er^{3+} energy levels and in the case of co-doped systems the two phenomena are taking place.

It is possible to calculate the **percentage of Er^{3+} emission by indirect or direct pumped**. To evaluate the the percentage of Er^{3+} emission obtained by indirect or direct excitation we have assumed that the direct contribution to be negligible at 476.5 nm and to have a similar value at 457.9 and 501.7 nm. Consequently the indirect contribution has been obtained by the a linear slightly decreasing function defined by the intensity at 457.9 and 501.7 nm and shifted to the 476.5 nm intensity value. Assuming that this linear function accounts for the indirect contribution in the whole studied wavelength range, the indirect contribution for these three wavelengths has been obtained by subtracting this direct contribution to the measured PL.

Assuming the relation of the equation B.1 it is possible to obtain a relation between the emission cross sections at 1.53 μm pumped at different wavelengths for an specific thin

film and to connect to the slope of the excitation curves.

$$I_{PL} \sim f_{Exc-Er}\ N_{Er}\ \sigma_a\ \frac{\tau}{\tau_{rad}} \tag{B.1}$$

To obtain the expression we have considered that the τ_{rad} is independent of the pump wavelength due that the τ_{rad} depends on the index of nanocomposite at the emission wavelength and, that the f_{Exc-Er} depends fundamentally from the geometry of contact of the two distributions of dopants and it is proportional to the pump flux, then for a unique thin film the ratio of excited fractions is only related to the pump fluxes. Assuming all this hypothesis the relative slope of the excitation curves is given by expression B.2.

$$Slope_{relative} = \frac{I_{PL-457.5} - I_{PL-514.5}}{I_{PL-457.5}} = 1 - \frac{\phi_{514.5}\sigma_{a-514.5}}{\phi_{457.5}\sigma_{a-457.5}} \tag{B.2}$$

The $Slope_{relative}$ is decreased gradually from 0.33 to 0.61 as a function of the Si NP diameter. Interestingly, the obtained values are close to the corresponding to the covered area by the Si NPs suggesting that there is a physical relation between the PL intensity and the absorption cross sections and that affects to the excitation curves shape.

Appendix C

Photoluminescence temporal analysis

In this Appendix the different methods to analyze the rise and decay photoluminescence (PL) curves are discussed. The PL dynamic models are applied to Er^{3+} and Si NP doped a-Al_2O_3 thin film with different sizes. Similar average lifetimes and rise-times values are obtained from the different methods however the information obtained about the physical properties of the extreme Er^{3+}Si NP coupling thin films is different but in sound agreement.

C.1 Analysis of Er^{3+} excitation and des-excitation dynamics (lifetimes and rise times)

Conventional analysis of Er ions lifetimes resolve the decay profile as a single-exponential decay function as all the Er^{3+} are located in an optimized homogeneous environment. Heterogenous dopant distributions in an host with the non radiative channels minimized (by post-deposition treatments) and/or without sensitizers show single-exponential rise and decay times. However our extreme Er^{3+}Si NP coupling a-Al_2O_3 thin films has been analyzed in as grown conditions without post-anneal treatment and then a more complex decay and rise profiles are expected. Determining the best fit function could provide us fundamental information about the interaction mechanism between Er^{3+} and Si NPs but always that have to can be justified from a physical point of view.

C.1.1 A rough approximation. Single-exponential function

Assume a co-doped film excited by pump photons at visible. This results an initial Er^{3+} excited population. When the pump beam disappears the excited state population decays with a rate $\Gamma + k_{nr}$ according to the expression C.1, where $N(t)$ is the number of excited

Er^{3+} at time t, Γ is the emissive rate[1], and k_{nr} is the non radiative decay rate.

$$\frac{dN(t)}{dt} = (\Gamma \ + \ k_{nr})N(t). \tag{C.1}$$

The Er^{3+} emission is a random event, in a homogeneous media each ion has the same probability of emitting in a given period of time. Thus the emission rate and the non radiative decay rate can be considered constants and the excited state population follows a exponential decay, $N(t) = N_0 \ e^{-t/\tau}$ where N_0 is the initial excited population.

In a photoluminescence experiment we do not observe the variation of excited state population as a function of the time, but the intensity of PL is proportional to this magnitude (expression B.1), then the for an indeterminate number of excited ions the intensity shows a exponential decay dependence (equation C.2) where τ is the inverse of the total decay rate $\tau = (\Gamma + k_{nr})^{-1}$.

$$I(t) = I_0 e^{-t/\tau} \tag{C.2}$$

The lifetime is the average of the time that a excited Er^{3+} ion remains in this excited state. Calculating the average time (expression C.4) in the excited state and assuming a exponential temporal dependence of the photoluminescence intensity, the life time is the inverse of the total decay rate $< t >= \tau$.

$$< t >= \frac{\int_0^\infty tI(t)dt}{\int_0^\infty I(t)dt} \tag{C.3}$$

$$\tag{C.4}$$

All the mathematical modeling is useful for the rise-times taking into account that $I_{Fit-rise}(t) = 1 - I_{Experimental}(t)$.

In summary, in a media with a homogeneous distribution of non-radiative channels and sensitizers the decay and rise time curves can be fitted by a single-exponential function. The Figure C.1 shows the decay and rise curves for a co-doped a-Al_2O_3 thin film at 1535 nm. It is clear that **the time dependence of the erbium photoluminescence is not well fitted by a single exponential**. Thus, the as grown PLD a-Al_2O_3 extreme coupling thin films shows a more complex behavior due to the heterogeneous Er^{3+} location and the single-exponential approximation is only useful to estimate the rough average lifetime and rise-time values.

[1] es lo mismo que emission rate?

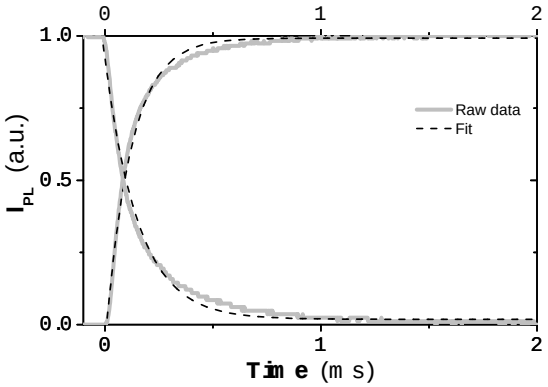

Figure C.1: Decay and Rise curves for the Si125Er thin film at 1535nm. The grey lines are the raw data and the black dash lines are the best fits using a single exponential for both curves.

C.1.2 Simplifying the lifetimes and rise-times estimations: 1/e.

In order to eliminate considerations about the shape of the PL dynamics and simplify the estimation of the lifetime and rise-times values it is possible to characterize the dynamic response by the time that the photoluminescence intensity decays $1/e$ of its initial value. The Figure C.2 shows the logarithmic plot of the photoluminescence decay and rise curves for the Si125Er thin film at 1535nm. If we consider the origin of time axis as in the beginning of the fall of the photoluminescence intensity, the intersection between the normalized raw data curve and the straight line that represents the constant value 1/e gives us the value of the 1/e lifetime.

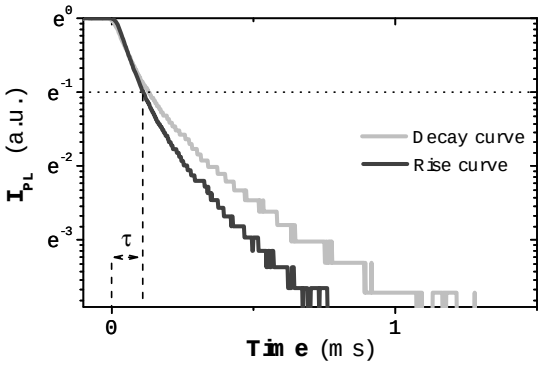

Figure C.2: Logarithmic plot of the decay and rise curves for the Si125Er thin film at 1535nm. The black dot line symbolize the 1/e value.

The Figure C.3 shows the logarithmic plot of the photoluminescence rise curves for different co-doped thin films. The value of the 1/e rise-time increases as the Si NP diameter

decreases (values at table **??**) however the differences between the PL rise curves are magnify for longer time domains. Thus the simplification of the dynamic curves by the 1/e estimation does not give enough information as it does not account for the longer lifetime/rise-time events.

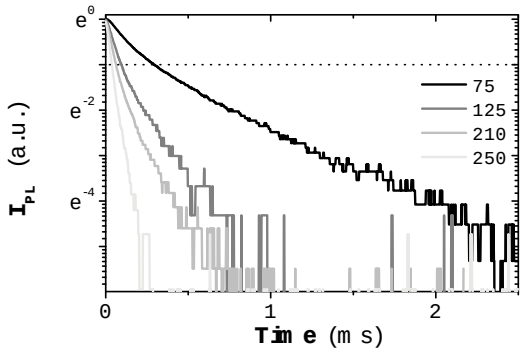

Figure C.3: Logarithmic plot of rise curves for the co-doped thin film at 1535nm. The black dot line symbolize the 1/e value.

Moreover, the longer lifetime/rise-time events are essential for the analysis of the decay and rise times. The gradual increment of the separation of the curves with the time is emphasized when the decay and rise curves are compared for the same thin film. The Figure C.3 shows the logarithmic plot of the PL decay and rise curves for the Si-125-Er thin film at 1535 nm. The PL rise curve and the decay curve are very similar for times below intersection point and the difference between the curves is found in the curve tails for $t > \tau_e$.

$< \tau >_{decay}$	Single-exponential (±0.010 ms)	τ_e (±0.010 ms)	Stretched exponential (±0.010 ms)	Multi-expo (±0.010 ms))
$Only - Er - 4$	0.321	0.200	0.265	0.489
$SE\phi 1.6$	0.470	0.373	0.413	0.605
$SE\phi 2.2$	0.175	0.108	0.147	0.260
$SE\phi 2.6$	0.179	0.102	0.108	0.202
$SE\phi 2.8$	0.167	0.102	0.108	0.209
$SE\phi 3.3$	0.130	0.057	0.046	0.098

Table C.1: Lifetimes values obtained from single, stretched and multi exponential fits and 1/e approximations

C.1.3 Stretched exponential. Lifetimes and rise-times dispersions

In fluorescence the most common method to analyze the dynamic curves is the multi-exponential function but there are many other situations in which a limited number of

discrete decay times does not expected and a continuous distribution of lifetimes is obtained. An alternative approach to fit complex photoluminescence dynamic curves is employing the stretched exponential function:

$$I(t) = I_0 e^{-(t/\tau_{KWW})^{\beta}}, \tag{C.5}$$

where I_0 is the fluorescence intensity at time t=0, τ_{KWW} is the decay constant and β is the inverse of the heterogeneity parameter ($h = 1/\beta$) with $0 < \beta \leq 1$. [120] A further advantage of the stretched exponential model is that describes the variations in the photoluminescence intensity without the need for making assumptions about the number of discrete components in a multiple-exponential model.

One motivation to apply the stretched exponential function is that, the stretched exponential curves can be expressed as a continuous distribution of lifetimes. From the mathematical point of view a stretched exponential is a superposition of uncoupled Debye processes defined by the expression C.6:

$$e^{-(t/\tau_{KWW})^{\beta}} = \int_0^{\infty} e^{-(t/\tau)} \rho(\tau) d\tau, \tag{C.6}$$

obtaining a distribution of Debye relaxation times $\rho(\tau)$.[148]. Often, the parameter τ_{KWW} is refereed as the average relaxation lifetime but τ_{KWW} is a characteristic property of the lifetimes distribution $\rho(\tau)$ but it is not the first order momentum. Taking into account the expression C.4 the average lifetime is defined as

$$< \tau >= \frac{\tau_{KWW}}{\beta} \Gamma(\frac{1}{\beta}) \tag{C.7}$$

Now, the objectives are to apply the stretched exponential model to the Er^{3+}-Si NPs extreme coupling thin films and to find what $\rho(\tau)$, τ_{KWW}, $< \tau >$ and β physically means.

The lifetimes distribution $\rho(\tau)$ is the probability distribution of lifetimes and gives us information about the probability of des-excitation of a emitter with a lifetime value determined. The $< \tau >$ is the mean value of this lifetime distribution and τ_{KWW} is a parameter characteristic of the lifetime distributions that gives us information that the lifetime is going to be equally likely to be less than τ_{KWW} as to be greater within a $\pm 20\%$. [149] But the most relevant parameter for the lifetimes distributions is β. The heterogeneity parameter is defined by $h = 1/\beta$ and is related to the stretching of the decay process being a direct measure of the width of the lifetime distribution.[150] However, the statistic definition of the width of $\rho(\tau)$ is $\Delta s = \sqrt{(s^2)_{average} - (s_{average})^2}$. Moreover the interpretation of β as the full width at half maximum (FWHM) has been proved not useful as physical interpretation and β can be related to the logarithmic FWHM of $\rho(\tau)$ but not

to the FWHM itself. [149]

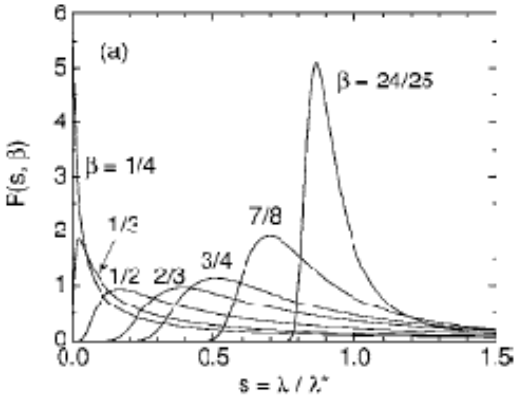

Figure C.4: Figure 2(a) from Johnston et al. [149]. Linear plot of the probability density of lifetimes ($P(s,\beta)$ is the normalized $\rho(\tau,\beta)$) versus the normalized relaxation rate $s = \lambda/\lambda^* = \tau_{KWW}/\tau$

One of the best method to understand the β meaning is analyzed the shape of the lifetime distributions. The figure C.4 shows the theoretic lifetime distributions obtained by Johnston in his work in the 2006 [149]. When $\beta = 1$ the stretched exponential is a pure exponential with $< \tau >= \tau_{KWW}$ and the lifetime distribution is a Dirac δ function. When β decreases the maximum of the lifetime is shifted to values higher than the τ_{KWW} and the lifetimes distribution is broader. Also, the absolute contribution of shorter lifetime components is reduced while lifetime components with larger lifetime are possible.

The stretched-exponential function (KWW[2] function) has been used as an alternative model to fit the fluorescence decay due the complexity of our material and because recently was developed to analyze the Er^{3+} lifetime and rise-time distributions.[122] For every Er^{3+} ion it may reasonable to believe that the relaxation or excitation response is exponential, but in co-doped systems there are a large distributions of environments within the film, as Si NPs of different sizes, different relative Er^{3+} - Si NP locations and then Er^{3+} - Si NP separation distances, each with different characteristics. These difference leads variations in the relaxation and excitation times, and in the experimental measurements can be reflected as an stretched exponential decay.[151]

[2]Khohlrausch-Williams-Watts

C.1.4 Multi-exponential decays ($n = 2$)

In a multi-exponential model the temporal dependence of the photoluminescence intensity is assumed as a sum of individual single exponential decays[119]:

$$I(t) = \sum_{i=1}^{n} \alpha_i e^{-t/\tau_i}, \tag{C.8}$$

where τ_i are the decay times, α_i the amplitude of the components at $t = 0$, and n is the number of decay times. This is the most commonly model used in biological fluorescence but the physical meaning of the parameters (α_i and τ_i) depends on the system being studied.

The values of α_i and τ_i can be used to determine the fractional contribution (f_i) of each Er^{3+} population to the steady-state intensity. The fractional contribution for the environment i is given by

$$f_i = \frac{\alpha_i \tau_i}{\sum_j \alpha_j \tau_j}. \tag{C.9}$$

The multi-exponential decay is perhaps the **most powerful model**. Almost any intensity decay can be fit using the expression C.8 independently of its complexity and taking into account the expression C.4 for a two component decay the average lifetime can be calculated by the expression C.10.

$$\bar{\tau} = \frac{\alpha_1 \tau_1^2 + \alpha_2 \tau_2^2}{\alpha_1 \tau_1 + \alpha_2 \tau_2} \tag{C.10}$$

Furthermore, the efficiency of one transfer process from a donor to an acceptor can be calculated from the lifetimes and the amplitude parameters of every component. The efficiency of the back-transfer process (E_{B-T}) is given by the expression C.11:

$$E_{B-T} = 1 - \frac{F_{DA}}{F_D} = 1 - \frac{\int_0^\infty I_{DA}(t)dt}{\int_0^\infty I_D(t)dt} = 1 - \frac{(\alpha_1 \tau_1 + \alpha_2 \tau_2)_{DA}}{(\alpha_1 \tau_1 + \alpha_2 \tau_2)_D} \tag{C.11}$$

where the subscript DA correspond to the co-doped thin films (donor and acceptor) and the subscript D correspond to the only donor doped film.[3]

[3]Buscar en el *Lakowicz − book −* 2006 la nomenclatura exacta para FDA, podría ser el PL yield?

Two dynamic components and the intra and inter band transitions

Surprisingly the experimental photoluminescence decay and rise curves fit a multi-exponential decay law with a discrete value n=2 for all the thin films, including the reference Er^{3+} only doped film. For values of n higher than two, the decays and rise-times takes similar values that can be reduced to two unique lifetimes. It is consistent with the discussion about the distribution of lifetimes defined by the stretched exponential, where there are contributions from fast and slow dynamic components in a distribution with a mean lifetime. The analysis of the stretch exponential function gives us information about the Er^{3+} location and the multi-exponential decay curves will give us information about the interaction mechanism inherent to the energy transfer processes from Si NPs to Er^{3+} ions and from Er^{3+} ions to Si NPs.

Agradecimientos

Llegar al final de una tesis doctoral es un largo camino no exento de momentos complicados en los que resulta imposible pensar en toda la gente que ha jugado un papel fundamental, tanto a nivel profesional como personal. Me gustaría agradecer en primer lugar a mi directora de tesis, Rosalía Serna Galán, por su esfuerzo y dedicación a lo largo de estos años y por haberme permitido llegar a establecer una relación sincera, lo que no es siempre fácil a lo largo de una tesis.

No puedo olvidarme de todo el Grupo de Procesado por Láser empezando por su líder Carmen Nieves, siempre dispuesta a trabajar y mejorar. Desde el punto de vista científico me ha dado la posibilidad de usar equipos punteros no disponibles en muchas partes del mundo, y he conseguido encontrar un foro abierto y pluridisciplinar. A los del 2026 (Pepe, Ángel, Vincenzo, George, Óscar, David, Josep, Pablo, Giorgio, Antonio), a los del 2025 (Miguel, José María, Jesús, Lorena), a los del 2024 (Ainara, Isi, Marcial, Alex, Fátima, Eduardo) y a los del 2021 (Javier S., Jan, Wojciech, Héctor, Daniel, Andrés, Alex, Javier H.). Con vosotros he crecido a nivel personal y profesional.

Me gustaría agradecer a todo el mundo del Instituto de Óptica porque a pesar de venir de disciplinas muy distintas siempre hemos encontrado nuestro punto común. Nunca podré olvidar esas comidas en el comedor de CSIC dónde ocupábamos mesas enteras y volvíamos locos a los camareros con listas interminables de cafés. Aquí tengo que mencionar con grande placer a todo el IOSA que sin saberlo habéis sido mi gran apoyo en estos últimos años.

Y por último y no por ello menos importante me gustaría agradecer a mi familia todo el apoyo mostrado en estos años, permitiéndome no sentirme sola y transfiriéndome fuerza. No se cómo agradeceros el apoyo prestado estos tiempo a pesar de la distancia y de esta emigración forzada.

Gracias a Martín, por enseñarme a amar y mantenerme a flote. Te querré siempre.

NUSA66
Sara Núñez-Sánchez

Bibliography

[1] A. M. Turing. Computing machinery and intelligence. *Mind*, 59:443–460, 1950.

[2] $http://en.wikipedia.org/wiki/alan_turing$.

[3] $http://en.wikipedia.org/wiki/john_von_neumann$.

[4] $http://en.wikipedia.org/wiki/eniac$.

[5] John Bardeen and Walter H. Brattain. Three electrode circuit element utilizing semiconductor materials, 1950.

[6] William Schockley. Circuit element utilizing semiconductive materials, 1951.

[7] Jack S. Kilby. Integrated semiconductive circuit structure, 1967.

[8] J. M. Martinez Duart, R.J. Martin Palma, and F. Agullo Rueda. *Nanotechnology for microelectronics and optoelectronics*. Elseiver, EMRS, 2006.

[9] S E. Miller. Integrated optics: an introduction. *Bell System Technical Journal*, 48:205969, 1969.

[10] Hiroshi Nishihara, Masamitsu Haruna, and Toshiaki Suhara. *Optical Integrated Circuits*. McGraw-Hill Optical and Electrooptical Engineering Series. Mc Graw-Hill Book Company, 1995.

[11] Gines Lifante. *Integrated photonics: fundamentals*. John Wiley and Sons, 2003.

[12] $http://es.wikipedia.org/wiki/amplificadoroperacional$.

[13] B. E. A. Saleh and M. C. Teich. Fundamentals of photonics, 2007.

[14] A. Polman. Erbium implanted thin film photonic materials. *Journal of Applied Physics*, 82:1–39, 1997.

[15] Buchal Ch, Siegrist Th, D. C. Jacobson, and J. M. Poate. 1.5 μm photoluminescence of er^{3+} in yf_3, luf_3, and laf_3 thin films. *Applied Physics Letters*, 68:438–440, 1996.

[16] R. Serna and C. N. Afonso. In situ growth of optically active erbium doped al_2o_3 thin films by pulsed laser deposition. *Applied Physics Letters*, 69:1541–1543, 1996.

[17] R. Serna, M. Jimenez de Castro, J. A. Chaos, C. N. Afonso, and I. Vickridge. The role of $er^{3+} - er^{3+}$ separation on the luminescence of er-doped al_2o_3 films prepared by pulsed laser deposition. *Applied Physics Letters*, 75:4073–4075, 1999.

[18] A. J. Kenyon, P. F. Trwoga, M. Federighi, and C. W. Pitt. Optical-properties of pecvd erbium-doped silicon-rich silica - evidence for energy-transfer between silicon microclusters and erbium ions. *Journal of Physics-Condensed Matter*, 6:L319–L324, 1994.

[19] Minoru Fujii and Masato Yoshida. Photoluminescence from sio2 films containing si nanocrystals and er: Effects of nanocrystalline. *Journal of Applied Physics*, 84:4525, 1998.

[20] M. Fujii, K. Imakita, K. Watanabe, and S. Hayashi. Coexistence of two different energy transfer processes in sio2 films containing si nanocrystals and er. *Journal of Applied Physics*, 95:272–280, 2004.

[21] G. Franzo, S. Boninelli, D. Pacifici, F. Priolo, F. Iacona, and C. Bongiorno. Sensitizing properties of amorphous si clusters on the 1.54 μm luminescence of er in si-rich sio_2. *Applied Physics Letters*, 82:3871–3873, 2003.

[22] B. Garrido, C. Garcia, S. Y. Seo, P. Pellegrino, D. Navarro-Urrios, N. Daldosso, L. Pavesi, F. Gourbilleau, and R. Rizk. Excitable er fraction and quenching phenomena in er-doped sio[sub 2] layers containing si nanoclusters. *Physical Review B (Condensed Matter and Materials Physics)*, 76:245308, 2007.

[23] K. Hijazi, R. Rizk, J. Cardin, L. Khomenkova, and F. Gourbilleau. Towards an optimum coupling between er ions and si-based sensitizers for integrated active photonics. *Journal of Applied Physics*, 106:024311, 2009.

[24] S. Nunez-Sanchez, R. Serna, J. Garcia Lopez, A. K. Petford-Long, M. Tanase, and B. Kabius. Tuning the er^{3+} sensitization by si nanoparticles in nanostructured as-grown al_2o_3 films. *Journal of Applied Physics*, 105:013118–5, 2009.

[25] I. Izeddin, D. Timmerman, T. Gregorkiewicz, A. S. Moskalenko, A. A. Prokofiev, I. N. Yassievich, and M. Fujii. Energy transfer in er-doped sio[sub 2] sensitized with si nanocrystals. *Physical Review B (Condensed Matter and Materials Physics)*, 78:035327, 2008.

[26] R. Serna, M. Jimenez de Castro, J. A. Chaos, A. Suarez-Garcia, C. N. Afonso, M. Fernandez, and I. Vickridge. Photoluminescence performance of pulsed-laser deposited al_2o_3 thin films with large erbium concentrations. *Journal of Applied Physics*, 90:5120–5125, 2001.

[27] V. Y. Timoshenko, M. G. Lisachenko, O. A. Shalygina, B. V. Kamenev, D. M. Zhigunov, S. A. Teterukov, P. K. Kashkarov, J. Heitmann, M. Schmidt, and M. Zacharias. Comparative study of photoluminescence of undoped and erbium-doped size-controlled nanocrystalline si/sio_2 multilayered structures. *Journal of Applied Physics*, 96:2254–2260, 2004.

[28] F. Gourbilleau, M. Levalois, C. Dufour, J. Vicens, and R. Rizk. Optimized conditions for an enhanced coupling rate between er ions and si nanoclusters for an improved 1.54-mu m emission. *Journal of Applied Physics*, 95:3717–3722, 2004.

[29] F. Gourbilleau, C. Dufour, R. Madelon, and R. Rizk. Effects of si nanocluster size and carrier-er interaction distance on the efficiency of energy transfer. *Journal of Luminescence*, 126:581–589, 2007.

[30] Hirasawa Makoto, Orii Takaaki, and Seto Takafumi. Size-dependent crystallization of si nanoparticles. *Applied Physics Letters*, 88:093119, 2006.

[31] R. Serna, D. Babonneau, A. Suarez-Garcia, C. N. Afonso, E. Fonda, A. Traverse, A. Naudon, and D. E. Hole. Effect of oxygen pressure on the optical and structural properties of $cu : al_2o_3$ nanocomposite films. *Physical Review B*, 66:205402, 2002.

[32] J. P. Barnes, A. K. Petford-Long, R. C. Doole, R. Serna, J. Gonzalo, A. Suarez-Garcia, C. N. Afonso, and D. Hole. Structural studies of ag nanocrystals embedded in amorphous al2o3 grown by pulsed laser deposition. *Nanotechnology*, 13:465–470, 2002.

[33] R. Serna, J. Gonzalo, A. Suarez-Garcia, C. N. Afonso, J. P. Barnes, A. K. Petford-Long, R. C. Doole, and D. Hole. Structural studies of pulsed-laser deposited nanocomposite metal-oxide films. *Journal of Microscopy*, 201:250–255, 2001.

[34] E.D. Pallik. *Handbook of Optical Constants of Solids.* Academic Press, San Diego, 1985.

[35] G. N. van den Hoven, E. Snoeks, A. Polman, J. W. M. van Uffelen, Y. S. Oei, and M. K. Smit. Photoluminescence characterization of er-implanted al_2o_3 films. *Applied Physics Letters*, 62:3065–3067, 1993.

[36] G. Allan, C. Delerue, and M. Lannoo. Electronic structure of amorphous silicon nanoclusters. *Physical Review Letters*, 78:3161, 1997.

[37] B. Garrido, C. Garcia, P. Pellegrino, D. Navarro-Urrios, N. Daldosso, L. Pavesi, F. Gourbilleau, and R. Rizk. Distance dependent interaction as the limiting factor for si nanocluster to er energy transfer in silica. *Applied Physics Letters*, 89:163103, 2006.

[38] J. H. Jhe, J. H. Shin, K. J. Kim, and D. W. Moon. The characteristic carrier-er interaction distance in er-doped a-si/sio2 superlattices formed by ion sputtering. *Applied Physics Letters*, 82:4489–4491, 2003.

[39] T. Kimura, H. Isshiki, S. Ide, T. Shimizu, T. Ishida, and R. Saito. Suppression of auger deexcitation and temperature quenching of the er-related 1.54 mu m emission with an ultrathin oxide interlayer in an er/sio2/si structure. *Journal of Applied Physics*, 93:2595–2601, 2003.

[40] S. Y. Seo, H. Jeong, J. H. Shin, H. W. Choi, H. J. Woo, and J. K. Kim. Effect of ion-irradiation induced defects on the nanocluster si/er^{3+} coupling in er-doped silicon-rich silicon oxide. *Applied Physics Letters*, 91, 2007.

[41] T. Takagahara. Theory of the quantum confinement effect on excitons in quantum dots of indirect-gap materials. *Physical Review*, 46:15578–15581, 1992.

[42] C. Delerue. Theoretical aspects of the luminescence of porous silicon. *Physical Review B*, 48:11024–11036, 1993.

[43] K. Sun, W. J. Xu, B. Zhang, L. P. You, G. Z. Ran, and G. G. Qin. Strong enhancement of er^{3+} 1.54 μm electroluminescence through amorphous si nanoparticles. *Nanotechnology*, 19, 2008.

[44] B. Garrido Fernandez, M. Lopez, C. Garcia, A. Perez-Rodriguez, J. R. Morante, C. Bonafos, M. Carrada, and A. Claverie. Influence of average size and interface passivation on the spectral emission of si nanocrystals embedded in sio[sub 2]. *Journal of Applied Physics*, 91:798–807, 2002.

[45] L. W. Wang and A. Zunger. Electronic-structure pseudopotential calculations of large (approximate to 1000 atoms) si quantum dots. *Journal of Physical Chemistry*, 98:2158–2165, 1994.

[46] $http://www.microscopy.ethz.ch/elmi-home.htm$.

[47] GATAN. *EELS Atlas*.

[48] D. Bouchet and C. Colliex. Experimental study of elnes at grain boundaries in alumina: intergranular radiation damage effects on a1-l-23 and o-k edges. *Ultramicroscopy*, 96:139–152, 2003.

[49] $http://www.cemes.fr/\ eelsdb/index.php?page=home.php$.

[50] Iacona Fabio, Bongiorno Corrado, Spinella Corrado, Boninelli Simona, and Priolo Francesco. Formation and evolution of luminescent si nanoclusters produced by thermal annealing of sio[sub x] films. *Journal of Applied Physics*, 95:3723–3732, 2004.

[51] C. Single, F. Zhou, H. Heidemeyer, F. E. Prins, D. P. Kern, and E. Plies. Oxidation properties of silicon dots on silicon oxide investigated using energy filtering transmission electron microscopy. *Journal of Vacuum Science and Technology B*, 16:3938–3942, 1998.

[52] L. Escobar-Alarcon, A. Arrieta, E. Camps, S. Romero, M. Fernandez, and E. Haro-Poniatowski. Influence of the plasma parameters on the properties of aluminum oxide thin films deposited by laser ablation. *Applied Physics a-Materials Science and Processing*, 93:605–609, 2008.

[53] F. Caridi, L. Torrisi, A. M. Mezzasalma, G. Mondio, and A. Borrielli. Al2o3 plasma production during pulsed laser deposition. *European Physical Journal D*, 54:467–472, 2009.

[54] M. J. de Castro, R. Serna, J. A. Chaos, C. N. Afonso, and E. R. Hodgson. Influence of defects on the photoluminescence of pulsed-laser deposited er-doped amorphous al2o3 films. In *10th International Conference on Radioation Effects in Insulators (REI-10)*, pages 793–797, Jena, Germany, 1999. Elsevier Science Bv.

[55] B. Garrido, M. Lopez, O. Gonzalez, A. Perez-Rodriguez, J. R. Morante, and C. Bonafos. Correlation between structural and optical properties of si nanocrystals embedded in sio[sub 2]: The mechanism of visible light emission. *Applied Physics Letters*, 77:3143–3145, 2000.

[56] Pallab Bhattacharya. *Semiconductor optoelectronic devices*. Prentice Hall, 1994.

[57] Peter Y. Yu and Manuel Cardona. *Fundamentals of Semiconductors. Physics and Materials Properties*. Physics and Astronomy. 3rd edition, 2003.

[58] D. Jaque J. Garcia Sole, L.E. Bausa. *An introduction to the optical spectroscopy of inorganic solids*. Wiley, 2005.

[59] R. B. Schoolar and J. R. Dixon. Optical constants of lead sulfide in the fundamental absorption edge region. *Physical Review*, 137:A667, 1965.

[60] G. G. Macfarlane and V. Roberts. Infrared absorption of silicon near the lattice edge. *Physical Review*, 98:1865, 1955.

[61] L. Pavesi. Silicon-based light sources for silicon integrated circuits. *Advances in Optical Technologies*, 2008, 2008.

[62] Shang Yuan Ren. Quantum confinement of edge states in si crystallites. *Physical Review B*, 55:4665, 1997.

[63] M. Hybertsen. Absorption and emission of light in nanoscale silicon structures. *Physical review letters*, 72:1514–1517, 1994.

[64] Kengo Nishio, Junichiro Koga, Toshio Yamaguchi, and Fumiko Yonezawa. Theoretical study of light-emission properties of amorphous silicon quantum dots. *Physical Review B*, 67:195304, 2003.

[65] A. Yoffe. Semiconductor quantum dots and related systems: electronic, optical, luminescence and related properties of low dimensional systems. *Advances in physics*, 50:1–208, 2001.

[66] M. Ben-Chorin, B. Averboukh, D. Kovalev, G. Polisski, and F. Koch. Influence of quantum confinement on the critical points of the band structure of si. *Physical review letters*, 77:763, 1996.

[67] W. Wilson. Quantum confinement in size-selected, surface-oxidized silicon nanocrystals science. *Science*, 262:1242–1244, 1993.

[68] C. S. Peng, Q. Huang, W. Q. Cheng, J. M. Zhou, Y. H. Zhang, T. T. Sheng, and C. H. Tung. Optical properties of ge self-organized quantum dots in si. *Physical Review B*, 57:8805, 1998.

[69] S. Ren. Quantum confinement in semiconductor ge quantum dots. *Solid State Communications*, 102:479–484, 1997.

[70] M. C. Bost and E. Mahan John. An investigation of the optical constants and band gap of chromium disilicide. *Journal of Applied Physics*, 63:839–844, 1988.

[71] D. L. Wood and J. Tauc. Weak absorption tails in amorphous semiconductors. *Physical Review B*, 5:3144, 1972.

[72] E. A. Davis and N. F. Mott. Conduction in non-crystalline systems .5. conductivity, optical absorption and photoconductivity in amorphous semiconductors. *Philosophical Magazine*, 22:903, 1970.

[73] J. Tauc, R. Grigorov, and A. Vancu. Optical properties and electronic structure of amorphous germanium. *Physica Status Solidi*, 15:627, 1966.

[74] T. M. Donovan, W. E. Spicer, J. M. Bennett, and E. J. Ashley. Optical properties of amorphous germanium films. *Physical Review B*, 2:397, 1970.

[75] J. S. Custer, O. Thompson Michael, D. C. Jacobson, J. M. Poate, S. Roorda, W. C. Sinke, and F. Spaepen. Density of amorphous si. *Applied Physics Letters*, 64:437–439, 1994.

[76] G. T. Fei, J. P. Barnes, A. K. Petford-Long, R. C. Doole, R. Serna, and J. Gonzalo. Structure and thermal stability of fe : Al2o3 nanocomposite films. *Journal of Physics D: Applied Physics*, 35:916–922, 2002.

[77] C. N. Afonso, J. Gonzalo, R. Serna, and J. Solis. *Laser ablation and its applications*. Springer Verlag, 2006.

[78] A. Stesmans and V. V. Afanas'ev. Paramagnetic defects in annealed ultrathin layers of sio_x, al_2o_3, and zro_2 on (100)si. *Applied Physics Letters*, 85:3792–3794, 2004.

[79] A. Stesmans and V. V. Afanasev. Interlayer-related paramagnetic defects in stacks of ultrathin layers of sio_x, al_2o_3, zro_2, and hfo_2 on (100)si. *Journal of Applied Physics*, 97, 2005.

[80] M. Jivanescu, A. Stesmans, and M. Zacharias. Inherent paramagnetic defects in layered si/sio_2 superstructures with si nanocrystals. *Journal of Applied Physics*, 104, 2008.

[81] Timothy H. Gfroerer. Photoluminescence in analysis of surfaces and interfaces. In R.A. Meyers, editor, *Encyclopedia of Analytical Chemistry*, pages 9209, 9231. John Wiley & Sons Ltd, Chichester, 2000.

[82] N. M. Park, T. S. Kim, and S. J. Park. Band gap engineering of amorphous silicon quantum dots for light-emitting diodes. *Applied Physics Letters*, 78:2575–2577, 2001.

[83] Shinji Takeoka, Minoru Fujii, and Shinji Hayashi. Size-dependent photoluminescence from surface-oxidized si nanocrystals in a weak confinement regime. *Physical Review B*, 62:16820, 2000.

[84] C. W. White, J. D. Budai, S. P. Withrow, J. G. Zhu, E. Sonder, R. A. Zuhr, A. Meldrum, D. M. Hembree, D. O. Henderson, and S. Prawer. Encapsulated semiconductor nanocrystals formed in insulators by ion beam synthesis. *Nuclear Instruments and Methods in Physics Research Section B-Beam Interactions with Materials and Atoms*, 141:228–240, 1998.

[85] M. Glover and A. Meldrum. Effect of "buffer layers" on the optical properties of silicon nanocrystal superlattices. *Optical Materials*, 27:977–982, 2005.

[86] M. Zacharias, J. Heitmann, R. Scholz, U. Kahler, M. Schmidt, and J. Blasing. Size-controlled highly luminescent silicon nanocrystals: A sio/sio_2 superlattice approach. *Applied Physics Letters*, 80:661–663, 2002.

[87] Iacona Fabio, Franzo Giorgia, and Spinella Corrado. Correlation between luminescence and structural properties of si nanocrystals. *Journal of Applied Physics*, 87:1295–1303, 2000.

[88] Vinciguerra Vincenzo, Franzo Giorgia, Priolo Francesco, Iacona Fabio, and Spinella Corrado. Quantum confinement and recombination dynamics in silicon nanocrystals embedded in si/sio_2 superlattices. *Journal of Applied Physics*, 87:8165–8173, 2000.

[89] Y. Q. Wang, W. D. Chen, X. B. Liao, and Z. X. Cao. Amorphous silicon nanoparticles in compound films grown on cold substrates for high-efficiency photoluminescence. *Nanotechnology*, 14:1235–1238, 2003.

[90] S. Boninelli, F. Iacona, G. Franzo, C. Bongiorno, C. Spinella, and F. Priolo. Thermal evolution and photoluminescence properties of nanometric si layers. *Nanotechnology*, 16:3012–3016, 2005.

[91] M. L. Brongersma, A. Polman, K. S. Min, E. Boer, T. Tambo, and H. A. Atwater. Tuning the emission wavelength of si nanocrystals in sio[sub 2] by oxidation. *Applied Physics Letters*, 72:2577–2579, 1998.

[92] L. Ferraioli, M. Cazzanelli, N. Daldosso, V. Mulloni, P. Bellutti, S. Yerci, R. Turan, A. N. Mikhaylov, D. I. Tetelbaum, L. Pavesi, and Ieee. *Dielectric matrix influence on the photoluminescence properties of silicon nanocrystals.* 2006 3rd IEEE International Conference on Group IV Photonics. Ieee, New York, 2006.

[93] S. Yerci, U. Serincan, I. Dogan, S. Tokay, M. Genisel, A. Aydinli, and R. Turan. Formation of silicon nanocrystals in sapphire by ion implantation and the origin of visible photoluminescence. *Journal of Applied Physics*, 100:074301, 2006.

[94] D. I. Tetelbaum, A. N. Mikhaylov, O. N. Gorshkov, A. P. Kasatkin, A. I. Belov, D. M. Gaponova, and S. V. Morozov. Ion beam synthesis of si nanocrystals in silicon dioxide and sapphire matrices - the photoluminescence study. *Vacuum*, 78:519–524, 2005.

[95] D. I. Tetelbaum, A. N. Mikhaylov, A. I. Belov, A. V. Ershov, E. A. Pitirimova, S. M. Plankina, V. N. Smirnov, A. I. Kovalev, R. Turan, S. Yerci, T. G. Finstad, and S. Foss. Properties of al_2o_3: nc-si nanostructures formed by implantation of silicon ions into sapphire and amorphous films of aluminum oxide. *Physics of the Solid State*, 51:409–416, 2009.

[96] L. Bi and J. Y. Feng. Nanocrystal and interface defects related photoluminescence in silicon-rich al2o3 films. *Journal of Luminescence*, 121:95–101, 2006.

[97] Q. Wan, T. H. Wang, M. Zhu, and C. L. Lin. Resonant tunneling of si nanocrystals embedded in al_2o_3 matrix synthesized by vacuum electron-beam co-evaporation. *Applied Physics Letters*, 81:538–540, 2002.

[98] P. P. Ong and Y. Zhu. Strong photoluminescence with fine structures from sandwich-structured films of silicon nanoparticles embedded in al_2o_3 matrices. *Physica E-Low-Dimensional Systems and Nanostructures*, 15:118–123, 2002.

[99] L. Patrone, D. Nelson, V. I. Safarov, M. Sentis, W. Marine, and S. Giorgio. Photoluminescence of silicon nanoclusters with reduced size dispersion produced by laser ablation. *Journal of Applied Physics*, 87:3829–3837, 2000.

[100] D. I. Tetelbaum, O. N. Gorshkov, A. V. Ershov, A. P. Kasatkin, V. A. Kamin, A. N. Mikhaylov, A. I. Belov, D. M. Gaponova, L. Pavesi, L. Ferraioli, T. G. Finstad, and S. Foss. Influence of the nature of oxide matrix on the photoluminescence spectrum of ion-synthesized silicon nanostructures. *Thin Solid Films*, 515:333–337, 2006.

[101] P. G. Kik, M. L. Brongersma, and A. Polman. Strong exciton-erbium coupling in si nanocrystal-doped sio[sub 2]. *Applied Physics Letters*, 76:2325–2327, 2000.

[102] J. A. Garcia, R. Plugaru, B. Mendez, J. Piqueras, and T. J. Tate. Resonant excitation of er ion luminescence in a nanocrystalline silicon matrix. *European Physical Journal-Applied Physics*, 27:75–79, 2004.

[103] Y. Song, C. H. Zhang, Z. G. Wang, Y. M. Sun, J. L. Duan, and Z. M. Zhao. Photoluminescence of inert-gas ion implanted sapphire after 230-mev pb ion irradiation. *Nuclear Instruments and Methods in Physics Research Section B: Beam Interactions with Materials and Atoms*, 245:210–213, 2006.

[104] T. Mohanty, N. C. Mishrab, F. Singh, S. V. Bhat, and D. Kanjilal. Color center formation in sapphire by swift heavy ion irradiation. *Radiation Measurements*, 36:723–727, 2003.

[105] K. H. Lee and J. H. Crawford. Luminescence of the f center in sapphire. *Physical Review B*, 19:3217, 1979.

[106] I. Izeddin, A. S. Moskalenko, I. N. Yassievich, M. Fujii, and T. Gregorkiewicz. Nanosecond dynamics of the near-infrared photoluminescence of er-doped sio2 sensitized with si nanocrystals. *Physical Review Letters*, 97:207401, 2006.

[107] C. J. Park, Y. H. Kwon, Y. H. Lee, T. W. Kang, H. Y. Cho, S. Kim, S. H. Choi, and R. G. Elliman. Origin of luminescence from si^--implanted $(1\bar{1}02)$ al_2o_3. *Applied Physics Letters*, 84:2667–2669, 2004.

[108] Albert Polman. Erbium as a probe of everything. *Physica B: Condensed Matter*, 300:78–90, 2001.

[109] Peter Horak, Wei H. Loh, and Anthony J. Kenyon. Modification of the er3+ radiative lifetime from proximity to silicon nanoclusters in silicon-rich silicon oxide. *Opt. Express*, 17:906–911, 2009.

[110] D.B. Chrisey and K.G. Hubler. *Pulsed Laser Deposition of Thin Films*. John Wiley and Sons, 1994.

[111] C. N. Afonso and J. Gonzalo. Pulsed laser deposition of thin films for optical applications. *Nuclear Instruments and Methods in Physics Research Section B-Beam Interactions with Materials and Atoms*, 116:404–409, 1996.

[112] J. Gonzalo, F. Vega, and C. N. Afonso. Plasma expansion dynamics in reactive and inert atmospheres during laser ablation of bi(2)sr(2)ca(1)cu(2)o(7 - y). *Journal of Applied Physics*, 77:6588–6593, 1995.

[113] G. M. Dalpian and J. R. Chelikowsky. Self-purification in semiconductor nanocrystals. *Physical Review Letters*, 96, 2006.

[114] G Dalpian and J Chelikowsky. Dalpian and chelikowsky reply. *Physical Review Letters*, 100:1, 2008.

[115] T. L. Chan, M. L. Tiago, E. Kaxiras, and J. R. Chelikowsky. Size limits on doping phosphorus into silicon nanocrystals. *Nano Letters*, 8:596–600, 2008.

[116] Jhe Ji-Hong, H. Shin Jung, Kim Kyung Joong, and Moon Dae Won. The characteristic carrier–er interaction distance in er-doped a-si/sio[sub 2] superlattices formed by ion sputtering. *Applied Physics Letters*, 82:4489–4491, 2003.

[117] O. Savchyn, F. R. Ruhge, P. G. Kik, R. M. Todi, K. R. Coffey, H. Nukala, and H. Heinrich. Luminescence-center-mediated excitation as the dominant er sensitization mechanism in er-doped silicon-rich sio_2 films. *Physical Review B*, 76:10, 2007.

[118] O. Savchyn, P. G. Kik, R. M. Todi, and K. R. Coffey. Effect of hydrogen passivation on luminescence-center-mediated er excitation in si-rich sio_2 with and without si nanocrystals. *Physical Review B*, 77:11, 2008.

[119] Joseph R Lakowicz. *Principles of Fluorescence Spectroscopy*. Springer, 2006.

[120] Jan Siegel, Daniel S. Elson, Stephen E. D. Webb, K. C. Benny Lee, Alexis Vlandas, Giovanni L. Gambaruto, Sandrine Leveque-Fort, M. John Lever, Paul J. Tadrous, Gordon W. H. Stamp, Andrew L. Wallace, Ann Sandison, Tim F. Watson, Fernando Alvarez, and Paul M. W. French. Studying biological tissue with fluorescence lifetime imaging: microscopy, endoscopy, and complex decay profiles. *Appl. Opt.*, 42:2995–3004, 2003.

[121] B. Sturman, E. Podivilov, and M. Gorkunov. Origin of stretched exponential relaxation for hopping-transport models. *Physical Review Letters*, 91:176602, 2003.

[122] A. J. Kenyon, M. Wojdak, I. Ahmad, W. H. Loh, and C. J. Oton. Generalized rate-equation analysis of excitation exchange between silicon nanoclusters and erbium ions. *Physical Review B (Condensed Matter and Materials Physics)*, 77:035318–9, 2008.

[123] Randy Ellingson. Solar cells: Slicing and dicing photons. *Nat Photon*, 2:72–73, 2008.

[124] D. Timmerman, I. Izeddin, P. Stallinga, I. N. Yassievich, and T. Gregorkiewicz. Space-separated quantum cutting with silicon nanocrystals for photovoltaic applications. *Nat Photon*, 2:105–109, 2008.

[125] Joseph M. Luther, Matthew C. Beard, Qing Song, Matt Law, Randy J. Ellingson, and Arthur J. Nozik. Multiple exciton generation in films of electronically coupled pbse quantum dots. *Nano Letters*, 7:1779–1784, 2007.

[126] Kei Watanabe, Minoru Fujii, and Shinji Hayashi. Resonant excitation of er^{3+} by the energy transfer from si nanocrystals. *Journal of Applied Physics*, 90:4761–4767, 2001.

[127] Lukas Novotny and Bert Hecht. *Principles of Nano-optics*. Cambridge university press, 2007.

[128] C. Bulutay. Interband, intraband, and excited-state direct photon absorption of silicon and germanium nanocrystals embedded in a wide band-gap lattice. *Physical Review B*, (20), 2007.

[129] Matthew C. Beard, Kelly P. Knutsen, Pingrong Yu, Joseph M. Luther, Qing Song, Wyatt K. Metzger, Randy J. Ellingson, and Arthur J. Nozik. Multiple exciton generation in colloidal silicon nanocrystals. *Nano Letters*, 7:2506–2512, 2007.

[130] Richard D. Schaller, Milan Sykora, Jeffrey M. Pietryga, and Victor I. Klimov. Seven excitons at a cost of one: redefining the limits for conversion efficiency of photons into charge carriers. *Nano Letters*, 6:424–429, 2006.

[131] R. D. Schaller and V. I. Klimov. High efficiency carrier multiplication in pbse nanocrystals: implications for solar energy conversion. *Physical Review Letters*, 92:186601, 2004.

[132] G. Franzo, V. Vinciguerra, and F. Priolo. The excitation mechanism of rare-earth ions in silicon nanocrystals. *Applied Physics a-Materials Science and Processing*, 69:3–12, 1999.

[133] A. J. Kenyon, C. E. Chryssou, C. W. Pitt, T. Shimizu-Iwayama, D. E. Hole, N. Sharma, and C. J. Humphreys. Luminescence from erbium-doped silicon nanocrystals in silica: Excitation mechanisms. *Journal of Applied Physics*, 91:367–374, 2002.

[134] Domenico Pacifici, Giorgia Franzo, Francesco Priolo, Fabio Iacona, and Luca Dal Negro. Modeling and perspectives of the si nanocrystals-er interaction for optical amplification. *Physical Review B*, 67:245301, 2003.

[135] A. A. Prokofiev, A. S. Moskalenko, and I. N. Yassievich. Excitation of er^{3+} ions in sio_2 with si nanocrystals. *Semiconductors*, 42:971–979, 2008.

[136] P. Noe, H. Okuno, J. B. Jager, E. Delamadeleine, O. Demichel, J. L. Rouviere, V. Calvo, C. Maurizio, and F. D'Acapito. The evolution of the fraction of er ions sensitized by si nanostructures in silicon-rich silicon oxide thin films. *Nanotechnology*, 20:8, 2009.

[137] S. Minissale, T. Gregorkiewicz, M. Forcales, and R. G. Elliman. On optical activity of er^{3+} ions in si-rich sio_2 waveguides. *Applied Physics Letters*, 89:171908–3, 2006.

[138] Roberto Guerra, Ivan Marri, Rita Magri, Layla Martin-Samos, Olivia Pulci, Elena Degoli, and Stefano Ossicini. Silicon nanocrystallites in a sio_2 matrix: Role of disorder and size. *Physical Review B*, 79:155320, 2009.

[139] Claude Cohen-Tannoudji, Bernard Diu, and Franck Laloe. *Quantum Mechanics*, volume One of *Textbook physics*. 1997.

[140] C. Garcia, P. Pellegrino, Y. Lebour, B. Garrido, F. Gourbilleau, and R. Rizk. Maximum fraction of er3+ ions optically pumped through si nanoclusters. *Journal of Luminescence*, 121:204–208, 2006.

[141] C. J. Oton, W. H. Loh, and A. J. Kenyon. er^{3+} excited state absorption and the low fraction of nanocluster-excitable er^{3+} in sio_x. *Applied Physics Letters*, 89:031116, 2006.

[142] Clifford R. Pollock. *Fundamentals of Optoelectronics*. Casson, Tom, 1 edition, 1995.

[143] Gerlas N. van den Hoven, Jan A. van der Elsken, Albert Polman, Cor van Dam, Koos W. M. van Uffelen, and Meint K. Smit. Absorption and emission cross sections of er^{3+} in al_2o_3 waveguides. *Applied Optics*, 36:3338–3441, 1997.

[144] Joseph T. Verdeyen. *Laser Electronics*. Solid state physical electronics. Prentice Hall, New Jersey, third edition edition, 1995.

[145] E. Desurvire. *Erbium-Doped Fiber Amplifiers, Principles and Applications*. Wiley-Interscience, 2002.

[146] E. Desurvire and J. R. Simpson. Evaluation of 4i15/2 and 4i13/2 stark-level energies in erbium-doped aluminosilicate glass fibers. *Opt. Lett.*, 15:547–549, 1990.

[147] Jose Garcia Sole, Luisa Bausa, and Daniel Jaque. *An Introduction to the Optical Spectroscopy of Inorganic Solids*. 2005.

[148] F. Alvarez, A. Alegra, and J. Colmenero. Relationship between the time-domain kohlrausch-williams-watts and frequency-domain havriliak-negami relaxation functions. *Physical Review B*, 44:7306, 1991.

[149] D. C. Johnston. Stretched exponential relaxation arising from a continuous sum of exponential decays. *Physical Review B (Condensed Matter and Materials Physics)*, 74:184430, 2006.

[150] K. C. B. Lee, J. Siegel, S. E. D. Webb, S. Leveque-Fort, M. J. Cole, R. Jones, K. Dowling, M. J. Lever, and P. M. W. French. Application of the stretched exponential function to fluorescence lifetime imaging. *Biophysical Journal*, 81:1265–1274, 2001.

[151] $http://en.wikipedia.org/wiki/stretched_exponential_function$.